

The Breakage of Needle-Shaped Crystals Under Pressure Filtration

Andrew Philip Shier

Submitted in accordance with the requirements for the degree of
Doctor of Philosophy

The University of Leeds
School of Chemistry

March 2017

The candidate confirms that the work submitted is his/her own and that appropriate credit has been given where reference has been made to the work of others.

This copy has been supplied on the understanding that it is copyright material and that no quotation from the thesis may be published without proper acknowledgement.

The right of Andrew Philip Shier to be identified as Author of this work has been asserted by him in accordance with the Copyright, Designs and Patents Act 1988.

© 2016 The University of Leeds and Andrew Philip Shier

Acknowledgements

I would first and foremost like to thank my supervisor Professor Frans Muller for the inspiration for this thesis and the personal training he has provided me with over the prior 3 years. I would also like to thank my co-supervisor Prof. Kevin Roberts for his input into the project. I'm grateful for the funding provided by the University of Leeds and the EPSRC, which helped to fund this research.

My colleagues within the iPRD laboratory have been invaluable in assisting my progression through this project, particularly Dr. Katie Jolley and Dr. Mary Bayana. I would also like to thank the staff in the department of chemistry for additional assistance, including Prof. John Blacker for his work as internal supervisor to the project, and Matthew Broadbent for his mechanical engineering expertise. I wish to thank Guangyi Xu and Bruno De Mello Reggiori for their help with a variety of crystallisation studies.

I would also like to express my gratitude to Professors Richard Holdich and Mojtaba Ghadiri for agreeing to be my external and internal examiners, respectively.

I am whole-heartedly grateful for the financial assistance provided by AstraZeneca and for granting me a unique working experience at their site in Macclesfield. I would particularly like to thank my industrial supervisor Claire Macleod, whose prior work helped to inspire this project.

I would also like to thank my friends within Leeds and London for providing some light relief from the trials of everyday postgraduate study. A great thanks to Dr. Mindaugas Paulauskas who gave me the impetus to begin learning programming, which has been a source of much enjoyment and frustration.

I also wish to thank my entire family, in particular my parents, for everything they have ever done in providing me with the best possible opportunities in life. It is due to their unwavering efforts that I have been given the chance to complete my higher education studies.

Finally I wish to thank my partner Abigail for her continuing love, support and companionship that she has provided me with over the last decade.

This thesis is dedicated to the memory of Eve, Clyde and Daisy.

Abstract

Pressure filtration is one of the most common solid-liquid separation techniques in use in the fine chemical and pharmaceutical industry. Typically pressure filtrations are conducted within the same unit operation as agitated drying, thus the opportunity to study the individual effects of filtration are often negated. Recent findings have shown pressure filtration to be a major cause of particle breakage, which has consequences for product quality, bioavailability and downstream operations like formulation.

A new method for the investigation of the effect of hydrodynamic stress on static crystals has been developed by continuously recirculating fluid through a bed of freshly crystallised particles. The method is compared to traditional batch pressure filtration tests with good correlation between results. Levels of breakage of needle-like glutamic acid crystals are found to increase with rises in pressure and fluid flow rate.

Particle size and shape data obtained from optical microscopy is critically analysed in order to determine the type and extent of crystal breakage. Automated methods have also been developed to filter particle data in order to provide a more representative measurement.

Small-scale centrifugal testing of particle beds has been conducted with an analytical photo-centrifuge. Needle-like crystal beds are found to consolidate to greater extents than more rounded particles, and also show evidence of inelastic behaviour. The more isometric particles conversely display elastic behaviour in response to the application of stress.

Modelling of particle data has simulated algorithmic breakage events to predict the breakage observed under pressure filtration, with good agreement between modelled and experimental particle size distributions. The structure of particle beds has also been modelled by generation of simulated needle-beds from particle length data.

Table of Contents

1	Introduction.....	1
1.1	Research Background.....	1
1.2	Research Structure.....	4
2	Background Theory and Literature Review.....	6
2.1	Introduction.....	6
2.2	Particle and Fluid flow Models.....	6
2.2.1	Background.....	6
2.2.2	Forces experienced under fluid flow.....	7
2.2.3	Flow through a packed bed of particles.....	9
2.3	Particle Size Characterisation.....	10
2.3.1	Particle definitions and material characterisation.....	10
2.3.2	Particle size representations.....	13
2.3.3	Methods of particle size analysis.....	13
2.3.3.1	Sampling.....	14
2.3.3.2	Optical analysis techniques.....	15
2.4	Crystals and Crystallisation.....	18
2.4.1	Crystallisation and solubility.....	18
2.4.1.1	Nucleation.....	20
2.4.2	Crystal form.....	21
2.4.2.1	Crystal habit/morphology.....	21
2.4.2.2	Polymorphic form.....	21
2.4.3	Industrial crystallisation and control.....	22
2.4.3.1	Batch Operation.....	22
2.4.3.2	Super-Saturation Control.....	23
2.4.3.3	Effect of Secondary Nucleation.....	24
2.4.3.4	Monitoring of Crystallisation.....	25
2.5	Filtration.....	25
2.5.1	Basics of industrial filtration.....	25
2.5.1.1	Filter media.....	26
2.5.2	Factors influencing filtration performance.....	27
2.5.2.1	Pressure Drop.....	27
2.5.2.2	Cake compressibility.....	28
2.5.2.3	Particle Shape/ Morphology.....	29

2.5.2.4	Suspension Solid Concentration.....	29
2.5.2.5	Particle size and size distribution	30
2.5.2.6	Scale-up	30
2.5.3	Filtrate rate modelling.....	31
2.6	Mechanical Properties of Particles / Breakage	33
2.6.1	Fundamentals of particle breakage.....	33
2.6.1.1	Stress and strain	35
2.6.1.2	Crack propagation	35
2.6.1.3	Tensile strength of a particle	36
2.6.1.4	Attrition	37
2.6.2	Process causes of breakage	38
2.6.2.1	Impact forces	38
2.6.2.2	Under filtration.....	38
3	Materials and Methods	41
3.1	Introduction.....	41
3.2	Design and Assembly of a Bench-scale Continuous Percolation Rig (CPR)	41
3.2.1	Equipment identification and problem overview.....	41
3.2.1.1	Theoretical estimation of flow through a packed bed & pump selection.....	43
3.2.1.2	Filter insert design (sampling of filter cake).....	45
3.2.1.3	Heat exchanger design	48
3.2.1.3.1	Theoretical basis for heat exchange design.....	48
3.2.1.4	Pump calibration	51
3.2.1.5	Thermal bath control.....	53
3.3	Operation of the Continuous Percolation Rig	55
3.3.1	Final equipment layout.....	55
3.3.2	Experimental method.....	58
3.3.2.1	Pre-experimental.....	58
3.3.2.2	Operation.....	59
3.3.2.3	Shutdown.....	59
3.4	500 mL Crystallisation Procedure.....	60
3.4.1	Glutamic acid	61
3.4.1.1	Beta (β) glutamic acid polymorph	61
3.4.1.2	Alpha (α) glutamic acid polymorph	62
3.4.2	Lesinurad	62
3.4.3	Urea and Urea-Biuret	62

3.5	2 L Batch Pressure Filter Methodology	62
3.5.1	Crystallisation preparations for 2 Litre scale	63
3.5.2	Batch filtration at 2 Litre scale.....	64
3.5.2.1	Performing pressure filtration.....	64
3.5.2.2	Retrieving the cake	64
3.6	Metastable Zone Width Determination with HEL AutoMATEs	65
3.7	Particle Sizing with the Morphologi G3 Optical Microscope.....	66
3.8	Particle Sizing with the Sympatec HELOS Laser Diffractometer.....	68
3.9	Optical Microscopy with Leitz Diaplan Optical Microscope	70
3.10	Use of the LUMiSizer for Centrifugation of Packed Beds.....	71
3.10.1	Sample preparation	71
3.10.2	Instrument standard operating procedure.....	71
4	Particle Engineering of Crystal Habits.....	73
4.1	Introduction.....	73
4.2	Glutamic Acid	73
4.2.1	Solubility data	74
4.3	Urea and Urea-Biuret	76
4.3.1	Solubility data	79
4.3.2	Morphological variation through control of crystallisation	81
4.4	Lesinurad	87
4.4.1	Solubility data	89
4.5	Conclusions.....	90
5	Particle Size Distribution Representations and Critical Analysis of Particle Data ...	92
5.1	Introduction.....	92
5.2	Literature Review	92
5.3	Methods of Representing Particle Size Distribution	95
3.1.1	Background on the collection of particle data with the Morphologi G3.	95
5.3.1	Particle size distribution representations.....	97
5.3.1.1	Method 1a – number fraction histogram.....	97
5.3.1.2	Method 1b – volume fraction histogram	98
5.3.1.3	Method 2a – number fraction based population density function.....	99
5.3.1.4	Method 2b – volume fraction-based population density function.....	100
5.3.1.5	Method 3a – volume-based number fraction distribution	101
5.3.1.6	Method 3b – volume/number-based population density function.....	104

5.3.1.7	Method 4 – aspect ratio number distribution.....	105
5.4	Validity of Data	107
5.4.1	Critical analysis of Morphologi G3 data.....	107
5.4.2	Data filtering.....	109
5.4.2.1	Manual filtering of data.....	114
5.4.2.2	Effects of data filtering on particle size distribution	115
5.4.2.3	Automation of data filtering through computational scripting.....	117
5.4.3	Reproducibility of measurement.....	121
5.5	Conclusions.....	125
6	Investigation into the Changes in Particle Size Distribution from Percolation of Liquid through a Packed Bed of Particles.....	128
6.1	Introduction.....	128
6.2	Use of the Continuous Percolation Rig to Investigate the Effects of Liquid Flowrate on Particle Size Reduction.....	128
6.2.1	Introduction.....	128
6.2.2	Data collection methods.....	129
6.2.3	Results and discussion.....	130
6.2.3.1	Experimental outline	130
6.2.3.2	Microscopic image analysis	133
6.2.3.3	Size and shape distribution analysis.....	139
6.2.3.4	Change in size and shape distribution across fluid flow rate.	144
6.2.3.4.1	Analysis of size changes due to flowrate	151
6.2.3.4.2	Critical analysis of experimental methods and discussion of error ...	153
6.2.3.5	Effect of continuous percolation time on size distribution	154
6.3	Batch Filtrations of Crystal Suspensions on a 2 Litre Scale	155
6.3.1	Introduction.....	155
6.3.2	Data collection methods.....	157
6.3.3	Calculation of filter resistances	158
6.3.4	Results and discussion.....	161
6.3.4.1	Experimental outline	161
6.3.4.2	Microscopic image analysis	163
6.3.4.3	Filtrate flow rate and cake compressibility	174
6.3.4.4	Dispersion pressure titration.....	179
6.3.4.5	Particle size analysis by Sympatec laser diffraction	185
6.3.4.5.1	Sample vial observations	185
6.3.4.5.2	Particle size distributions.....	186

6.3.4.5.3	Changes in size fractions of the distribution	193
6.3.4.6	Morphologi G3 data analysis	197
6.4	Conclusions.....	204
7	Investigation into the Centrifugal Settling Behaviour of Crystal Beds	206
7.1	Introduction.....	206
7.2	Literature Review	209
7.2.1	Background.....	209
7.2.2	Use of the LUMiSizer	210
7.3	LUMiSizer Measurement Technique	211
7.4	A Model for the Calculation of Compressive Pressure Forces within a Bed of Particles	212
7.4.1	Pressure drop over the bed	212
7.4.2	Model results.....	215
7.5	Experimental Results and Discussion	217
7.5.1	Experimental outline	217
7.5.2	Traces of sediment bed height over time whilst under centrifugation.	220
7.5.2.1	Glutamic acid.....	220
7.5.2.2	Urea and urea-biuret.....	222
7.5.2.3	Lesinurad	224
7.5.3	Bed Relaxation.....	224
7.5.4	Particle Image and Size Analysis.....	228
7.6	Conclusions.....	232
8	Modelling of Breakage and Needle Particle Beds.....	234
8.1	Introduction.....	234
8.2	Literature Review	234
8.3	Modelling of Experimental Filtration Data and Predictions of Breakage.....	236
8.3.1	Model structure.....	236
8.3.1.1	Calculation of estimated pressure drop for experiments in the CPR.....	238
8.3.2	Model results.....	240
8.3.2.1	Probability factors	240
8.3.2.2	Predicted size distributions and commentary on model fit ...	242
8.4	Modelling of Needle-like Crystal Beds	246
8.4.1	Introduction and experimental input to the model	246
8.4.2	Model structure.....	247
8.4.2.1	Object oriented programming and the ‘particle object’	247
8.4.2.2	Particle generation and legality.....	248

8.4.2.3	Evaluation of particle contacts in 2D space.....	249
8.4.2.4	Data structure – ‘sectors’ to narrow search for contacts.....	250
8.4.2.5	Placement of particles in 3d space	250
8.4.2.5.1	Placement with 0 contacts.....	251
8.4.2.5.2	Evaluation of particle/contact height	251
8.4.2.5.3	Placement with 1 contact	252
8.4.2.5.4	Placement with 2 contacts.....	254
8.4.2.5.5	Placement with more than 2 contacts.....	254
8.4.2.6	Assignment, determination and calculation of various bed properties	256
8.4.3	Model output and discussion of data	258
8.4.3.1	Visual bed structure.....	258
8.4.3.2	Bed bulk density	259
8.4.3.3	Particle contact points.....	261
8.4.4	Discussion of model applicability and limitations	263
8.5	Conclusions.....	265
9	Conclusions and Future Experimentation	268
9.1	Introduction.....	268
9.2	Conclusions and Thesis Summary	268
9.3	Future Work	273
10	Appendices	275
10.1	Appendix A: Additional 2 Litre Filtration Microscopic Images	275
10.2	Appendix B: Additional Bed Building Modelling Data	277
11	References.....	283

List of Tables

Table 3-1: List of values used to estimate fluid flow through a packed bed of diameter 3.5 cm.....	44
Table 3-2: Table of estimated power to be transferred from the process fluid.....	49
Table 3-3: Differential liquid flow between empty filter tube and tube containing glutamic acid cake (L/h)	53
Table 3-4: List of components of the CPR	55
Table 3-5: List of labels for samples selected for particle size analysis	60
Table 4-1: Variations in morphology from crystallisation of pure urea in ethanol and methanol.....	84
Table 4-2: Variations in morphology from crystallisation of urea/biuret in ethanol and methanol.....	85
Table 5-1: Selections of particles resulting from data filtering on the G3 software interface – particles are sorted into a ‘cloud distribution’ of elongation vs. circularity, after which areas of the distribution can be manually highlighted to view particles within the selected parameter range	111
Table 5-2: Boundary conditions of elongation vs. circularity for a single data-set	114
Table 6-1: Information on seed batches used for experimentation	131
Table 6-2: Experiments performed with the percolation rig (500 mL crystallising solution volume).....	132
Table 6-3: Changes in size fractions f_s , f_m and f_L for LF and PF powder samples tested in the CPR across flowrates 31.1 – 159.5 L/h.....	147
Table 6-4: Changes in shape fractions f_e , f_p and f_r for LF and PF powder samples tested in the CPR across flowrates 31.1 – 159.5 L/h	148
Table 6-5: Changes in size and aspect ratio fractions for exps. 40c and 40d	155
Table 6-6: Constants and variables used in the calculation of cake and medium resistances.....	160
Table 6-7: Table of experiments conducted in the 2L crystallisation vessel and 2L pressure filter	162
Table 6-8: Microscopic images of beta-glutamic acid samples before and after filtration	164
Table 6-9: Microscopic images of alpha-glutamic acid samples before and after filtration	167
Table 6-10: Microscopic images of Lesinurad samples before and after filtration	170
Table 6-11: Cake resistance and log(cake resistance) for the 3 crystal systems	178
Table 6-12: Experimental conditions for particle sizing of each compound.....	185
Table 6-13: Particle sizes binding the size fractions f_s , f_m , f_L	194
Table 6-14: Calculated f_s , f_m , f_L , Δf_s , Δf_m and Δf_L for β -glutamic acid, α -glutamic acid and Lesinurad.....	194

Table 7-1: Data from calculation of the total integrated compressive pressure acting over a bed of beta-glutamic acid particles.....	215
Table 7-2: Total compressive pressure over the particle beds for the systems investigated.....	216
Table 7-3: Table of systems investigated.....	218
Table 7-4: Experimental bed heights and bulk density as a function of centrifugal rpm	218
Table 7-5: Bed relaxations for each particle system at a range of centrifugal decelerations.....	225
Table 8-1: List of values used to estimate fluid flow through a packed bed of diameter 3.5 cm.....	239
Table 8-2: List of values used to estimate fluid flow through a packed bed at a flowrate of 31.1 L/h.....	239
Table 8-3: List of values used to estimate fluid flow through a packed bed at a flowrate of 127.5 L/h.....	239
Table 8-4: Probability factors for particles of a particular aspect ratio.....	240
Table 8-5: Probability factors for a selection of particles based on their size (modelled volume).....	240
Table 8-6: Probability factors for a range of filtration pressures.....	241
Table 8-7: Masses of 11 mm³ vacuum filtered beta-glutamic acid samples.....	256
Table 8-8: Mean bulk bed properties for the simulation ran with differing particle input counts.....	258
Table 10-1: Additional microscope images for beta-glutamic acid 'PFB' samples filtered on 2 L scale.....	275
Table 10-2: Additional simulation data for bed building model of varying particle addition counts.....	277

List of Figures

Figure 1-1: Flow chart of the project structure	4
Figure 2-1: Force balance on a spherical particle falling through a liquid	7
Figure 2-2: Comparison of different 2D shape sizes	11
Figure 2-3: Schematic of the illumination of a sample by a cone of light.....	16
Figure 2-4: Schematic of the laser diffraction principle	17
Figure 2-5: Regions of the Solubility Curve. Reproduced from[37].....	19
Figure 2-6: Free energy changes under nucleation. Reproduced from[19]	20
Figure 2-7: Effect of increasing pressure on filtration flowrate for particle beds of varying compressibility	28
Figure 2-8: Effect of curvature on the concentration of stress. Reproduced from[86]	34
Figure 2-9: Example stress-strain graph (not indicative of any particular material). Reproduced from[86].....	35
Figure 3-1: Basic proposed schematic for the 'continuous filter' rig design	42
Figure 3-2: The filter tube (pen shown for size reference – pen is approx. 145 mm long x 12mm diameter).....	42
Figure 3-3: AutoCAD schematic of the filter-chamber insert.....	46
Figure 3-4: (Left) Technical drawing of the filter insert; (Right) The finished equipment.	47
Figure 3-5: Schematic of counter-current tube-in-tube heat exchanger design	48
Figure 3-6: Technical drawing of the final heat exchanger design.....	50
Figure 3-7: P200 pumping calibration plot of delivery vs. inverter frequency.....	52
Figure 3-8: Raspberry Pi micro-computer controller	54
Figure 3-9: GUI of Python software interface for control of Julabo heater-chiller.....	54
Figure 3-10: Photograph of the final constructed rig (Julabo heater-chiller bath not pictured).....	56
Figure 3-11: Process flow diagram of the final design	56
Figure 3-12: Technical drawing of the final design (equipment excluding pump is to scale; pipe-lines are not)	57
Figure 3-13: Block diagram of the CPR operation procedure	58
Figure 3-14: The HEL 500 mL calorimeter apparatus	61
Figure 3-15: (Left) 2 Litre glass crystallisation vessel; (Right) 2 Litre pressure filter/dryer	63
Figure 3-16: (Left) Sampling the cake from inside the pressure filter; (Right) The filter medium with cake material resting on top – used as a source of material from the bottom of the cake.....	65
Figure 3-17: The HEL AutoMATE parallel reactor apparatus	66
Figure 3-18: The Malvern Morphologi G3 optical microscope	67

Figure 3-19: Morphologi G3 sample dispersion unit (a), measuring spatula (b) and sample cell (c)	68
Figure 3-20: The Sympatec HELOS laser diffraction particle sizer.....	69
Figure 3-21: A sample vial containing beta-glutamic acid loaded into the ASPIROS sample delivery system, ready for injection into the analysis module	69
Figure 3-22: Leitz Diaplan optical microscope	70
Figure 3-23: SOP for samples operated in the LUMiSizer – screenshot taken from software GUI.....	72
Figure 4-1: Chemical structure of L-glutamic acid[95]	73
Figure 4-2: (Left) Needle-like beta(β)-glutamic acid; (Right) prismatic alpha(α)-glutamic acid	74
Figure 4-3: Solubility of LGA in water [97, 99-101]	75
Figure 4-4: Literature data versus predicted solubility based on line-fitting.....	76
Figure 4-5: Chemical structures of Urea and Biuret.....	77
Figure 4-6: Urea’s typical crystal morphology from polar solvents (crystal faces highlighted)	77
Figure 4-7: Solubility curve for urea in EtOH (literature solubility from Lee and Lahti[106])	79
Figure 4-8: Van’t Hoff plot of literature and measured solubility for urea in ethanol	80
Figure 4-9: Solubility curve for urea in MeOH (literature solubility from Lee and Lahti[106])	80
Figure 4-10: Van’t Hoff plot of literature and measured solubility for urea in methanol.	81
Figure 4-11: Chemical structure of Lesinurad (Mol. weight of 404.29)[108]	88
Figure 4-12: Lesinurad needle-like particles.....	88
Figure 4-13: Solubility data for Lesinurad	89
Figure 4-14: Van’t Hoff plot of Lesinurad solubility in acetonitrile	89
Figure 5-1: Schematic of needles in a typical resting state on a flat surface	96
Figure 5-2: Histogram of $F(N_i)$ vs d_i for beta-glutamic acid before and after percolation at 47.2 L/h	98
Figure 5-3: Histogram of $F(V_i)$ vs. d_i for beta-glutamic acid before and after percolation at 47.2 L/h	99
Figure 5-4: Population density function of dP_N/dd_i for beta-glutamic acid before and after percolation at 47.2 L/h.....	100
Figure 5-5: Population density function of dP_V/dd_i for beta-glutamic acid before and after percolation at 47.2 L/h.....	101
Figure 5-6: Modelling a needle-like (glutamic acid) particle as a rectangular cuboid with length ‘L’, width ‘W’ and depth ‘0.5 * W’ (width = 2 * depth).....	102
Figure 5-7: Volume-based number fraction histogram of $F(N_i)$ vs. $\ln(V_p)$, assuming cuboidal particles of volume $l_p * 0.5 * w_p^2$; for beta-glutamic acid before and after percolation at 47.2 L/h.....	103

Figure 5-8: Volume-based population density function of $dP_N/d\ln(V_p)$ vs. $\ln(V_p)$, assuming cuboidal particles of volume $l_p \cdot 0.5 \cdot w_p^2$; for beta-glutamic acid before and after percolation at 47.2 L/h	104
Figure 5-9: Distribution of number fraction of particles of aspect ratio in bracket 'i' vs. aspect ratio for beta-glutamic acid before and after percolation at 47.2 L/h	105
Figure 5-10: Change in aspect ratio of a theoretical particle breaking into 2 fragments.	106
Figure 5-11: Scaled representation of particle size areas – the particle has CE diameter equal to 193 microns but an area of $L \cdot W$ equivalent to a particle of CE diameter equal to 633 microns.....	107
Figure 5-12: Example crystal of beta-glutamic acid as scanned from Morphologi G3 Optical Microscope	108
Figure 5-13: Examples of 'poorly scanned' 'crystals'	108
Figure 5-14: Particle size distribution of elongation vs. circularity, with 'desired' particles (i.e. particles that will stay as part of the distribution data) highlighted using a parameter-defined polygon. Particles outside the distribution are removed from the data-set	114
Figure 5-15: Filtered and unfiltered number distribution data (method 1a) for beta-glutamic acid before and after percolation at 47.2 L/h	115
Figure 5-16: Filtered and unfiltered volume distribution data (method 2b) for beta-glutamic acid before and after percolation at 47.2 L/h. Arrows represent the shift in the data from the unfiltered to the filtered datasets – indicates a large overall reduction in average size	116
Figure 5-17: Filtered and unfiltered number-volume distribution data (method 3a) for beta-glutamic acid before and after percolation at 47.2 L/h	117
Figure 5-18: Example initial hand-drawn polygon overlaid onto a cloud plot of particles (screenshot within Morphologi G3 software GUI)	118
Figure 5-19: Updated polygon with boundaries dictating the extents of the filtering algorithm.....	118
Figure 5-20: Screenshot of the 'Particle PyFilter' software GUI.....	120
Figure 5-21: Comparison of manual-filtering of data with automatic filtering by software algorithm for beta-glutamic acid before and after percolation at 47.2 L/h.....	121
Figure 5-22: Results of a variability analysis for 4 separate measurements of LF samples of beta-glutamic acid (i.e. no percolation performed)	122
Figure 5-23: Results of a variability analysis for 4 separate measurements of PF samples of beta-glutamic acid (i.e. percolated at 47.2 L/h)	122
Figure 5-24: Mean values of number fraction of $\ln V_p$ for 4 separately measured samples with standard deviation; for beta-glutamic acid before and after percolation at 47.2 L/h. The 'thickness' of the distribution is therefore evident from the y-axis deviation in the results	123

Figure 5-25: Curves of (mean value + standard deviation) and (mean value – standard deviation) for 4 separately measured samples of LF and PF powder samples of beta-glutamic acid before and after percolation at 47.2 L/h; number fraction vs. $\ln V_p$. Distribution ‘thickness’ is evident from the separation between each sample types’ curves124

Figure 5-26: Mean values of $\ln V_p$ vs a single dataset containing all particles from samples 1-4 for each LF and PF sample set; for beta-glutamic acid before and after percolation at 47.2 L/h.....125

Figure 6-1: Microscopic images of beta-glutamic acid crystals before and after percolation at 31.1 L/h flow rate; left column: vacuum filtered samples (no percolation); right column: samples tested in CPR. Sample images obtained from experiment ‘10b’ material. No significant difference is observed in the crystal morphology134

Figure 6-2: Microscopic images of beta-glutamic acid crystals before and after percolation at 127.5 L/h flow rate; left column: vacuum filtered samples (no percolation); right column: samples percolated in CPR. Sample images obtained from experiment ‘40f’ material. Significant changes in particle size are observed137

Figure 6-3: Microscopic images of beta-glutamic acid crystals before and after percolation at 127.5 L/h flow rate; left column: samples tested in CPR from the TOP of the cake; right column: samples tested in CPR from the BOTTOM of the cake. Sample images obtained from experiment ‘40f’ material. More breakage is evident in the PFB sample than in the PFT138

Figure 6-4: $l_p*0.5*w_p^2$ distribution for 31.1 L/h percolation of beta-glutamic acid (exp. 10b).....139

Figure 6-5: Aspect ratio distribution for 31.1 L/h percolation of beta-glutamic acid (exp. 10b)140

Figure 6-6: $l_p*0.5*w_p^2$ distribution for 127.5 L/h percolation of beta-glutamic acid (exp. 40f).....140

Figure 6-7: Aspect ratio distribution for 127.5 L/h percolation of beta-glutamic acid (exp. 40f)141

Figure 6-8: Normalised modelled particle volume changes at percolation flow of 31.1 L/h (exp. 10b)143

Figure 6-9: Normalised modelled particle volume changes at percolation flow of 127.5 L/h (exp. 40f)143

Figure 6-10: Graphical depictions of the fractions by which the particle modelled volume size distributions are divided by144

Figure 6-11: Graphical depictions of the fractions by which the aspect ratio size distributions are divided by145

Figure 6-12: Changes in size fractions of modelled particle volume as a function of CPR flowrate, for beta-glutamic acid with and without percolation149

Figure 6-13: Changes in shape fractions of aspect ratio as a function of CPR flowrate, for beta-glutamic acid with and without percolation.....149

Figure 6-14: Mean changes in size fractions as a function of fluid flowrate, for beta-glutamic acid with and without percolation. Error bars represent standard deviation150

Figure 6-15: Mean changes in aspect ratio fractions as a function of fluid flowrate, for beta-glutamic acid with and without percolation. Error bars represent standard deviation	150
Figure 6-16: Critical points in the breakage of particles under percolation.....	152
Figure 6-17: $I_p \cdot 0.5 \cdot w_p^2$ distribution for 127.5 L/h percolation of β -glutamic acid (exps. 40c and 40d)	154
Figure 6-18: Aspect ratio distribution for 127.5 L/h percolation of β -glutamic acid (exps. 40c and 40d)	154
Figure 6-19: The 2 L scale pressure filter/dryer	156
Figure 6-20: Plot of filtrate flow out of the 2 Litre pressure filter over time for Lesinurad at 1.6 bar pressure	159
Figure 6-21: t/V vs volume of collected filtrate for Lesinurad at 1.6 bar filtration pressure	160
Figure 6-22: Filtrate mass flow over time for the 3 systems at filtration pressures of 0.5, 1.6 and 3 bar	174
Figure 6-23: t/V against volume for β -glutamic acid filtered in 2 Litre pressure filter at 0.5, 1.6 and 3 bar	176
Figure 6-24: t/V against volume for α -glutamic acid filtered in 2 Litre pressure filter at 0.5, 1.6 and 3 bar	176
Figure 6-25: t/V against volume for Lesinurad filtered in 2 Litre pressure filter at 0.5, 1.6 and 3 bar.....	177
Figure 6-26: $\log(\alpha)$ against $\log(P)$ for calculation of compressibility indices.....	178
Figure 6-27: β -glutamic acid particle size distributions for pressure titration test from 0.5 – 4 bar dispersion	180
Figure 6-28: α -glutamic acid particle size distributions for pressure titration test from 0.5 – 4 bar dispersion	181
Figure 6-29: Lesinurad particle size distributions for pressure titration test from 0.5 – 5 bar dispersion	181
Figure 6-30: Lesinurad particle size distributions at 0.5 bar dispersion	183
Figure 6-31: Lesinurad particle size distributions at 1 bar dispersion	183
Figure 6-32: Sympatec HELOS sample vials containing Lesinurad powder filtered at 1.6 bar.....	185
Figure 6-33: Particle size distributions for the 3 systems filtered at 0.5 bar	186
Figure 6-34: Particle size distributions for the 3 systems filtered at 1.6 bar	187
Figure 6-35: Particle size distributions for the 3 systems filtered at 3 bar	187
Figure 6-36: Size distributions of pressure filtered samples for beta-glutamic acid filtered at 0.5, 1.6 and 3 bar	189
Figure 6-37: Size distributions of pressure filtered samples for alpha-glutamic acid filtered at 0.5, 1.6 and 3 bar	189
Figure 6-38: Size distributions of pressure filtered samples for Lesinurad filtered at 0.5, 1.6 and 3 bar.....	190

Figure 6-39: Particle size distributions for beta-glutamic tested with a minimal pressure ('0' bar) filtration.....	192
Figure 6-40: Large fragmented crystals in the 3 bar PFB samples of: (Left) beta-glutamic acid; (Right) Lesinurad.....	193
Figure 6-41: Changes in particle size of LF and PF samples of beta-glutamic acid	195
Figure 6-42: Changes in particle size of LF and PF samples of alpha-glutamic acid.....	195
Figure 6-43: Changes in particle size of LF and PF samples of Lesinurad.....	196
Figure 6-44: Volume distribution for 0.5 bar filtration of beta-glutamic acid	198
Figure 6-45: Volume distribution for 1.6 bar filtration of beta-glutamic acid	198
Figure 6-46: Volume distribution for 3 bar filtration of beta-glutamic acid	199
Figure 6-47: $I_p * 0.5 * w_p^2$ distribution for 1.6 bar filtration of glutamic acid.....	200
Figure 6-48: Aspect ratio distribution for 0.5 bar filtration of beta-glutamic acid.....	200
Figure 6-49: $I_p * 0.5 * w_p^2$ distribution for 1.6 bar filtration of glutamic acid.....	201
Figure 6-50: Aspect ratio distribution for 1.6 bar filtration of beta-glutamic acid.....	201
Figure 6-51: $I_p * 0.5 * w_p^2$ distribution for 3 bar filtration of glutamic acid	202
Figure 6-52: Aspect ratio distribution for 3 bar filtration of beta-glutamic acid.....	202
Figure 7-1: The LUMiSizer benchtop centrifuge	206
Figure 7-2: LUMiSizer measurement technique; IR source produces radiation which is either transmitted or scattered by the sample contents (Reproduced from LUM GmbH)[127]	207
Figure 7-3: Schematic of LUMiSizer polymer sample cell (dimensions in mm).....	207
Figure 7-4: LUMiSizer bed height can be tracked through monitoring of transmitted radiation over time (Reproduced from LUM GmbH)[127]	208
Figure 7-5: LUMiSizer raw data as displayed on SEPView software - sample transmissivity vs. height for Urea particles in saturated mother liquor (MeOH) after 34 hours	212
Figure 7-6: Schematic of particle bed separated into slices of height dr ; compressive force is imparted towards the base by the weight of particles above each slice ..	214
Figure 7-7: Total compressive pressure drop over a bed of particles situated in a LUMiSizer cell; for alpha and beta-glutamic acid. Other systems evaluated display similar power-law trends in pressure with rising centrifugal rotational speeds	216
Figure 7-8: LUMiSizer sample cells containing urea; before and after centrifugation	219
Figure 7-9: Fractional bed height vs time for beta-glutamic acid over 34 hours.....	220
Figure 7-10: Fractional bed height vs time for alpha-LGA over 34 hours	220
Figure 7-11: Fractional bed height vs time for urea over 34 hours	222
Figure 7-12: Fractional bed height vs time for urea + biuret over 34 hours	222
Figure 7-13: Fractional bed height vs time for Lesinurad over 34 hours	224
Figure 7-14: Bed relaxations (Δ fractional bed height) upon changing from high to low centrifugation	225

Figure 7-15: Bed relaxations vs centrifuge rpm for α -glutamic acid and urea-biuret.....	226
Figure 7-16: Bed relaxations vs centrifuge rpm for needle-like systems.....	227
Figure 7-17: Optical microscope images of beta-glutamic acid needles after vacuum-filtration (top), continuous percolation at 95L/h (middle), and after centrifugation for 34 hours in the LUMiSizer (max rpm of 2200) (bottom).....	229
Figure 7-18: Modelled volume ($L_p * 0.5 * w_p^2$) size distributions of vacuum/lightly filtered (LF), percolated (PF) and LUMiSizer-centrifuged (CF) samples of beta-glutamic acid	230
Figure 7-19: Aspect ratio distributions of LF, PF and CF (centrifuged) samples of beta-glutamic acid	231
Figure 8-1: Parent needle particle breaking into 2 'child' particles.....	238
Figure 8-2: Probability factor as a function of filtration pressure (the identification of Equation 8-3 constants from the linear equation are exemplified).....	242
Figure 8-3: Modelled distribution for 0.5 bar batch 2 Litre pressure filtration of beta-glutamic acid – fraction of broken particles relative to total = 0.137	244
Figure 8-4: Modelled distribution for 1.6 bar batch 2 Litre pressure filtration for beta-glutamic acid– fraction of broken particles relative to total = 0.256	244
Figure 8-5: Modelled distribution for 3 bar batch 2 Litre pressure filtration for beta-glutamic acid– fraction of broken particles relative to total = 0.328	245
Figure 8-6: Modelled distribution for 31.1 L/h flowrate percolation of beta-glutamic acid (note modelled distribution is compared to the 'PF' distribution as data for particles from the base of the cake is not available) – fraction of broken particles relative to total = 0.05	245
Figure 8-7: Modelled distribution for 127.5 L/h flowrate percolation of beta-glutamic acid– fraction of broken particles relative to total = 0.427	246
Figure 8-8: Plan view schematic of particle placement on the canvas (not to scale)	248
Figure 8-9: Plan-view schematic for the method of solving particle-particle interactions (not to scale).....	250
Figure 8-10: Calculation of contact height (c_z) by law of similar triangles.....	251
Figure 8-11: Finding particle lean from Pythagoras' theorem	253
Figure 8-12: Placement of particles over multiple contacts; 1) Particle falls from arbitrary height with equal z_1, z_2 ; 2) Particle meets contact and begins to rotate around fixed pivot 'p'; 3) Particle stops rotation and is successfully 'placed' when another surface is encountered; 4) When multiple contacts are encountered, a falling particle would come to rest on the 2 highest contact points (i.e. placement as the green line depicts; red lines depict illegal resting points)	255
Figure 8-13: Example of model visual data output for simulation of 101,189 particles; left – z-axis view of particle bed; right (top) – x-axis view of particle bed; right (bottom) – y-axis view of particle bed. Particles are coloured according to number of particle contacts.....	259
Figure 8-14: Bulk density of differential height fractions of the bed as a function of bed height for simulations of differing particle counts	260

Figure 8-15: Bulk density of differential height fractions of the bed as a function of bed height for simulations of differing particle counts (with focus on data around bed heights of 0 – 0.0008 m)	260
Figure 8-16: Average number of contact points per particle as a function of bed height	262
Figure 8-17: Number of contacts vs particle length for a simulation of 101,189 particles	263
Figure 10-1: Bed structure for a simulation of 5,000 particles	280
Figure 10-2: Bed structure for a simulation of 10,000 particles.....	280
Figure 10-3: Bed structure for a simulation of 15,000 particles.....	280
Figure 10-4: Bed structure for a simulation of 20,000 particles.....	281
Figure 10-5: Bed structure for a simulation of 30,000 particles.....	281
Figure 10-6: Bed structure for a simulation of 40,000 particles.....	281
Figure 10-7: Bed structure for a simulation of 50,000 particles.....	282
Figure 10-8: Bed structure for a simulation of 75,000 particles.....	282
Figure 10-9: Bed structure for a simulation of 101,189 particles.....	282

Nomenclature

A	Area	m^2
A_{bed}	Particle bed area	m^2
a	Centrifugal acceleration	$rad.m.s^{-2}$
C_D	Coefficient of drag	—
c	y-intercept of line	—
c^*	Solubility concentration	$mol.m^3$
c_p	Specific heat capacity	$J.kg^{-1}.K^{-1}$
c_s	Solution concentration	$mol.m^3$
c_x	Particle contact x coordinate	—
c_y	Particle contact y coordinate	—
c_z	Particle contact z coordinate	—
D	Diameter (of particle bed)	m
d_i	Particle diameter 'i'	m
d_p	Particle diameter	m
d_V	Circle equivalent volume diameter	m
d_s	Circle equivalent surface area diameter	m
E	Young's Modulus	—
E_k	Kinetic energy	$kg.m^2.s^{-2}$
F	Force	$kg.m.s^{-2}$
F_b	Buoyancy force	$kg.m.s^{-2}$
F_D	Drag force	$kg.m.s^{-2}$
F_g	Gravitational force	$kg.m.s^{-2}$
$F_{N.i}$	Frequency distribution function (number)	—
$F_{V.i}$	Frequency distribution function (volume)	—
$F_{AspR.i}$	Frequency distribution function (AspR)	—
F_c	Continuous frequency distribution function	—

f	Revolutions per second	s^{-1}
f_e	Fraction of 'elongated' particles	—
f_L	Fraction of 'large' particles	—
f_m	Fraction of 'medium' particles	—
f_p	Fraction of 'prismatic' particles	—
f_r	Fraction of 'rounded' particles	—
f_s	Fraction of 'small' particles	—
G	G-force	—
g	Gravitational acceleration	$m.s^{-2}$
H	Particle bed height	m
Hz	Hertz	s^{-1}
ΔH_d	Enthalpy change of formation	$J.mol^{-1}$
h	Height of liquid	m
h_i	Height of i th interval	m^{-1}
h_p	Particle height	m
I_0	Intensity of emitted radiation	$J.s^{-1}$
I	Intensity of transmitted radiation	$J.s^{-1}$
K_c	Fracture toughness	$N.m^{\frac{3}{2}}$
K_m	Filtration concentration factor	$kg.m^{-3}$
k_{asp}	Constant of breakage probability	—
k_b	Boltzmann constant	$J.K^{-1}$
k_h	Constant in Hooke's Law (spring constant)	$N.m^{-1}$
$k_{pres.1}$	Constant of breakage probability	—
$k_{pres.2}$	Constant of breakage probability	—
k_r	Constant in Darcy equation	—
k_{size}	Constant of breakage probability	—
L_b	Length of packed bed	m
L_c	Half of total crack length	m

L_p	Size of product crystals	m
L_s	Size of seed crystals	m
l	Optical path length	m
l_p	Particle length	m
M_p	Mass of product crystals	kg
M_s	Mass of seed crystals	kg
m	Gradient of line	–
\dot{m}	Mass flow rate	$kg.s^{-1}$
m_c	Filter cake mass	kg
m_r	Ratio of mass of wet cake:dry cake	–
m_p	Mass of particles	kg
N_a	Agitator speed	$rev.s^{-1}$
N_i	Number of particles in bracket 'i'	–
N_{tot}	Total number of particles	–
n	Compressibility index	–
n_i	Refractive index	–
P	Pressure	$kg.m^{-1}.s^{-2}$
ΔP_c	Pressure drop over the cake	$kg.m^{-1}.s^{-2}$
ΔP_m	Pressure drop over the filter medium	$kg.m^{-1}.s^{-2}$
P_N	Number-based population density	–
P_V	Volume-based population density	–
Q	Power	$J.s^{-1}$
Q_f	Volumetric flow	$m^3.s^{-1}$
R	Universal gas constant	$J.mol^{-1}K^{-1}$
Re_p	Particle Reynolds Number	–
r	Radius of centrifugal acceleration	m
r_c	Radius of circle	$pixels$
r_{crit}	Critical radius of nuclei	m

S	Shape factor (of needle)	m^{-2}
S_p	Particle surface area	m^2
S_f	Fraction of solids in system	—
S_z	Constant in Zwietering equation	—
T	Temperature	K
ΔT_A	Temp. difference at end 'A'	K
ΔT_B	Temp. difference at end 'B'	K
ΔT_m	Log-mean temperature difference	K
T_{ref}	Reference temperature of dissolution	K
t	Time	s
t_b	Batch time (of crystallisation)	s
U	Overall heat transfer coefficient	$J. s^{-1}. m^{-2}. K^{-1}$
u	Superficial velocity	$m. s^{-1}$
u_i	Superficial velocity per unit porosity	$m. s^{-1}$
V	Volume	m^3
V_{bed}	Volume of a bed of particles	m^3
V_i	Volume of particles in bracket 'i'	m^3
V_p	Particle volume	m^3
V_{tot}	Total volume of particles	m^3
v	Linear velocity	$m. s^{-1}$
v_t	Terminal velocity (of a particle)	$m. s^{-1}$
W_p	Weight of particles	$kg. m. s^{-2}$
w_p	Particle width	m
x_c	x coordinate of centre of a circle	—
x_{eq}	Equilibrium concentration	$mol. mol^{-1}$
x_{ext}	Strain	—
y_c	y coordinate of centre of a circle	—
x_i	x coordinate of particle i	—

y_i	y coordinate of particle	—
z_i	z coordinate of particle (height coordinate)	—

Greek Symbols

α	Cake resistance relative to dry cake mass	$m.kg^{-1}$
α_a	Optical collection angle	<i>radians</i>
α_{ave}	Average specific cake resistance	$m.kg^{-1}$
α_0	Unit average specific cake resistance	$m.kg^{-1}$
α_v	Volume fraction of particles	—
β_m	Filter medium resistance	m^{-1}
γ_e	Surface energy	$N.m^{-1}$
ϵ	Void fraction	—
ϵ_x	Extinction coefficient	m^{-1}
η_{att}	Attrition propensity	—
λ	Wavelength	m
μ	Dynamic viscosity	$kg.s^{-1}.m^{-1}$
ν_k	Kinematic viscosity	$m^2.s^{-1}$
ρ_B	Bulk density (of particle bed)	$kg.m^{-3}$
ρ_f	Fluid density	$kg.m^{-3}$
ρ_p	Particle density	$kg.m^{-3}$
σ	Stress	$kg.m^{-1}.s^{-2}$
σ_{crit}	Critical stress of crystal failure	$kg.m^{-1}.s^{-2}$
σ_{ss}	Supersaturation	$mol.m^3$ or —
σ_T	Tensile stress required for crack formation	$kg.m^{-1}.s^{-2}$
ϕ_s	Sphericity	—
ϕ_c	Circularity	—
φ	Solids fraction	—
ω	Angular velocity	s^{-1}

ω_{mv} Molecular volume $m^3 \cdot mol^{-1}$

List of abbreviations

2D 2-dimensional (length, width)

3D 3-dimensional (length, width, height)

AFM Atomic force microscope

API Active pharmaceutical ingredient

CF Centrifuged

CPR Continuous percolation rig

GUI Graphical user interface

LF Vacuum or 'lightly' filtered

PF Solid sample obtained from bulk of percolation rig cake

PFB Sample obtained from bottom of percolation rig cake

PFT Sample obtained from top of percolation rig cake

rpm Revolutions/rotations per minute

SOP Standard operating procedure

SEM Scanning electron microscopy

Chapter 1

1 Introduction

1.1 Research Background

The world-wide pharmaceutical market today is a trillion-dollar endeavour; on course to be worth a total of \$1.1 trillion by the end of 2014. With a typical cost of \$1 billion in discovering, developing and introducing a new drug into the market[1], the need for cost control and more efficient manufacturing practices has never been more urgent. Reducing costs is directly related to the reliability of the process.

Developing a reliable, predictable and reproducible method of active ingredient formation is thus a chief objective in any Active Pharmaceutical Ingredient (API) manufacturing process. A carefully planned design reduces waste and imparts greater quality into the final product. Identifying the extent of impurity production or minimising the risk of unwanted polymorph formation is a requirement of the New Drug Application (NDA); thereby proving you have a greater control over the process and unexpected conditions/by-products are avoided.

The NDA involves satisfying a considerable number of regulations imposed by the Food and Drug Administration (FDA)[2], many of which can involve the application of significant time and resources; thus it is important to reduce the costs associated with this. Pilot plant testing is implemented as a transition stage from lab-scale operations to industrial scale processing, as operational parameters can change significantly with magnitude increases in scale.

Many organisations now place greater importance on the issue of scale-up so as to reduce costs in advance. Knowledge of scale-up factors allows investigation into process issues that may become problematic in the future (heat and mass transfer, rate of agitation, time scales etc.). Ultimately, pilot scale testing gives operators the additional data they require to move forward with a process and make it commercially viable, reproducible and safe.

Solution crystallisation is common-place among the fine chemical and pharmaceutical industry. This combines a level of impurity rejection with maximised yields, making it a highly efficient separation process. Crystallisation and its operating conditions are also utilised for controlling polymorphic form, crystal size and chemical and physical stability of the final product which is important for manufacturing stable, long-life products. The process of controlling physical and chemical properties of an API through design is known as particle engineering[3].

Predominantly, the crystallisation process is followed by a separation process (e.g. a pressure filtration) and a drying stage to remove the remaining residual moisture. These unit operations are known to cause breakage, attrition and agglomeration, and hence changes in the PSD, potentially impairing downstream operations[4-9].

Batch filter/dryer equipment is prevalent among the fine chemical industry[3], as it is quicker and cheaper to avoid transferring a crystal mass between separate vessels to remove moisture. Because of the simultaneous operation of batch filter/dryers (and the ease of drying lab-scale powder masses), the study of the effect of individual filter and agitated drying techniques on particle properties is rarely considered independently.

Whilst the field of particle engineering has advanced significantly over the years, particle breakage and attrition have continued to cause problems with downstream processing (filtration, drying), product formulation and bioactivity of APIs.

Previous studies, in particular by Lekhal et al, have assumed the effect of particle breakage is mainly due to the use of agitated drying[7, 8], however Macleod and Muller recently provided evidence that for needle-shaped particles the majority of breakage occurs under pressure filtration, with subsequent size reduction under drying being far less significant[9]. This was also recently observed by Hamilton et al, although they observed attrition under drying also[5]. Cornehl et al have observed the breakage of Lysozyme crystals under filtration, although as protein structures these are more sensitive to mechanical pressures than most organics[10].

As appreciable time and effort is invested into particle engineering, it is inherently counter-productive to then subject the crystal mass to undesirable PSD changes (such as in filtration/drying). A more holistic approach to process design should take the entire production route into account, so that efforts to produce perfect crystals under crystallisation are not undone by poorly designed filtration and drying processes. This is also relevant to formulation-stage processes such as tableting and granulation, which rely on the even distribution of API/filler particles in order to provide the correct dosage in the final product.

The premise is therefore that the act of filtration has an adverse effect of the PSD of a crystallised mass; compressive stresses exerted on particle beds leads to the compaction and consolidation of the bed, which in turn leads to rearrangement and breakage of crystals as inter-particle contacts are severed. To examine this whilst retaining similarity to industrial processes, fresh particle beds are to be generated by crystallisation.

Furthermore it is known that some crystals exhibit differing mechanical properties when in varying states of dryness through to saturation with moisture[11]. Although this was reported

to apply to protein crystals (which are comparatively weaker and more brittle than organic crystals) under crystallisation, this could apply to tougher particles when subjected to harsher forces i.e. those experienced in a pressurised particle bed. For these reasons, and to retain comparability to industrial filtration processes, the generation of freshly crystallised material is essential to this project.

Control of the PSD is thus imperative at every stage in the process, and this project seeks to understand the control of this parameter at a multi-scale level; from the quantification of small-scale beds under centrifugation to bench-scale 2 Litre batch filtrations. This will aid in the design of industrial scale-up and separation operations.

Hence the key question identified to be answered is:

“How is the particle size distribution of a crystal bed influenced by the forces experienced under pressure filtration?”

This will be answered under the following premises:

- Particle engineering has advanced such that crystal size, size distribution, habit and polymorph can all be controlled to do a degree through crystallisation techniques
- Crystal habits, physical properties and packing behaviour influence particle behaviour under processing
- The compaction of particle beds under pressure filtration causes crystal breakage and structural rearrangement of the bed as compressive forces are transmitted through a network of interconnected particles
- Isolation therefore leads to broadening of the PSD through the breakage of crystals
- Production of fines under filtration can lead to inefficient separations and blinding of filter cloths, as well as further downstream processing issues
- A holistic approach to process design is required to improve the final API properties

development over the course of the project. Material generated in this phase is utilised for additional experimentation, for example for use in evaluating physical properties of the crystals.

Stage 3 consists of the actual experimentation (Chapter 6); crystal material together with its mother liquor is fed into the CPR and is subjected to hydrodynamic stress over a range of flow rates. Larger scale batch crystallisations are performed using a 2 Litre scale pressure filter. These experiments are designed with direct filtration performance correlation to industrially relevant systems in mind.

Smaller scale studies include the use of a centrifuge to impart pressure to a crystal bed (Chapter 7). Utilisation of the centrifuge provides an opportunity to link small scale compression performance to larger scale filtration performance. The small sample size requirements (~1 mL) could help to provide indications of future filtration problems (i.e. on scale-up) for active pharmaceutical ingredients (APIs) that are in short supply.

Stage 4 consists of experimental analysis. Breakage cannot be precisely quantified at larger scales as the particle beds consist of hundreds of thousands – millions of individual crystals packed into a structure. The extent of breakage is studied via the level of size reduction in the overall distribution of particle sizes. It is also necessary to critically assess the methods by which particle size analysis are undertaken in order to ascertain the validity of the data (Chapter 5).

Modelling of crystal size and strength data is a crucial aspect of the project and is also undertaken at this stage. Modelling aims to interpolate and extrapolate experimental data in order to produce theoretical and/or heuristic models that will enable the prediction of the extent of breakage based on the particle shape and stresses that are placed upon the crystal bed (Chapter 8).

Stage 5 is an amalgamation of all existing data and methods. These are used to link the compression performances of crystals from small scale centrifugal compression to large scale batch and percolation, where beds of crystals are subjected to hydrodynamic stresses and tensile forces within their packed bed structure (Chapter 8 / Chapter 9).

Chapter 2

2 Background Theory and Literature Review

2.1 Introduction

This chapter presents a summary of the appropriate background and review of existing literature into the underlying phenomena associated with solid/liquid flow, characterisation of particles, crystallisation from solution, industrial filtration and breakage of particles.

2.2 Particle and Fluid flow Models

2.2.1 Background

The forces experienced by a particle under processing are numerous. For the purposes of this project however, the life of a particle is considered from birth under crystallisation to its final isolation.

A particle is first formed from nucleation in a crystallising vessel. Immediately, it is exposed to the hydrodynamic and viscous drag forces from the fluid it precipitates from. These are dependent on the velocity and viscosity of the solution, and in turn the particle is affected based on its surface area and its shape (i.e. specific surface area/roughness).

Additionally the particle is subjected to forces from the vessel agitator and from other particles, in the form of impact and shear. Particle-impeller, particle-wall and particle-particle collisions are a major source of breakage, especially at industrial scale, where the forces and masses involved are magnified[12]. Particle-particle collisions are also more likely when particle concentrations are increased.

When under isolation particles compact into beds, and thus feel the weight of particles above them. Particles in the lower portions of the bed are more tightly confined by neighbouring particles, and experience higher stresses[12]. Confinement also limits the extent to which particles can flex/rotate and distribute forces[13]. If the operation employs a pressure gradient, then particles will feel the effect of pressure in the form of viscous drag, which is dependent on their surface areas and orientation to the direction of fluid flow.

Under drying, liquid solvent is removed and particles are left bound by solid bridges. Agitation is usually employed to increase heat and mass transfer, but this results in a significant level of breakage due to impeller forces.

2.2.2 Forces experienced under fluid flow

The simplest case to imagine is a single, rigid, smooth, spherical particle falling through a liquid of infinite bounds. If the particle falls at a constant velocity (i.e. terminal velocity) then the forces acting upon it are balanced; a gravitational force pulling the particle downwards (weight) and buoyancy and drag forces in opposition to this[14]:

$$F_D = F_g - F_b$$

Equation 2-1

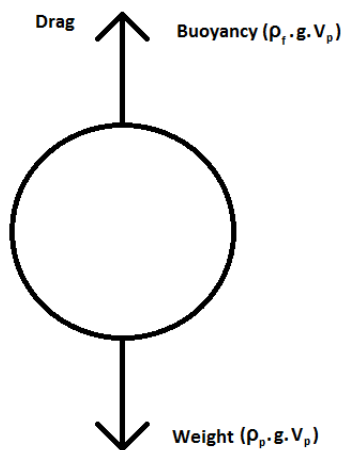


Figure 2-1: Force balance on a spherical particle falling through a liquid

All parts of the particle surface are exposed to stresses generated by the flowing fluid; the normal stress (acting perpendicular to the particle surface) and a shear stress (acting at a tangent). Normal stress is experienced as a number of components; the first component is the hydrostatic pressure at any particular point on the particle surface. The integral of this normal stress over the surface of the particle is the buoyancy force (F_b). This force is dependent on the volume of fluid displaced by the particle and thus acts vertically upwards[15]:

$$F_b = \rho_f V_p g$$

Equation 2-2

The second component of normal stress results from the difference in pressure of the fluid at the particle surface from the hydrostatic pressure; the integral of this stress over the particle surface yields the hydrodynamic pressure acting over the particle[15].

Similarly to buoyancy, the force of the particle's weight is given by[15]:

$$F_g = \rho_p V_p g \quad \text{Equation 2-3}$$

Therefore the force of drag acting upon the particle results from combination of Equation 2-1, Equation 2-2 and Equation 2-3:

$$F_D = (\rho_p - \rho_f) V_p g \quad \text{Equation 2-4}$$

The size of the force is dependent on the particle velocity (v), cross-sectional area (A), density of the fluid and the coefficient of drag, C_D [14]:

$$F_D = \frac{C_D A \rho_f v^2}{2} \quad \text{Equation 2-5}$$

The coefficient of drag is heavily dependent on the particle Reynolds number, i.e. it is dependent on the flow regime of the fluid as it passes over the particle. The particle Reynolds number is defined by[16]:

$$Re_p = \frac{\rho_f v d_p}{\mu} \quad \text{Equation 2-6}$$

At low Reynolds numbers viscous forces dominate and thus drag on the particle is almost entirely due to the viscosity of the fluid. As Re increases turbulent eddies form behind the particle and increase the level of acting drag. The dependence of Re of the drag coefficient is well defined from experimental data, but theoretical correlations are more difficult to achieve. For low Re approximately less than 0.1, Stokes' law holds[17]:

$$C_D = \frac{24}{Re_p} \quad \text{Equation 2-7}$$

For the assumption of spherical particles (projected particle area is $\pi d^2/4$) the combination of Equation 2-5, Equation 2-6 and Equation 2-7, the drag force thus reduces to:

$$F_D = 3\pi\mu d_p v \quad \text{Equation 2-8}$$

Therefore in the laminar region the force of drag is directly proportional to the fluid viscosity, particle diameter and particle settling velocity. If Equation 2-8 is substituted back into Equation 2-4 (assuming a spherical particle volume of $\pi d^3/6$), then the well-known Stokes equation results, from which the terminal settling velocity of a particular sized particle can be obtained (this is often used as a means of particle size measurement from analysis of particle settling rates)[14]:

$$v_t = \frac{d_p^2(\rho_p - \rho_f) g}{18\mu} \quad \text{Equation 2-9}$$

In the laminar region the effect of viscous forces are dominant and thus the effect of particle shape can be neglected.

For $1 < Re < 1000$ (the 'transition' region), inertial influences are significant and thus cannot be neglected. However the complexity is such that theoretical relations cannot be defined, and the drag coefficient must be correlated from experimental data. For higher Reynolds numbers ($1000 < Re < 30,000$) (Newton's Range), the drag coefficient remains roughly constant, thus for spherical particles under turbulent flow[18]:

$$C_D \cong 0.44 \quad \text{Equation 2-10}$$

At Reynolds numbers above approximately 30,000, drag across the particle begins to reduce again due to boundary layer separation, although this kind of turbulence is very rarely encountered in industrial processing[19].

2.2.3 Flow through a packed bed of particles

The first attempts to describe percolation rate came from Darcy, in 1856, when his study of the public water systems led him to develop relationship describing the flow of water through packed beds of sand[20]. He found that liquid flow is directly proportional to the pressure drop across the bed. The relationship was developed on the assumption that flow through porous media was analogous to capillary flow, and empirical forms of the equation were developed specifically for filtration procedures[21]. In its modern form, the equation incorporates the viscosity of the fluid:

$$\frac{Q_f}{A} = \frac{k_r \Delta P}{\mu L_b} \quad \text{Equation 2-11}$$

Where k_r is the permeability. Kozeny developed a semi-empirical modification based on Darcy's law in 1927[22], which was then modified by Carman in 1937[23] and 1956[24] to yield:

$$\frac{\Delta P}{L_b} = 180 \frac{(1 - \epsilon)^2 \mu \cdot u_i}{\epsilon^3 d_p^2} \quad \text{Equation 2-12}$$

The Carman-Kozeny equation is applicable only for low Reynolds numbers (i.e. the laminar region – approx. $< Re$ of 1). Where a correlation for higher Reynolds numbers is required, the empirical Ergun equation[25] is more often used; which applies over a wider range of Reynolds

numbers. The '150/Re' term is a fit for the laminar region whilst the '1.75' term adds a heuristic correction factor to account for the inertial losses encountered above Reynolds numbers greater than 1. The Ergun equation is as follows:

$$\frac{\Delta P}{H} = \left(\frac{150}{Re_p} + 1.75 \right) \times \frac{\rho_f u_i^2}{d_p} \times \frac{1 - \epsilon}{\epsilon^3} \quad \text{Equation 2-13}$$

$$Re_p = \frac{\rho_f u_i d_p}{\mu(1 - \epsilon)} \quad \text{where } u_i = \frac{u}{\epsilon} \quad \text{Equation 2-14}$$

The suggested particle diameter for use in calculation is that of the Sauter mean diameter, otherwise known as the 'volume-surface mean' diameter. This is the ratio of the sum of the total volume of particles in a distribution to the total surface area[15]:

$$\text{Sauter mean diameter, } d_{3,2} = \frac{\sum N_i d_i^3}{\sum N_i d_i^2} \quad \text{Equation 2-15}$$

2.3 Particle Size Characterisation

2.3.1 Particle definitions and material characterisation

A powder or collection of particulates is characterised by a number of properties, e.g. its size distribution, flowability, cohesiveness, bulk density and packing style. Within the pharmaceutical industry these properties can have a significant effect on the final formulated product i.e. whether the product can be tableted or not (cohesiveness; packing), the ease with which this can be accomplished (flowability; segregation) and other factors like safety (to the operator from dust hazards or the patient from size distribution and segregation) and bioavailability (size distribution/segregation).

Bulk powder properties are influenced by the constituent particles from which they are formed; chiefly the size and shape of the particles but also their density, hardness/toughness, and physiochemical properties such as the polymorph or inter-particle interactions (cohesiveness/static charging). It is therefore of vital importance to actively control and monitor such properties from within the bulk of the powder.

The bulk density is used to characterise the mass of solid particles occupied per unit volume, as a certain volume of the bed mass is normally occupied by voids (filled by air or some other carrier medium). The bulk density ρ_B is thus related to the particle true density ρ_p by[19]:

$$\rho_B = \rho_p(1 - \epsilon) \quad \text{Equation 2-16}$$

Where ϵ is the volume fraction of the voids relative to the whole (approximately 0.4 for uniform sized spheres in a settled bed[19]; 0.26 for densely packed particles[26]) and is dependent on a number of packing factors e.g. particle size, shape and size distribution.

One of the more important bulk crystal properties that will be investigated in this thesis is the particle size distribution; the range of particle sizes present in the powder. A theoretical sample composed completely of particles with a single size would be classified as *monodisperse*. In practice, these are almost non-existent (save for plant pollen or polymer latex spheres formed under zero-G) and most real powder samples show some degree of *polydispersity* (i.e. composed of multiple particle sizes)[15].

Equally important to the analysis of powder distributions is the particle shape. For real systems it is not uncommon that a powder sample would be almost entirely composed of a single shape of particle. The problem arises when attempting to define that shape and using it to compare particle size between powders.



Figure 2-2: Comparison of different 2D shape sizes

For example, the schematic in Figure 2-2 depicts a square (i.e. a cubic particle viewed in 2D) with equal side lengths of 2 by 2 units alongside a rectangle (i.e. a needle-like particle) with units of 0.5 by 8 and a circle of equivalent projected area diameter 2.25. Each of these 'particles' has an area of 4 units and apparently are equally sized, yet they clearly differ greatly in shape. This highlights the real problem of attempting to measure size with irregularly shaped particles.

As alluded to, the sizing of spherical particles is relatively simple in practice and is undertaken by measuring the diameter of the sphere, which is easily comparable to other spherical particles. However, with pharmaceuticals particles are rarely spherical. Irregularly shaped particles can be transformed through image analysis to approximate their size. As in Figure 2-2, a 2D image of the particle is converted to an area; a circle is then formed from this area, from which its diameter is taken as the particles' size. This is known as the *circle equivalent diameter* (CE diameter).

The CE diameter is of course dependent on the particles' orientation (typically its 'preferred' orientation, to be precise – e.g. for needles this is likely to be their long, flat edges as opposed

to their tips). Other non-orientation dependent equivalencies in common use are the spherical equivalent volume and spherical equivalent surface area, which are described by:

$$d_v = \left(\frac{6V_p}{\pi} \right)^{\frac{1}{3}} \quad \text{Equation 2-17}$$

Where d_v is the diameter of a sphere with the same volume as that of the particle (V_p). And for surface area:

$$d_s = \left(\frac{S_p}{\pi} \right)^{\frac{1}{2}} \quad \text{Equation 2-18}$$

Where d_s is the diameter of a sphere with the same surface area as that of the particle (S_p). Where the volume and surface area of a sphere are, respectively:

$$V_{sphere} = \frac{(\pi d)^3}{6} \quad \text{and} \quad S_{sphere} = \pi d^2 \quad \text{Equation 2-19}$$

Hence these factors can be used as a standardised method of comparing irregular particle sizes[17].

The circle equivalencies can provide rough approximations of sizes of particles but for needle-like particles as commonly encountered in the pharmaceutical industry additional, more specific parameters are required to adequately characterise the particle shapes. As this study is involved in the breakage of particles, then it is envisioned that not only the size but the shape of the particle will radically change upon breakage.

Wadell defined the sphericity as the ratio of surface areas for a sphere and a particle of equivalent volume (which also equals the ratio of volume and surface-equivalent sphere diameters)[27]:

$$\begin{aligned} \phi_s &= \frac{\text{surface area of sphere of equal volume to the particle}}{\text{surface area of the particle}} \\ &= \left(\frac{d_v}{d_s} \right)^2 \end{aligned} \quad \text{Equation 2-20}$$

Hence for a perfect sphere $\phi = 1$ and for all other irregular particles $\phi < 1$. It follows that for 2 dimensional shapes the circularity can be evaluated in a similar fashion:

$$\phi_c = \frac{\text{perimeter of circle of equal area to the particle}}{\text{perimeter of the particle}} \quad \text{Equation 2-21}$$

Where a perfect circle has circularity equal to 1 and for irregular particles circularity < 1 [17].

The aspect ratio of a particle is a measure of the ratio of an objects 'width' to its 'length', on a scale of 0 - 1. An isotropic shape such as a square or circle would thus have an aspect ratio equal to 1. At the other extreme, a needle e.g. of width 5 microns having a length of 100 microns would have an aspect ratio of 0.05 (5 / 100).

2.3.2 Particle size representations

The most common method of displaying particle sizes is with a distribution function, the most fundamental of which is the number distribution. These are typically represented as histograms with the number of particles collected into size intervals based on their particle size, and plot as rectangles alongside the count frequency. To aid in comparison between the blocks, frequency counts are converted into fractional values based on the total number of counts and the interval size. This results in the frequency distribution function, in which the total area of all of the rectangles is equal to 1[15]:

$$F_{N,i} = \frac{N_i}{N_{tot}} = h_i \Delta d_i \quad \sum_i h_i \Delta d_i = 1 \quad \text{Equation 2-22}$$

Histograms are discrete distributions, thus continuous distributions can be approximated by plotting a smooth curve through the peaks of the histogram at each interval's mean value. This results in the continuous frequency distribution function, F_c , in which the fraction of particles that lie within 2 specific particle diameters can be calculated via integration of the curve between these limits. The sum to infinity therefore equals 1[15]:

$$F_{0 \rightarrow \infty} = \int_0^{\infty} F_c \Delta d_i = 1 \quad \text{Equation 2-23}$$

A density distribution is commonly attributed a numerical subscript that is indicative of the basis from which it is formed: 0 (number based), 1 (length), 2 (projected area or surface area) or 3 (volume). The volume-based frequency distribution is most commonly encountered in the pharmaceutical industry[28].

2.3.3 Methods of particle size analysis

It is (in real terms) impossible to manually record the size of thousands of different particles; thankfully automated methods of particle sizing exist to simplify the process. The micronisation of silicon chips and magnitude orders of processing power increases have made these counters (and the hardware they rely on) relatively cheap and effective.

One of the oldest known methods of particle sizing involves sieving, where particles are agitated on layers of mesh screens to separate those that can pass through the pores from

those that cannot. Mesh fractions are weighed in order to estimate the approximate number/mass of particles above the mesh size. Sieving suffers from a number of limitations, e.g. blinding of the mesh, or particles with 2 small dimensions and 1 large (i.e. needles) passing through the mesh after a period of agitation[15].

Particle sizing can also be carried out with sedimentation methods, i.e. particles are dropped through a fluid medium and the rate at which they fall/settle is dependent on their size (correlated through the Stokes velocity)[14].

Although modern equipment is highly automated and technical, it still suffers from a number of basic drawbacks. These typically fall into a number of categories: limitations of the instrument (e.g. will only accept small sample size, long sample time), limitations in procedure (e.g. poor/excessive particle dispersion), operator error (inaccurate equipment calibration, poor standard operating procedure) and errors in sampling.

2.3.3.1 Sampling

Before instruments can be used to resolve particle properties, samples of material must be obtained, as it is almost always infeasible to sample the entire bulk. The endpoint of proper sampling is to collect a representative sample (of the bulk), one in which a full range of particle sizes from smallest to largest is contained within, and in the same proportions as the bulk powder. If the quality of the sample is high then it follows that the data obtained is accurate and representative.

Errors in sampling are usually either random, statistical anomalies (which cannot be fully eliminated but can be alleviated through increased sample numbers or mass) or errors due to segregation of the powder, which tend to be more significant.

Allen lists the so-called 'golden rules' of industrial sampling as[17]:

- A powder should be sampled in motion
- It is better to sample all the powder for short periods of time rather than some of the powder for longer periods of time

For free flowing powders where segregation is severe it is almost impossible to glean a representative sample from a motionless powder. Non-free flowing powders (such as cohesive, moistened or fibrous material) do not tend to segregate so readily, and thus it can be assumed that such a sample taken and stored will retain its 'history' i.e. if the bulk material was non-segregated then the sample can be assumed to be non-segregated also. This has implications for the handling of needle-like powders, as the intertwining particles create

cohesive networks that hinder segregation, thus increasing the likelihood of a sample retaining its representativeness to the bulk[17].

2.3.3.2 Optical analysis techniques

In previous years the collection of quantitative data using microscopy was a tedious and labour intensive process, which still resulted in under representation of the sample and subsequently poor data. Nowadays the proliferation of automated particle counters and sophisticated image analysis software means that it is feasible to gather sufficient quantitative data from microscopy, as well as from other optical methods e.g. Maaß et al have successfully used on-line image recognition analysis to determine particle (fluid droplets) size at a rate of 250 images per minute[29]. The goal within this area of research has always been to reduce the great workloads required for particle analysis, which when factoring in the sampling, preparation and experimentation, can be significant.

Automated particle counters operate by scanning particles to produce electromagnetic signals which are picked up and resolved by a detector, before being processed to yield data on the particles. These systems are still limited however by the presence of agglomerates or contacting/overlapping particles (both of which are not easily inferred by machines)[30]; which skew the resultant size distributions as the agglomerate/overlapping particles are counted as a single particle. This is particularly problematic with long needles, due to their tendency to contact and/or overlap[31].

Methods to combat this are being developed through the use of software algorithms, e.g. Zhang has developed an image analysis technique to characterise the overlapping particles in samples of anthracite. By applying colour to the particles, the image analysis algorithm is able to highlight the overlapping particles and apply correction factors to yield a better estimate of the particle size[32]. Wu et al have built a computer model to count and estimate the lengths of needle-shaped carbamazepine crystals. Their algorithm effectively manages to distinguish separate needles from large networks of overlapping crystals within a timeframe of 5 seconds; thus allowing for on-line analysis[31]. Larsen et al performed similar MATLAB-based analysis for the determination of size distributions of needles[33].

Sources agree however that microscopy is the only optical analysis method in which particles can be directly observed and measured; thus it retains a significant advantage over alternative techniques[15, 17, 28]. Optical microscopy also allows for verification of the particle shape and surface features. Although a popular analysis technique in the pharmaceutical industry, microscopy suffers from a lack of resolution, both spatial and depth-wise. Wide particle size distributions also cause problems with optical imaging due to the lack of focus, where only a

subset of the distribution can be in focus at any one time. The limit of spatial resolution is given by[17]:

$$\text{limit of resolution} = \frac{\lambda}{n_i \sin \alpha_a} \quad \text{Equation 2-24}$$

Where n_i is the refractive index of the medium between the objective and object, and α_a is half of the collection angle, as depicted by Figure 2-3. The denominator of Equation 2-24 is usually referred to as the numerical aperture, and is a common term used to indicate the effective resolving power of different objective lenses.

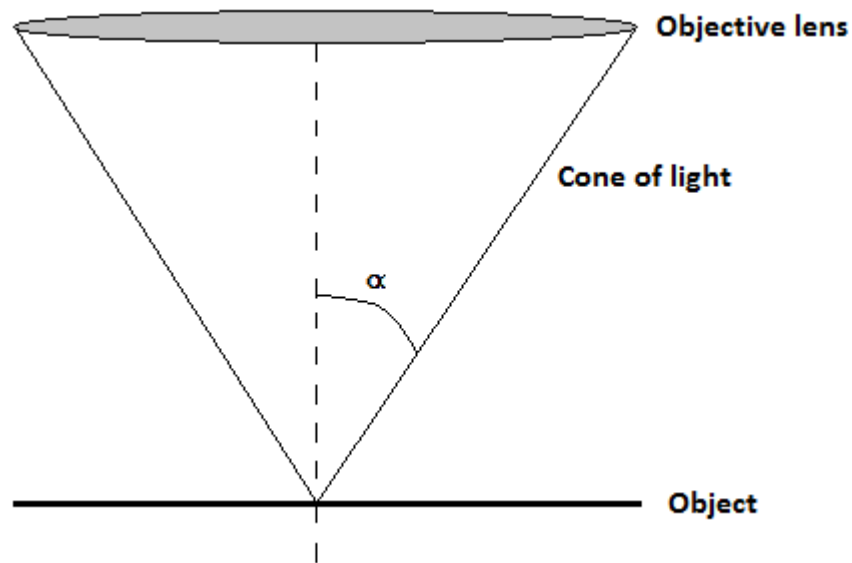


Figure 2-3: Schematic of the illumination of a sample by a cone of light

The resolution is therefore largely dependent on the numerical aperture of the microscope in use, which in turn is usually dependent on the quality of the objective lens, although this can be increased slightly by using oil as a dispersing medium (as opposed to air/nothing). Although theoretically the wavelength of light allows for resolving of features down to around 0.5 microns, in practice this value is higher; BS3406 does not even recommend using light microscopy to image features below 3 microns[34]. The upper limit of practicality is reached at approximately 1 mm; features larger than this are observable by the human eye, and even under low (e.g. 5x) zoom a 1 mm object would extend beyond the field of view.

Microscopy is also known to overestimate particle sizes relative to techniques that image particles in motion. This is due to the fixed (resting) positions of the particles on the dispersing slide. Particles tend to lie with their maximum presentable area facing the observer (preferred orientation), meaning their smallest dimensions are hidden from view and not measured[28]. This has significant implications for the measurement of highly irregular particles, particularly plate-like particles as these will almost always lie with their height obscured from view.

Whilst microscopy excels in its depth of analysis, this comes at a cost to its rate of operability and sample sizes. Human operators are required to distribute representative samples of only a few micrograms out of a bulk and even then it may take several minutes to study a very finite number of crystals. Automated dispersal/counting systems can aid in speeding up the process and making it quantitative but the rate of analysis per particle is still miniscule compared to laser diffraction techniques.

Laser diffraction is a popular industry standard device due to its quick sample time, precision, reproducibility and flexibility of operation[28]. The theoretical basis for the most common application of laser diffraction was first shown by Fraunhofer in 1817[35]. The Fraunhofer solution is an approximation of the complex Mie theory, but is applicable for particles substantially larger than the wavelength of light (approximately > 2 microns); hence limitations are encountered with particles smaller than this[15].

Many modern devices consist of a He/Ne laser source (typically 632.8 nm wavelength) and a series of lenses as depicted by Figure 2-4. A stream of particles is injected into the system and passes through the laser source, interfering with the light in the process.

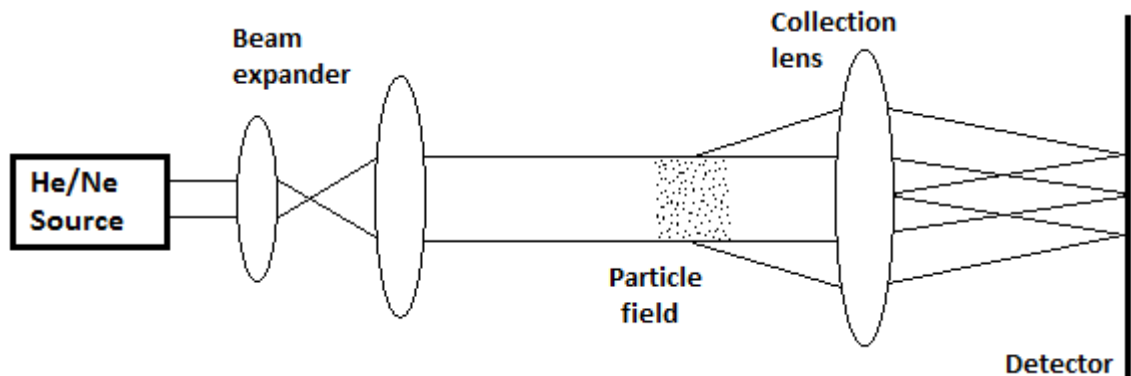


Figure 2-4: Schematic of the laser diffraction principle

Scattered laser light is focused onto a position sensitive detector, which produces a radial diffraction pattern of light and dark rings, the spacings of which are proportional to the measured particle size. The integral of the light intensity distribution leads to the density distribution of the measured particles[36].

The measured particle size is thus a function of the diffraction of a beam of light around a stream of randomly orientated particles. This corresponds to the distance between two tangents of the particle (known as the Feret's diameter[17]). This has implications for highly irregular particles (needles/plates) which can be imaged in their vastly differing dimensions depending on their random orientations. For this reason, laser diffraction has been known to overestimate the particle sizes of irregularly shaped particles[28].

Nonetheless, the technique has far superior analysis times to microscopy (ms – seconds) and is therefore able to analyse a far greater number of particles in any one measurement, thus adding to its reproducibility and representativeness. Laser diffraction techniques are common in industrial settings where their response times provide the opportunity for in-situ analysis and on-line control of process operations e.g. via feedback control[15].

2.4 Crystals and Crystallisation

2.4.1 Crystallisation and solubility

Crystallisation is a widely used separation technique that is capable of imparting a high level of selectivity and purity in the final product. It can be performed from a range of multi-phase mixtures and compositions, but most commonly crystals are grown from the melt or from solution.

The organisation of solid molecules from solution into a regular, repeating structure creates a crystal lattice. The lattice is highly selective in which molecules can be incorporated into it, hence the potential for generating high purity solid products.

Crystallisation is governed by the laws of thermodynamics, and thus can be manipulated by knowledge of phase equilibria. The Gibbs phase rule dictates the number of equilibrium states a system can have, based on the number of components and constituent phases involved[37]:

$$\text{Degrees of Freedom} = \text{No. Components} + \text{No. Phases} - 2$$

The degrees of freedom a system has defines the number of variables that must be constant for an equilibrium to be established, thus allowing variation of operating parameters (temperature, pressure, composition) in order to predict the process and estimate yields.

Practically, the use of solubility is of major importance in the design and control of crystallisation processes. Solubility tends to vary with temperature for all compounds; the plot of this relationship is known as the solubility curve. For ideal compounds, devoid of solvent-solute interactions, the enthalpy change allows calculation of solubility[38]:

$$\ln x_{eq} = \frac{\Delta H_d}{R} \left(\frac{1}{T_{ref}} - \frac{1}{T} \right) \quad \text{Equation 2-25}$$

For calculation of non-ideal solubility (where solvent-solute interactions influence the enthalpy change), an empirical power-law function can be used, with values of the constants a, b, c and d available in the literature for common compounds[39]:

$$x_{eq} = a + bT + cT^2 + dT^3 \quad \text{Equation 2-26}$$

Figure 2-5 displays the regions in a typical solubility diagram. The solubility curve describes the relationship between solution concentration and temperature. Below this line, the solution is under-saturated and thus any solid present will dissolve to satisfy thermodynamic equilibrium. Dissolving additional solid at constant temperature will lead to saturation of the solution once the point of equilibrium reaches the solubility curve, and thus no additional solid will dissolve at constant temperature.

If more solid is dissolved than the equilibrium allows, then the solution becomes super-saturated (the labile zone). The metastable zone lies in-between the labile and stable regions. Shifting the equilibrium of the system between these zones is the basis of solid recovery in crystallisation, where the difference in concentration generates the driving force for this.

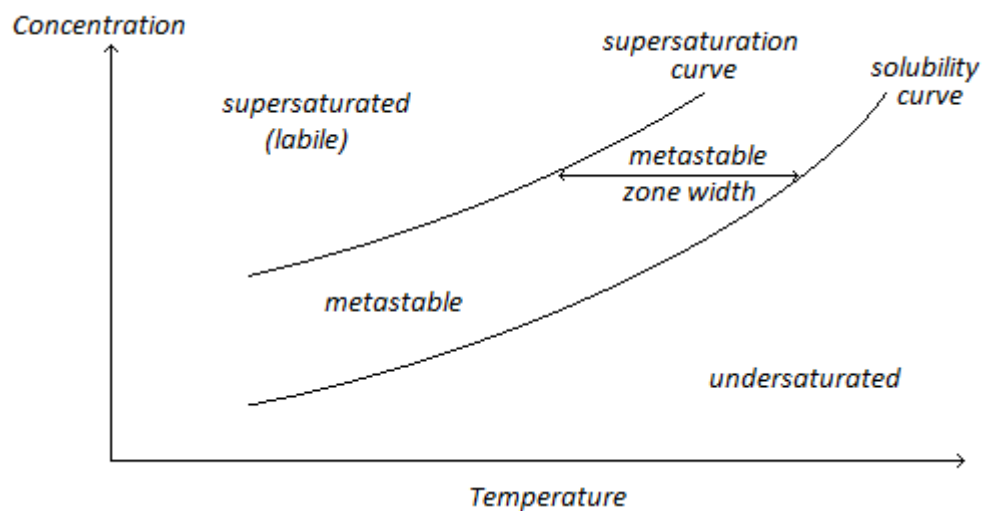


Figure 2-5: Regions of the Solubility Curve. Reproduced from[37]

The super-saturation driving force is commonly written as a concentration differential[40]:

$$\sigma_{ss} = c_s - c^* \quad \text{Equation 2-27}$$

Alternatively, super-saturation can be measured as the ratio between the solid weight fraction in solution to the solubility weight fraction[41]:

$$\sigma_{ss} = \frac{c_s}{c^*} \quad \text{Equation 2-28}$$

Super-saturation has a substantial impact on the rates of crystal nucleation and growth.

2.4.1.1 Nucleation

Nucleation is the formation of stable molecular clusters of solute molecules. Clusters are constantly forming and dissociating in solution; only those that reach a certain critical radius grow to become new crystal particles. The critical radius is a function of the free energy barrier to formation, and can be calculated from:

$$r_{crit} = \frac{2\omega_{mv}\gamma_e}{k_b T \ln(1 + \sigma_{ss})} \quad \text{Equation 2-29}$$

Figure 2-6 depicts this graphically. The combination of cluster volume and surface energies (total ΔG) must surpass the critical radius in order for stable nuclei to form.

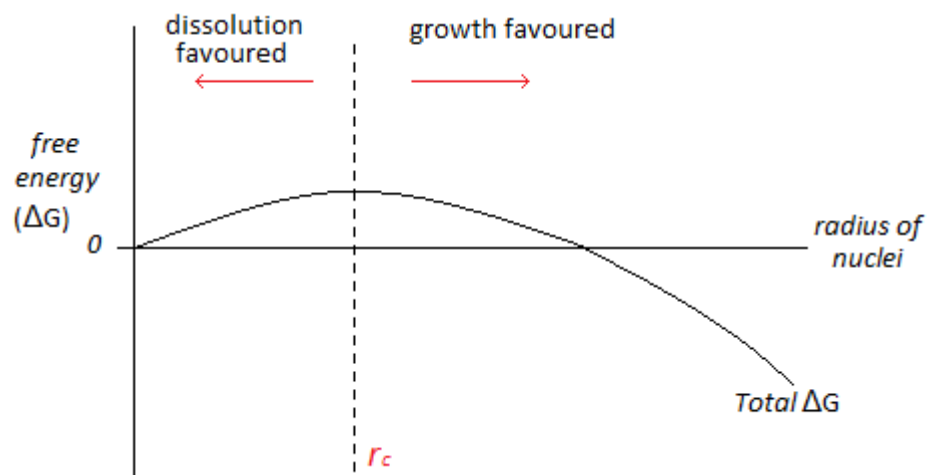


Figure 2-6: Free energy changes under nucleation. Reproduced from [19]

There are 2 types of nucleation: Primary nucleation occurs in the absence of crystal matter, whilst secondary nucleation is induced by crystal matter.

Primary nucleation can be further subdivided into homogeneous and heterogeneous nucleation; homogeneous is spontaneous nucleation from the diffusion of solid particles to form a stable cluster, heterogeneous occurs in the presence of foreign bodies, such as the agitator surface or an impurity particle. Nucleation occurring on pre-existing crystal matter is termed secondary.

In practice, homogeneous nucleation is rare [37], and requires high super-saturation. The presence of a surface to adhere to substantially lowers the free energy required for stable nuclei, hence the more common occurrences of heterogeneous and secondary nucleation.

Secondary nucleation can be induced by a number of methods, seeding being the most common. Existing 'seeds' of crystal matter of the desired product are added to the solution; in order to control the number of crystals, size or size distribution. The solute molecules then preferentially adhere and grow the seed surfaces.

Collisions or agitation in the vessel can result in attrition and breakage, which often leads to uncontrolled nucleation as these fragments can act as secondary nuclei.

2.4.2 Crystal form

2.4.2.1 Crystal habit/morphology

The general shape of a crystal is known as its crystal habit, or morphology. Habit is determined by the point group symmetry and the relative growth rates of faces bound to the crystal (in turn a function of the operating/growth conditions).

In consequence, the properties of crystals can vary based on the morphology that they take on. Crystal shape influences surface chemistry, specific surface area, flow-ability, packing behaviour, compressibility and surface defects.

The morphology of a crystal is often described by a number of qualitative terms based on their external shape; needles, plates, rods, spheres, cubes and tablets all exist, and tend to show varying properties e.g. needles having a large specific surface area exhibit high dissolution rates and flow poorly, plates can stack and block filters etc. Spherical particles are most easily processed but are rare within the pharmaceutical and fine chemical industry.

A number of controllable factors can influence the habit of a processed crystal; mainly super-saturation, solvent choice and impurities in solution. Super-saturation can be used to control elongation of crystals but must be balanced against the effect on nucleation; solvents can influence habit via production of solvates; whilst impurities can have a profound effect on the final morphology due to surface interactions.

Urea for example crystallises as long needles from pure solution. When crystallised in the presence of the dimer biuret (itself an impurity by-product of urea's synthesis), the biuret molecules hydrogen bond into the surfaces of the crystal and themselves offer fewer hydrogen bonding sites for subsequent molecules to take up. This acts to slow growth of the crystal in the [001] plane, the predominant growth plane. The resultant shape has a higher aspect than that of the pure urea crystal[42].

2.4.2.2 Polymorphic form

Substances capable of forming 2 or more different crystal structures exhibit polymorphism. Polymorphs have differing arrangements of molecules; as a result this can change their crystal habits or physical properties. Polymorphs formed with a certain amount of solvent impurity incorporated into the crystal structure are termed pseudo-polymorphs, or solvates. A solvate

formed with water is known as a hydrate (hydrates are often preferred due to toxicity concerns with products destined for human consumption[43]).

Polymorphic form can also influence mechanical properties, stability, melting point, particle size and crucially solubility. The difference in solubility (especially when an unknown polymorph is formed) can substantially affect bioavailability (e.g. rate of dissolution) of the final formulated product[7], which makes this an appreciable concern in industry. For example, thin, flattened structures (needles/plates) will tend to dissolve faster than e.g. spheres or cubes, due to their high specific surface areas.

XRD and DSC in particular are helpful in characterising polymorph type. XRD can detect the variation in crystallographic planes; this has been applied to continuous monitoring of polymorph form under crystallisation[44]. DSC exploits the dissimilar melting points and phase transformations to determine the form. Optical/SEM microscopy can also provide visual confirmation of analytical findings, i.e. for polymorphs which exhibit varying morphology[6, 40, 41].

When nucleating, typically the thermodynamically least stable polymorph forms first, which then tends to transform to a more stable polymorph subsequently (Ostwald's rule of stages). Pre-seeding with a known polymorphic form has been shown to be a reliable method of reproducing the required polymorph from multi-polymorphic systems[43]; so much so that the effects of other process parameters (temperature, mixing, cooling rate) are negated[45].

2.4.3 Industrial crystallisation and control

2.4.3.1 Batch Operation

Batch operations are favoured in the fine, agro chemical and pharmaceutical market due to the greater versatility they offer to the highly specialised chemical reaction pathways. As these reactors tend to be universally designed in shape, performing a batch crystallisation places emphasis on the mode of operation[37].

Methods for generating super-saturation include cooling, evaporation and addition of anti-solvent. All rely on the principle of a reduction in solution capacity for retention of solid. Cooling reduces the solubility of the solute in the solvent, evaporation removes solvent directly, and addition of a miscible anti-solvent (that the desired product has poor solubility in) also acts to force solid out of solution[43].

Anti-solvent addition has the largest potential for super-saturation generation and yield maximisation[6], but this can lead to excess uncontrolled nucleation (or formation of weakly bound networks[46]) if feed rates are not regulated[38, 43].

Cooling crystallisations are largely governed by the shape of the solubility curve. Solubility can be determined simply by gravimetric analysis[38, 47], or through the use of optical methods (such as turbidity/FBRM).

If product solubility is strongly dependent on temperature, then cooling has the potential for high yields. If solubility is largely independent of temperature, then solvent evaporation/addition would be the preferred option to maximise yield[19]. Cooling methods typically have low yields, but Muller, Fielding and Black have provided methods to determine the best solvents for improving cooling crystallisation yields[38].

A high initial cooling rate can lead to scaling on the reactor walls; with uncontrolled nucleation taking effect and the crystal build-up reducing the cooling capacity of the system. A more controlled cooling rate is low at first, to minimise nucleation, but increases with time as more surface area available for growth appears[6]. Thus a model which ensures a constant rate of super-saturation throughout the process was first postulated by Mullin and Nyvlt[48], and has been shown to apply to cooling, evaporation and solvent addition regimes.

$$T = T_{initial} - (T_{initial} - T_{final}) \left(\frac{t}{t_b} \right)^4 \quad \text{Equation 2-30}$$

For seeded systems, the exponent reduces to 3. Kim et al. found that use of this profile (albeit for acid addition) lead to a final product with superior handling and flow properties, with improved filter/drying characteristics. They also found longer crystallisations or a larger amount of seeds both resulted in greater mean crystal size[6].

2.4.3.2 Super-Saturation Control

The success of any crystallisation relies on the control over super-saturation. Super-saturation is vital for imparting purity, controlling crystal size/shape/morphology and final size distribution of the product[49]. This driving force also governs nucleation and growth of crystals, and the width of the metastable zone is useful in controlling these[50].

At high super-saturation (high cooling, evaporation or solvent addition rates), nucleation and growth are both enhanced. The increase in nucleation is more pronounced however, leading to uncontrolled nucleation, generation of fines and a broad crystal size distribution (CSD)[6]. This effectively sets an upper limit on the final crystal size, as available solute for growth must be distributed over a large number of crystals[19].

Nyvt showed that nucleation rate grows exponentially up to a certain critical value of super-saturation, after which, the excessive nucleation of new small crystals will dominate any attempts to increase super-saturation further[51].

Generally crystallisers are operated within the metastable zone, where nucleation is less dominant. The metastable zone width (MSZW) is dependent on the temperature, solvent, seeding, stirring and cooling rate. The effect of impurities is also well reported on[52]; it is common for impurities to widen the metastable zone[53] (though there are obviously exceptions), or change the nucleation rate[49].

Typically the MSZW can be elucidated using the 'polythermal method' – cooling of saturated solutions of various concentrations until spontaneous nucleation is observed. The resultant data points can be fitted to a curve and/or used for calculation of nucleation orders[54].

Keeping the super-saturation low (within the MSZW) encourages growth over nucleation, favouring fewer, larger crystals. The result is a much narrower CSD of similar sized particles [6, 37, 43]. The effect is greater with seeding; solute attachment onto existing seed molecules is thermodynamically preferred to the formation of new nuclei. By assuming all solute deposits onto seeds of initial mono-disperse size L_s , then the mass of seeds (M_s) is related to the product yield mass (M_p) of size L_p by[48]:

$$\frac{L_p}{L_s} = \left(\frac{M_p}{M_s}\right)^{\frac{1}{3}} \quad \text{Equation 2-31}$$

Seeding of super-saturated solutions has many benefits; quick precipitation of crystals, better control over crystal size and size distribution[6, 48], polymorph control[45] etc. Crystals can be grown, characterised by sieving to ascertain accurate size, and then used as seeds for subsequent crystallisations. This results in a more controlled mean crystal size[48].

2.4.3.3 Effect of Secondary Nucleation

At low super-saturation, contact nucleation is the main source of secondary nuclei[45, 55]. Particle-particle or particle-impeller collisions may result in fragmentation, shear or attrition that breaks off small parts of the crystals; the resultant matter can then act as secondary nuclei[37].

The generation of secondary nuclei is a barrier to narrow CSD, due to growth of fines. The rate of appearance is time dependent (i.e. a longer batch gives greater chance of particle-particle collisions etc.). Ottens, Janse and De Jong found linear relationships between the net nucleation rate and energy dissipated by the agitator and/or concentration of solids[55],

indicating a strong dependence on particle-agitator collisions. Super-saturation had less of an influence on nucleation rate.

Liang et al reported into the effect of agitator material on the secondary nucleation rate. They tested with stainless steel (hard) and Perspex (soft) agitators, confirming that increasing hardness increases the nucleation rate by particle collisions. However they also found that heterogeneous nucleation was influenced by the surface roughness of the agitator; with the smaller contact angles on smooth surfaces providing fewer opportunities for crystal growth[56].

The need to minimise secondary nucleation events must be balanced with the requirement for good mixing and avoidance of fouling[43]. The Zwietering equation can be used to approximate the minimum agitation velocity required to suspend particles in solution[57]:

$$N_a = S_z \left[v_k^{0.1} d_p^{0.2} S_f^{0.15} d_{impeller}^{-0.85} \left(\frac{g(\rho_p - \rho_f)}{\rho_f} \right)^{0.45} \right] \quad \text{Equation 2-32}$$

Where S_z is a constant based on the geometry of the vessel; values can be correlated from the literature[19, 57].

2.4.3.4 Monitoring of Crystallisation

Dissolution of solids can be measured by optical turbidity; when all solid mass has disappeared, turbidity is at a minimum. Upon the onset of nucleation, crystals appear and turbidity rises sharply; this can be used to monitor crystallisation progress[45, 58]. The same principle applies when using FBRM, which can be extended to monitoring appearance/disappearance over a specific size range of crystals over time (above a crystal size of 1 μm)[50].

Monitoring of super-saturation can be performed by attenuated total reflection Fourier transfer Infra-red (ATR FTIR) spectroscopy. This has been shown to be effective at doing this by measurement of solution concentration; as solids precipitate, their unique infra-red bands are picked up by the receiver, ascertaining the solids concentration over time[58, 59].

2.5 Filtration

2.5.1 Basics of industrial filtration

Filtration is the physical separation unit operation in which a solid phase is separated from a liquid (the 'filtrate') through a porous medium ('filter medium'). There are 2 major forms of filtration: 'cake filtration' (retention of solids on top of the medium) and 'depth filtration'

(retention of solids within the medium itself; useful for purification of liquids by removal of undesired solids). Cake filtration is pertinent in this case as isolation of the solid from the unwanted fluid is desired.

In the initial stages of cake filtration, particles are ideally captured over the surface of the medium via 'bridging' – a structural arrangement of particles that 'bridges' over the medium pores. Subsequent layers are built as additional particles come to rest over the initial bridges. The concentration of the particle structure continues to grow to form a 'filter cake'. The cake subsequently acts as the new filter medium as the channels between the particles permit the flow of liquid. As more layers are deposited the liquid solvent has further to travel, thus the cake's resistance to flow increases; hence a constant driving force will lead to a reduction in flow-rate over time[60].

Gravity is the simplest form of filtration, but suffers from poor throughput. Applying a vacuum below the medium can increase flow-rates (practical max. $\Delta P = 0.8$ bar), but the greatest separation power comes from applying a positive pressure (either by nitrogen pressurisation above the cake or an induced centrifugal force)[61].

Pressure filters are the most common type encountered in industry. They can achieve high specific driving forces as they are less bulky than other technologies (except centrifugal filters, but these are more expensive and complex). They are also typically sealable thus allowing treatment of flammable/toxic mixtures[62].

Filtration is predominantly measured both by fractional recovery of solids (relative to the concentration of solid in the feed) and liquid content of the final cake. For measuring the porosity of the bed, volume fraction is most often used, as density has little effect on packing behaviour[60].

At the end of filtration, the cake is washed (at discretion) and then discharged for further processing i.e. drying/comminution/formulation.

2.5.1.1 Filter media

The filter medium is a thin, porous sheet that provides support to settling particles whilst allowing liquid to pass through. The trapping of particles facilitates growth of the cake as subsequent particle layers are deposited[63].

In cake filtration, the filter medium pores are sensitive to blockage by fine particles. If a significant number of particles are caught within the medium pores then 'blinding' occurs, rendering the medium less permissive to the passage of liquid. If pore size is appropriately small, solids build in layers and this also increases resistance to flow. The end result is a

reduction in filter efficiency and flow-rate (vs. the pressure drop), but an increase in solids retention efficiency[60].

The chosen material of the medium varies depending on the suspension properties. Common constructs include cloth fabrics, metallic weaves, or other porous materials such as carbon (coal) and ceramics[62].

For systems in which blinding, cleaning or damage to the medium are problematic, filter aids may be employed. Filter aids can improve the filtration efficiency by housing binding sites for impurities and/or fines (i.e. such as in depth filtration). The resultant cake is still permeable to liquid whilst the filter bed entrains fines that would otherwise blind the cloth, thereby increasing filtrate flow. They are either applied directly to the filter medium or can be dispersed in the suspension as a pre-treatment to filtration[43, 62].

2.5.2 Factors influencing filtration performance

2.5.2.1 Pressure Drop

The pressure drop is created by viscous drag within the filtration process, and has a governing role in the rate at which the process operates. Increasing the pressure in the chamber has the general effect of increasing the rate of filtrate flow and cake growth, but the rate at which flow rises is lessened with increasing pressure difference[64]. This sets a practical limit on the operable pressure drop, influenced largely by the particle compressibility.

A larger pressure differential can also result in faster cake formation with an increased concentration[64]. It may however lead to the densification of agglomerates within the cake and a reduction in fluid channel sizes; this is known as cake collapse[26].

Antelmi et al investigated cake collapse under pressure with aggregated spherical latex particles. Collapse occurs when aggregates are compressed, dispersing them into constituent particles and reducing cake porosity. They found for increasing pressure, solid fraction rises, showing voids are filled in a compressible cake. Limitations were reached at a solid fraction of 0.46, when further rises in pressure had a minimal effect on the cake, as it has reached an 'incompressible' state.

To limit cake collapse, the authors recommend the use of non-spherical particles, as these bridge more effectively to resist collapse, requiring a shear force to disturb them (spherical particles pack with the minimum contact area, thus reducing the friction between them), or a higher inter-particle friction (such that particles are less inclined to slide over each other)[26]. An operation strategy in which low pressures are used initially (when chances of collapse are

heightened), before slowly ramping up to the operating pressure over time, can help to alleviate cake collapse[62].

2.5.2.2 Cake compressibility

As liquid flows through the cake the force of viscous drag acts on the particles, attempting to pull the particles towards the medium. If the cake is able to withstand these effects and retain its porosity and structure over the filtration process, then it is defined as incompressible. Compressible cakes will incur some form of structural re-organisation under pressure, wherein a porosity gradient is created with a maximum concentration of particles nearest the medium[65].

Most cakes are compressible to some extent, and in general, the extent of compressibility increases with decreasing particle size; smaller particles being easier to squeeze into cake voids and pack together tighter[62].

The compressibility of a particle bed has a large effect on filtration. Soft particles can deform when subjected to high pressures, causing them to widen and reduce liquid channel widths, blocking them and increasing the resistance to flow[60]. For highly compressible particles, the relationship between pressure drop and cake resistance increases almost proportionally until a critical pressure is reached. At this point, the flow rate reaches a maximum and plateaus, meaning that flow channels have collapsed and liquid throughput is poor. This makes subsequent increases in pressure indifferent to filtrate flow[66].

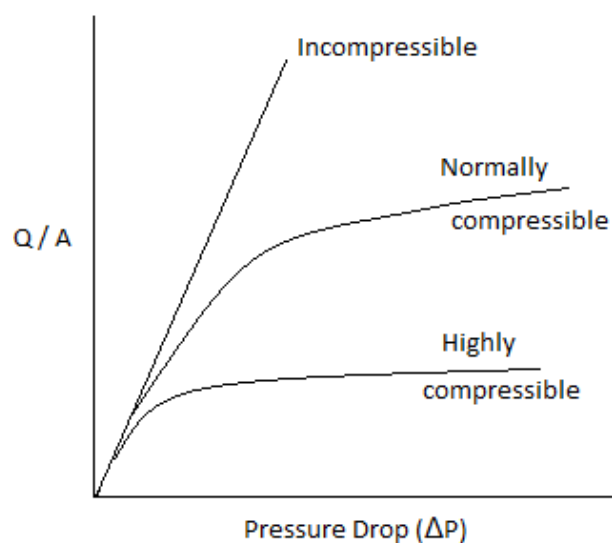


Figure 2-7: Effect of increasing pressure on filtration flowrate for particle beds of varying compressibility

Incompressible cakes are more likely to pack regularly and bridge appropriately over the filter medium. In this case increasing the driving force increases the rate of filtrate flow proportionally[66].

The critical angle of particle-particle contact is also factor in compressibility. For a particle 'A' settling onto particle 'B', the angle of contact determines the likelihood of 'A' depositing onto 'B'. If the angle is small then adhesion of A to B is probable; when the contact angle reaches the critical value, then friction between the particles is low and A slides over the surface of B. The critical angle is related to packing characteristics; inter-particle forces, specific surface area, shape and PSD all influence the chance of particle deposition on a particular cite in the cake[67].

In general, pharmaceutical solids form cakes with little to moderate compressibility (low specific cake resistance), meaning lab-scale filtrations operated at low-medium pressures are likely to be more predictable on scale-up[66].

2.5.2.3 Particle Shape/ Morphology

Particle shape and bed porosity are closely linked. For example, fibrous particles form open structures (porosity of approx. 0.9), whilst spheres pack tightly (porosity of 0.3-0.45)[60]. Plate-like crystals stack in layers and give poor filtration performance[37].

As with particle size, the specific surface area has a strong influence through the particle shape. Thus for reduction of viscous drag, larger, smoother particles are preferred[64].

Beck et al investigated the multiple polymorphs of L-glutamic acid, and found the flaky, spherical form to have a resistance of 40 times that of the needle form; which in turn was slightly more resistant than the polyhedral form. The additional resistance was accounted for by increased compressibility and specific surface area[41].

Walker and Svarovsky modelled filtration and investigated packing characteristics. Simulations based on smooth, spherical particles tended to over-predict cake resistance due to the lower packing-porosity of spheres[68]. Experimentally, irregular-shaped particles have a greater chance of bridging together and creating additional voids in the cake[67]. An increased voidage is conducive to liquid flow as the higher porosity lowers the resistance of the cake (i.e. there are more channels for filtrate to travel through).

2.5.2.4 Suspension Solid Concentration

The solid concentration of the suspension is a matter of balance. A higher initial solid fraction will correspond to a larger throughput, and thus lowers the power input/cost of pumping.

However a higher solid fraction means fewer channels are available for liquid flow[60]. For both incompressible and compressible systems, Tarleton and Willmer found lower concentrations led to an increased filtration rate; higher concentrations produced thicker cakes[69].

A higher concentration also increases the chances particles will bridge over the medium, which acts to reduce blinding. The minimum concentration required to initiate bridging is a function of the suspension properties, but is typically around 0.5% by volume[30]. Depending on the strength of the inter-particle forces or friction, bridges can be destabilised if there is a sudden change in flow direction or velocity, causing a reduction in porosity[64].

2.5.2.5 Particle size and size distribution

A theoretically ideal filtration would consist of large mono-disperse spherical particles. As a general trend, specific cake resistance is inversely proportional to particle size; as filtrate viscous drag on particles is a function of specific surface area. Thus the smaller the particles, the higher the total drag, and the lower the flow becomes. Experimental evidence suggests a doubling of the particle size results in a 50% increase in the volume of collected filtrate.[64]. Liquid can sometimes carry fines towards the medium, further increasing overall resistance and the chance of blinding or bleeding[62].

These points contribute to the influence of PSD; a wider distribution contains more fines which decreases porosity as smaller particles are able to pack more tightly between voids[64]. Hence particles should ideally be as large as possible; either by control of crystallisation conditions or pre-treatment of the feed e.g. agglomeration[26].

As size distributions are often characterised by a certain particle size relative to the spread e.g. the mean, mode, etc., Wakeman suggests characterising filtration PSDs by the 5 or 10% size, as invariably the smaller particles end up dictating the operation[64].

2.5.2.6 Scale-up

The scale-up of filtrations has typically been estimated with the aid of lab and pilot-scale experiments, such as the compression-permeability method (CP Cell method)[70]. Filtrations are performed and the porosity/resistance scale-up constants are obtained, from which estimations of large scale operation can be made. Frequently problems are encountered at scale due to high cake resistances and thus very slow filtrations; as such empiricism and heuristics are frequently the best tools available for prediction[69].

The advent of computer processing has significantly advanced the field of filtration scale-up. Primary efforts based on spread-sheet calculations allowed the solving of complex equations; albeit very slowly. Early models attempted to predict cake build-up from fundamental design equations, but many assumptions were made i.e. perfectly smooth particles, cake building in equivalent layers, no friction etc., but fairly good agreement with experimental data was observed.

Proliferation of computing power has now made modelling common practice, but a full-proof method is yet to be perfected. Literature is proliferated with successful methods that have come from the application of fundamental design equations, with constants obtained from lab-scale experiments[63, 65, 67-69, 71-79]. For instance, Holdich has made available internet-based computational tools for the selection of filtration equipment based on data that can be obtained with a few simple experiments[80].

For the scale-up of low-resistance cakes filtration times should be short and encounter fewer problems, hence these would usually only require a simple model for estimation of large-scale cake properties. For all other filtrations, a more rigorous model is often required[66].

Murugesan et al used a dynamic pressure modulation method with the software DynoChem. Their results of estimated filtration times had a reasonable agreement with experimental data[66].

Lu and Hwang calculated the critical angle of friction for settling particles in a cake, in order to study the mechanisms of cake formation. The model, which agreed well with experimental data, can also be used to predict the pressure distribution, porosity and specific cake resistance[67]. This model was subsequently updated to account for specific surface area of the particles and the medium resistance[74].

Interestingly, Tarleton and Willmer presented evidence that the scale-up 'constants' can function as variables. In testing an incompressible calcite system, their data showed somewhat random values of specific cake resistance over the range of filtration areas examined; a minimum was obtained for an area of 23 cm². For the compressible zinc sulphide, they found no minimum, but a gradually increasing level of average cake resistance as filter area rose. The authors acknowledge the contradiction of existing literature, but claim the results were supported by substantial repeat experiments[69].

2.5.3 Filtrate rate modelling

The basis of the common filtration rate model is taken from Darcy's law for flow through packed beds. The total pressure drop across the cake can be thought of as 2 separate terms; a

pressure drop due to the filter medium, and a pressure drop due to the interaction of the fluid with the particles (pressure drop over the cake):

$$\Delta P = \Delta P_c + \Delta P_m \quad \text{Equation 2-33}$$

Application of Darcy's law to this assumption thus yields the following relationship[26]:

$$\frac{dV}{dt} = \frac{A\Delta P}{\mu(\beta_m + \alpha)} \quad \text{Equation 2-34}$$

Where the resistances of the cake (α) and medium (β_m) are expressed as separate terms. The medium resistance can be determined from filtration of a pure liquid. Ruth et al examined the existing theory in 1933, and concluded that theory based on Poiseuille's law could only be applied to incompressible cakes[81]. Carman then suggested the parabolic law of filtration in 1938, whereby the volume of filtrate collected for an incompressible cake in time could be expressed by^[82]:

$$t = aV^2 + bV \quad \text{Equation 2-35}$$

Thus by dividing by V:

$$\frac{t}{V} = aV + b \quad \text{Equation 2-36}$$

A plot of 'y = mx + c' therefore yields a straight line, allowing calculation of the constants 'a' and 'b' from the gradient and y-intercept, respectively.

As the initial periods of constant pressure filtration are non-linear, extrapolation of the straight line trend can sometimes produce a negative intercept. This can be corrected for by assuming 2 stages of filtration; first accounting for the initial changing cake height, and subsequently when the cake has reached a constant resistance[83, 84]. Readings of t/V are only taken at steady-state, once the cake has been allowed the build at low pressure[82].

Ruth later showed that the resistance of a cake was proportional to the mass of cake forming at the medium, under constant pressure and porosity[70]. The equation he proposed is now widely used to model filtration flow rate[26, 41, 63, 65, 66, 69, 70, 73, 77, 79]:

$$t = \frac{\alpha \cdot \mu \cdot C_{eff}}{2A^2\Delta P} V^2 + \frac{\beta_m \cdot \mu}{A\Delta P} V \quad \text{Equation 2-37}$$

The average specific cake resistance (α_{ave}) is related to unit average specific cake resistance, α_0 , by:

$$\alpha_{ave} = (1 - n)\alpha_0\Delta P_c^n \quad \text{Equation 2-38}$$

Where ΔP_c is the pressure drop over the cake, and 'n' the compressibility index constant, which is found experimentally. For an incompressible cake, $n = 0$; increasing compressibility increases the value of the constant. The effective solids concentration (dry cake mass per unit volume filtrate) is given by:

$$K_m = \frac{\rho_f \cdot S_f}{(1 - S_f \cdot m_r)} \quad \text{Equation 2-39}$$

Where S_f is the solids mass fraction in the feed, and 'm_r' is ratio of mass of wet cake to dry cake, calculated as:

$$m_r = \left(1 + \epsilon \left(\frac{\rho_f}{\rho_p} \right) \right) \quad \text{Equation 2-40}$$

Where ϵ is the void volume fraction in the cake. The Ruth equation can thus be written:

$$t = \frac{\alpha \cdot \mu \cdot \rho_p \cdot S_f}{2A^2\Delta P \left(1 - S_f \left(1 + \epsilon \left(\frac{\rho_f}{\rho_p} \right) \right) \right)} V^2 + \frac{\mu \cdot \beta_m}{A\Delta P} V \quad \text{Equation 2-41}$$

Hence with the design equation and a simple lab filtration experiment, the values of 'a' and 'b' (Equation 2-36) can be calculated from known quantities and constant pressure experimental data. These constants can be used for estimation of cake properties to aid scale-up[66].

2.6 Mechanical Properties of Particles / Breakage

2.6.1 Fundamentals of particle breakage

Breakage can be subdivided into the 2 main modes of attrition and fragmentation (total failure). Attrition involves the gradual chipping of small fines from the surface of particles. Fragmentation is the fracture of particles into 2 or more major fragments, as well a number of smaller fines[40].

The propensity for materials to fracture is largely dependent on particle and bulk properties of the solid e.g. particle strength (tensile strength, toughness, Young's Modulus, hardness), particle shape, particle size/size distribution, material surface energy, moisture content and bulk density, as well as the material deformation behaviour (i.e. elastic or inelastic)[12].

The method of application of stress also plays a key role. The intensity, rate and type (e.g. compressive/shear) of stress is likely to influence particle breakage, as are the number of points of force loading (in general fewer points of loading ultimately result in a higher application of stress[85]).

Typically breakage occurs in materials at points of structural instability e.g. cracks, joints and weak bonds. This is due to the fact that stresses tend to concentrate in regions where there are changes in area, with the extent of curvature governing the extent to which the stresses magnify[86] (Figure 2-8). As an object is subjected to load, energy is absorbed in the form of strain until a critical point is reached and the object breaks[85].

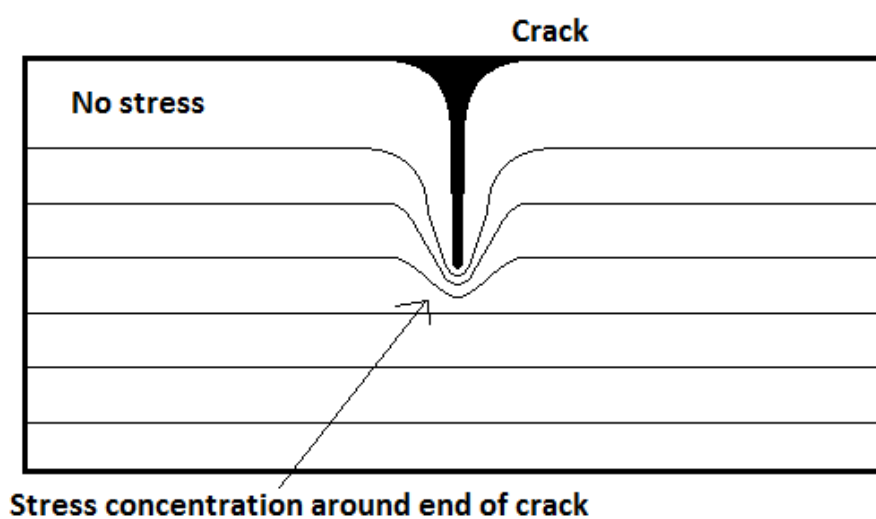


Figure 2-8: Effect of curvature on the concentration of stress. Reproduced from[86]

Typical loading modes include tension (by pulling), compression (by crushing), torsion (by twisting), shear (by cutting), attrition (by scraping), impaction and bending. These provide a basis for much of the fundamental understanding of breakage mechanics; via the use of single particle breakage tests. These are categorised into single impact, double impact and slow compression tests[85]. These methods are preferable due to the avoidance of particle-particle interactions that could affect the result[87].

Single impact tests consist of dropping or accelerating particles onto a target in order to break them. Double impact tests are similar except the particle typically rests on a surface whilst an object is accelerated towards the particle. Slow compression is usually performed by uniaxially stressing the particles at low rates. Tests that load particles at low enough rates to allow stresses to propagate equally throughout the particle are known as quasi-static tests[85].

It is of vital importance to characterise and control the extent of particle breakage, as particularly in the pharmaceutical industry many compounds are fragile and susceptible to breakage[9, 10, 88, 89].

2.6.1.1 Stress and strain

Stress is defined as the force acting per unit area, whilst strain is the ratio of the extension of a body relative to its original length. Stress and strain are related to each other via Hooke's law, which states[86]:

$$\text{stress } (\sigma) = k_h \times \text{strain}(x_{ext}) \quad \text{Equation 2-42}$$

Where k is a constant that is material dependent. Thus strain is directly proportional to the stress a material is subjected to (under elastic conditions). Plotting stress against strain forms the stress-strain graph, from which several characteristics can be gleaned (Figure 2-9).

The line from A-B is the elastic region, whereby stress is directly proportional to the strain induced. The gradient of the line A-B (stress/strain) is the Young's modulus of the material. Point C is the yield limit, after which brittle materials will break if subjected to increased stress.

In the region C-D, ductile materials will undergo plastic (permanent) deformation when increased stress is applied, and a disproportionately large amount of extension is seen for small increases in stress. At point D, the ultimate stress of the material, breakage occurs.

Strong materials have high yield stresses and thus require high stresses to deform them plastically or break them. Hard materials require larger inputs of stress to deform them in the first place, thus the gradient of the stress-strain curve is higher than that for soft materials.

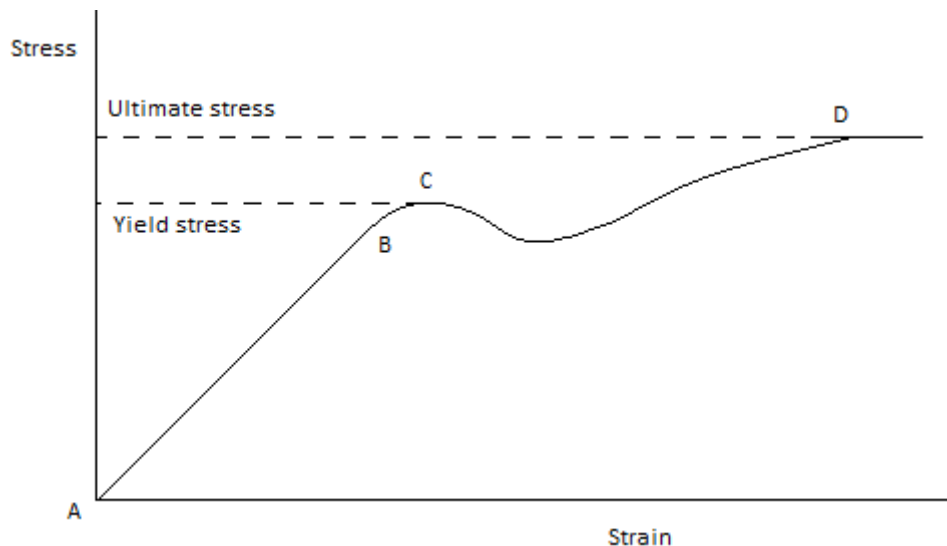


Figure 2-9: Example stress-strain graph (not indicative of any particular material). Reproduced from[86]

2.6.1.2 Crack propagation

Breakage of particles is initiated by propagation of interior cracks, which is related to the ability of a material to conduct or absorb stress. If a material is deformed, it will undergo

extension (strain) in accordance with its elastic limit of stress; removing the stress causes the material to return to its original configuration. When deformed past its elastic limit, a ductile material may deform permanently but not break; brittle materials will fracture when exposed to these excessive stresses. Ductile materials may still break when subjected to stresses above their ultimate limits[86].

When particles fracture, new surface area is created, which requires an input of energy. The application of stress provides an input of energy that the material can absorb in the form of strain energy. If there is enough strain energy stored within the material then existing cracks will self-propagate. When the strain energy is equal to or greater than the surface energy that would be created with the crack, then fracture is possible[86]. This is governed by the Griffith equation, whereby the tensile stress required for crack formation (σ_T) is[90]:

$$\sigma_T = \sqrt{\frac{E \cdot \gamma_e}{L_c}} \quad \text{Equation 2-43}$$

Where L_c is half of the total crack length and γ_e is the surface energy of the material. A low surface energy is conducive to cracking, whilst high surface energy materials are less likely to propagate cracks[86]. Generally, cracks are propagated in high-stress areas of a particle and develop from the origin of the crack[87].

In practice however it is difficult to apply quantitative fracture mechanics due to the difficulty in calculating the stress fields within irregular particles (i.e. most particles)[85]; hence most analysis is concentrated on empirical methods of breakage characterisation[89].

The crystallinity of a material is known to affect its fracture mechanism. Amorphous materials obstruct the development of cracks more effectively than crystalline materials; lattice planes provide a lower fracture energy path for cracks to propagate along[87]. This leads to differing mechanisms of size reduction; amorphous materials tend to break into large and small particles whilst crystalline particles are more likely to fracture into a narrow range of sized particles[86].

From the knowledge that a critical size of indentation will lead to the formation of cracks[88], the work required to propagate a crack in a substance due to release of elastic strain energy can be estimated using the Vickers hardness.

2.6.1.3 Tensile strength of a particle

A particle's tensile strength can be estimated by subjecting it to a point load compression test. For elastic spherical particles, an approximation of tensile strength (σ_T) can be found from[85]:

$$\sigma_T = \frac{2.8F_f}{\pi D_{load}^2} \quad \text{Equation 2-44}$$

Where F_f is the fracture force, and D_{load} the distance between loading points in the compression test. Roberts et al formulated die-cast beams by compacting powders under hydraulic pressure, with the resultant structures tested for their tensile strength using a 3-point beam compression test. The tensile strength was calculated from[91]:

$$\sigma_T = \frac{3FL_p}{2w_p \cdot h_p^2} \quad \text{Equation 2-45}$$

A derivative of the Euler-Bernoulli beam bending theory[9]:

$$\sigma_T = \frac{6FL_p}{w_p \cdot h_p^2} \quad \text{Equation 2-46}$$

Where L_p , w_p and h_p are length, width and height of the beams, and F the force required for breakage. They found critical tensile strengths for the beams in the region of 5-35 MPa; however these values are not easily applicable for individual particles as they are determined from compacted powders.

The tensile strength of a bed of particles is difficult to measure in practice however. Macleod and Muller used a variable pressure attrition test (VPAT) to quantify particle strengths, although this is only useful for bulk powder measurements and not with single particles[9].

2.6.1.4 Attrition

Ghadiri and Zhang developed an equation for the attrition propensity of a material (η_{att}), which is heavily reliant on the impact velocity of the particle (v) and its fracture toughness, (K_c)[87]:

$$\eta_{att} = \frac{\rho_p \cdot v^2 \cdot l_p \cdot H}{K_c^2} \quad \text{Equation 2-47}$$

Where ρ_s is the solid density and H the material hardness. The model was developed for the attrition of particle fines due to the generation of lateral cracks just below the particle surface (hence attrition is observed as opposed to fracture), and has been shown to accurately represent the attritional behaviour of aspirin particles subjected to impact[92].

Hare and Ghadiri investigated the size changes due to shear stress in aspirin (cuboidal) and paracetamol (rhombohedral); both fairly isometric blocky morphologies. They found an attritional breakage mechanism in both cases, in which fines are the predominant breakage product[89].

2.6.2 Process causes of breakage

2.6.2.1 Impact forces

Impellers contribute to secondary nuclei formation due to particle-impeller collisions (and resultant particle-particle or particle-wall contacts). The energy involved in impact can be estimated from the kinetic energy equation[88]:

$$E_k = \frac{1}{2} \rho_p d_p^3 v^2 \quad \text{Equation 2-48}$$

Assuming typical contact velocities of between 3-20 ms⁻¹ and a solid density of 2000 kg.m⁻³, the range of impact energies lies approximately between 10⁻⁸ and 4x10⁻⁴ J.

2.6.2.2 Under filtration

Typical breakage under processing is assumed to come from particle collisions and agitation (such as from agitated drying). However there is evidence that pressure filtration could contribute significantly to particle breakage.

Macleod and Muller investigated the common assumption that the majority of breakage tends to occur under agitated drying, by evaluating the particle size distribution of a range of compounds before, during and after separate filtration and drying stages. They found for 8 out of 9 systems tested there was an appreciable decrease in the fraction of large particles and a corresponding increase in the fraction of small particles, with the majority of this change occurring during filtration[9].

There remains the possibility that the size reduction observed under pressure filtration could have been due to de-agglomeration of aggregates. SEM images appear to show ‘fractured’ edges of crystals, and images captured before the filtration stage are claimed to be un-agglomerated before processing has begun. Yet the authors concede that further evidence must be collected in order to completely rule out the possibility[9]. A variable pressure attrition test (VPAT) is recommended to differentiate between disintegration of agglomerates and breakage of particles.

Interestingly, the authors also found a comparatively low level of breakage after agitated drying. This is contrary to the experience of Lekhal et al[7, 8], Kim et al[6] and Hamilton et al[5], who have all found significant breakage under agitated drying. Macleod and Muller only found breakage under drying for 1 compound, with a tablet-like morphology.

The recent findings of Hamilton et al offer some corroboration with the filtration-breakage findings, as they also reported an increase in the number of shorter needles and a decrease in

the number of large needles post-filtration. However these results are difficult to compare directly as their crystals were re-slurried (raw material added to solvent) as opposed to Macleod and Muller who recrystallized theirs, which could equate to differing crystal properties[5].

More recently, Cornehl et al have provided more evidence of breakage under pressure filtration. They filtered (freshly re-crystallised) protein crystals of lysozyme in isometric and needle morphologies, and found evidence of breakage in both cases, albeit with differing mechanisms. By tracking the fraction of small, modal and large crystal sizes, they concluded that the majority of breakage of the isometric crystals came from attrition and chipping of edges from the larger particles, whilst the needles were completely broken (corresponding to large increases in the fraction of fines present in samples)[10].

The authors also noted that the majority of breakage occurred within short timescales (1-2 minutes over the course of an over-night filtration), leading them to conclude that it is the maximum value of pressure attained and not the duration that dictates the extent of breakage. This could be an interesting aspect to test within this project; made possible by the continuous percolation rig being proposed (to be discussed).

Hence there is an increasing amount of evidence for the phenomenon of filtration crystal breakage, and it will be important to not only show proof of concept, but being able to generate models based on particle properties. The premise behind the pressure filtration breakage is addressed by development of a simplified model, developed by Macleod and Muller[9].

Needles in the particle bed come to rest with a number of contact points between them. As such, these contact points resist the pressure generated by the filter-unit to sustain the structure of the bed. The force per unit area acting upon these contacts is high, and as there are multiple contacts acting on each particle, these act as a pivot for the transmission of forces. If the force exerted on one of these particles exceeds the ultimate strength of the material, then breakage occurs.

The final model illustrates the factors that determine the tensile strength, and thus the breakage propensity of a particular material; hence the maximum tensile strength of a particle can be approximated from[9]:

$$\sigma_{crit} \approx 6\Delta P \left(\frac{\rho_p}{\rho_b}\right) \left(\frac{L_p}{h_p}\right)^{0.5} \frac{h_p}{w_p} \quad \text{Equation 2-49}$$

And hence the factors that were seen to influence breakage are the pressure drop, true particle (skeletal) density compared to bulk density, and the particle dimensions (length, height and breadth); this was alluded to by Hamilton et al who recognised that minimal breakage was observed at filtration pressures of 0.5 bar[5], as the stresses generated (1-4 MPa) are on average far lower than the typical strength of common pharmaceutical solids (5-14 MPa); which incidentally are the kind of pressure magnitudes experienced when filtering at 2 bar[9].

The model however takes no account of fundamental material properties (hardness, strength, toughness etc.) and hence does not comply fully with the results observed.

Chapter 3

3 Materials and Methods

3.1 Introduction

This chapter presents the methodologies by which practical experimental investigations into particle breakage are conducted. The design and construction of the continuous percolation rig (CPR) is described in detail, as is the method for calibrating the pump that powers liquid circulation around the system. Crystallisation techniques used to generate the raw material used for much of experimentation are also detailed.

3.2 Design and Assembly of a Bench-scale Continuous Percolation Rig (CPR)

3.2.1 Equipment identification and problem overview

The general layout of the proposed rig is depicted in Figure 3-1. Fluid is recirculated in a loop, via a reservoir (open to atmosphere) and pump, around the filter chamber. The particles inside are compressed by the liquid pressure of the mother liquor bearing down upon them.

A nitrogen supply to the filter chamber will enable the drying of the cake post-percolation; this can be provided from a nitrogen outlet within a fume hood. The supply pressure/flow can be controlled using a pressure regulator; this will also provide relief to the system in case of overpressure.

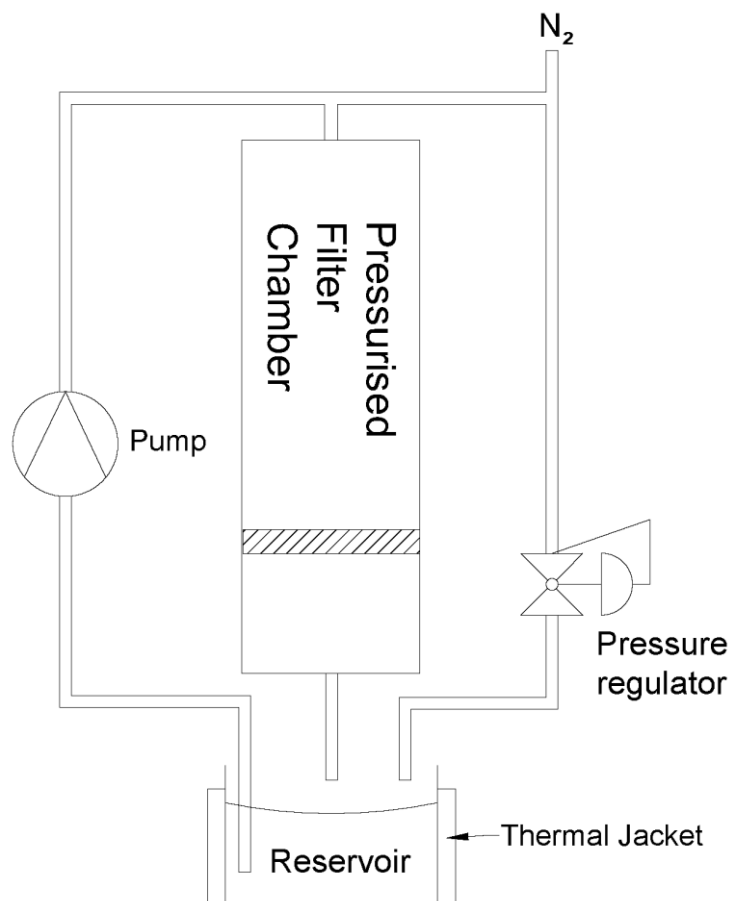


Figure 3-1: Basic proposed schematic for the 'continuous filter' rig design

The proposed filter volume will consist of a 334 mm x 35 mm type 304 stainless steel tube; 320 cm³ in volume with 9.62 cm² of filtration area. The stainless steel construction will offer solid chemical resistance to a wide range of potential solvents. The tube is rated to approx. 200 °C and 13.8 bar pressure, hence should easily accommodate the proposed experimentation.



Figure 3-2: The filter tube (pen shown for size reference – pen is approx. 145 mm long x 12mm diameter)

The filter tube consists of removable top and base caps. The top cap contains 2 ¼" Swagelok inputs, whilst the bottom cap houses a filter medium support and bottom run off valve.

A reservoir is necessary to house the supply of fluid and ensure a consistent source is available to the pump. A jacketed glass vessel, cooled with thermal fluid to keep the temperature of the saturated solution constant, should suffice for this purpose.

3.2.1.1 Theoretical estimation of flow through a packed bed & pump selection

For continuous operation, the effluent from the filter unit must be recirculated and pumped back into the filter tube. At pressure differentials of approx. 1-5 bar, and a filter tube diameter of 35 mm, a significant flow rate will be induced. A pump capable of performing this operation must be identified, purchased and integrated into the system.

The expectant flow rate can be approximated from the empirical Ergun equation, which is typically used to calculate pressure drops through packed beds[25]:

$$\frac{\Delta P}{H} = \left(\frac{150}{Re_p} + 1.75 \right) \times \frac{\rho_f u_i^2}{d_p} \times \frac{1 - \epsilon}{\epsilon^3} \quad \text{Equation 3-1}$$

$$Re_p = \frac{\rho_f u_i d_p}{\mu(1 - \epsilon)} \quad \text{where } u_i = \frac{u}{\epsilon} \quad \text{Equation 3-2}$$

By re-arranging for the superficial velocity, u_i , the flow through the bed can be estimated:

$$u_i^2 = \frac{\Delta P}{H} \times \frac{\epsilon^3}{1 - \epsilon} \times \frac{1}{\left(\frac{150}{Re_p} + 1.75 \right)} \times \frac{d_p}{\rho_f} \quad \text{Equation 3-3}$$

The (modified) particle Reynolds Number is dependent on the superficial velocity, which is the current unknown variable. Hence an iterative solution is developed in which an initial value for u_i is substituted into Equation 3-3 and used to find the resultant superficial velocity recursively. When the difference between the sum of the squares of the 2 values of u_i is minimised, then the algorithm has obtained a solution.

The variables listed in Table 3-1 are used to calculate an estimate for the fluid flow. The bed height is assumed at 5 cm; not atypical for a particle bed but large enough to allow for unforeseen circumstances. The fluid density and viscosity are taken as that of water[93]. A porosity of 0.5 is assumed for a bed of needles.

The particle diameter is difficult to estimate, not only due to needle-like particles having irregular aspect ratios, but due to the fact that the filter cake will contain a whole distribution of particles sizes, not just a single one. A value of 50 microns is taken as an approximation, based on the fact that although many crystals are likely to be much larger, filtrations are often limited by the smaller particles (as these pack tighter and reduce the flow of liquid to a greater extent).

Table 3-1: List of values used to estimate fluid flow through a packed bed of diameter 3.5 cm

Parameter	Symbol	Value	Units
Pressure Dif.	ΔP	100000	$\text{kg}\cdot\text{s}^{-2}\cdot\text{m}^{-1}$
Bed Height	H	0.05	m
Particle Diameter	d_p	0.00005	m
Fluid Density	ρ_f	998	$\text{kg}\cdot\text{m}^{-3}$
Fluid Viscosity	μ	0.001	$\text{kg}\cdot\text{m}^{-1}\cdot\text{s}^{-1}$
Porosity	ϵ	0.5	-
Bed Area	A	0.000962	m^2

The recursive algorithm is performed using a range of pressures from 1 bar gauge to 5 bar gauge; thereby encompassing a wide range of possible filtration pressures (however 1-2 bar would be typical industrially).

Parsing the results of the algorithm and converting the superficial velocity into a volumetric flow rate provides the final range of solutions – from 28 (1 bar) to 132 (5 bar) L/h; an appreciable transfer of material. Allowing for an approx. 20% margin of error gives a rough value of 160 L/h; hence the selected pump should be able to cover this value.

Knowing the approximate pump specification, a Kepner-Tregoe decision making analysis is employed to narrow down a choice of several prospective pumps. These are factored in terms of the capable delivery, delivery pressure, price, size/weight and materials of construction (i.e. its chemical compatibility). The Wanner Engineering Hydra-Cell P200 diaphragm pump (Wanner Engineering, Inc.; Minneapolis, USA) is selected due to its favourable decision-matrix score.

The P200 provides a flow rate of up to 160 L/h and is capable of imparting up to 100 bar pressure at temperatures of up to 120 °C; all beyond target specifications. Fluid is pumped by 3 internal diaphragms which help provide a stable, pulse-free flow. As a positive displacement pump, the P200 will pump a specific volume of fluid with each cycle, thus ensuring that liquid flow will not change with a change in pressure; a desired trait considering the fluid pressure will be changing throughout experimentation.

Positive displacement pumps however have no natural ‘shut-down’ mechanism (unlike centrifugal pumps for example), and as such will continue to pump against a dead end until the outlet pressure becomes critical, at which point the pump or system could suffer irreversible damage.

As saturated solutions are to be pumped, the build-up of precipitated solids in the system are inevitable. Although the process line can be cleaned with fresh solvent in-between experimentation, there is no guarantee that narrow-bore ¼” lines will not become blocked

during the course of a single experiment. It is also possible that the filter medium could blind, or the solids residing above in the filter tube could restrict flow to the point at which the pressure spikes.

All of these eventualities render the use of a safety relief valve essential. The valve is ideally placed as close as possible to the outlet of the pump. This will ensure that any sudden and unanticipated pressure spikes are alleviated via routing the flow back into the reservoir tank.

3.2.1.2 Filter insert design (sampling of filter cake)

To facilitate easier sampling of solid material, a removable 'insert' has been designed to contain the contents of the filter tube (Figure 3-3). Its hollow cavity will hold the crystal material whilst the rig is in operation; when the experiment is finished the insert is simply removed from the filter tube, thus removing the cake also. The base of the insert is 'lipped' so that it cannot become trapped within the filter tube.

The key design motivator is the difficulty in removing a cake of particles from the filter tube; previously the operator would need to scrape, dig or otherwise disturb the cake in order to loosen it from within the filter tube (which could potentially damage the crystals inside). With the filter insert, the cake can be removed from the inner tube relatively unharmed.

Another design consideration is the ability to remove particles from differing heights of the cake. The filter insert contains a cut-out hole approximately 10 mm in width that allows the operator to remove crystals from specific areas or heights of the cake, whilst it is still in-tact and identification of the particle source is still known.

A flow-breaker has also been designed to reduce the effects of turbulence in the tube. Consisting of a PTFE plate with cut-out voids to permit flow, it is designed to break up any turbulent jets forming around the tube inlet, and to help keep the cake in a consistent state of compaction.

The insert is to be constructed from stainless steel for its chemical resistance and strength. The extra weight (compared to say aluminium) is not considered to be a problem for operation.

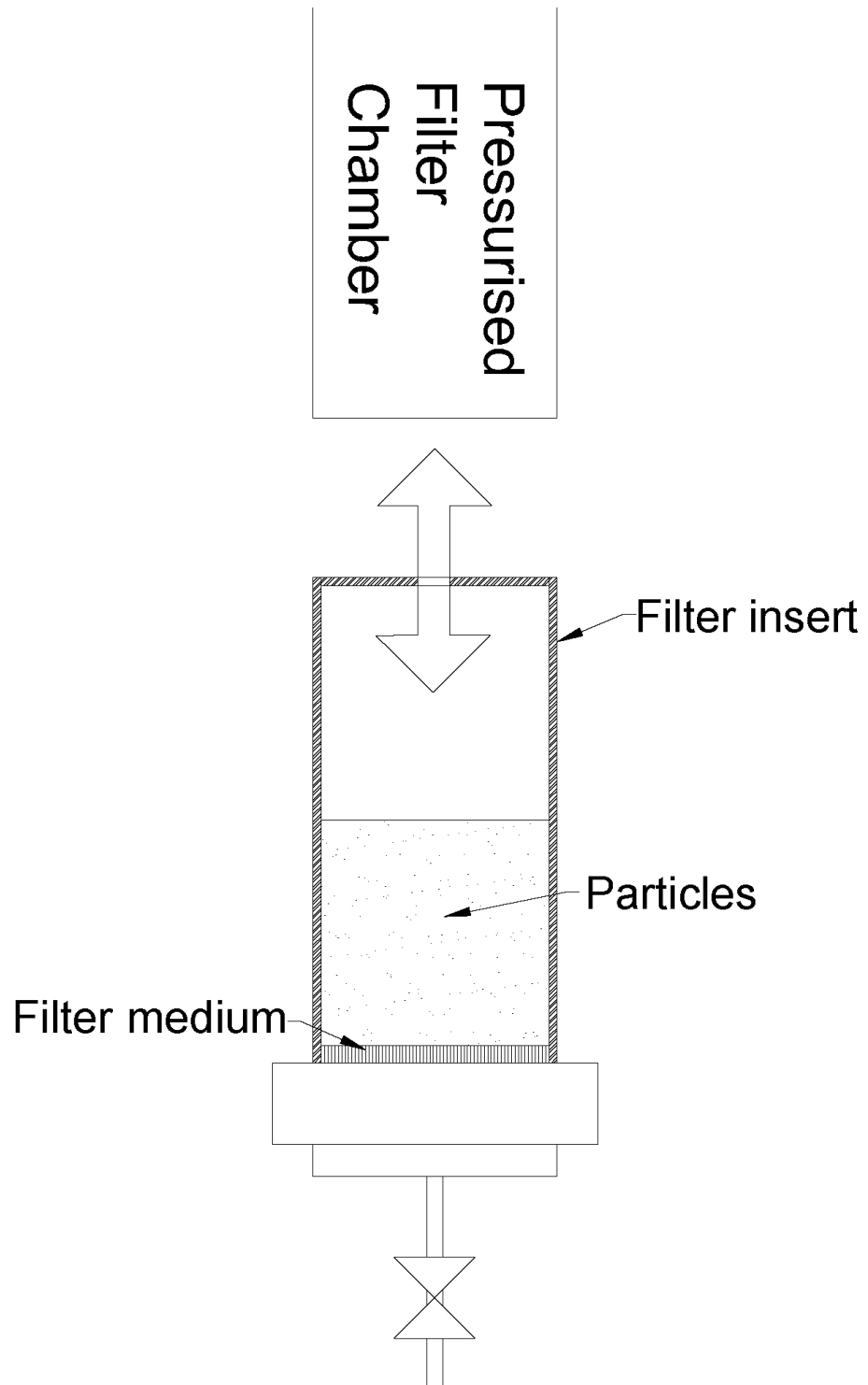


Figure 3-3: AutoCAD schematic of the filter-chamber insert

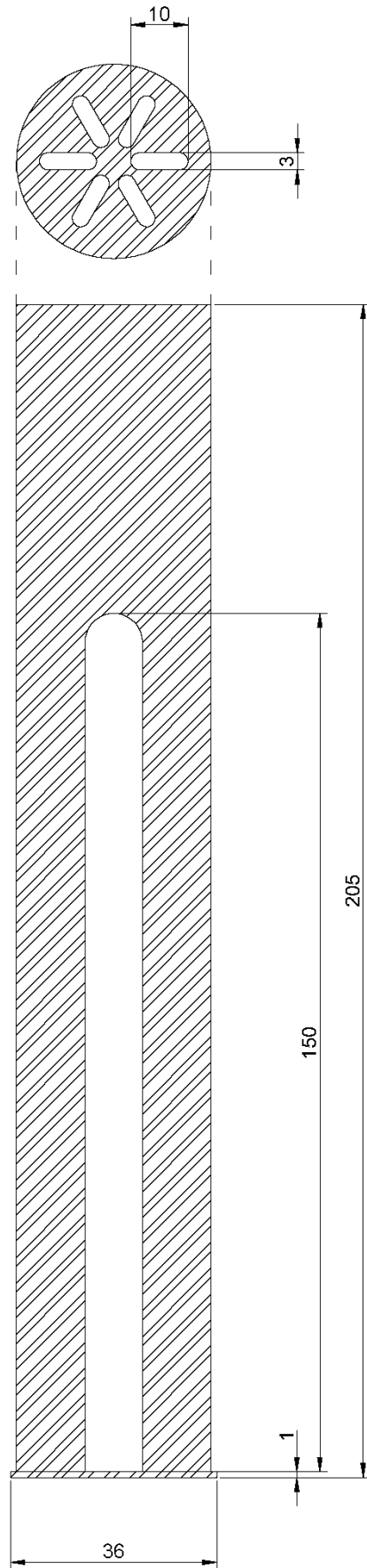


Figure 3-4: (Left) Technical drawing of the filter insert; (Right) The finished equipment

3.2.1.3 Heat exchanger design

The action of imparting energy to the pumped fluid has the undesired side-effect of raising the temperature of the solution. For an experiment in which the temperature should ideally remain as stable as possible (such that a saturated solution is not to become unsaturated and therefore begin to dissolve more solid – thus having the effect of ‘shrinking’ the size of the crystals and distorting our expected results), a rise in temperature of the mother liquor is unacceptable.

Therefore to combat temperature rises a heat exchanger is proposed, designed to lie immediately downstream of the pump, and carry thermal fluid from a Julabo FP50-HD heater-chiller unit. This would help to counter-act any cumulative heat effects produced by the pump.

The process fluid is carried via a ¼” stainless steel tube; hence the natural form of heat exchanger suitable for this application would be a tube-in-tube arrangement, with the thermal fluid tube housed around the outer shell of the process line (illustrated by the schematic in Figure 3-5). This will enable a simple retroactive fit to be incorporated into the percolation rig.

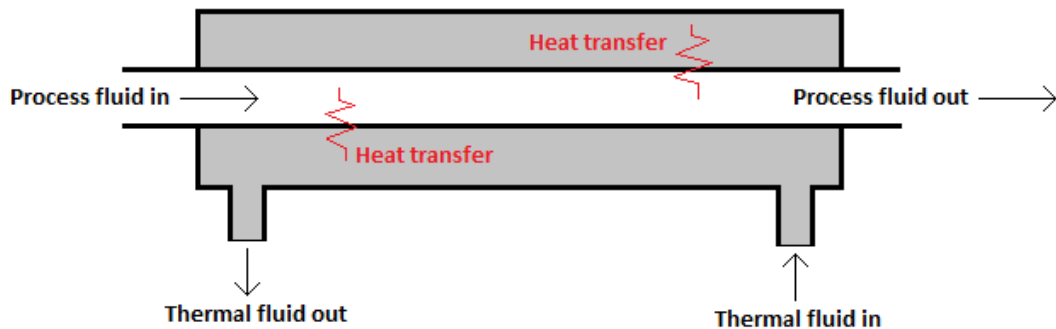


Figure 3-5: Schematic of counter-current tube-in-tube heat exchanger design

3.2.1.3.1 Theoretical basis for heat exchange design

The basis of any heat exchange design is found from the following well known design equation[93]:

$$Q = U \cdot A \cdot \Delta T_m \quad \text{Equation 3-4}$$

Where Q is the power in Watts, U the overall heat transfer coefficient and ΔT_m the log mean temperature difference. The surface area, A , is the desired unknown, hence the equation can be re-arranged as:

$$A = \frac{Q}{U \Delta T_m} \quad \text{Equation 3-5}$$

Before constructing the heat exchanger, it is necessary to know how much heat transfer area is required i.e. what is the required length of physical encapsulation of the process line.

To be able to calculate an area, several quantities are required to be estimated due to a lack of an existing comparable system. As the heat duty will vary with the operating conditions (e.g. the heat imparted by the pump is greater at higher operational flow rates), it is prudent to make estimates based on more extreme scenarios; hence the heat exchanger is designed with high flow rates and high duties in mind.

The energy (per unit time) required to increase 1 kg of material by 1 °C is given by:

$$Q = \dot{m} \cdot c_p \cdot \Delta T \quad \text{Equation 3-6}$$

Where the mass flow is calculated by assuming a volumetric flow rate equal to that of the maximum rate the pump can provide; this is approximately equal to 2.66 L/min. The solvent in the process line has an effect on the ability to remove heat; this is influenced by its specific heat capacity. Water has a high specific heat capacity and is thus requires more energy to reduce (or increase) its temperature.

The estimated temperature drop is based on preliminary experimentation, in which water was found to suffer a reduced level of temperature increase when compared to the alcohols; hence this is reflected in the estimated temperature drop that will need to be achieved. Excess capacity is accounted for by assuming a relatively large required drop in fluid temperature per pass (0.5 – 1 °C). The required power is roughly equal to 90 W in each case, hence a value of 100 W is assumed.

Table 3-2: Table of estimated power to be transferred from the process fluid

Solvent	Density (kg/m ³)	C _p (J/kg.K)	Mass Flow (kg/min)	Est. temp. drop (K)	Power Req. (W)
MeOH	791	2490	2.104	1	87.32
EtOH	789	2510	2.099	1	87.80
Water	1000	4182	2.660	0.5	92.70

The overall heat transfer coefficient is a proportionality constant used as a measure of the efficacy of heat transfer. Full evaluation of all associated resistances is complex and often inaccurate, as much of the data required is not available to the designer until the heat exchanger is operating. Typically the value of U is estimated based on tables of data for comparable systems[93]. A relatively conservative estimate of 600 W/m².K is taken for the basis of this design.

The final variable is the log-mean temperature difference, ΔT_m :

$$\Delta T_m = \frac{\Delta T_A - \Delta T_B}{\ln \Delta T_A - \ln \Delta T_B} \quad \text{Equation 3-7}$$

Where ΔT_x is the difference in temperature between the streams exiting the heat exchanger at end 'x'. When cooling jacketed vessels, the temperature of the jacket is typically set at ± 10 - 12 °C. Assuming a process fluid temperature of 20.5 °C at the inlet and 19.5 °C at the outlet, and a coolant inlet temperature of 8 °C and outlet of 9 °C, the log-mean temperature difference is:

$$\Delta T_m = \frac{12.5 - 10.5}{\ln 12.5 - \ln 10.5} = 11.47^\circ\text{C} \quad \text{Equation 3-8}$$

The estimated heat exchanger area is therefore:

$$A = \frac{100}{600 \times 11.47} = 0.015\text{m}^2 \quad \text{Equation 3-9}$$

Assuming the exterior of a $\frac{1}{4}$ " diameter tube is the contact area available for heat transfer, then the length of tubing that is to be covered is roughly equal to 72 cm. Taking a final +10% margin for contingency gives a final design length of ~ 80 cm.

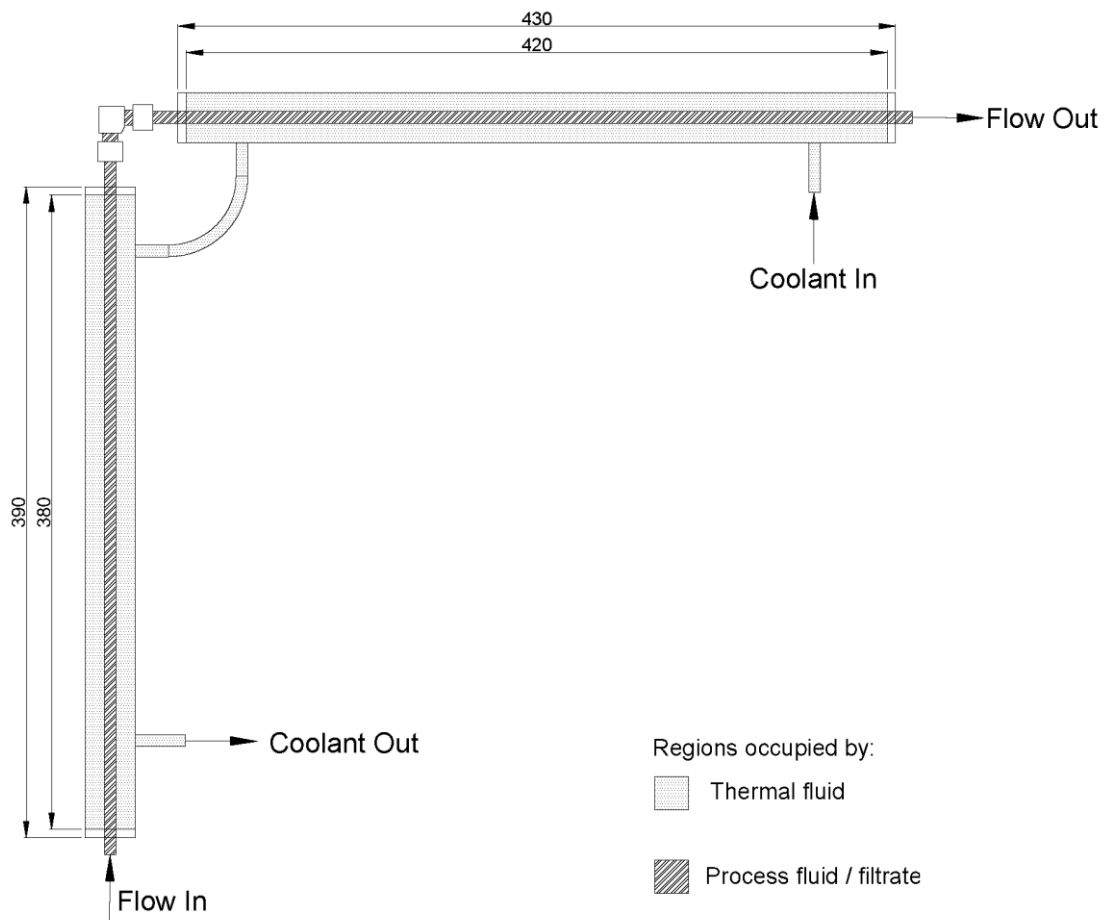


Figure 3-6: Technical drawing of the final heat exchanger design

The final heat exchanger design is depicted in Figure 3-6. The design is envisioned as an 'L-shape' to account for the length of coverage required and the layout of the existing components in the rig.

3.2.1.4 Pump calibration

The flow rate provided by the pump can be accurately determined from the inverter frequency; this requires a calibration of the pump. This is performed under several conditions to note variations in flow/resistance of the filter. All measurements are performed under the following premises (following standard operating procedures as previously detailed unless otherwise stated):

- 1 The pump is run for 20 minutes initially.
- 2 The maximum speed required is assumed to be a flow rate equivalent to that of a 50 Hz motor frequency. The pump delivery is measured at this maximum speed via the use of a calibration cylinder – i.e. the return line from the filter tube is directed into a volumetric measuring cylinder of 100/250 mL, and the time taken to fill this cylinder with liquid is measured.
- 3 Pump delivery under chosen conditions is measured for a number of different inverter frequency rates (i.e. 10, 20, 30, 40, 50 Hz); allowing several minutes in between each frequency adjustment.
- 4 These values are plot using the x-axis for Hz and the vertical axis for L/min flow. A straight line is drawn through the points to complete the calibration curve.

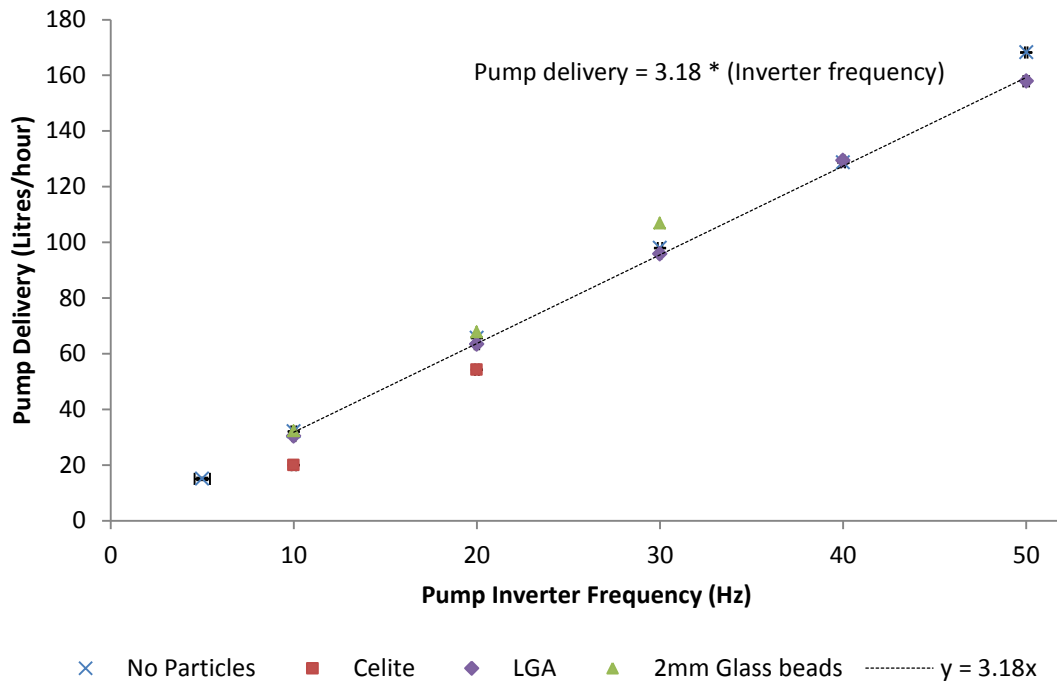


Figure 3-7: P200 pumping calibration plot of delivery vs. inverter frequency

Pump delivery in L/h is plotted against the inverter frequency, such that flow rates can be directly ascribed to a frequency setting used for percolation experiments i.e. this simplifies operation as the user controls the pump by setting a frequency.

The P200 pump is initially calibrated with the filter tube empty (i.e. only pure distilled water is recirculated), so as to create a 'zeroed' instance of system operation (the generation of pressure in the pump acts to slow down liquid flow slightly – the effect is negligible at lower pressures). A calibration is also presented using glutamic acid needles as part of percolation testing, and of Celite, a tight-packing silica often used as a filter aid.

A cake height of approximately 5 cm, typical for a pressure filtration, is used for the calibration with beta-glutamic acid.

The plot produces a linear trend in which pump delivery or liquid flow is directly proportional to the inverter frequency. This trend is clear whether the filter cake is present or not; in actuality the difference in observed flow rate between a glutamic acid cake and an empty filter tube is minimal up until frequencies of 50 Hz, for which there is a slight derivation from linearity.

In addition to deviations in flow rate at 50 Hz operation (~6%), operation at low flow rates corresponding to 10 Hz produced an appreciable deviation (~5%), showing that extremes of operation tend to produce the greatest irregularities in flow.

Table 3-3: Differential liquid flow between empty filter tube and tube containing glutamic acid cake (L/h)

Flow Rate of liquid (L/h)	Inverter Frequency (Hz)				
	10	20	30	40	50
No particles	32.04	65.66	97.99	128.72	168.22
β -glutamic acid	30.38	63.40	95.82	129.35	157.87
Δ Flow rate (L/h)	1.66	2.25	2.18	-0.63	10.36

The Celite calibration test shows appreciable deviation from an empty tube, showing reduced flow rates for a comparable power input. The reduction in flow is as expected; Celite is a fine powder and packs in a tight configuration (i.e. there are fewer voids available for liquid passage). The data is limited however, due to sudden pressure spikes detected when attempting to operate at frequencies above 20 Hz, hence the experiment was terminated.

The pump calibration serves as a reference table to allow percolation to be conducted, whilst having confidence that a liquid flow with a high degree of accuracy can be assigned to a particular setting of inverter frequency.

3.2.1.5 Thermal bath control

The temperature of the saturated solution within the system is controlled using a heater-chiller bath, which recirculates thermal fluid to the reservoir jacket and the heat-exchanger. However, the temperature of the liquid inside is under a state of flux, and is variable even whilst under a steady-state percolation. This gives rise to the need to update the thermal fluid temperature on the heater-chiller bath. This is possible by manually entering the hardware's configuration settings, inputting a new temperature and confirming it, however the process is labour-intensive and would require almost constant updating of the thermal fluid temperature in response to the current process liquid temperature. There is also no way in which to log the temperature data.

A piece of software has been engineered to simplify the entire process and provide a user-friendly interface that enables control of the heater-chiller system. The software is built *Python*; an open sourced, 'C-based' object oriented programming language[94]. The hardware communicates via an RS232 port, fed into a Raspberry Pi micro-computer (Figure 3-8), which runs the actual software.

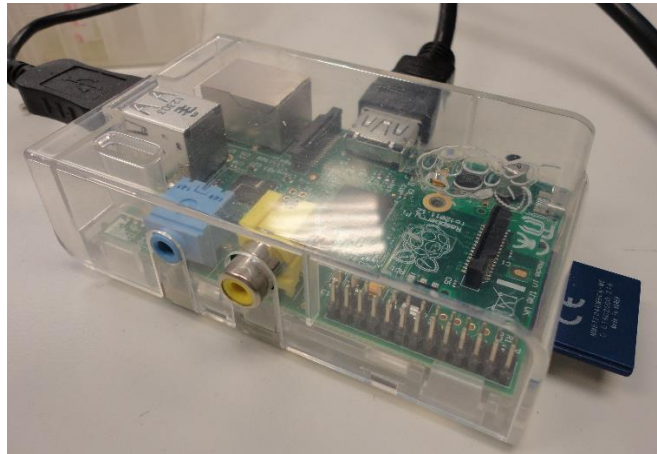


Figure 3-8: Raspberry Pi micro-computer controller

The control software is designed with user-friendliness in mind; hence the graphical user interface (GUI) is built to display a range of input options and status indicators e.g. on/off control and temperature selection. Temperature data is plot against time within the on-screen graph, whilst automated data-logging is handled by the software.

With regards to solving the initial problem of constant maintenance of the bath temperature, an algorithm is designed within the software that serves to regulate the process liquid temperature via a feedback loop. The current process fluid temperature is recorded and compared versus a set-point at which the controller regulates around (e.g. 20 °C). The new desired bath temperature is calculated based on the magnitude of the difference between the current bath temperature and the difference from the set-point, thus providing a progressively ‘damped’ temperature profile.

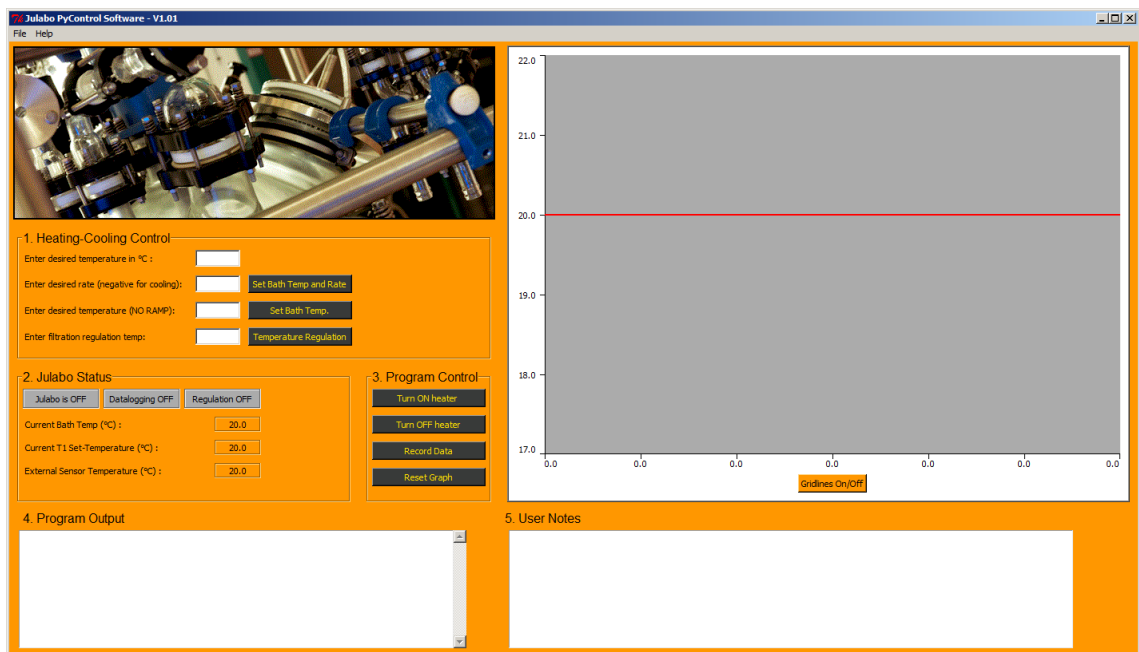


Figure 3-9: GUI of Python software interface for control of Julabo heater-chiller

3.3 Operation of the Continuous Percolation Rig

3.3.1 Final equipment layout

The final assembled version of the CPR is illustrated with the following Figures; a photograph of the actual assembled equipment (Figure 3-10), a process flow chart (Figure 3-11) and a part-to-scale technical drawing (Figure 3-12).

Table 3-4: List of components of the CPR

1 – <i>Hydra-Cell</i> P200 diaphragm pump
2 – Heat exchanger
3 – Filter tube isolation valve
4 – Nitrogen supply isolation valve
5 – <i>Parker-Veriflo</i> back pressure regulator
6 – 0-10 bar pressure gauge
7 – Filter tube
8 – Filter outlet isolation valve
9 – <i>ProChem</i> safety relief valve
10 – Reservoir vessel (1 Litre)
11 – <i>ABB</i> Inverter drive
12 – <i>Julabo</i> heater-chiller oil bath

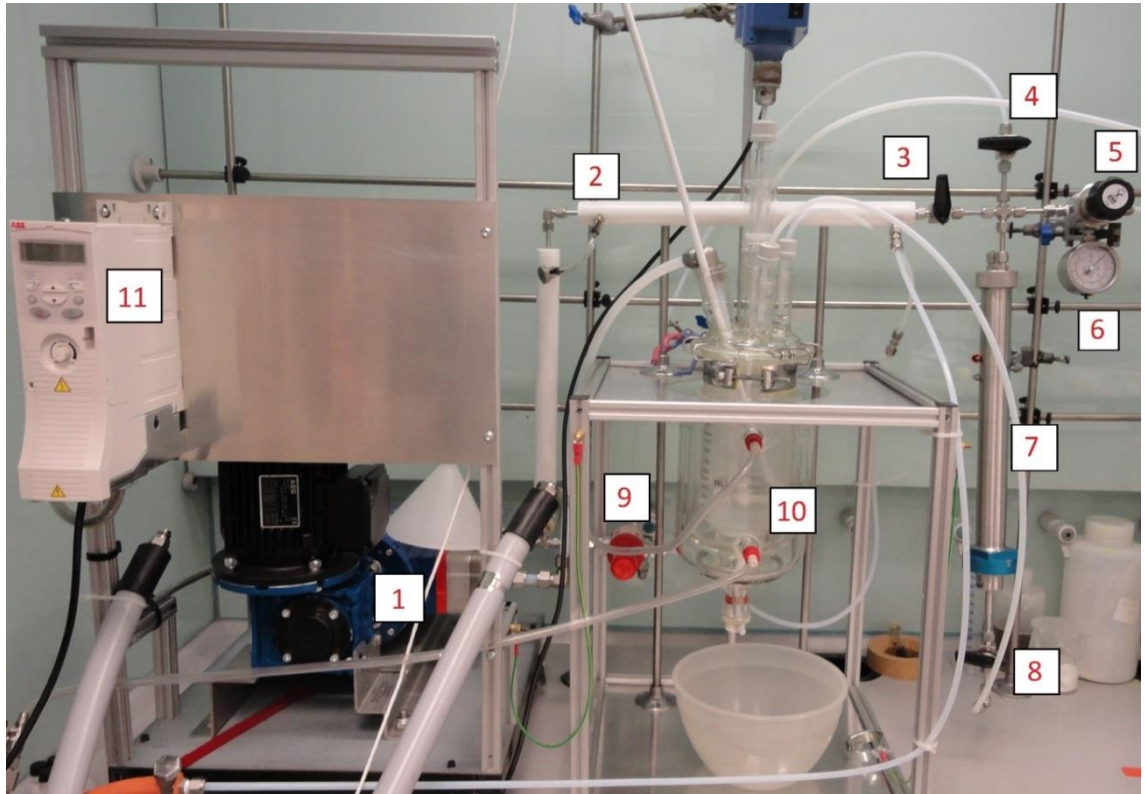


Figure 3-10: Photograph of the final constructed rig (Julabo heater-chiller bath not pictured)

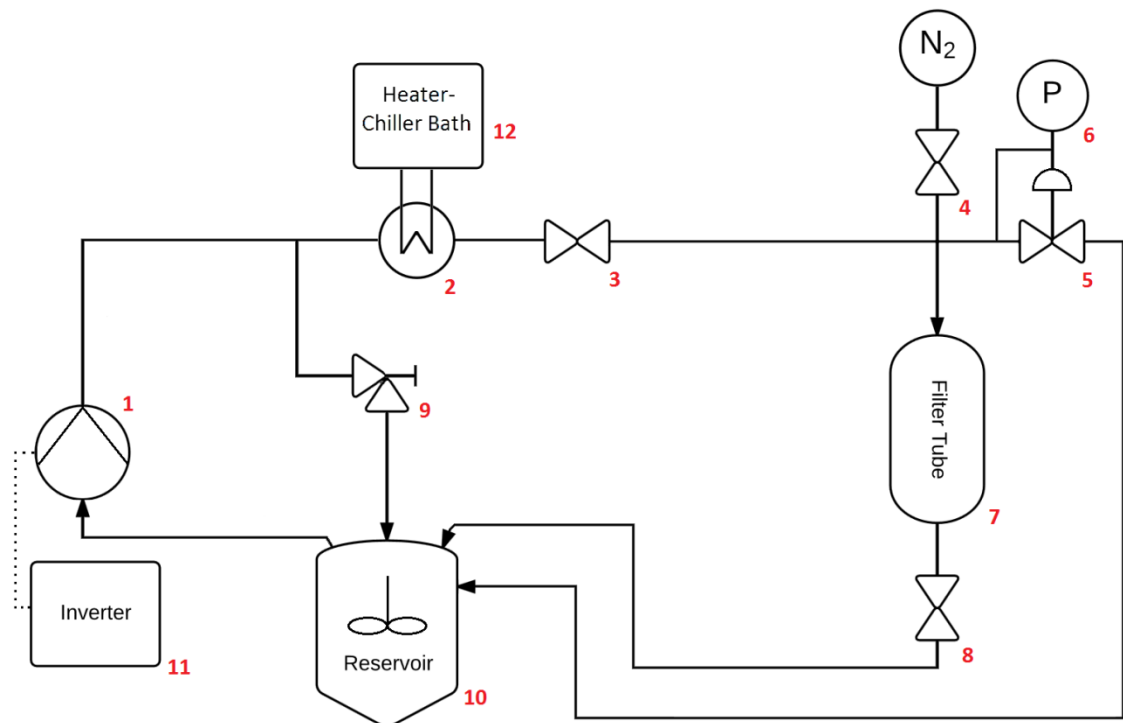


Figure 3-11: Process flow diagram of the final design

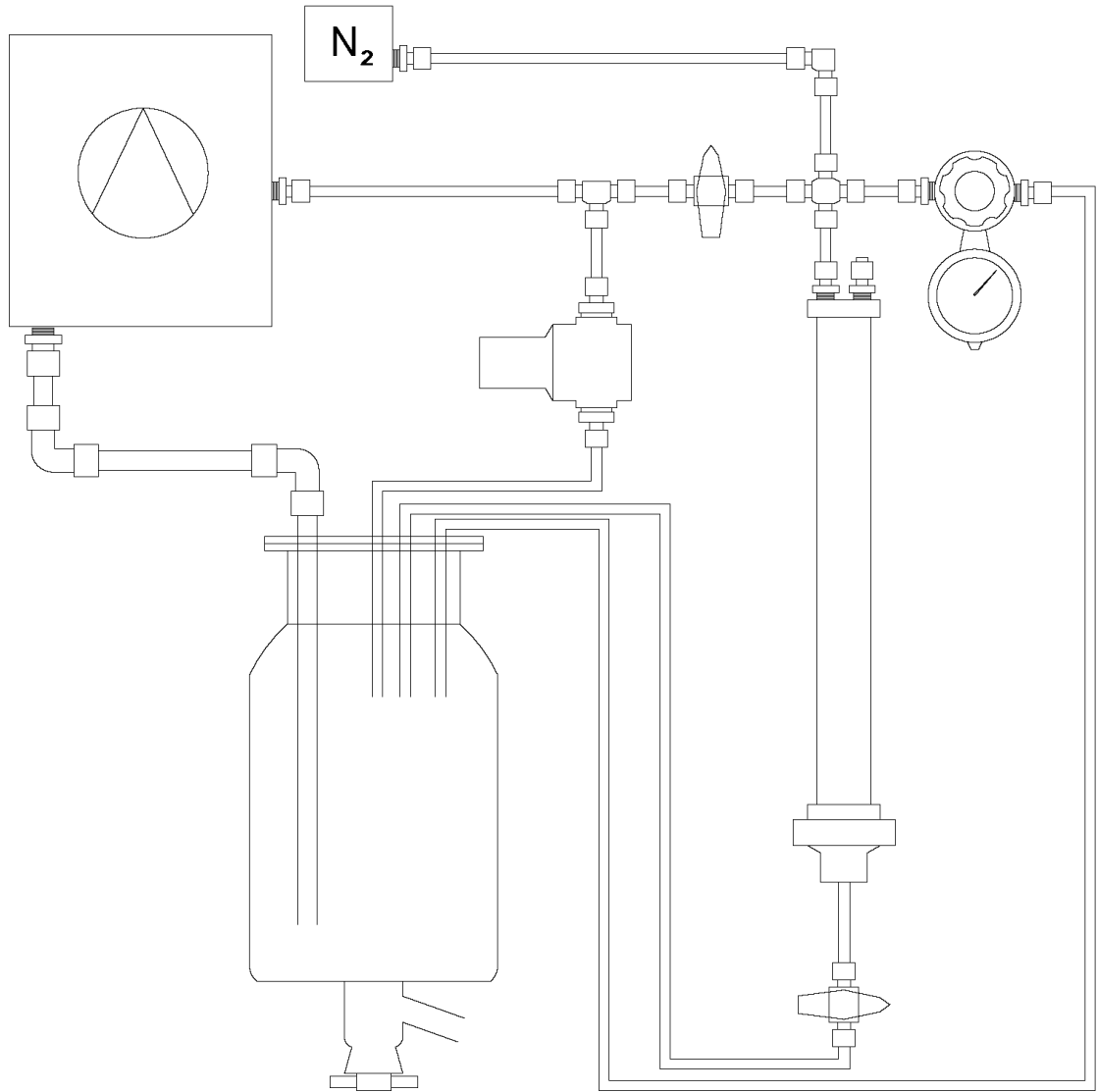


Figure 3-12: Technical drawing of the final design (equipment excluding pump is to scale; pipe-lines are not)

3.3.2 Experimental method

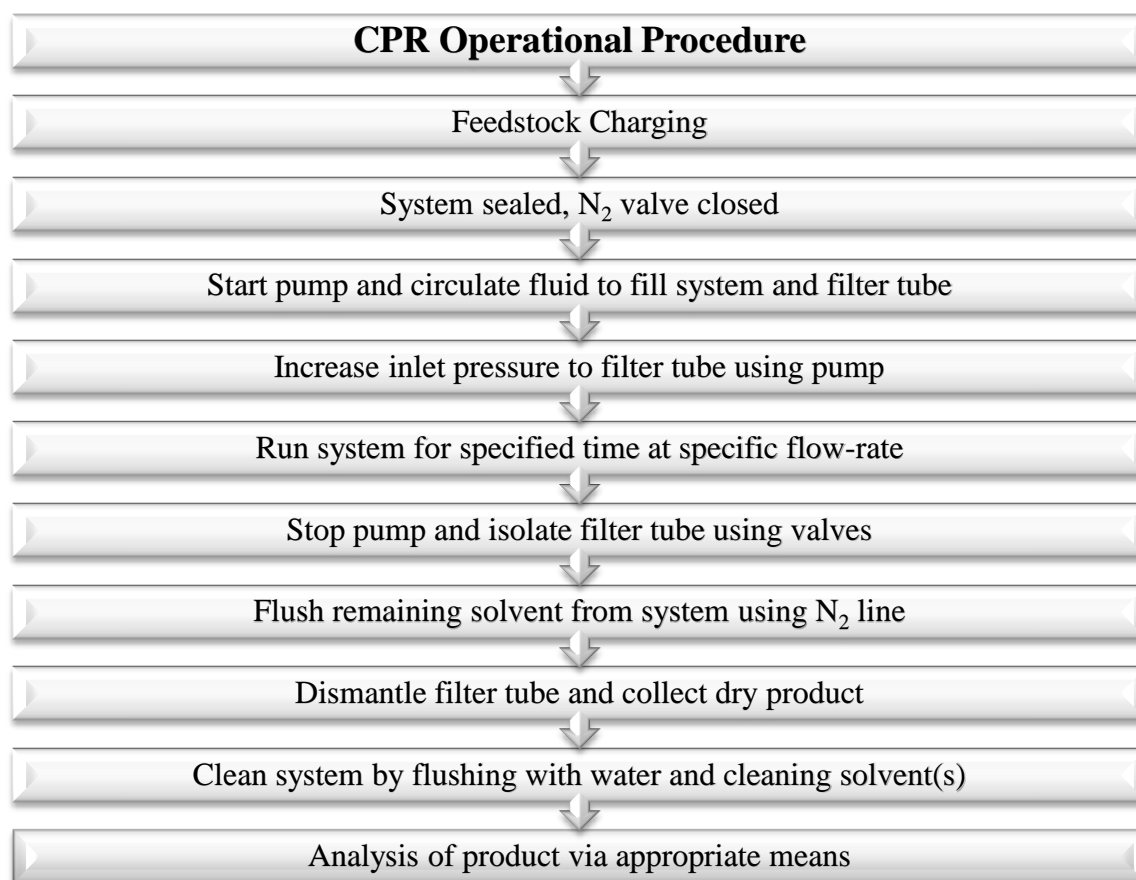


Figure 3-13: Block diagram of the CPR operation procedure

3.3.2.1 Pre-experimental

The system is checked to ensure it is clean and free from contaminants from previous experimentation. The filter insert is placed inside the filter tube and crystal slurry is poured in, taking care to keep the tube horizontal (so slurry does not fall out). Once the crystals are contained within the tube, the filter tube is fixed in place with the top and bottom caps screwed on to create a tight seal. Remaining mother liquor is charged to the solvent reservoir, where the pump will begin uptake of the fluid once switched on.

A small sample of crystal slurry is held back and instead filtered using a light vacuum pressure (<200 mbar) with a Buchner filter. This sample, when dried, is used as a control for the post-crystallisation size distribution.

The safety relief (9) and back-pressure (5) valves are set to the correct safety release pressures (safety relief valve is set to a maximum of 10 bar), and the reservoir is checked to ensure an adequate supply of liquid is present. All connections are sealed tight to prevent leaks. Valves 3 and 8 are opened and valve 4 is closed.

3.3.2.2 Operation

The P200 pump is initiated first by turning the dial (motor speed control) on the inverter drive (11) fully anti-clockwise (such that pump starts-up at the minimum speed). The pump is then started under minimal flow conditions. After checking for unsteady/erratic flows and ensuring the liquid flowing from the filter tube is air-free, pump speed can be increased, whilst ensuring a consistent supply of liquid remains in the liquid reservoir.

Recirculation through the system is dependent on the motor speed, which is controlled by adjusting the frequency of the inverter in Hz. In order to increase pump flow to a desired value for any particular experiment, the motor rotation frequency must be carefully and slowly adjusted; checking that pressure and temperature of the solution are not rising too fast. Pressure is monitored via the pressure gauge reading, whilst liquid temperature can be monitored from the Python software interface.

When the specified system pressure and flow-rate is found the system will be in continuous operation. The rig is not left unattended in case of emergencies. The safety relief valve is calibrated to relieve over-pressure, but should not permit liquid flow during normal operation. Percolation of crystals is then timed from the point at which optimal conditions are reached until the desired experiment is completed, when the pump motor is switched off.

3.3.2.3 Shutdown

At the completion of an experiment, the inverter is turned down to minimal flow conditions and the pump motor switched off. Liquid still remains in the filter tube, hence the nitrogen supply line valve (4) is opened and the filter tube isolation valve (3) is closed, before N₂ is allowed to flow into the tube. Remaining mother liquor is then flushed from the tube, whilst taking care to avoid N₂ pressure from rising above 0.5 bar (such that breakage could only realistically be attributed to liquid pressure). The solid cake is then dried for 1-2 hours.

Once the cake is dry, the filter tube is unscrewed and the filter insert removed. The particles are removed from the insert and left in glass dishes to dry further. The CPR is cleaned with a water-acetone mixture by recirculating it around the system. After leaving to dry overnight, crystals are collected and labelled for subsequent analysis, according to the following parameters (where applicable):

Table 3-5: List of labels for samples selected for particle size analysis

Sample Label	Description
LF	Sample has been 'lightly' or vacuum filtered in lab-scale Buchner filter
PF	Sample randomly selected from bulk of dried cake material
PFB	Sample isolated from bottom of cake
PFT	Sample isolated from top of cake

It should be noted that not all experiments are sampled for size analysis through the depth of the cake, but all experiments have a light, vacuum filtered sample and percolation sample from the bulk of the cake. Each experiment has its own individual crystallisation batch sampled with a vacuum filtered sample in order to account for random variations in the size distribution of crystallised material.

The notation system in Table 3-5 also applied to the samples isolated from the 2 Litre batch filter (described in section 3.5).

3.4 500 mL Crystallisation Procedure

The 500 mL calorimeter apparatus (Figure 3-14) supplied by HEL is selected for the preparation of crystal material due to its favourable temperature control. The system is fully controlled with software designed by HEL, and provides the option to create SOPs for multi-step operations at differing conditions. This enables for example, a step to heat up the solution, a step to hold for seeding, a step for cooling etc.



Figure 3-14: The HEL 500 mL calorimeter apparatus

The equipment contains a motorised pitched-blade glass agitator, jacketed cooling provided by a Julabo FP50/HD (with Pt100 temperature probe) and an air cooled condenser. For all experiments, agitation is imparted at 300 rpm.

3.4.1 Glutamic acid

Glutamic acid (β -form) with 99% purity is obtained from Sigma-Aldrich, and is used without further purification.

3.4.1.1 Beta (β) glutamic acid polymorph

40 mg/mL glutamic acid powder and 500 mL deionised water is added to the 500 mL vessel (20 g) and heated to 70 °C for 60 minutes to dissolve the solid, under 300 rpm agitation throughout. The solution is then cooled over 30 minutes to 60 °C to supersaturate the solution, and seed material (3wt% - 0.6 g) is added. Seed material is formed from crushed β -glutamic acid material from previous experimentation. The solution is held for 2.5 hours at 60 °C to allow the seed to grow, before cooling to 20 °C overnight at 0.06 °C/min. The contents are held at 20 °C until required for filtration, percolation or other experimentation.

3.4.1.2 Alpha (α) glutamic acid polymorph

40 mg/mL glutamic acid powder and 500 mL deionised water is added to the 500 mL vessel (20 g) and heated to 70 °C for 60 minutes to dissolve the solid. The solution is then cooled at 1 °C/min to 20°C and held for approx. 30 mins, with 300 rpm agitation throughout the experiment.

3.4.2 Lesinurad

50 mg/mL Lesinurad powder (supplied by AstraZeneca) is added to 300 mL Acetonitrile within the 500 mL vessel (15 g), and heated to 60 °C with 300 rpm agitation for 60 minutes to ensure dissolution. The saturated solution is cooled to 52 °C for 3wt% seed to be added. Cooling is initiated at 0.06 °C/min until the solution reaches 20 °C.

3.4.3 Urea and Urea-Biuret

200 mg/mL urea (99%; Merck) is charged to the HEL calorimeter vessel with 500 mL methanol (99.9%; Sigma-Aldrich). The solution is agitated at 300 rpm throughout. The contents are heated to 45 °C to dissolve the solid and cooled at 1 °C/min to 20 °C to initiate unseeded nucleation.

To generate urea-biuret impurity crystals, 200 mg/mL urea and a certain wt% of biuret (97%; Alfa-Aesar) – typically 6wt% – is added to 500 mL methanol. The solution contents are heated to 50 °C to dissolve and then cooling is initiated at 1 °C/min until the temperature reaches 20 °C.

3.5 2 L Batch Pressure Filter Methodology

A 2 L glass vessel (Figure 3-15; left) is utilised to perform the large scale operations. The vessel is fitted with a double pitched-blade steel agitator, jacketed cooling provided by a Julabo FP32/HL (with Pt100 temperature probe) and water-cooled condenser.



Figure 3-15: (Left) 2 Litre glass crystallisation vessel; (Right) 2 Litre pressure filter/dryer

The batch pressure filter/dryer at AstraZeneca's Macclesfield site is Hastelloy C22 constructed and has a capacity of 2 L total volume, with an 8 cm diameter filter plate. The filter and internals have been specially constructed as to be a scaled-down representation of a pilot plant reactor, also situated at the Macclesfield site. Solution is input to the reactor via a vacuum hose.

Drying of the cake is provided by nitrogen. The unit houses a motorised pitched-blade impeller capable of being raised/lowered in or out of the filter cake, to assist in drying the particles. A thermal jacket around the main body of the filter chamber can also be used to warm the particles when drying. Additional features include a pressure gauge, sight-glass and a balance to measure the rate of filtration.

3.5.1 Crystallisation preparations for 2 Litre scale

Preparations for crystallisations on 2 Litre scale were performed in a similar method to those at 500 mL scale, i.e. identical solid concentrations. 40 mg/mL glutamic acid (80 g) is charged to the reactor with 2 Litres of deionised water in order to generate α or β form crystals.

To generate the α -form, an unseeded fast-cooling procedure (approx. 1 °C/min) is followed, after which the solution is held at 20 °C for 40 minutes prior to filtration. For β -form crystals, the solution is cooled to 60 °C for addition of seed material (ground glutamic acid needles; 3wt% - 2.4 g), and held for 2.5 hours before cooling over 12 hours to 20 °C.

For crystallisation of Lesinurad, 40 mg/mL powder (80 g) is charged to the reactor with a 50:50 mixture by volume (2 L total) of deionised water and Acetonitrile (99%; Fisher Scientific). The mixture is heated to 62 °C to fully dissolve the solid, and cooled to 45 °C to supersaturate the solution. 3wt% seed (2.4 g) is added to the solution and the contents are held for 2.5 hours before cooling to 20 °C over 12 hours.

3.5.2 Batch filtration at 2 Litre scale

3.5.2.1 Performing pressure filtration

The equipment is checked by initiating a pressure test – the unit is sealed and nitrogen pumped into the chamber to the desired filtration pressure. The nitrogen supply valve is closed to seal the system and checks are made to ensure there is no significant loss of pressure (which would indicate an imperfect seal). The filter chamber is opened to the atmosphere again for solution charging.

The contents of the 2 L crystallisation vessel are poured into a large Duran bottle for transport over to the filter (at this point, a sample of the solution would be taken as a 'lightly' filtered sample). It is desirable to keep the mixture well suspended, to avoid any settling of the crystals. The filter chamber vacuum is switched on and the hose inlet valve is opened. The solution is then sucked into the filter chamber by placing the inlet hose into the Duran bottle; material is taken from the bottom whilst agitating the mixture to retain as much suspension of the solids as possible.

The filtration is then initiated by re-pressurising the system to the desired pressure, and fully opening the bottom run-off valve to allow the passage of filtrate through. Data of filtrate mass over time is logged using a Python script that communicates with the Mettler-Toledo PG-S3000 balance. The final mass and volume of collected filtrate are recorded.

Once the filtration has completed, nitrogen supply to the filter chamber is switched on to dry the cake. The pressure is set low at <0.2 bar, and left overnight to dry with the bottom run-off valve opened to atmosphere.

3.5.2.2 Retrieving the cake

To dismantle the system, firstly the nitrogen source is closed off, and the bottom run-off valve and connected piping are removed. The filter's securing mechanism is untightened so that the chamber can be pulled out to the side for access. At this point, the filter cake is exposed from the open-topped chamber (Figure 3-16; left); hence a sample from the top of the cake can be carefully extracted using a spatula (the 'PFT' sample). The cake height is also noted.



Figure 3-16: (Left) Sampling the cake from inside the pressure filter; (Right) The filter medium with cake material resting on top – used as a source of material from the bottom of the cake

To extract the remaining powder, the exposed top of the chamber is temporarily sealed with a PTFE cap and the entire chamber removed from its housing. It is then inverted to expose the fixing bolts. These are removed with an Allen key to separate the chamber body from its base. The base is then lifted off leaving the filter medium behind. A sample from the bottom of the cake (the 'PFB' sample) is taken from the particles remaining on the filter medium base (Figure 3-16; right).

Finally a polyethylene bag is placed over the exposed base and secured to prevent operator exposure. The filter chamber is then reinverted as the powder is collected by the bag; a sample of the remaining powder is collected as the 'pressure filtered' (PF) sample.

3.6 Metastable Zone Width Determination with HEL AutoMATES

The HEL AutoMATES are small-scale (~30 mL) parallel reactors fitted with temperature and turbidity probes (and overhead stirrers). The turbidity probes, whilst not as accurate (or capable of elucidating particle size) as an on-line laser diffraction system, provide an in-sight into the crystallisation process within the vessel.

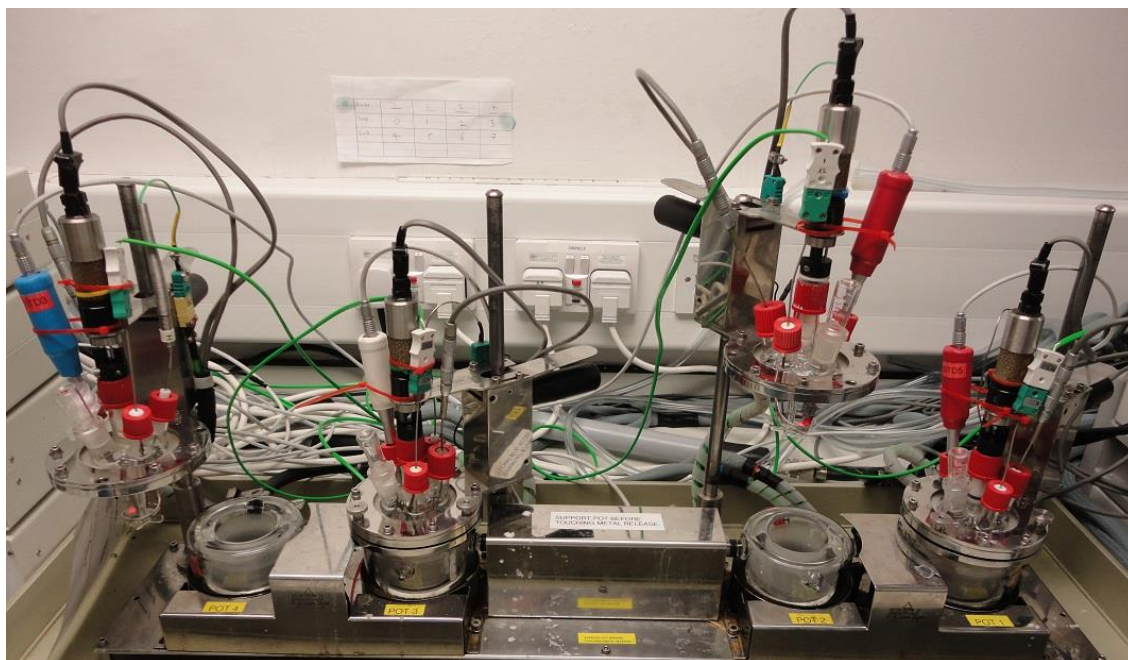


Figure 3-17: The HEL AutoMATE parallel reactor apparatus

Transparent solutions (i.e. like those of pure solvent, or solvent with fully dissolved solid) provide little resistance for the turbidity probe signal to be scattered or obstructed, hence a large portion of the emitted radiation is received back via the detector. Opaque solutions hinder and disrupt the emitted signal and therefore only a tiny fraction of the emitted radiation is received by the detector.

The result is a feed of data representative of a solution that has either crystallised (opaque) or not (clear), and the temperatures over which these boundaries lie; the basis of which enables crystallisations to be designed.

Experimental procedures are handled in an identical method to those of the 500 mL HEL vessel – i.e. identical solution concentrations are utilised. The actual method is also similar, as the software used to generate SOPs is almost identical (having been created by the same manufacturer).

The data acquisition is handled via National Instruments hardware and channelled into a LabVIEW script, which outputs data into a comma-separated file format.

3.7 Particle Sizing with the Morphologi G3 Optical Microscope

The Morphologi G3 (Malvern Instruments Ltd; Malvern, UK) is an optical microscope capable of dispersing and capturing images of particles. Dry powder is aerated with nitrogen to disperse the particles over a specified area, after which the G3 software scans across the powder, capturing images of the individual particles. Images and associated particle data are

saved within a database, such that subsequent analysis and extraction of data can be undertaken.

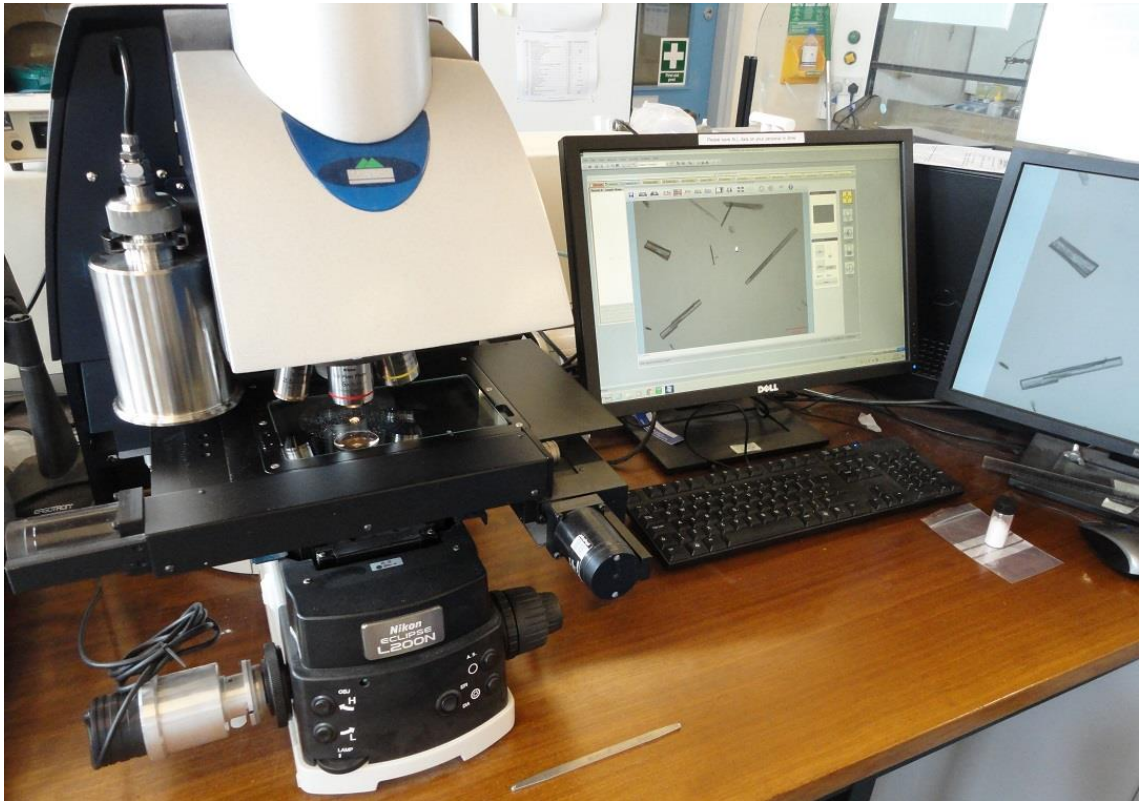


Figure 3-18: The Malvern Morphologi G3 optical microscope

Dry crystallised samples are collected from each batch and labelled. A small volume of sample powder is taken (13 mm^3) with the G3 measuring spatula (Figure 3-19; b), and the excess scraped off to ensure a constant volume of sample is acquired for each measurement. The sample volume is placed into the sample cell (Figure 3-19; c), which in turn is placed into the sample dispersion unit (Figure 3-19; a). The nitrogen supply is connected and the unit is sealed.

The sample stage glass is cleaned with acetone/water and wiped down to remove any traces of moisture and foreign particles/dust, which can influence the final result (dust and fibres are recorded as 'particles' by the G3).

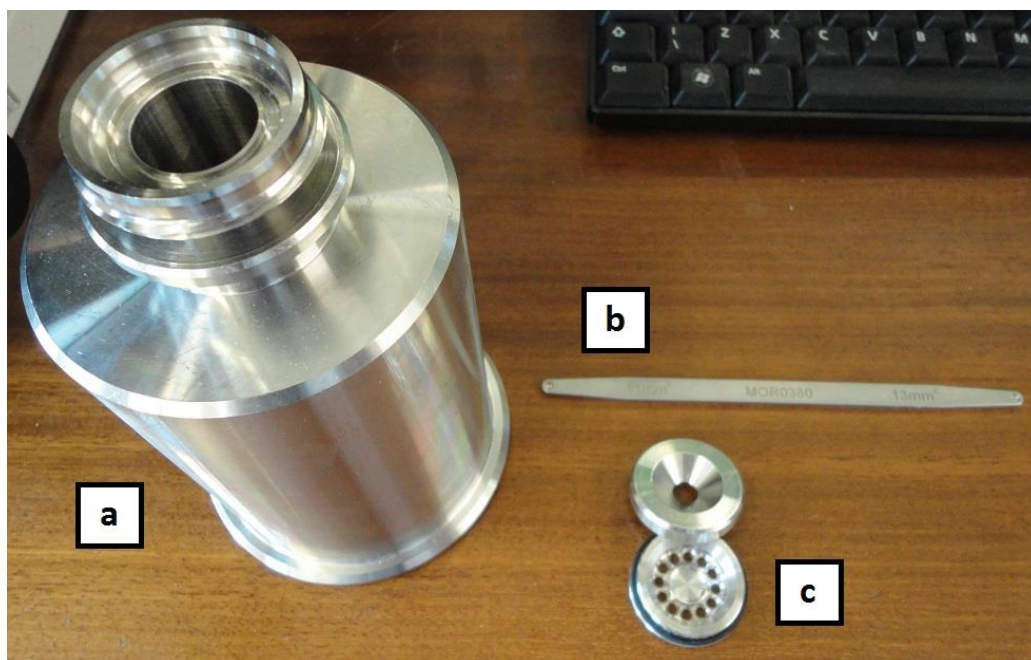


Figure 3-19: Morphologi G3 sample dispersion unit (a), measuring spatula (b) and sample cell (c)

The sample dispersion unit moves into place and forms a seal with the glass slide beneath it. The sample is dispersed with 0.5 bar ‘pulse’ of nitrogen to aerate the sample, and is allowed to settle over 1 minute into an approx. 5540 mm² circle. This helps to reduce the effects of agglomeration and stacking of particles, thereby increasing the accuracy of the result. An imaging SOP plan is devised based on the required scan area and magnification – this leads to an experiment time of between 30 mins to 1 hour.

Typically a 5x lens is utilised as this yields an appropriate balance between the resolution of the image and the magnification of particle features; this is sufficient to image particles of approx. 3-4 microns up to approximately 500 microns.

Numerical data are stored alongside photographic images of the associated particles for later reference. For analysis, the data is exported to raw text files, which are imported into a spreadsheet for further analysis.

3.8 Particle Sizing with the Sympatec HELOS Laser Diffractometer

The Sympatec HELOS (Sympatec GmbH; Clausthal-Zellerfeld, Germany) uses a dry-dispersion laser diffraction method to record particle sizes over a population of crystals. A vacuum pump draws a dry powder sample through a chamber in which it is irradiated. Light is scattered to specific angles dependent on the size of the 2-dimensional cross-section of the particles, and resolved by a Fourier lens. Radiation received by the detector is then able to resolve the particle size from analysis of the particles’ diffraction pattern.



Figure 3-20: The Sympatec HELOS laser diffraction particle sizer

Dried powder samples are weighed out in the sample vials using a high-accuracy balance. The vial cap is secured (tight enough to remain in place but loose enough so as not to disrupt the equipment mechanism that automatically removes the lids), and placed within the sample holder inside the head unit of the machine (Figure 3-21) – the ‘ASPIROS’ dispersion system.



Figure 3-21: A sample vial containing beta-glutamic acid loaded into the ASPIROS sample delivery system, ready for injection into the analysis module

The equipment is then adjusted for the appropriate sample delivery (see section 6.3.4.4); a dispersion pressure, sample feed rate (the speed at which the sample vial is moved towards the vacuum inlet line) and lens (dependent on expectant particle size) are selected. The

desired dispersion pressure is calibrated using a Venturi meter. Before each sample is tested, the detector is zeroed. After each measurement, the empty vial and cap are removed from the sample holder unit in order to prevent obstruction of the delivery mechanism, and the new sample vial loaded.

Data is viewable in graphical format within the software, and can be exported to text files for further analysis.

3.9 Optical Microscopy with Leitz Diaplan Optical Microscope

The Leitz Diaplan optical microscope (Leica Microsystems GmbH; Wetzlar, Germany) is a standard laboratory grade microscope with reflected and transmitted light functionality. A DeltaPix Indenio 55CIII camera provides an opportunity to capture static images from samples by interpreting the data via the DeltaPix computer software.

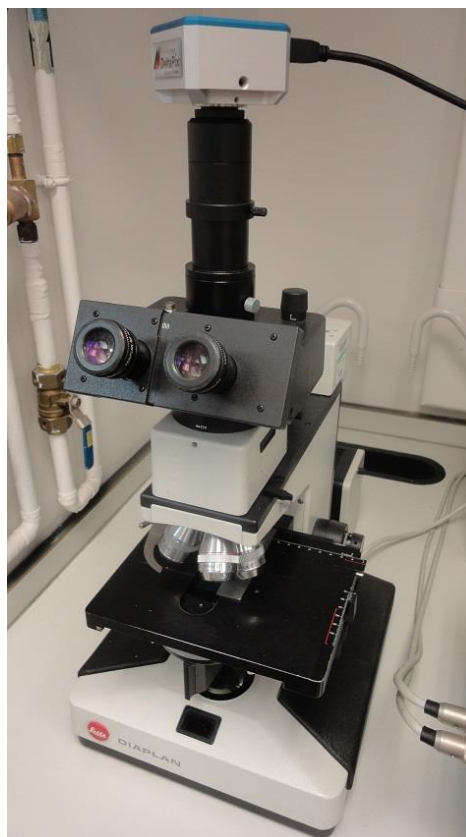


Figure 3-22: Leitz Diaplan optical microscope

Samples of powder are sparingly distributed over a standard 76 x 26 mm glass slide with the excess tapped off to ensure a flat, dispersed layer of powder remains on the slide. The slide is then secured in place by the sample holder lever and the microscope optics turned on. For most situations the 5x lens is utilised as this provides the greatest depth resolution, and most crystals studied are large enough to be imaged with this level of magnification.

The stage is moved into place using the x and y stage control knobs. The sample is brought into focus using the focus knob and/or the fine focus. Finally the light intensity is fine-tuned in order to yield the best image result.

Images are captured and saved in digital format using the DeltaPix software, after which they may be manipulated e.g. by adding dimensions from within the software. The optics are calibrated using a calibration slide with existing pre-defined measurements imprinted onto it.

3.10 Use of the LUMiSizer for Centrifugation of Packed Beds

3.10.1 Sample preparation

A batch of crystals is made up in the HEL calorimeter in the appropriate method (see section 3.4). Solution liquor is drained directly to a 250 mL beaker containing a set of glass baffles and a magnetic stirrer bar. The beaker containing mother liquor is placed onto a heater/stirrer plate and set to agitate at 800 rpm. The high agitation rate coupled with the use of a baffled vessel ensures a homogenous distribution of particles throughout the beaker; providing reproducibility to each volume of sample obtained via syringe.

1 mL of solution is drawn from the beaker using a 1 mL disposable syringe (without the needle) and injected into each LUMiSizer cell. The lack of needle allows for more crystals to be taken up by the syringe and hence produces a more representative result. A polypropylene cap is placed onto the cell to seal the contents. For beta-glutamic acid, an additional sample is retained, dried and tested for particle size distribution.

3.10.2 Instrument standard operating procedure

A standard operating procedure is planned via input of the number of samples and sample positions to be run, along with timing and centrifuge speed for each interval. The number and frequency of measurements to be taken is also assigned. Temperature control is also applied throughout the experiment (set constant at 20 °C for all experiments).

The radiation sensor for each cell position (1-12) is calibrated and normalised before each experiment to produce a zero reading. It is crucial to apply this step before cells are inserted into the centrifuge.

The central rotor cap is removed to allow for sample placement. Cells are shaken gently beforehand to unsettle the contents before being hooked into place within the centrifuge disk. Cells lay horizontally on their flat faces; perpendicular to the measuring signal and detector.

The rotor cap is refastened to secure the vials in place. The machine lid is closed to seal the system.

Cells placed in the centrifuge must be balanced by an equal and opposite mass when rotating. Hence when operating a number of samples less than the maximum (12), samples are paired and placed into opposite 'clock-face' positions (e.g. a sample at position 12 is balanced with a sample at position 6).

Each sample is run according to the SOP detailed in Figure 3-23.

Profiles	Interval	Speed	Light Factor
30	30	350	1.00
8	900	350	1.00
24	900	780	1.00
8	900	350	1.00
24	900	1100	1.00
8	900	350	1.00
24	900	1560	1.00
8	900	350	1.00
24	900	2200	1.00
8	900	350	1.00

SOP Duration:

1 day(s) 10 hour(s) 15 minute(s) and 0 second(s)

Figure 3-23: SOP for samples operated in the LUMiSizer – screenshot taken from software GUI

The total experimental time is 1 day, 10 hours and 15 minutes. This is calculated from the summation of all individual steps, which are bound by the number of profiles (measurements) to be taken, along with the interval in which they are separated e.g. for step 1 (top of table in Figure 3-23) 30 measurements are recorded in total; once every 30 seconds, for a total time of 15 minutes.

Upon completion of the experiment, the sample cells are removed from the LUMiSizer. Raw data is exported to a spreadsheet for analysis.

Chapter 4

4 Particle Engineering of Crystal Habits

4.1 Introduction

The generation of fresh crystal material is a fundamental requirement to the project's aim of a reproduction of industrial crystallisation. As part of this aim, methods for crystallisation of the desired product in a particular habit, size and size distribution will need to be developed i.e. elements of particle engineering are required.

The following chapter presents the reasoned crystallisation methodologies that have been developed to facilitate this, along with some of the analytical methods required to characterise the resultant crystals.

It is the aim that through development of appropriate methodologies, a range of crystal habits are to be generated for the case study molecules described previously. In order to ascertain the morphologies that are produced, optical microscopy will be heavily employed.

The combination of desired particle morphology and favourable material experimentation properties are to be used to identify case study stems to take forward for further experimentation (i.e. filtration).

4.2 Glutamic Acid

L-glutamic acid (LGA) ($C_5H_9NO_4$) is a non-essential amino acid mainly used as an additive in food products. The molecule consists of a 5-carbon chain bound by carboxylic acid groups, with an amine side-chain; hence some hydrogen bonding is possible[95].

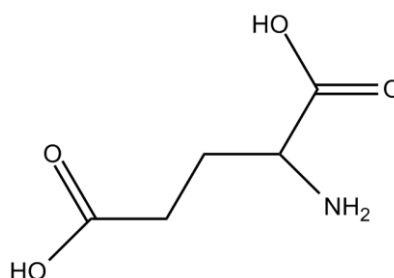


Figure 4-1: Chemical structure of L-glutamic acid[95]

LGA exhibits polymorphism in the form of 2 differing morphologies (Figure 4-2); the metastable alpha-form (prismatic), and the stable beta-form (needle-like)[96]. Both forms can be produced relatively easily by manipulation of the crystallisation process conditions (solution concentration; cooling rate; seeding)[97]. Prismatic crystals are typically desired for their improved filtration and drying characteristics, hence the metastable crystal is the predominant form favoured in industrial processing[95].

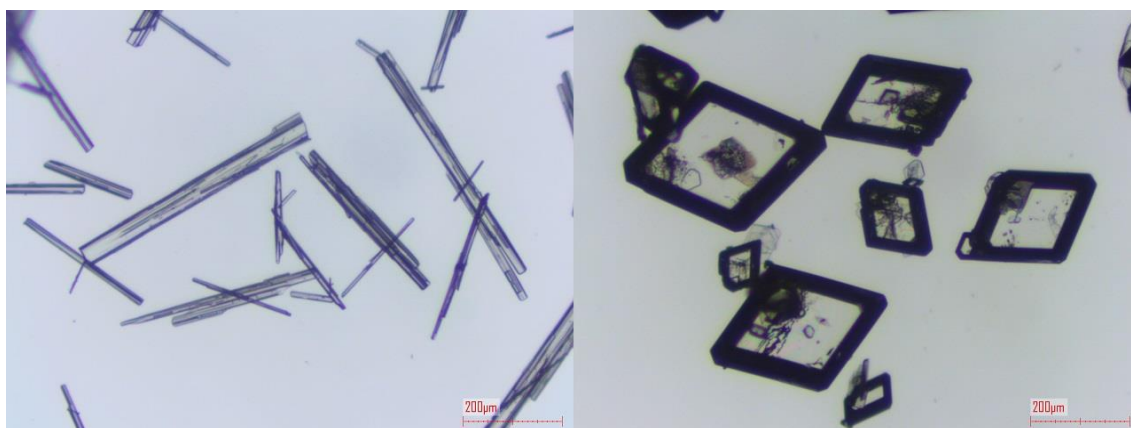


Figure 4-2: (Left) Needle-like beta(β)-glutamic acid; (Right) prismatic alpha(α)-glutamic acid

The α -form exhibits greater solubility than β -LGA over all temperature ranges, hence the β -form will be preferred inherently in any low-supersaturation crystallisation; although to be safe the contents of a crystallising mixture should be held at high temperatures to ensure solution mediated transformation to the β -polymorph[98]. High supersaturation or ‘crash-cool’ methods are known to yield the α -form.

Particle sizes of the needle-like beta form are typically in the region of 30 – 600 microns in length, whilst alpha-glutamic particles are typically 200-400 microns in size; a lower spread of sizes relative to the needles.

Glutamic acid therefore presents an acceptable case-study for the investigation of needle breakage under filtration/percolation, with the option to prepare prismatic form crystals that are anticipated to show a different breakage mechanism and/or different levels of size reduction.

4.2.1 Solubility data

All solubility data is modelled using an ideal solubility model[38], where the gradient of the straight line is the enthalpy of dissolution divided by the universal gas constant, R:

$$\ln x_{eq} = \frac{\Delta H_d}{R} \left(\frac{1}{T_{ref}} - \frac{1}{T} \right) \quad \text{Equation 4-1}$$

The solubility of LGA has been studied extensively in the literature, and is known to be fairly soluble in water due to the polar characteristics of the molecule. This leads to a lack of solubility in organic solvents but also interestingly in alcohols e.g. in ethanol 0.00035 g LGA/100 g EtOH at 25 °C[99]; these therefore make good wash and anti-solvents for crystallisation and purification from water.

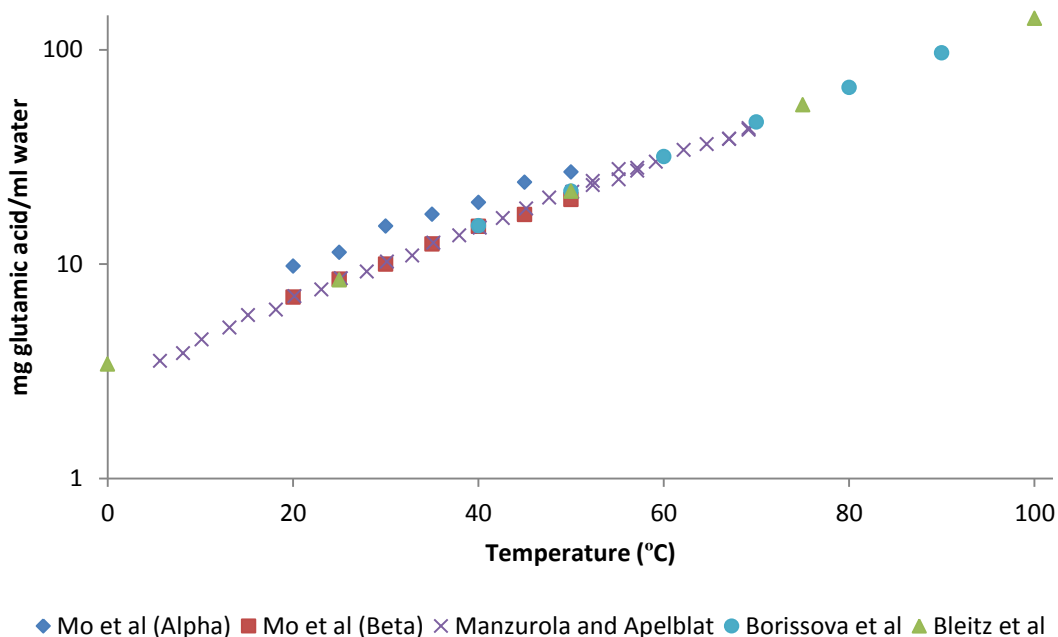


Figure 4-3: Solubility of LGA in water [97, 99-101]

Figure 4-3 displays the solubility for glutamic acid in water, obtained from literature data. By fitting a line to all the data the solubility for any particular desired temperature can be obtained (Figure 4-4).

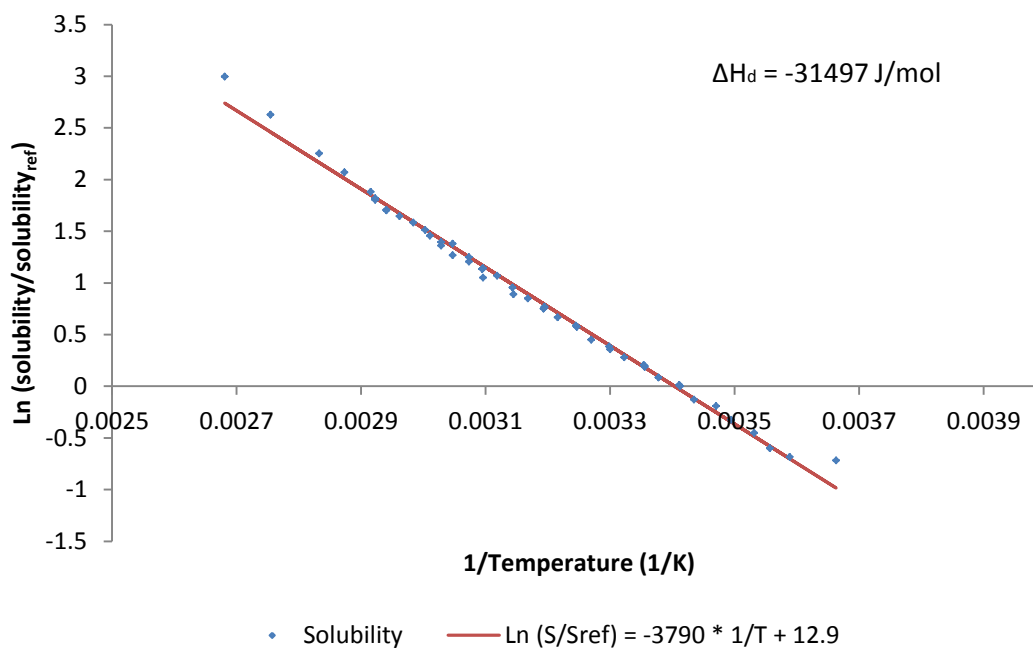


Figure 4-4: Literature data versus predicted solubility based on line-fitting

Crystallisations are thus designed on the basis of the preceding solubility data, whilst alpha and beta form glutamic acid can be produced by modification of the cooling rate of crystallisation. Metastable zone width is large with glutamic acid, making spontaneous nucleation improbable and thus simplifying the process of conducting seeded crystallisations.

This all results in a system that is exceptionally easy to manipulate and obtain desired crystal morphology from. Full methodologies are described in Chapter 3, but in general the alpha-form is obtained through fast cooling (high supersaturation) unseeded cooling, with the beta-form easily obtained from seeded slow cooled experimentation.

4.3 Urea and Urea-Biuret

Urea is a commodity chemical commonly industrially synthesised from ammonia and CO_2 ; the reaction also producing a small amount of the impurity biuret from a decomposition reaction. Urea has uses in the agrochemical sector as a component in fertilisers (because of its high nitrogen content) and as a precursor to many pharmaceutical and fine chemical products[37].

Urea crystallises as a white solid in the tetragonal system, space group $P\bar{4}_21m$, $a = 5.576$, $c = 4.684$, with 2 molecules in its unit cell[102]. Carbonyl diamide, as it is otherwise known, is a highly polar molecule, as is evident from the molecular structure (Figure 4-5). Hence it would be expected to show strong anisotropic growth of its crystal faces in polar solvents, due to the increased strength of solvent-solute interactions within solution[103].

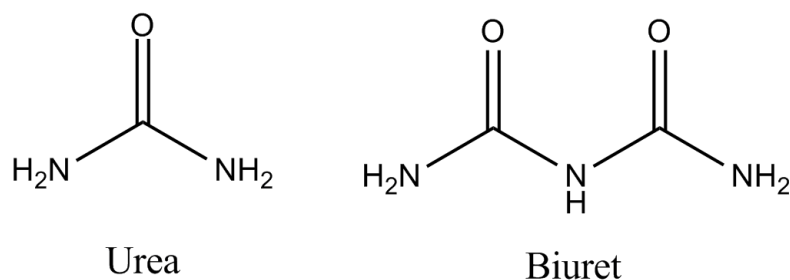


Figure 4-5: Chemical structures of Urea and Biuret

Urea's crystal morphology is also known to be strongly influenced by the extent of supersaturation in solution. High aspect ratios are expected from high supersaturation, whilst lowering the supersaturation (i.e. slower cooling) tends to reduce the aspect ratio[103]. A typical crystal grown from low supersaturation yields an elongated prism (Figure 4-6), whilst long needles with length:width ratios of 50:1 are obtainable from high supersaturation growth. This is due to the fast growth rates in the [001] direction relative to the [110] direction, in which the slower growing faces define the habit[42]. Hence the pure urea system presents a versatile morphology with relative ease of production.

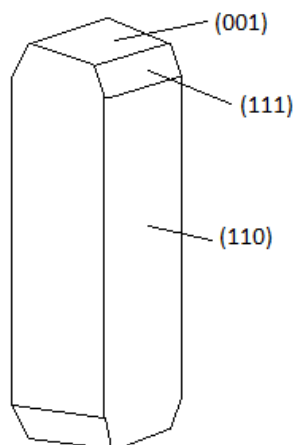


Figure 4-6: Urea's typical crystal morphology from polar solvents (crystal faces highlighted)

The impurity biuret presents an opportunity to generate additional habits, by crystallising urea with a small fraction of biuret (1-6 wt.%) in solution. This can result in reduced growth rates in the [001] direction, whilst the [110] directional growth remains largely unaffected. This has the practical effect of reducing the aspect ratio of the final crystal, yielding a 'stubby' prism[42].

Davey et al[42] experimented with a urea-biuret system and reasoned that 2 molecules of urea are replaced by a single molecule of biuret in the growing crystal. Urea crystallises regularly with alternate molecules facing to, and away from, the (110) face. Each molecule is able to hydrogen bond with its neighbours, allowing regular crystal growth.

In the presence of biuret, regular hydrogen bonding is disrupted by the replacement of 2 urea molecules by a single biuret molecule. Bonding in the [110] direction is unaffected, hence normal growth rates are observed for this surface. Incoming urea molecules from the [001] direction however, are slow to attach to this surface because of a lack of NH₂ groups to hydrogen bond with. Hence a reduced growth rate of the [001] direction is observed[42].

The authors noted that the growth rate of the (001) surface is strongly dependent on the biuret concentration, with sharp drop-offs in growth over small concentration ranges. Hence a 6wt.% biuret addition can almost completely inhibit growth in the [001] direction. Higher supersaturations require a larger concentration of biuret to inhibit growth, indicating that the reduction in growth is a time-dependent process; possibly a function of the rate of adsorption of biuret onto the urea surfaces[42].

Bisker-Leib and Doherty modelled the growth of urea from polar and non-polar solvents. They found urea grown from water and methanol to be a good match for that of the experimentally observed elongated needle. Simulations of urea grown from benzene produced a cubic morphology (i.e. isotropic dimensions), which shows additional morphological variation could be obtained by use of non-polar solvents[102].

Pure biuret is reported to form plates from ethanol[104], but is considerably more toxic than pure urea and solubility data is scarce. This presents an opportunity for crystallisation of breakable plates, but they will likely have different intrinsic bonding strengths to urea and are unlikely to be directly comparable.

One of the major problems associated with the handling of urea is that of solid bridge formation. This has been investigated extensively by Kirsch[105]. The high solubility of urea in water leads to the uptake of water molecules and subsequent formation of networks of interconnected particles with an associated tensile strength. The strength of the solid bridges is found to increase over time.

The problem specific to this work is that when investigation of particle size is necessary, the formation of aggregates is likely to mask any ability to distinguish individual crystals. As has been found with experimentation, even over short time scales required for filtration (up to an hour) the formation of a strong solid cake is evitable. This ultimately requires physical force to break the cake in order to obtain samples of powder for testing, and thus any breakage due to filtration is difficult to ascribe to the percolation.

4.3.1 Solubility data

The solubility of urea in water is extremely high; approximately 1 g/mL at 20°C[106]. Crystallisations with water would require excessive amounts of material, result in low recoveries and saturated solutions would be too rich in solute molecules; hence making small adjustments in solution temperature could result in uncontrolled nucleation/growth – a problem when filtering continuously to ascertain size changes. Alcoholic solvents are much more conducive to controlled crystallisations, even if the solubility of urea in them is still high.

Literature solubility is plot alongside measured solubility and labile curve data obtained from turbidity measurements in Figure 4-7 (in ethanol) and Figure 4-9 (methanol).

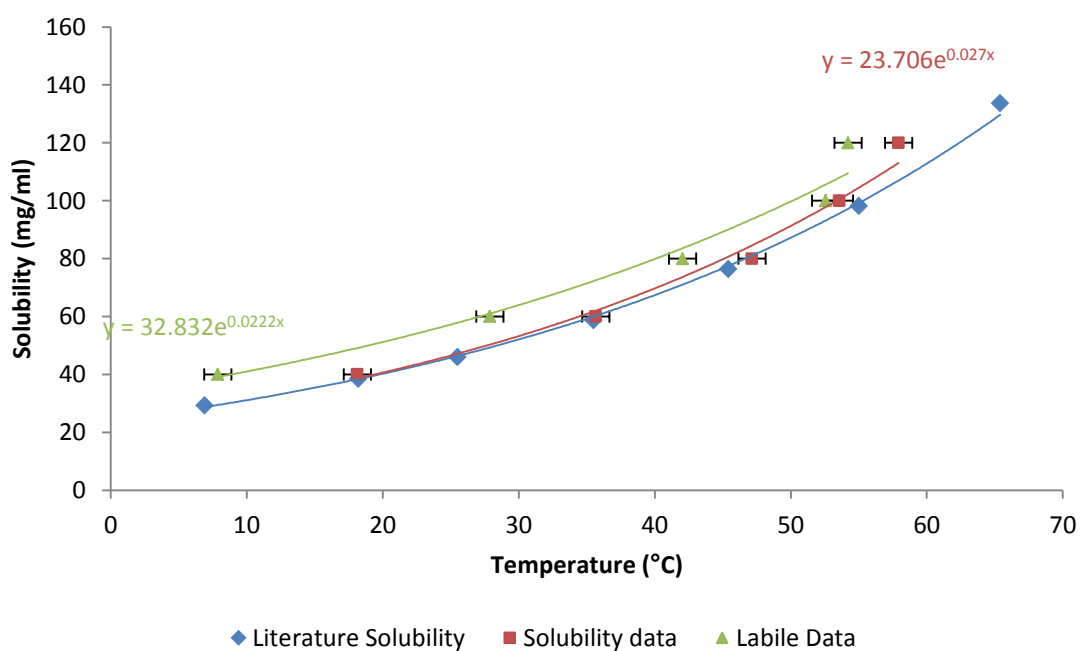


Figure 4-7: Solubility curve for urea in EtOH (literature solubility from Lee and Lahti[106])

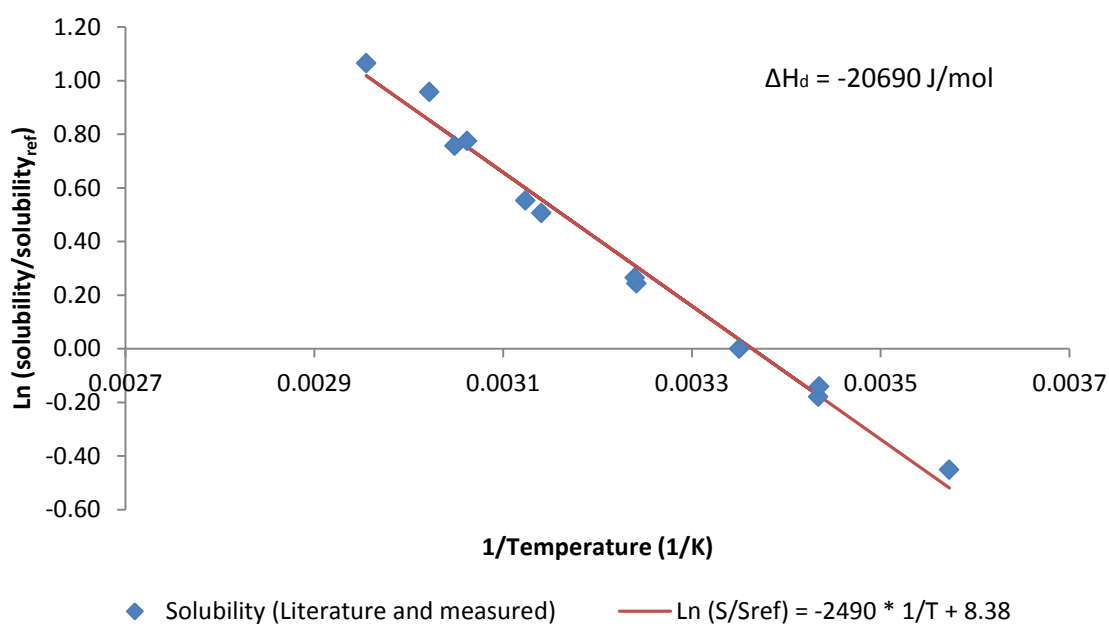


Figure 4-8: Van't Hoff plot of literature and measured solubility for urea in ethanol

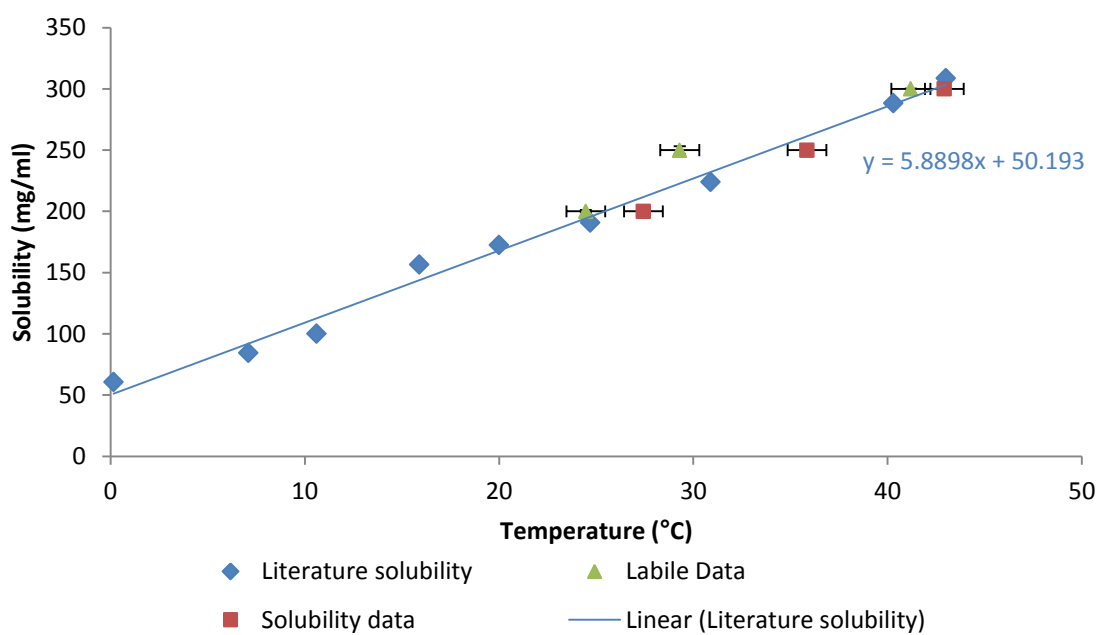


Figure 4-9: Solubility curve for urea in MeOH (literature solubility from Lee and Lahti[106])

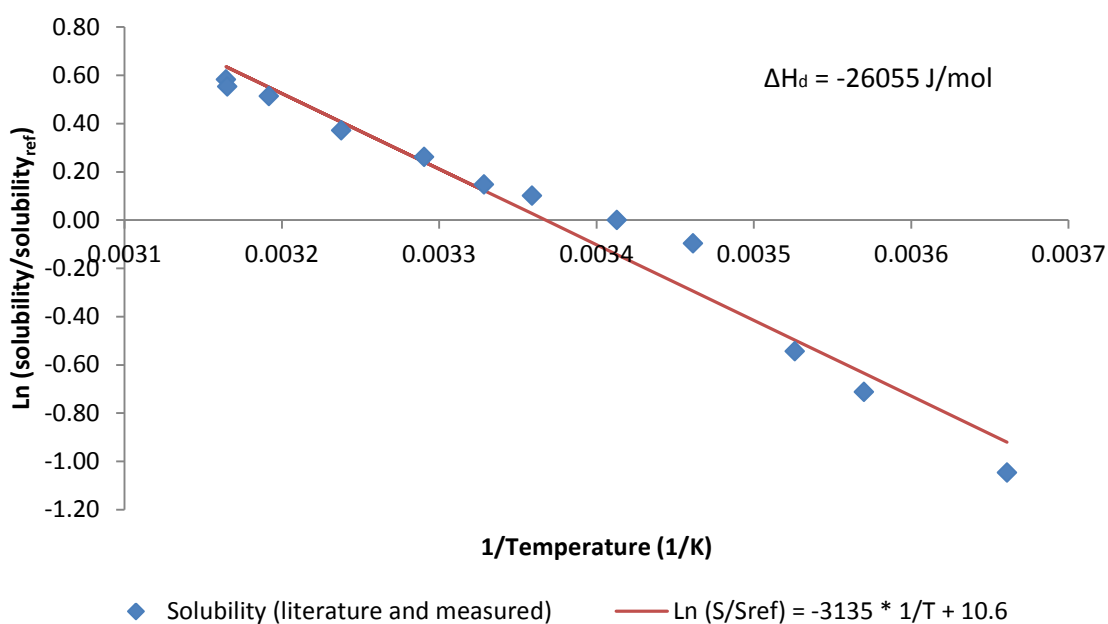


Figure 4-10: Van't Hoff plot of literature and measured solubility for urea in methanol

Solubility of urea in EtOH displays a typical exponential trend whilst unusually urea in MeOH appears to vary linearly with temperature. For both solvents however the metastable zone width is observed to be very narrow, particularly so with methanol. This has implications for controlled crystallisations using seeding, as the narrow MSZW makes spontaneous nucleation probable (which has further implications for producing repeatable crystal distributions).

In addition the inaccuracy of the turbidity measurements make definition of the MSZW difficult and erroneous. Solubility data shows decent agreement with literature solubility on the whole however, with the exception of high concentration loadings in EtOH, in which deviations in literature solubility tend to rise. Errors are encountered due to the higher enthalpies of dissolution associated with more solid dissolving, which can significantly affect the temperature of the small-scale reactor vessels. Due to the low width of the metastable zone, seeding (where utilised) is typically conducted via cooling 1-2°C into the MSZ. Seeding proves problematic with methanol even in these ranges, hence crystallisations are conducted unseeded.

4.3.2 Morphological variation through control of crystallisation

The rate at which at cooling crystallisation proceeds is commonly known to affect crystal size; in general, the faster the cool (higher supersaturation), the smaller the final crystals are; high supersaturation tends to favour spontaneous nucleation over growth, and thus solute molecules tend to precipitate out as nuclei rather than attaching on to growing surfaces. Slow

cooling (lower supersaturations) allows the solute molecules more time to attach on to growing surfaces, and as long as the driving force of supersaturation remains low, the chances of forming critical nuclei is lessened; hence larger crystals result.

Example images are displayed in Table 4-1. The urea system harbours a strong dependence of cooling rate and crystallisation solvent on the resultant particle shape. Urea is a highly polar molecule, and thus in more polar solvents, anisotropic growth is favoured. What is observed are more elongated, needle-like crystals when urea is grown from methanol.

The dependence on cooling rate highlights the stages of growth undergone. Crystals grow initially with high growth rates in the [001] directions. Longer crystallisation times allow for the growth of slower growing faces such as the [110] faces. This has the effect of 'thickening' the crystals when produced with low supersaturations.

The less polar ethanol tends to produce more prismatic habits, with a reduction observed in the high length:width ratios found in the MeOH crystals, as slightly more isotropic growth is favoured on the [110] faces. Unlike the crystals grown from MeOH, crystals produced in EtOH show a strong dependence of cooling rate on the particle size, with the largest sizes evident at slow crystallisation rates.

The addition of small quantities of the impurity biuret to the crystallising solution is also capable of inducing dramatic changes in the morphology of urea crystals; as shown by Table 4-2. For urea in EtOH, an inverse dependence of particle elongation with increasing biuret addition is evident, with many particles in the 6 and 8% addition samples with approximate aspect ratios close to 1. The 8% addition particles also exhibit a certain level of 3-dimensional rounding, as opposed to particles from addition levels <8% in which the dominant form is still cuboidal.

It is apparent that a critical concentration of biuret occurs approximately in the region of 6-8wt%; at this point the presence of long needles in the sample are non-existent. The biuret molecules have saturated the high-rate [001] growth face of the urea crystals and thus more isotropic crystal growth is favoured across other faces.

In MeOH urea also experiences a drastic reduction in growth rate in the [001] plane. The effect is seemingly more pronounced than that of EtOH. Compared to pure urea in MeOH in which long needles are the dominant form, and 1wt% addition of biuret in which needle-like and prismatic crystals are still present, the 3wt% addition represents a dramatic change in aspect ratio. Many isotropically shaped square particles are apparent at this level of biuret addition.

The distribution of morphologies does appear however to have a higher spread than those in EtOH. This is due to the effects of the unseeded crystallisation giving a greater precedence to uncontrolled nucleation and growth.

In methanol the urea-biuret system also approaches a critical point at 3wt% biuret addition; after which the presence of long needles in the sample is almost completely suppressed.

Table 4-1: Variations in morphology from crystallisation of pure urea in ethanol and methanol

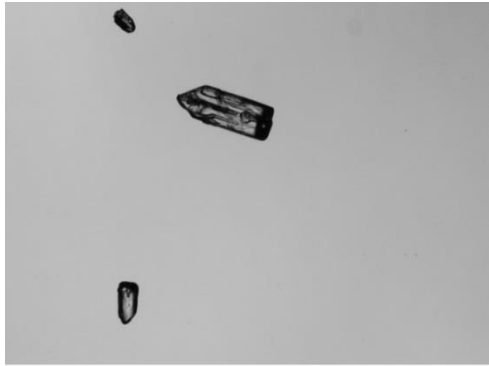
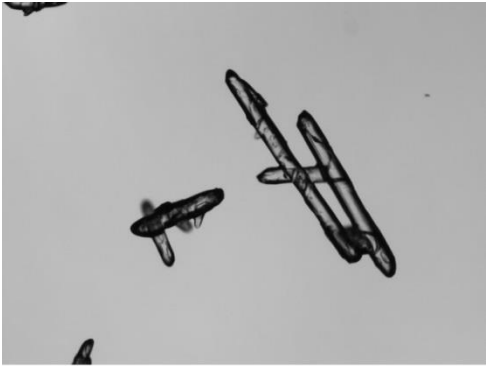
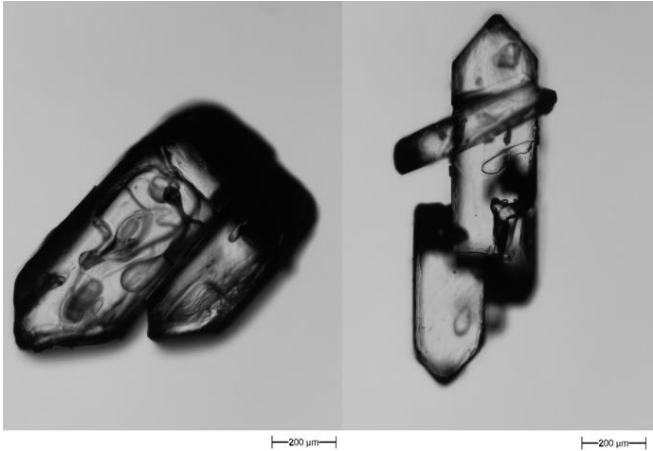
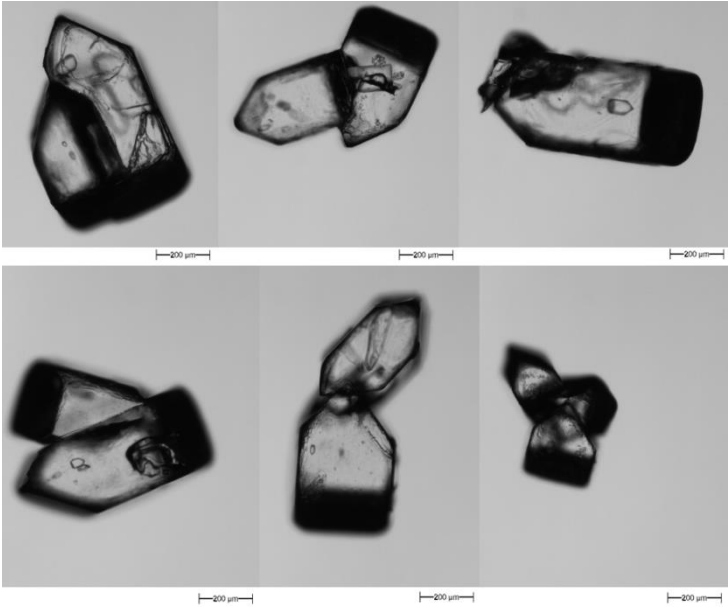
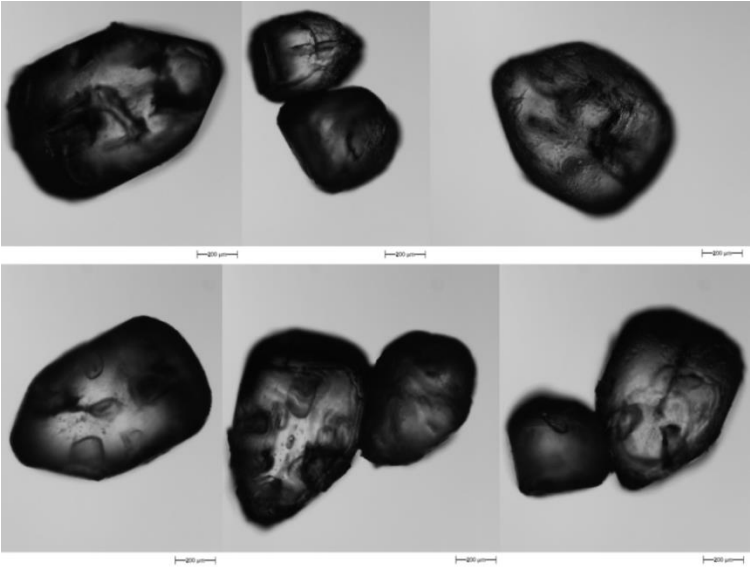
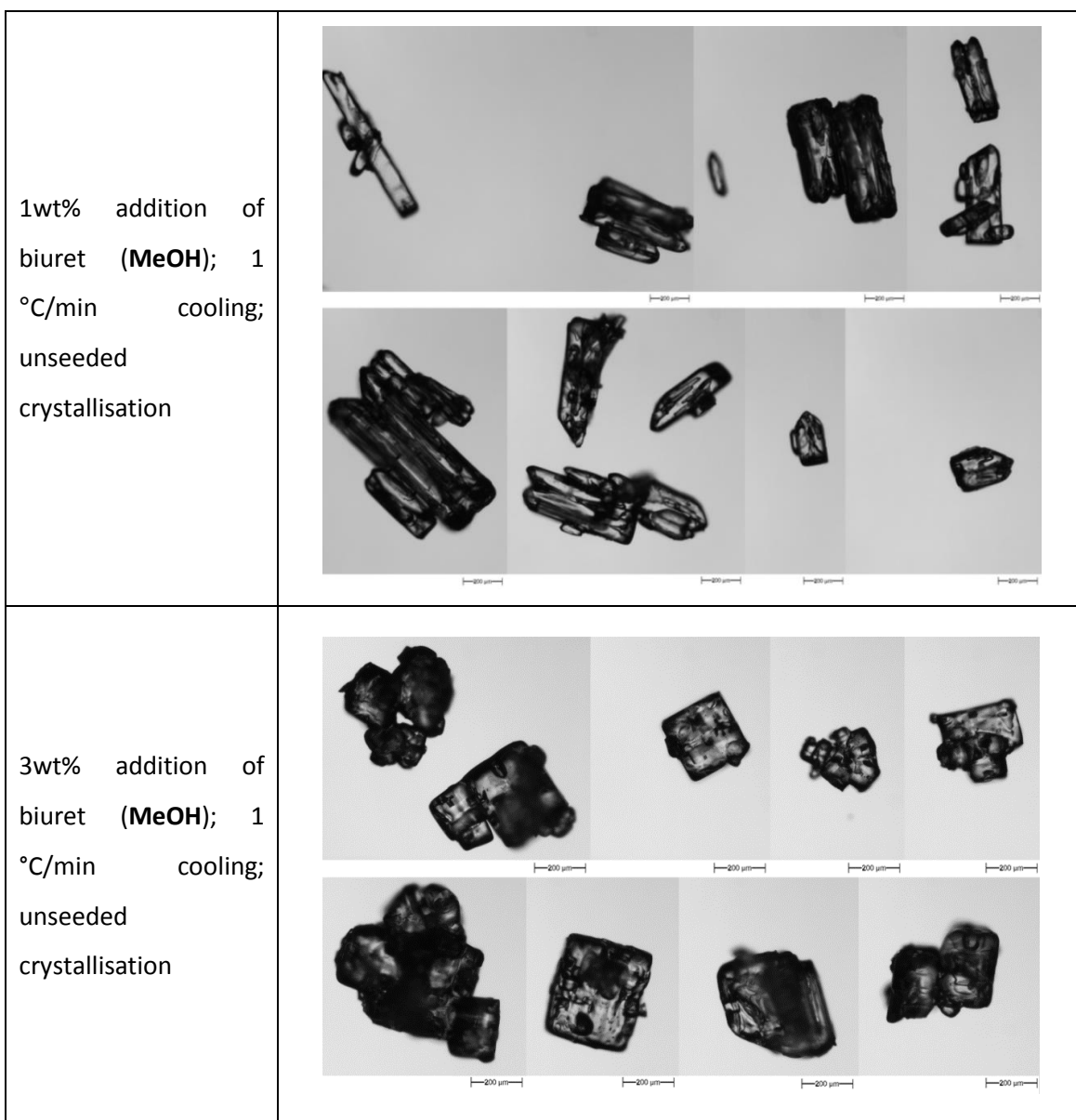
Solvent	Cooling rate of 1 °C/min, unseeded crystallisation	Cooling rate of 0.1 °C/min (EtOH; seeded); cooling rate of 0.5 °C/min (MeOH; unseeded)	Cooling rate of 0.06 °C/min, seeded crystallisation
Ethanol			
Methanol			

Table 4-2: Variations in morphology from crystallisation of urea/biuret in ethanol and methanol

<p>0wt% addition (pure urea) of biuret in ETHANOL; 0.06 °C/min cooling; seeded crystallisation</p>	
<p>2wt% addition of biuret (EtOH); 0.06 °C/min cooling; seeded crystallisation</p>	
<p>4wt% addition of biuret (EtOH); 0.06 °C/min cooling; seeded crystallisation</p>	

<p>6wt% addition of biuret (EtOH); 0.06 °C/min cooling; seeded crystallisation</p>	 <p>Micrographs showing seeded crystallisation with 6wt% addition of biuret in EtOH. The images display several large, dark, angular crystals with complex, multi-faceted shapes. Each image includes a 200 µm scale bar.</p>
<p>8wt% addition of biuret (EtOH); 0.06 °C/min cooling; seeded crystallisation</p>	 <p>Micrographs showing seeded crystallisation with 8wt% addition of biuret in EtOH. The images display several large, dark, rounded crystals with complex, multi-faceted shapes. Each image includes a 200 µm scale bar.</p>
<p>0wt% addition (pure urea) of biuret in METHANOL; 1 °C/min cooling; unseeded crystallisation</p>	 <p>Micrograph showing unseeded crystallisation with 0wt% addition of biuret in Methanol. The image displays a single, long, thin, needle-like crystal with a sharp point. A 200 µm scale bar is present at the bottom right.</p>



4.4 Lesinurad

Lesinurad, otherwise known by its trade name Zurampic[™], is an off-white crystal solid produced and marketed by AstraZeneca. Lesinurad has recently been granted approval for the treatment of gout[107], following successful phase III clinical trial results. The chemical structure of the compound is shown in Figure 4-11.

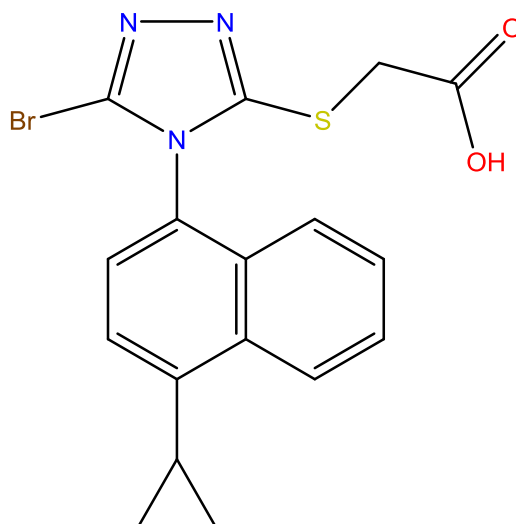


Figure 4-11: Chemical structure of Lesinurad (Mol. weight of 404.29)[108]

Lesinurad crystallises as small needles/plate-like crystals and thus already exhibits the desired morphology for filtration analysis (Figure 4-12). This compound has also been known to exhibit difficulties under filtration hence is the subject of much experimental work at AstraZeneca. Particle sizes are small; typically 20-60 microns length for the needles.

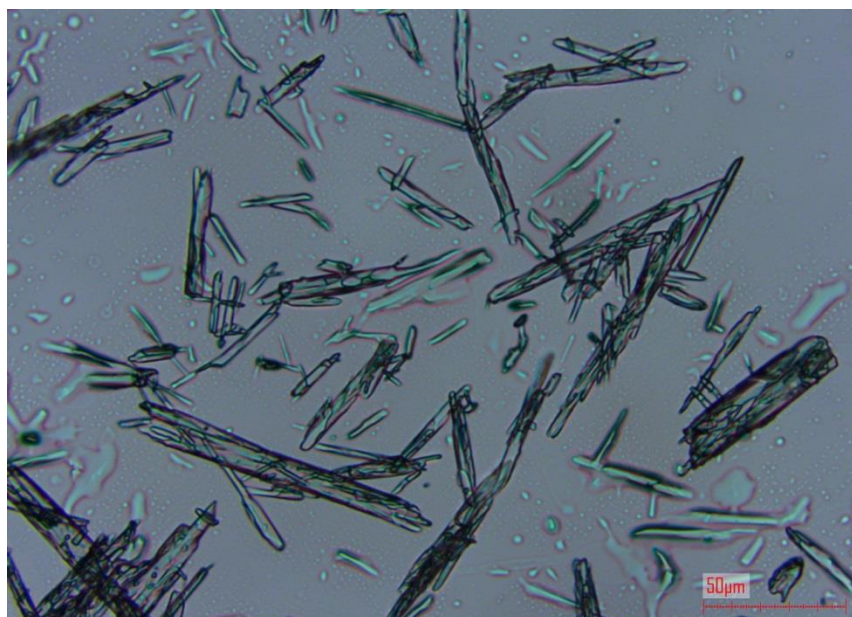


Figure 4-12: Lesinurad needle-like particles

As the compound is a developmental one, limited data is available; however a solubility curve for the compound is available in the solvent acetonitrile (Figure 4-13), which displays promising characteristics as a process solvent.

4.4.1 Solubility data

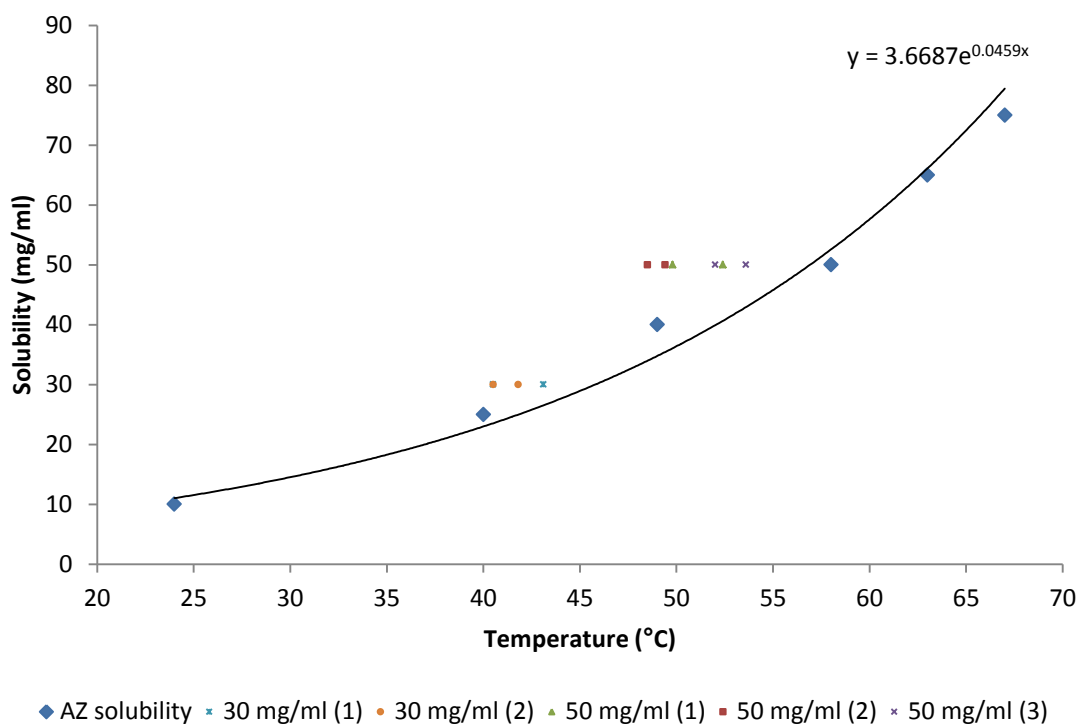


Figure 4-13: Solubility data for Lesinurad

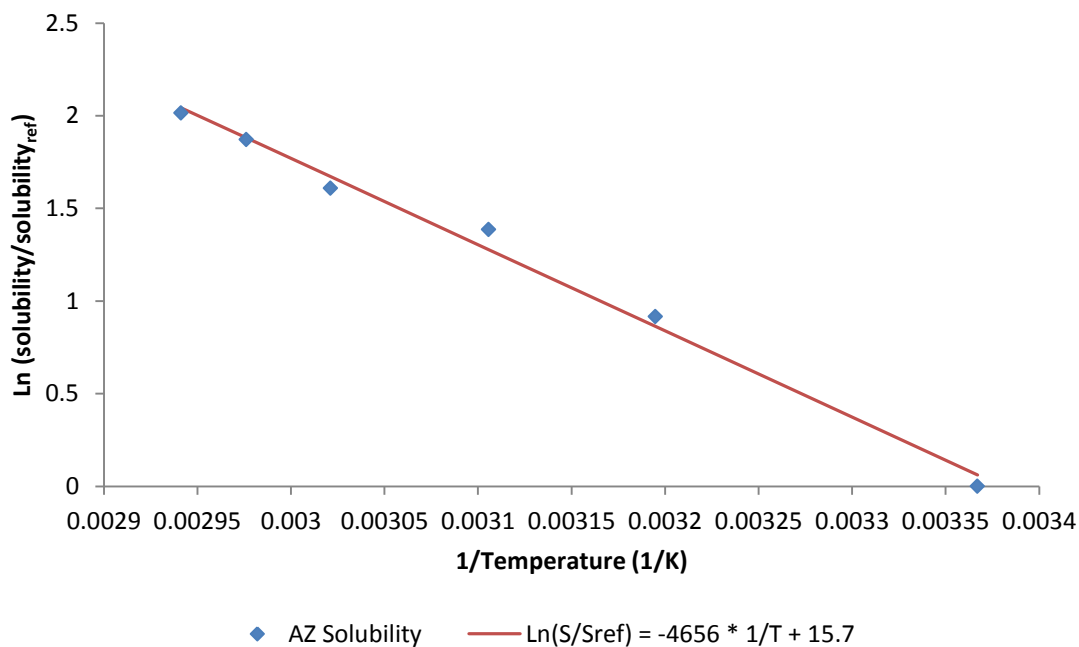


Figure 4-14: Van't Hoff plot of Lesinurad solubility in acetonitrile

The data is obtained from a Crystal16 study on 1 mL scale, which is anticipated to deviate from solubility data obtained on scale due to mass transfer effects. Additional data is obtained from the HEL AutoMATEs and is also visible in Figure 4-13. Concentrations of 30 and 50 mg/mL are

investigated to quantify any major differences between the small-scale data, and to obtain a metastable zone width.

The Lesinurad system is very slow to crystallise however and hence no acceptable data on the size of the metastable zone is obtained. Spontaneous nucleation does occur but only within extended time periods; much larger than the rate of cooling utilised (0.1 °C/min). For example a batch at 50 mg/mL concentration left overnight at 20 °C took approximately 2.7 hours to crystallise (time period from first point of nucleation until fully crystallised i.e. this does not even include the induction time!). A similarly concentrated batch left at 10 °C took approximately 2.5 hours (including time taken cooling to 10 °C).

Crystallisation time is even longer for less concentration solutions; a 30 mg/mL batch left overnight appears to show the first evidence of nucleation at approx. 8.7 °C. With continual cooling, 45 minutes later, the batch temperature reaches a stable value of -6 °C yet the transmissivity still only registers 79%. The solution takes another 2.5 hours for the turbidity reading to stabilise and crystallisation can be said to be complete.

The batches of data are hence of low quality and cannot be relied upon for any valid data. All the above evidence points towards a case for the use of seeded crystallisations, as primary nucleation is clearly not a viable option. It also raises the possibility of the use of an anti-solvent in order to increase the potential yields of further crystallisations. As part of the aforementioned solubility screens performed at AstraZeneca, water is identified as a potential anti-solvent, having shown little or no solubility for Lesinurad.

4.5 Conclusions

The glutamic acid system presents an acceptable case to take forward and begin testing under filtration/percolation. A needle particle shape should be suited for breakage and is easily obtained. In addition the ability to form the alpha-polymorph yields the option to examine a sturdier crystal morphology that would be anticipated to break under different circumstances i.e. attritional breakages as opposed to total fracture.

The urea/urea-biuret system presents a case with a wide range of particle sizes and shapes that are easily formed through crystallisation control and impurity addition. Modification of the solution cooling rate leads to increased thickness of the particles; thus indicating a time-dependent growth rate of these crystal faces. Increased solvent polarity appears to favour the growth of the [001] directions; evident from crystals grown from methanol being more needle-like than those grown from ethanol.

The investigations into the impurity biuret allow the characterisation of a critical point of biuret addition after which the growing urea faces are saturated with biuret molecules; hence exhibit vastly reduced rates of growth in the [001] direction. In ethanol this appears to be approximately 6-8wt%; in methanol this is only 3wt%; although admittedly greater concentrations are yet to be experimented with.

The particles themselves however, are susceptible to the formation of solid bridges under crystallisation and particularly drying, making their handling properties poor. Macroscopically this is observable as significant cohesiveness of the particles.

This is compounded by the difficulty in retrieving powder samples of urea suitable for particle size analysis; after crystallisation and drying a compacted 'block' of urea is obtained with significant strength. To obtain any reasonable quantities of particles for size analysis the 'block' of particles must be agitated and broken up by hand – meaning any potential size reduction could be completely obscured by this process (as it is likely that this will also cause breakage of the particles).

For a project in which the characterisation of discrete particles is paramount, the formation of strong aggregates such as these is unacceptable and thus the urea system cannot be progressed with further.

Lesinurad is a proprietary AstraZeneca compound that crystallises with small prismatic-needles and has been known to suffer from problematic filtrations. This presents the opportunity to demonstrate our proposed filtration/breakage method on an industrial system of significant relevance.

Chapter 5

5 Particle Size Distribution Representations and Critical Analysis of Particle Data

5.1 Introduction

As the characterisation of particle breakage is the primary aim of this thesis, it is also a chief concern that the methods by which particles are analysed for any signs of fracture are robust, reliable and repeatable. Therefore this chapter is a description of the methodologies behind the representations of particle size distributions, and a critical analysis of the data obtained from optical microscopy.

If hypothetically particle breakage is occurring, then the question is how are we to know this is the case. A review into the different representations of particle size distribution is conducted in order to identify the most appropriate methods of particle size analysis.

In addition information obtained from the Morphologi G3 is critically analysed in order to ascertain the validity of the data. The instrument represents a potentially vital source of detailed information on particle size properties and its ability to scan and measure individual particles is seen as a vital tool in the characterisation of particle size changes.

5.2 Literature Review

Automated image analysis is a relatively new technique in particle sizing but has advanced the field significantly. Where before particle analysis (e.g. by sieving) was a laborious and time-consuming process, now the application of algorithmic particle counters are able to provide sufficient objective numerical data in a timely manner. An example of such a particle counter is the Morphologi G3 optical microscope (Malvern Instruments Ltd; Malvern, UK).

The Malvern G3 Morphologi is an optical microscope, dispersal system and built-in software package capable of dispersing a small sample of powder onto a glass slide, such that the microscope can digitally image the particles by scanning across the visible powder mass. An algorithm in the Morphologi G3 software translates the particles' preferred 2D plane (the one facing the microscope camera) of the particle into a greyscale image composed of pixels.

Various particle parameters are then calculated based on the scanned image (circle-equivalent diameter, length, width, circularity, elongation, aspect ratio, area, perimeter etc.).

Needle-like distributions tend to be far wider due to the measurement of a range of cross-sections of the needle; depending on the angle of measurement the width or length is captured; hence for a single particle a range of sizes can potentially be obtained. Mean values of particle size are likely to significantly underestimate the true means.

It should be noted however that this effect is reduced with static microscopy, as preferred orientation of the needles is likely to keep the longest faces pointed at the imaging camera. In particular the nature of the analysis means that all particles are likely to be imaged in a similar manner (i.e. all showing their longest dimensions; all laying on flat faces); this results in a bias of the instrument to measure these particular sizes. Some might actually consider this an advantage over e.g. laser diffraction, in which the needle is likely to be imaged in a random orientation, as the width of the distribution is likely to be smaller.

With this in mind, the Morphologi G3 has found significant application on a variety of different particle systems within the particle sizing and shape characterisation fields; typically with mineralogical and pharmaceutical based systems.

There is sufficient published literature around the use of the instrument, for instance Gamble et al have used the Morphologi G3 alongside SEM and laser diffraction techniques in order to characterise the extent of attrition of a spray-dried product (with hollow morphology), with good correlation between analysis techniques[109]. Additional work by Olusanmi et al[110], Kinnunen et al[111] and Qu et al[112, 113] have also used the Morphologi G3 alongside laser diffraction techniques in order to characterise particle shape factors in addition to size. Qu et al found the particle sizes measured by the instrument to be larger than those measured under diffraction; they attributed this to insufficient dispersion of the powders giving rise to the measurement of overlapping particles[113].

Petrak et al have developed a theoretical model to relate chord length distributions of particles to the particle shape, with applications in the coating of particles with excipients to the correct degree. By relating the chord length distributions of random chords taken from spherical and ellipsoidal shapes they found good agreement with experimentally observed data (from the Morphologi G3); approximately 8% deviations in aspect ratio and sphericity[114].

Ulusoy and Kursun used the instrument to investigate differences in shape of 2 milling procedures and claimed to have found variation in shape; however the data does not appear to indicate significant differences (and this is perhaps a testament to the sensitivity of the instrument)[115]. Additionally they used the data produced by the Morphologi G3 without

further modification or analysis, which is a common occurrence with the use of the instrument.

Many documented uses of the microscope appear to have taken the data from the in-built software GUI without further modification[112-114, 116-121]; or if post-analysis was performed then it was not detailed. The use of, e.g. circle-equivalent diameter or use of a mean value to describe irregularly shaped particles is a well-known source of error in particle size analysis. Admittedly some of the literature concerns the characterisation of near-spherical particles, wherein the data are likely to be of greater validity, but the measurement of needle-like crystals in particular under microscopy should ideally be accompanied with some deeper analysis of what the data actually represents (as will be explained in section 5.4).

For instance Pretoro et al investigated extrusion processing of which needle-like crystals are a component, and found significant discrepancies between the mean values of particle length and width and visual observations of large needles e.g. for a batch of nimesulide needles mean length and width are 274 and 76.4 microns respectively, whilst particles exceeding 900 x 200 microns are observed under microscopy[117]. The authors attributed this to the dispersion settings favouring smaller particles over large particles but gave no consideration to the effects of overlapping particles within the data.

Zhang et al have developed an interesting system in which 3D photographs of needle-like beta-glutamic acid crystals are captured in real time during crystallisation. The stereo imaging system works together with image analysis algorithms to render a particle size distribution of the crystallising mass as it progresses, enabling monitoring of crystal growth over time. The Morphologi G3 is used for offline analysis of particle size; wherein the authors acknowledge the presence of large agglomerates/overlapping particles contributing to error in the data, however to correct for this they increased the dispersion pressure to the maximum permitted (approx. 5 bar)[119].

Not only is this likely to fracture the delicate crystals (as evidenced within this chapter and other chapters in this thesis), but it has apparently not solved their problem; a characteristic 'bump' of oversized particles (see Figure 5-17 for analogous data within this work) is clearly evident within their volume distribution data. This 'bump' is attributed to improperly scanned particles within the dataset, and can be removed through proper post-experimental filtering of particle data (see section 5.4.2).

The authors conclude that use of the number-distribution to represent particle size alleviates this problem, as the conjoined particles have little influence on this representation. However it is often the largest particles that determine the properties of the powder (packing

characteristics, flowability etc.); hence the proliferation of the volume distribution within industry[28]. Thus methods must be sought to alleviate these erroneous fractions of the distributions if the particle size data are to be trusted.

There are examples in the literature of post-experimental analysis on the data obtained from the Morphologi G3[109-111, 115, 122-124]. For instance Olusanmi et al and Kinnunen et al both used the instrument's in-built software filters to remove irregular and/or overlapping particles through a combination of particle convexity and solidity[110, 111]; where the convexity is the actual particle perimeter divided by the particle's convex hull (i.e. imagine wrapping an elastic band around the particle – the perimeter bound by the 'elastic band' is the convex hull), and the solidity is the particle's area divided by the area enclosed by the convex hull. These are both therefore measures of a particles' 'spikiness'.

Duval et al[123] forwent the automated software filters in favour of manual removal of all inappropriate particles – theoretically this is the best solution (due to the human input) but is highly impractical for the filtering of multiple datasets of many thousands of particles. The authors also performed a variability analysis and found 3 dispersions of a single sample to yield consistent data (mean values within <1.15% of the standard deviation); concluding that in future it should be viable to ascertain reliable data from a single sample. This is investigated in section 5.4.3.

With existing literature in mind there is a clear gap for an in-depth analysis of the significant volumes of data obtained from the Morphologi G3. This instrument harbours the potential for a much more powerful analysis than can be achieved by use of relatively indiscriminate techniques e.g. laser diffraction, and thus this chapter presents an overview of the Morphologi G3 and the ways in which the data can be manipulated for the investigation into crystal breakage.

5.3 Methods of Representing Particle Size Distribution

3.1.1 Background on the collection of particle data with the Morphologi G3

A key aim of the project is to accurately, representatively and confidently produce a particle size distribution of the crystal mass being sampled. As only tiny fractions of the original cake are actually measured by the instrument, representative samples can only be built through adequate depth of analysis. Confidence in the data is therefore vital, as particle sizing methods in 2-dimensions can never fully represent a 3-dimensional particle. Therefore a robust method of analysis must take into account this limitation and attempt to account for it.

Particles will tend to preferentially lie on their larger flat faces (i.e. for a needle, this means they will tend to lie on their longest face as opposed to standing on their ends (see Figure 5-1).

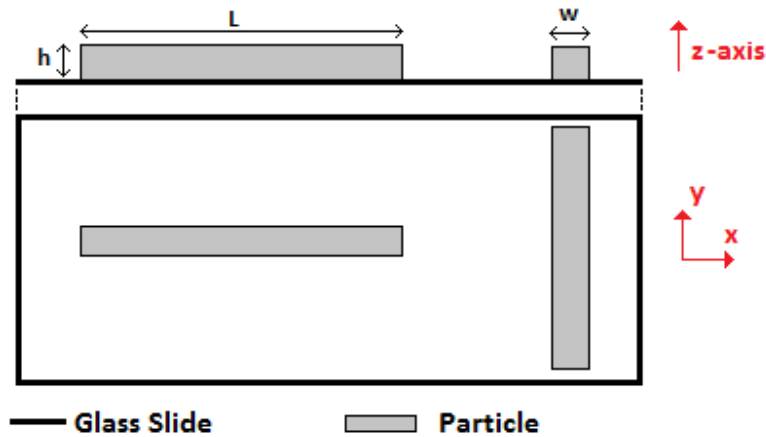


Figure 5-1: Schematic of needles in a typical resting state on a flat surface

Once scanned by the instrument, particle parameters are calculated based on the pixelated image. The circle equivalent diameter (CE diameter) is calculated by equating the area of pixels constituting a particle into a circle, and calculating the diameter of this circle; hence its use as a standardised method of comparing particles of various sizes and shapes. For the bulk of the size distribution analysis, the CE diameter will be taken as a means of comparing the particle size.

Data representing individual particles are sorted into various means of display, as alternate methods will highlight different features of the size distribution. Number distributions tend to skew results in favour of the most populous particle sizes, and for most if not all distributions, these tend to be the smallest particles; hence a number distribution will place bias upon the fines.

A volume distribution sorts the particles by the fraction of volume they occupy relative to the total; fines in this instance carry very little weighting as the majority of the powder bed volume is held within the medium and large size particles. Therefore the two are utilised together to help to create a holistic picture of the size distribution.

It should be noted however, that the error inherent in the very smallest particles of the distributions (approximately < 5 microns) is greater than that of larger particles, particularly when analysis of particle shape is concerned. This is due to the nature of the image analysis technique, where smaller particles are imaged with lower resolutions (i.e. their computerised image is constructed from fewer pixels). In these instances a small range of discrete particle sizes are assigned to many particles; this is observable from 'spiky' peaks e.g. in Figure 5-2 and Figure 5-4, due to their reliance on number fractions of particles.

The following data is collected and presented from CPR experiment 15b (see Chapter 6); i.e. particle size distributions are indicative of before (LF) and after (PF) percolation at 47.2 L/h. Therefore all data represent distributions of beta-glutamic acid particles. Where stated, any dataset referred to as 'LF' represents the 'lightly filtered', or vacuum filtered sample. 'PF' refers to the sample that is subject to percolation within the CPR. 4 separate measurements are taken on the Morphologi G3 for each of the 'LF' and 'PF' samples, and the final data points are averaged to produce a mean dataset; this dataset is plotted in all instances. The maximum standard deviation of any individual data point is ~ 0.01 ; most are considerably less (~ 0.001). The variability of datasets is discussed in more detail in section 5.4.3.

5.3.1 Particle size distribution representations

5.3.1.1 Method 1a – number fraction histogram

A histogram of N_i/N_{tot} vs. d_i ; where particles are sorted by CE diameter into bins of size Δd_i , where the fraction of particles in bracket 'i' ($F_{N,i}$) is:

$$F_{N,i} = \frac{N_i}{N_{tot}} = h_i \Delta d_i \quad \sum F_{N,i} = 1 \quad \text{Equation 5-1}$$

And interval size Δd_i is:

$$\Delta d_i = d_i - d_{i-1} \quad \text{Equation 5-2}$$

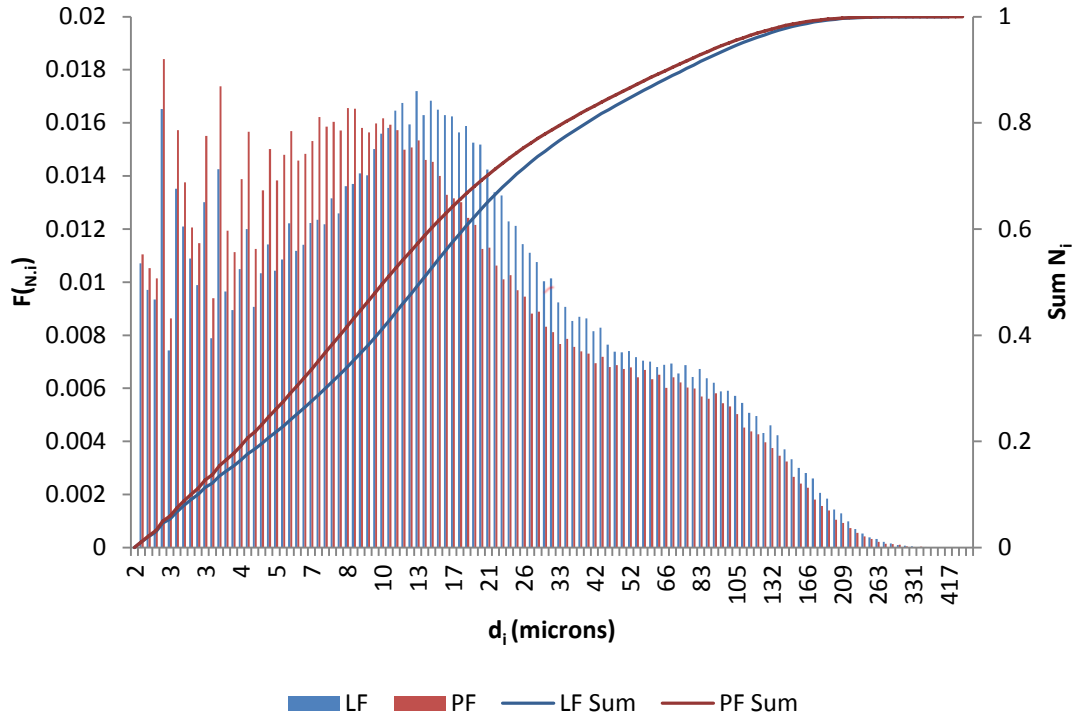


Figure 5-2: Histogram of $F(N_i)$ vs d_i for beta-glutamic acid before and after percolation at 47.2 L/h

A trend to be identified from the number distribution (Figure 5-2) is the general shift of the particle size distribution to the left of the plot (indicating a general reduction in size), from a vacuum filtered sample (LF) to the percolated sample (PF). It is observed that the fraction of large particles (>100 microns) is higher in the LF sample than the PF. The central peak in the curve (representing particles approximately 8-50 microns in size) also shifts to the left, showing that the most common particle sizes for each sample are significantly different (PF size being lower than the LF sample).

5.3.1.2 Method 1b – volume fraction histogram

A histogram of V_i/V_{tot} vs. d_i ; where particles are sorted by CE diameter into bins of size Δd_i , and the volume inside each bin is assumed to be the number of particles in each bin multiplied by the volume of a sphere of diameter d_i .

$$F_{V,i} = \frac{V_i}{V_{tot}} \quad \sum F_{V,i} = 1 \quad \text{Equation 5-3}$$

$$V_{tot} = \sum V_i = \sum N_i \times \frac{1}{6} \pi d_{p,i}^3 \quad \text{Equation 5-4}$$

$$\text{Interval size} = \Delta d_i = d_i - d_{i-1} \quad \text{Equation 5-5}$$

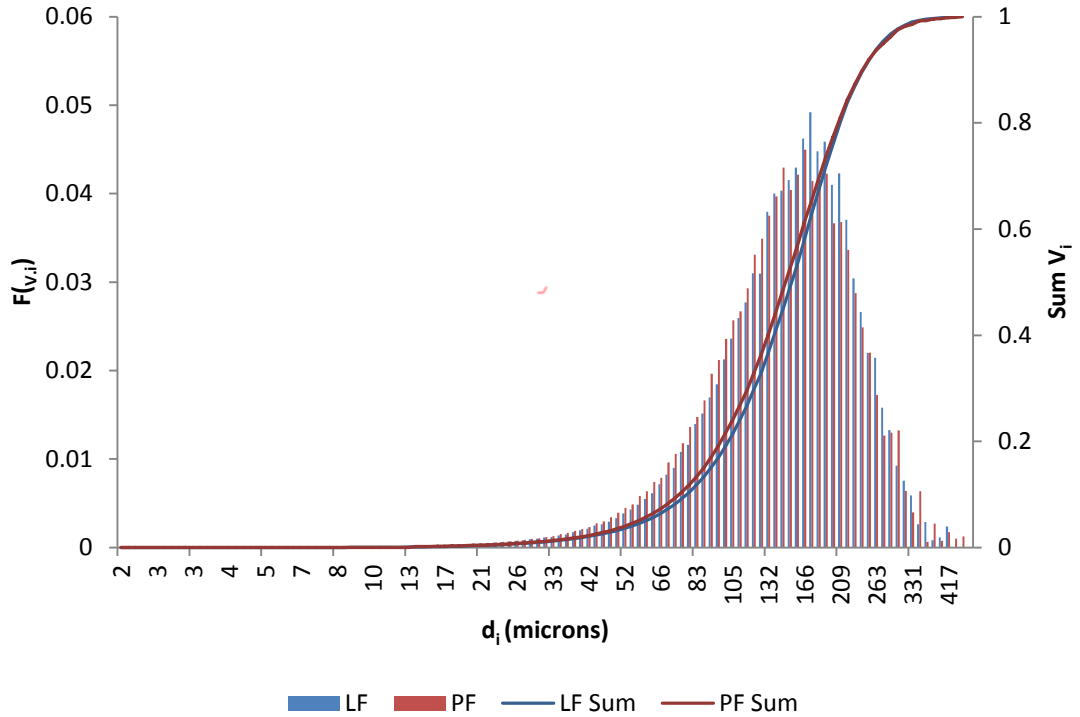


Figure 5-3: Histogram of $F(V_i)$ vs. d_i for beta-glutamic acid before and after percolation at 47.2 L/h

The volume distribution histogram (Figure 5-3) displays little difference between samples, with only very slight variations visible between samples. The LF sample however does display a higher peak than the PF histogram, possibly indicating a slightly narrower spread of particle sizes (as would be expected).

5.3.1.3 Method 2a – number fraction based population density function

A number-based probability density function of $dP_N/d\Delta d_i$ vs. d_i , where $d\Delta d_i$ is the differential particle size ($d_i - d_{i-1}$) i.e. the probability interval width.

$$\frac{dP_N}{d\Delta d_i} = \frac{N_i}{N_{tot}} \times \frac{1}{d_i - d_{i-1}} \quad \text{Equation 5-6}$$

$$\int_0^{\infty} \frac{dP_N}{d\Delta d_i} d\Delta d_i = 1 = \sum \frac{\Delta P_i}{\Delta d_i} \times \Delta d_i \quad \text{Equation 5-7}$$

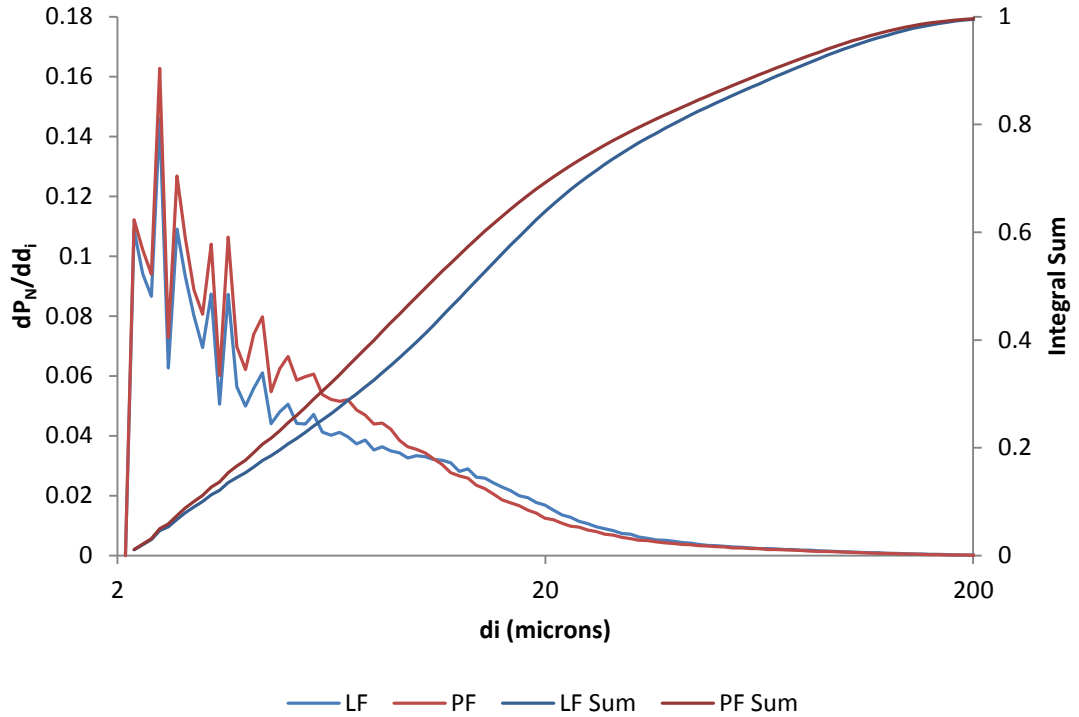


Figure 5-4: Population density function of dP_N/dd_i for beta-glutamic acid before and after percolation at 47.2 L/h

The number-based probability density function (Figure 5-4) displays similar trends to those identified in the number distribution histogram, i.e. that the probability of finding a smaller particle in the PF sample is higher than that of the LF sample, and conversely for particles of size approx. 10-50 microns the reverse is true. The characteristic ‘cross-over’ of the plots illustrate this idea – that above a certain range (approx. 11 microns or so) you are more likely to find a larger particle in the LF sample, whilst below this range, you are more likely to find a smaller particle in the PF sample.

5.3.1.4 Method 2b – volume fraction-based population density function

A volume-based probability density function of $dP_V/d\Delta d_i$ vs. d_i ; where particle volume is calculated based on the assumption for method 1b.

$$\frac{dP_V}{d\Delta d_i} = \frac{V_i}{V_{tot}} \times \frac{1}{d_i - d_{i-1}} \quad \text{Equation 5-8}$$

$$\int_0^{\infty} \frac{dP_V}{d\Delta d_i} d\Delta d_i = 1 = \sum \frac{\Delta P_i}{\Delta d_i} \times \Delta d_i \quad \text{Equation 5-9}$$

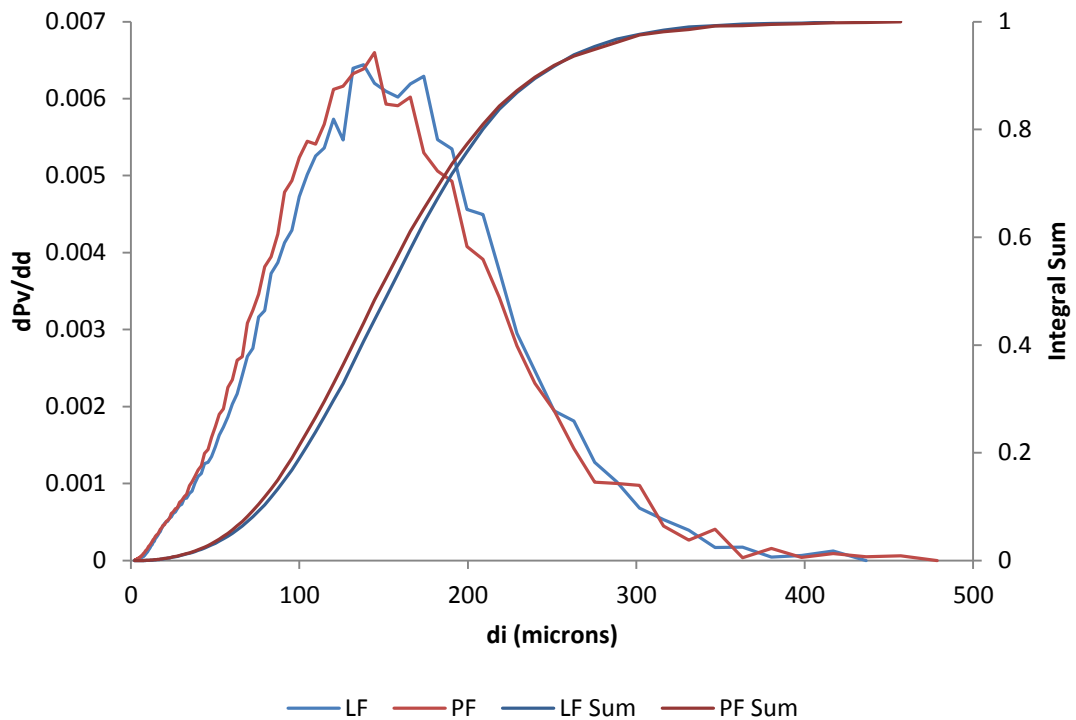


Figure 5-5: Population density function of dP_v/dd_i for beta-glutamic acid before and after percolation at 47.2 L/h

Similarly to the volume fraction histogram previously mentioned, the volume-based probability density function (Figure 5-5) fails to appropriately highlight many changes in particle size from LF \rightarrow PF. Once again, a slight trend of the curve shifting to the left is observed, but the effect is less pronounced than in other (number-based) plots. The largest particle sizes (300-500 micron range) are more affected by random fluctuations in samples (mainly particles that after dispersion on the G3 end up resting against each other, and are therefore scanned as 'one' particle, instead of many) and hence the curve is 'spikier' here, and no clear trends are observed.

5.3.1.5 Method 3a – volume-based number fraction distribution

As an alternative (and potentially more fitting) method for comparing particle size by CE diameter, needle-like crystals could be seen to be better represented as 'shoe-box' like rectangular cuboids (Figure 5-6). The Morphologi G3 records scanned particles with specific lengths and widths, meaning 2 of the dimensions are known quantities – the length 'L' and the width 'W'.

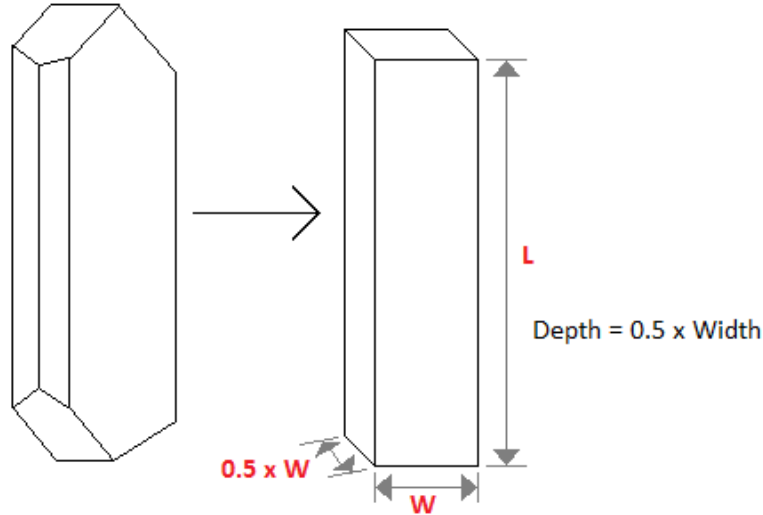


Figure 5-6: Modelling a needle-like (glutamic acid) particle as a rectangular cuboid with length 'L', width 'W' and depth '0.5 * W' (width = 2 * depth)

If it is assumed that these needles lie on a flat surface as envisaged in Figure 5-1 (i.e. their preferred orientation), then assuming for a non-plate-like particle that the 'missing dimension' i.e. the depth/height (estimated from microscopy), is equal to half of the width of the particle, then an assumed volume for the particle can be equated from:

$$V_p = l_p \times w_p \times 0.5 \times w_p = 0.5 \times l_p \times w_p^2 \quad \text{Equation 5-10}$$

Particles can now be sorted into bins depending on their calculated volume, with the number of particles in each 'volume bin' plot as a fraction of the total number of particles i.e. a volume-based number fraction. The natural log of the particle volume in cubic microns is sorted into bins of size ΔV ($V_i - V_{i-1}$), where the particles in ΔV are defined by:

$$\ln V_{i-1} < \ln V_i < \ln V_{i+1} \quad \text{Equation 5-11}$$

If the calculated particle volume lies within the range defined by the bin $\ln(\Delta V)$, then the fraction of particles in this bin is:

$$N_{\Delta \ln V_i} = \frac{N_i}{N_{tot}} \quad \text{Equation 5-12}$$

And the total number of particles is:

$$N_{tot} = \sum N_{\Delta \ln V_i} \quad \text{Equation 5-13}$$

Thus the number fraction of particles in each bin is plot vs. the natural log of the particle volume:

$$\frac{N_i}{N_{tot}} \text{ vs. } \ln V_i$$

Equation 5-14

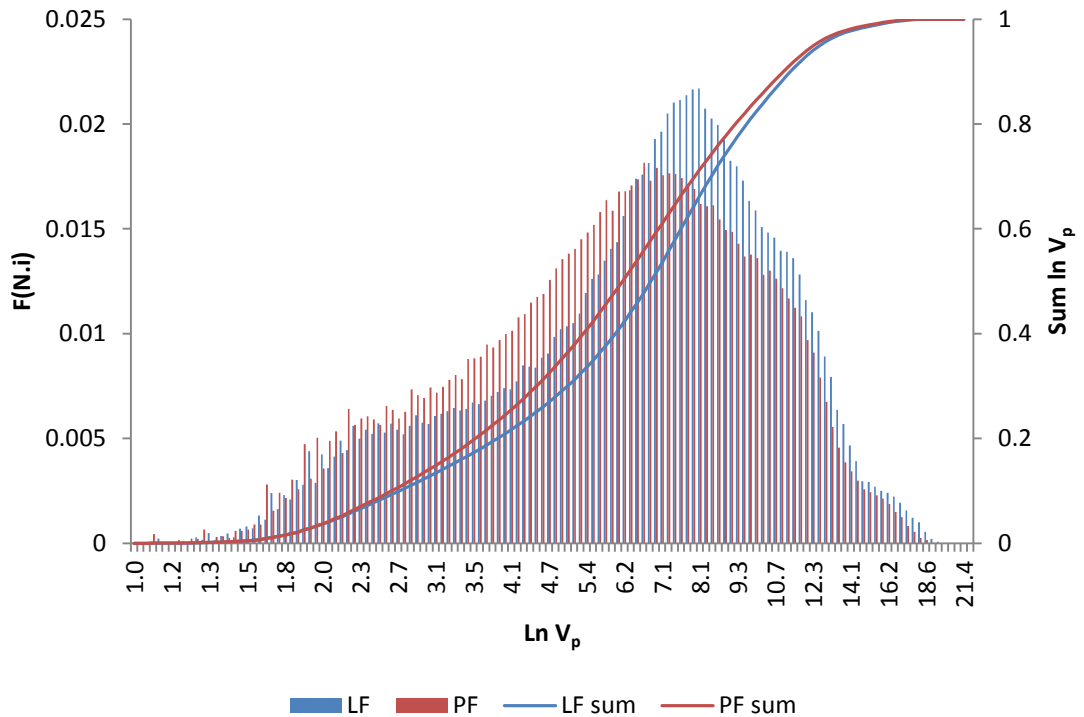


Figure 5-7: Volume-based number fraction histogram of $F(N_i)$ vs. $\ln(V_p)$, assuming cuboidal particles of volume $l_p \cdot 0.5 \cdot w_p^2$; for beta-glutamic acid before and after percolation at 47.2 L/h

The volume-based number distribution histogram (Figure 5-7) simplifies the analysis of the data by spreading out the distribution over a wider range; the result is that multiple individual peaks can be identified from within the distribution that they combine to form. Clear peaks are observable for the fines ($<5 \ln V_p$), medium sized particles ($\sim 8 \ln V_p$) and the larger particles ($>15 \ln V_p$). Again, a clear and characteristic ‘shift to the left’ is observed in the PF sample peak relative to the LF sample. At all points, the fractions of large and medium sized particles in the PF sample are lower than those of the LF. The ‘crossover’ point occurs at a particle volume of approx. $7.5 \ln V_p$; after which the PF sample has a considerably larger fraction of small particle volumes compared to the LF.

In real terms the shifting of the distributions to the left corresponds to a reduction in the perceived volume hold-up of particles. Before experimentation a larger fraction of sample volume is held by large particles with high length. After experimentation (and presumably after breakage occurs) particle lengths reduce (width is assumed to remain roughly constant, if not reduce) and therefore the calculated particle volume results in a larger hold-up of sample volume within the lower size ranges.

The interesting part of this methodology is that the distribution is dependent on (and generated from) particle shape, and hence should be more sensitive to changes in these shapes, e.g. when needles break into smaller fragments. This is discussed further in section 5.3.1.7.

5.3.1.6 Method 3b – volume/number-based population density function

A probability density function of $dP_N/d(\ln V_p)$ vs. $\ln(V_p)$, based on the previous calculation (method 3a) of sorting particles into number fractions in bins of size ΔV ($\ln V_i - \ln V_{i-1}$):

$$\frac{dP_N}{d\ln V} = \frac{N_i}{N_{tot}} \times \frac{1}{\ln V_i - \ln V_{i-1}} \quad \text{Equation 5-15}$$

$$\int_0^{\infty} \frac{dP_N}{d\ln V} d\ln V = 1 = \sum \frac{\Delta P_i}{\Delta \ln V_i} \times \Delta \ln V_i \quad \text{Equation 5-16}$$

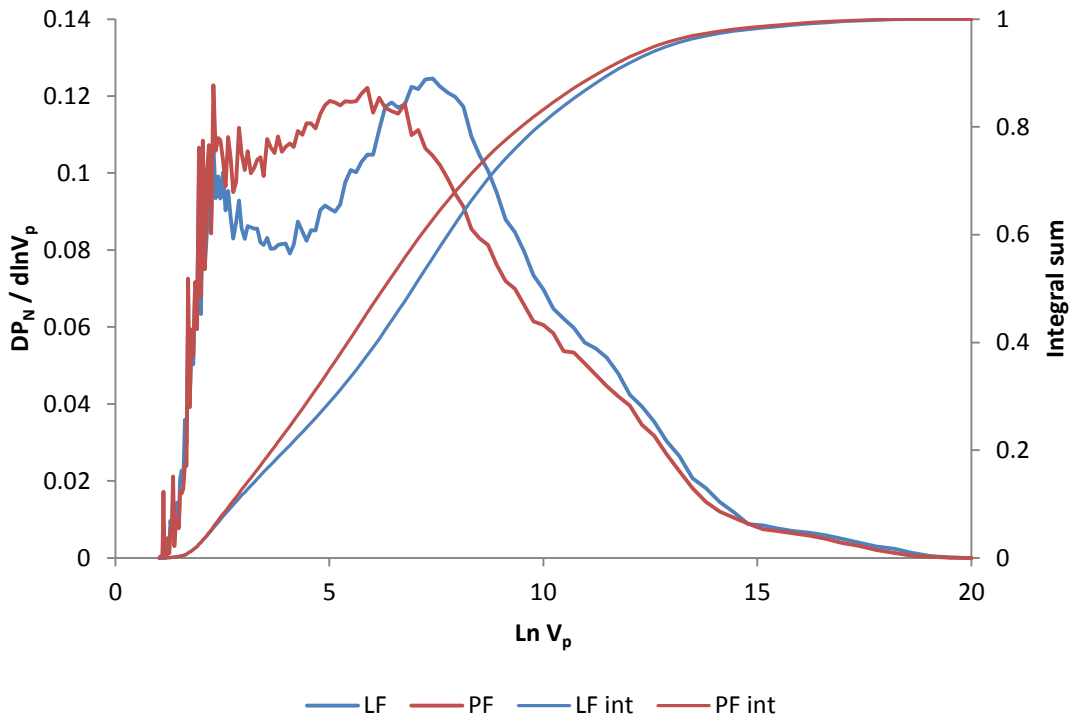


Figure 5-8: Volume-based population density function of $dP_N/d\ln(V_p)$ vs. $\ln(V_p)$, assuming cuboidal particles of volume $l_p * 0.5 * w_p^2$; for beta-glutamic acid before and after percolation at 47.2 L/h

The population density function (Figure 5-8) also highlights the large differences previously mentioned; showing there is a much higher probability of finding a low-volume particle ($<7 \ln V_p$) in the PF sample than in the LF sample. Similarly the chances of finding any higher volume particles ($>10 \ln V_p$) are always greater in the LF sample. A clear shift in the modal peak of the functions has also taken place, showing a general trend towards decreases in particle size.

5.3.1.7 Method 4 – aspect ratio number distribution

This method involves the sorting of particles into a number-based histogram of the aspect ratios of the particles. The aspect ratio is here defined by taking the ratio of the measured particle's width to its length, where the width is always the smaller dimension; hence the value of aspect ratio is a value always between 0 and 1.

This produces a histogram of $N_{AspR,i}/N_{tot}$ (number of particles of aspect ratio 'i' / total number of particles) vs. $AspR_i$; where particles are sorted by aspect ratio into bins of size $\Delta AspR_i$, where the fraction of particles in bracket 'i' (F_{Ni}) is:

$$F_{AspR,i} = \frac{N_{AspR,i}}{N_{tot}} \quad \sum F_{AspR,i} = 1 \quad \text{Equation 5-17}$$

And the interval size $\Delta AspR_i$ is constant at 0.02.

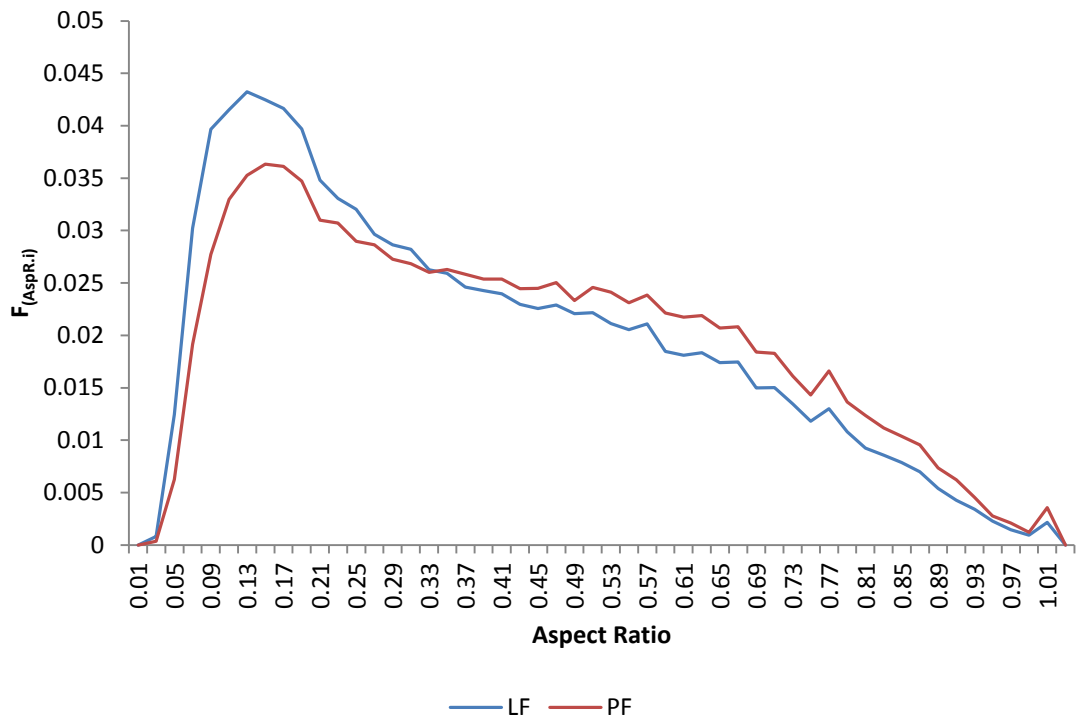


Figure 5-9: Distribution of number fraction of particles of aspect ratio in bracket 'i' vs. aspect ratio for beta-glutamic acid before and after percolation at 47.2 L/h

The aspect ratio distribution (Figure 5-9) is, in certain respects, one of the most important analysis methods available when examining the potential cleavage of particles into smaller fragments.

For example, a particle of width 100 microns and length 1000 microns has an aspect ratio of 0.1 (100 / 1000); if this particle theoretically divides into 2 via breakage then these particles each have an aspect ratio of 0.2 (100 / 500) (Figure 5-10).

It is assumed that needle-like particles preferentially break perpendicular to their longest dimensions i.e. as depicted by Figure 5-10, due to the increased stresses caused by the greater moment (force x length), and the uneven distribution of balancing forces from the packing structure of needles.

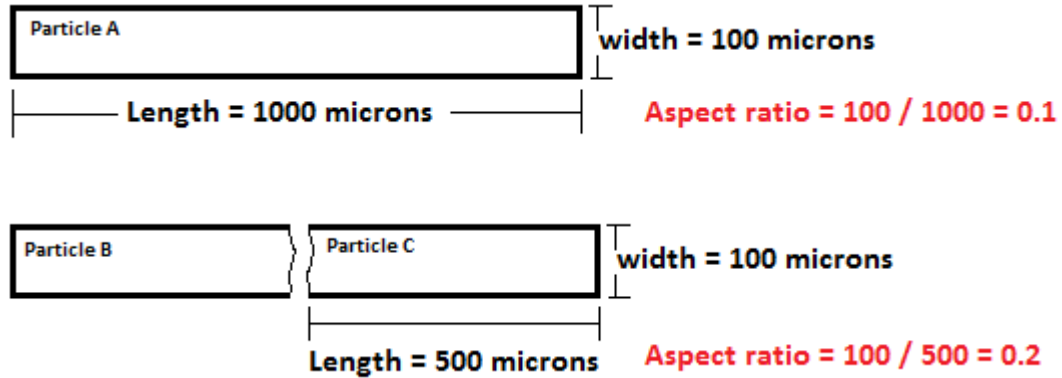


Figure 5-10: Change in aspect ratio of a theoretical particle breaking into 2 fragments

One would therefore subsequently expect the distribution of aspect ratios to reduce in the 'elongated' region and increase in the 'rounded' region i.e. elongated, needle-like particles will disappear as they break into fragments with lower lengths (assuming particle widths remain roughly constant). In their place particles with more equal widths/lengths appear in the distribution; thus particles with aspect ratios closer to 1 are produced as a result of breakage.

It can be observed from Figure 5-9 that the sample taken from the CPR has a significantly altered aspect ratio distribution when compared to the LF control sample. The LF sample displays evidence indicating the presence of long needles due to its tall peak in the < 0.2 range; this peak is shifted greatly in the PF sample. The spread of aspect ratios also rises after percolation (indicated by the flattened, widening curve); interestingly this can also be observed from Figure 5-7 (which is also dependent on particle shape).

These signs point to the potential breakage of needle crystals into shorter fragments.

It should be noted that here the Morphologi G3 defines as the aspect ratio as the ratio of the 'width' of the particle to its 'length', and defines the width as the shortest of the 2 dimensions, whatever is measured. Therefore the aspect ratio is always a value between 0 and 1. The 'elongation' of the particle is the value of $(1 - \text{aspect ratio})$; these definitions are to be used henceforth in the description of any and all data.

Needle-like particles therefore have 'low' aspect ratios (values close to 0) and high elongations (close to 1), whilst more rounded or square particles have 'high' aspect ratios (values close to 1) and low elongations (close to 0).

5.4 Validity of Data

5.4.1 Critical analysis of Morphologi G3 data

As a continuation into the modelling of needle particles as 'shoe-box-like' particles (in order to calculate their volume), comparison of assumed surface area (i.e. the length multiplied by the width of the particle) with the area as scanned by the Morphologi G3 produces a range of values. Some particles' L*W area matches well with the scanned pixel area, whilst other particle areas can be up to ~20 times out. Investigating this further reveals some particles with immediately obvious discrepancies in size – e.g. a particle with parameters of CE diameter of 193 microns; length of 668 microns; width of 471 microns; is represented by the scaled shapes shown below. Clearly these are not of equal area.

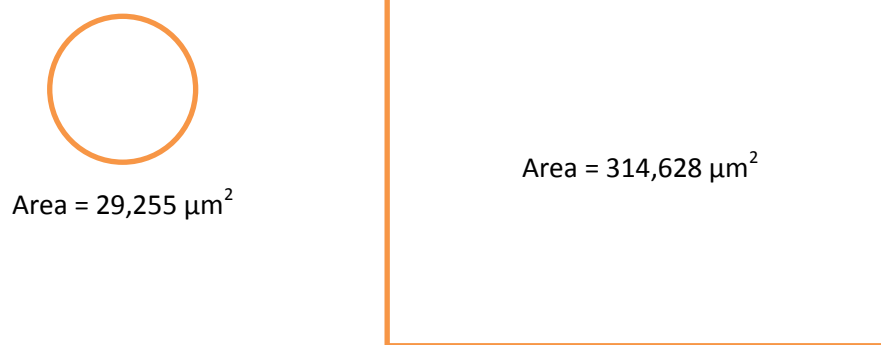


Figure 5-11: Scaled representation of particle size areas – the particle has CE diameter equal to 193 microns but an area of L*W equivalent to a particle of CE diameter equal to 633 microns

The Morphologi G3 allows post-experimental examination of all scanned particles, as image files are retained within the logs of the machine. Examination of a typically well-matched (calculated area:scanned area) particle is displayed in Figure 5-12.

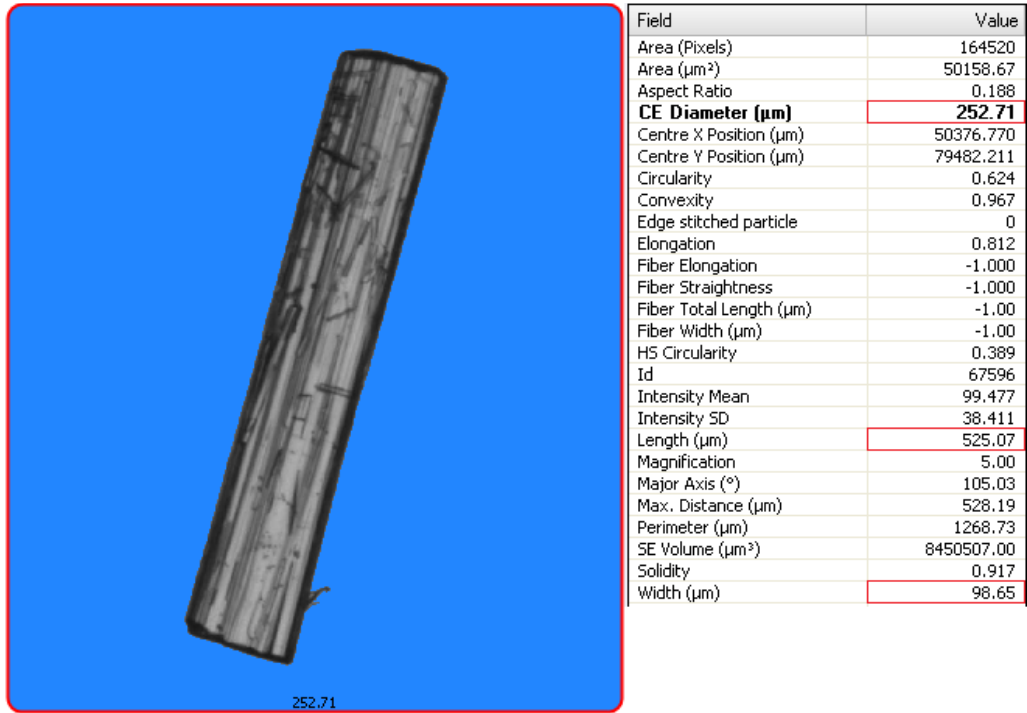


Figure 5-12: Example crystal of beta-glutamic acid as scanned from Morphologi G3 Optical Microscope

The area ratio can be evaluated as such, using data from the crystal properties:

$$Error = \frac{Scanned\ Area}{Length \times Width} = \frac{50,159\ \mu m^2}{525.07\ \mu m \times 98.65\ \mu m} = 0.968$$

→ ~3% deviation

Equation 5-18

Hence a typical well-scanned particle will give an approximate over-estimation of roughly 3% extra area. Although non-trivial, it is none-the-less an acceptable error given the original assumption of shoe-box shaped particles.

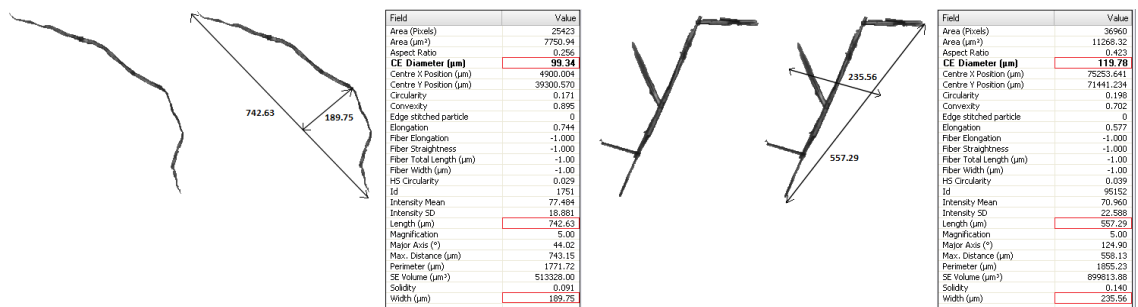


Figure 5-13: Examples of ‘poorly scanned’ ‘crystals’

Figure 5-13 displays several typical poorly scanned ‘crystals’; however a human observer will easily realise they are not regular crystals. Figure 5-13; right, is an artefact of particles coming to rest too close to each other whilst under dispersion. With no significant gap between the crystals, the software algorithm cannot differentiate between single particles and groups of 2 or more, and are thus recorded as a single particle. Figure 5-13; left, is an example of an

atypical fibrous strand that occasionally comes to rest upon the glass slide, and is also classified as a 'particle' in any distribution.

It can be seen that by assuming these 'particles' are shoe-box cuboids, that significant errors are to be encountered, e.g.:

$$Error = \frac{11,268 \mu m^2}{557.29 \mu m \times 235.56 \mu m} = 0.09 \rightarrow \sim 90\% \text{ deviation} \quad \text{Equation 5-19}$$

It is clear that when assigning a 'length' and 'width' to any particle, the software encases the particle in some form of box, of which it's dimensions are taken for these values; hence the huge over-estimation of a 560 x 235 micron needle (clearly not a fair representation of this particle). It is also obvious that these particles will negatively hamper data whether or not any 'shoe-like' assumptions are made; thus to ensure integrity of CE diameter data also, some form of data filtering is required to remove these particles (note – manual removal of every non-particle-like data point is theoretically possible, but practically impossible with average samples of tens of thousands of particles).

5.4.2 Data filtering

To begin data filtering, particles are sorted into a 'cloud' plot of their elongation vs. their circularity within the G3 software interface.

Circularity here is defined in a similar way to the CE diameter – with a circle of equivalent area to that of the particle. The ratio of this area-equivalent circle's perimeter to the perimeter of the actual particle is taken – this is the particle's circularity. A perfect circle will obviously have a circularity equal to 1 whilst high aspect ratio, rough or irregular shaped 'spiky' objects will have circularities much lower than this.

Particles within the distribution can be highlighted for viewing by selecting boundary conditions based on particle circularity and elongation. These can be entered manually or 'drawn' using rectangles or polygons of the user's choice.

Table 5-1 displays a series of images of the particles selected for detailed viewing based on their elongation/circularity. Manually viewing particles in this way helps to gather qualitative information on the sorts of images that have been captured, and whether they accurately represent the crystals they were scanned from.

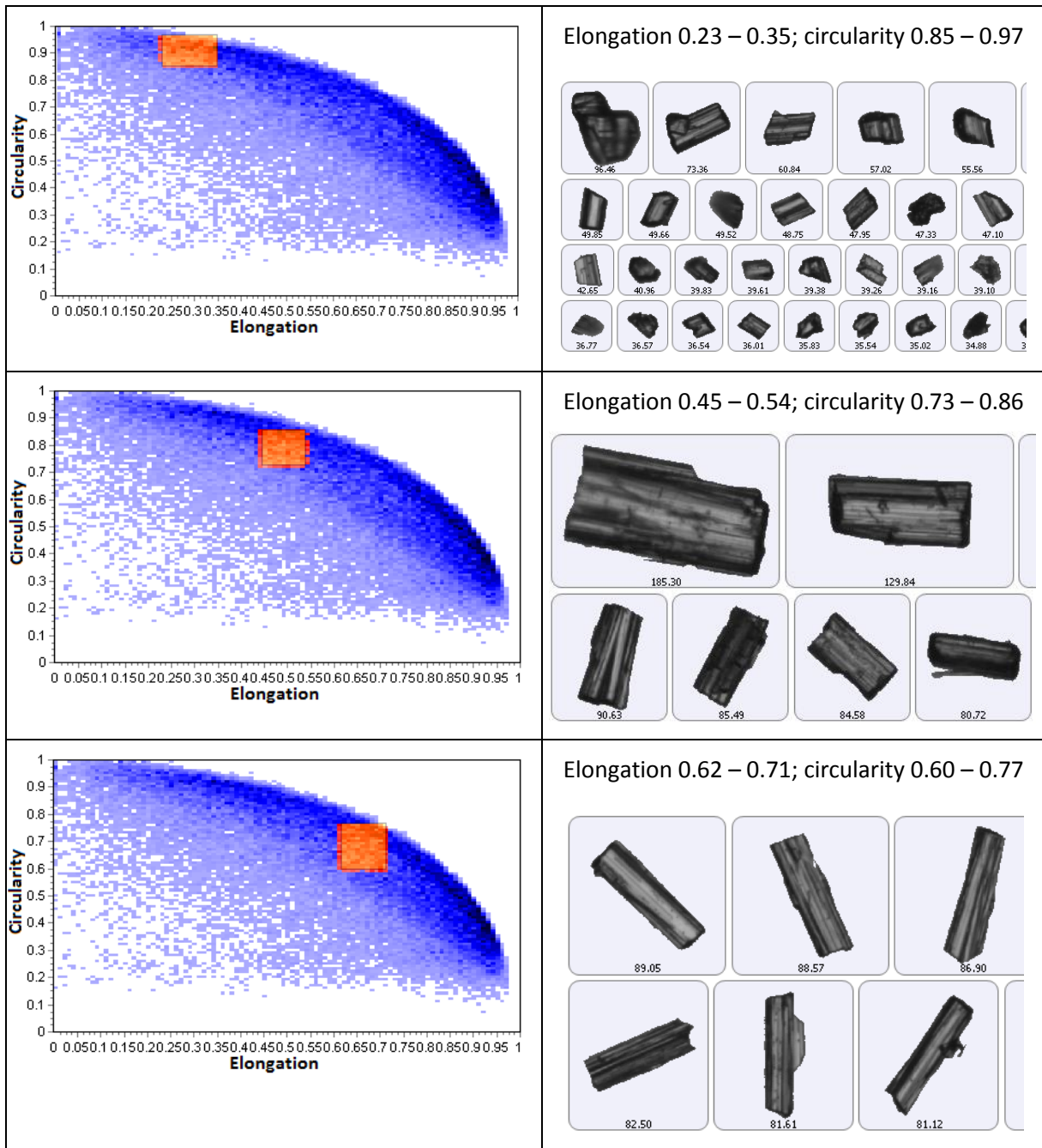
As can be observed from the table, there are areas within the distribution (tending to be the higher particle density areas – shown by a deeper blue colour in the 'particle cloud') where the quality of images tends to be good. These areas correspond to particles with either high

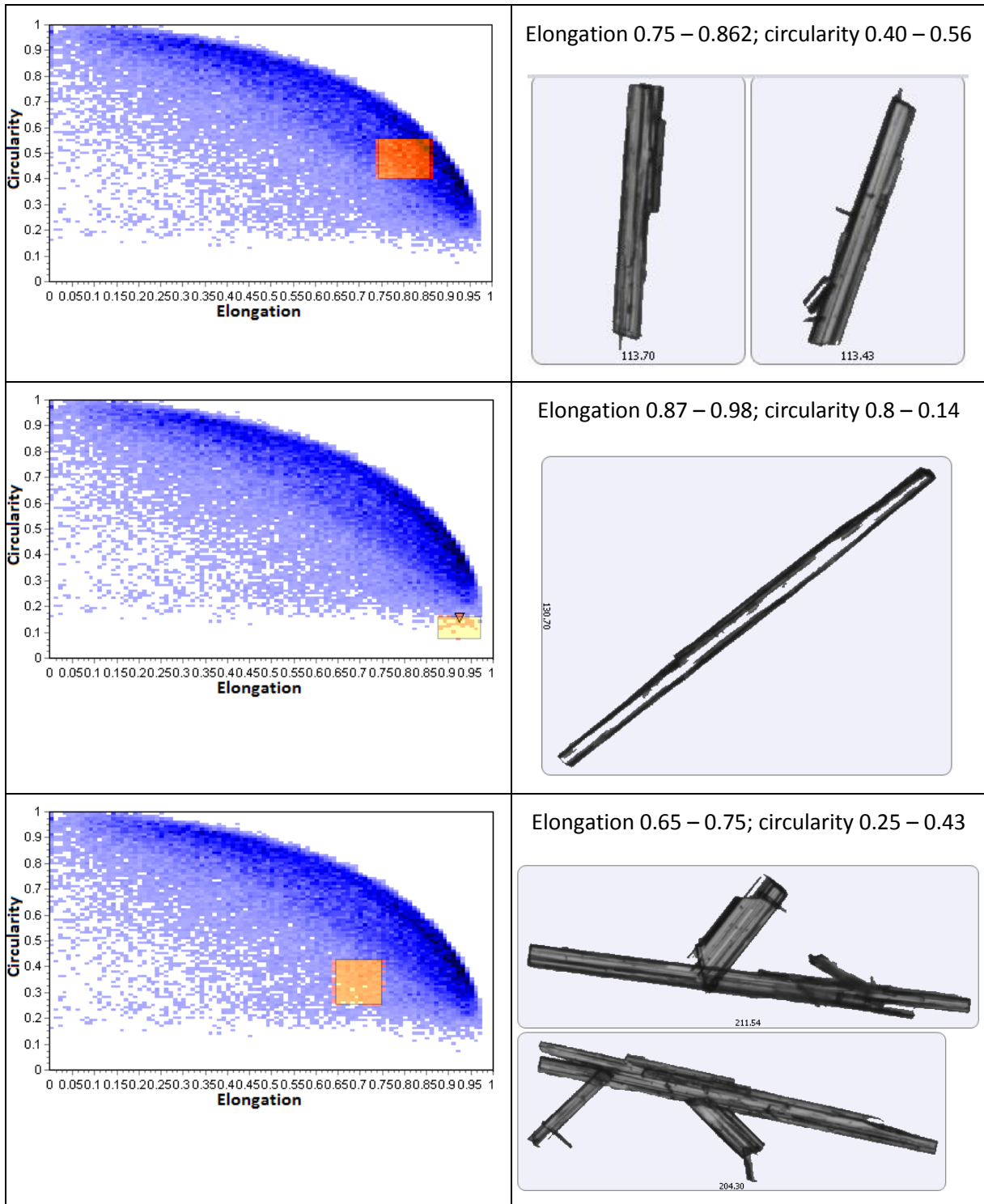
circularity/low elongation, or a high elongation/low circularity; or a mixture of high circularity/high elongation. Crystals within these boundaries tend to have a low deviation of their scanned area vs. their calculated ($L*W$) area.

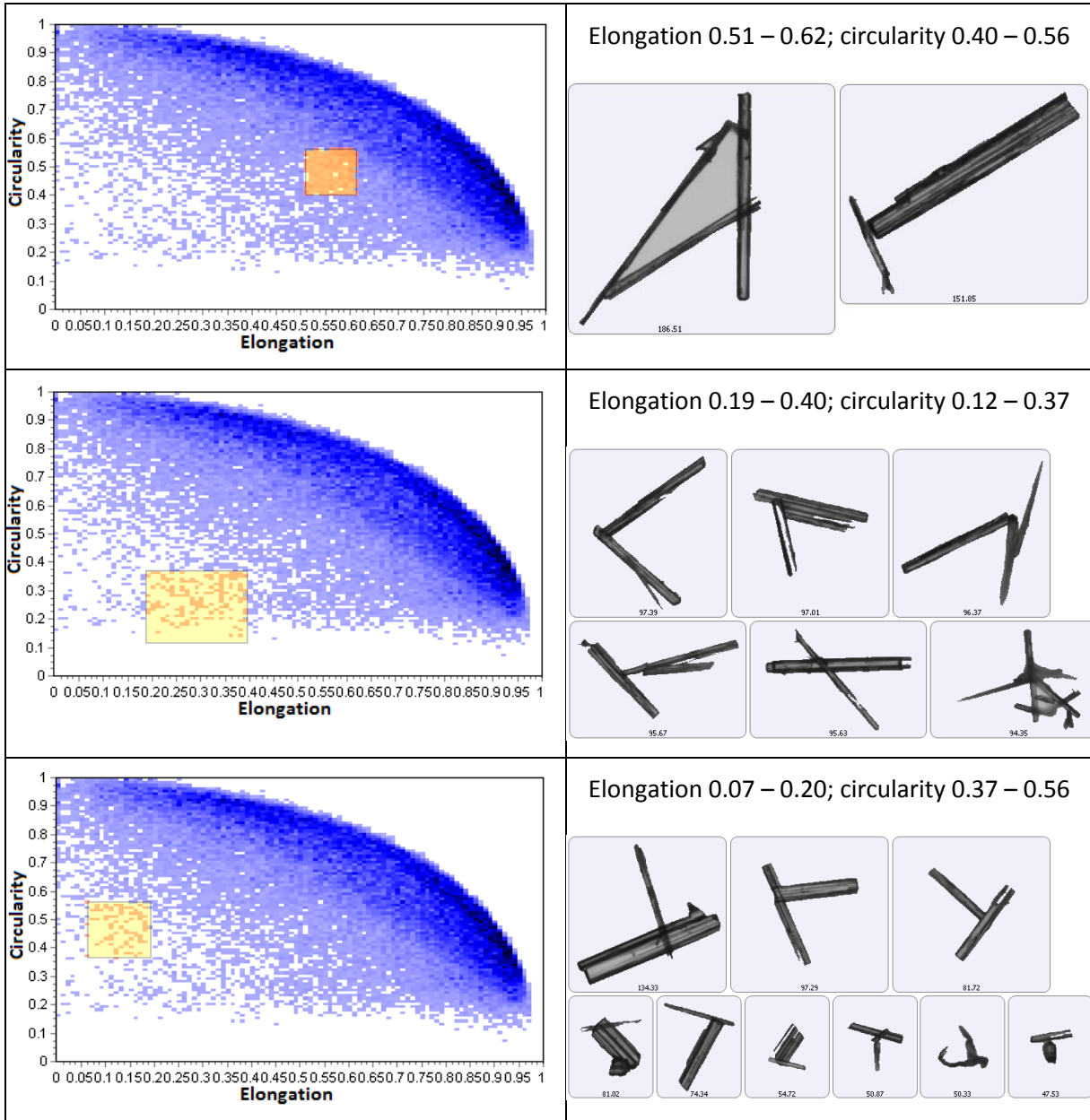
The low particle density areas (light blue shades/sporadic dots in the 'cloud') tend to house particles that have either been scanned poorly, or represent multiple particles captured as a single image. These are generally located in the low circularity/low elongation areas of the distribution. In addition, these particles tend to be the ones that have very poor scanned area: calculated area ratios, and thus would be excluded through the use of any filtering system.

Interestingly, particles with very high elongation (above ~ 0.9) and very low circularity (below ~ 0.15) tend to have been scanned as 'hollow' particles, with some of the pixelated area within them 'missing' from the image (see table). These particles would still tend to be included in any final distribution, as an $L*W$ value would accurately represent the area of this particle, even if it didn't correlate well with the area as recorded by the G3 (as 'area' is quite clearly missing from these crystals). This $L*W$ value would actually be of greater use than the CE diameter for these particles (which is directly related to the pixelated area of the scanned particle).

Table 5-1: Selections of particles resulting from data filtering on the G3 software interface – particles are sorted into a ‘cloud distribution’ of elongation vs. circularity, after which areas of the distribution can be manually highlighted to view particles within the selected parameter range







5.4.2.1 Manual filtering of data

Collecting the 'desired' particles into a group in which the 'undesired' particles can be filtered out is a manual operation. A polygon is hand-drawn using the software to encapsulate particles into the boundary conditions below (Table 5-2). Note that these values are approximate as they are manually-defined.

Table 5-2: Boundary conditions of elongation vs. circularity for a single data-set

Elongation	Circularity	Matching point in Figure 5-14
0.993 (~1)	0.978 (~1)	A
0.992 (~1)	0.058 (~0)	B
0.836	0.063 (~0)	C
0.826	0.397	D
0.540	0.683	E
0.052	0.915	F
0	0.915	G
0	1	H

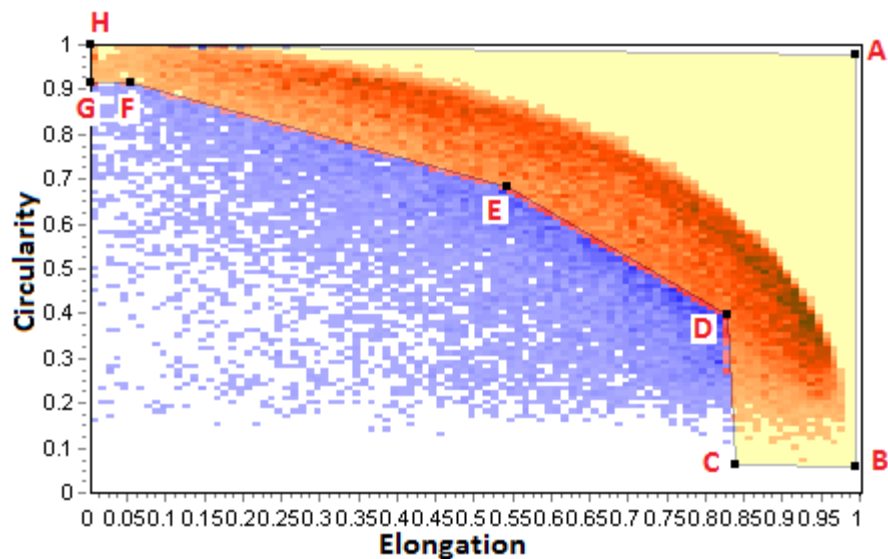


Figure 5-14: Particle size distribution of elongation vs. circularity, with 'desired' particles (i.e. particles that will stay as part of the distribution data) highlighted using a parameter-defined polygon. Particles outside the distribution are removed from the data-set

The polygon is also illustrated in Figure 5-14. Note that there are no particles (and never are) in the top-right corners of the plot (highest circularities and elongations; a particle cannot be highly circular and also highly elongated by definition), but these are defined to simplify the polygon.

Once data is filtered using this method, approximately 10-15% of the particles are removed from any particular sample.

5.4.2.2 Effects of data filtering on particle size distribution

To prove distributions are not dramatically altered by the removal of these particles, and to analyse for any potential improvement in presentation, 'filtered' and 'unfiltered' datasets are presented together, using method '1a', and the result is displayed in Figure 5-15.

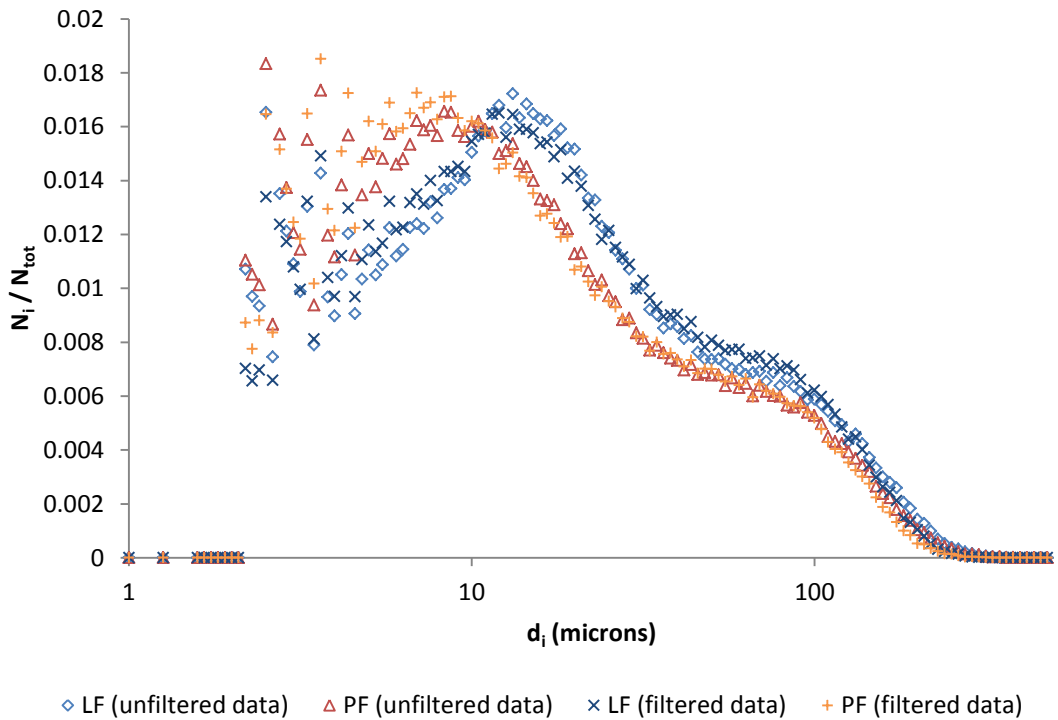


Figure 5-15: Filtered and unfiltered number distribution data (method 1a) for beta-glutamic acid before and after percolation at 47.2 L/h

For simplicity, the summation curves are removed; similarly, although technically a histogram, the data is presented as an x-y scatter plot to better highlight the subtle differences between the 2 datasets (*as will be the case for histogram data from this point onwards*). Using method 1a exemplifies the smaller sizes in the distribution; the fines (<10 micron) region of the curve tends to be subject to large amounts of scatter and less reliable data, thus little difference can be gleaned from this area of the plot.

For particles in the medium size ranges, only subtle differences are observed e.g. unfiltered 'LF' samples appear to contain more particles in the ~10 micron range, whilst the filtered 'LF' samples have slightly higher fractions of ~70-100 micron particles. In the 100+ micron range, a small shift in the peak moves it downwards and to the left (i.e. fewer particles in the distribution rest in these bins).

Similarly, few differences are obvious when comparing the 'PF' samples; except that a proportion of larger sized (>100 micron) particles also appear to have been lost through data filtering, although the difference is subtle.

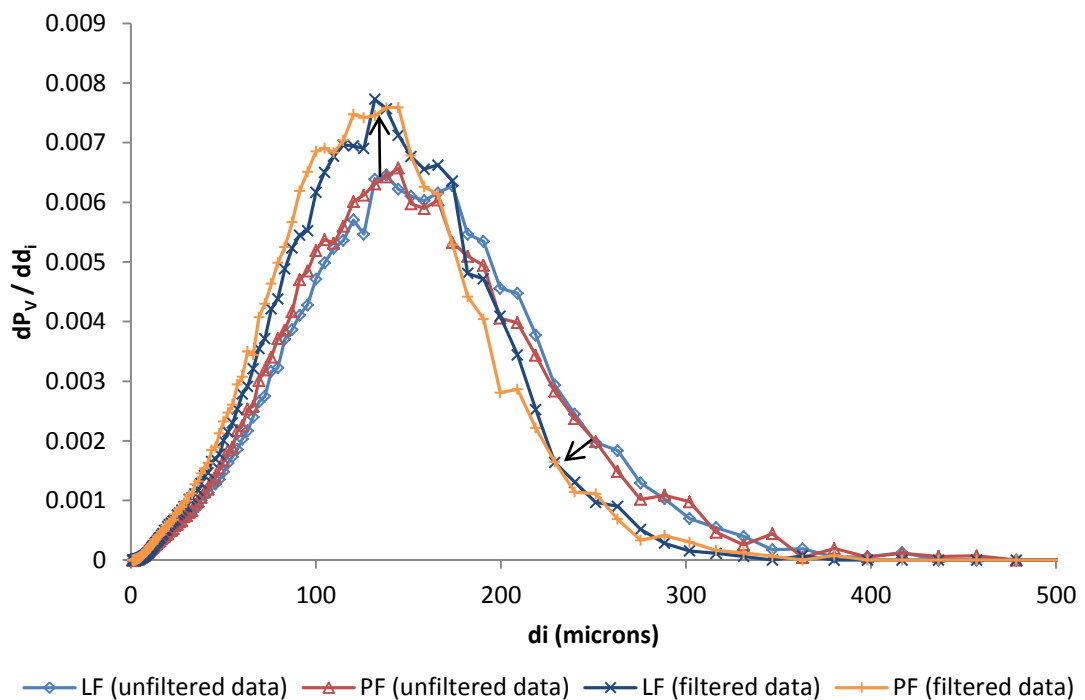


Figure 5-16: Filtered and unfiltered volume distribution data (method 2b) for beta-glutamic acid before and after percolation at 47.2 L/h. Arrows represent the shift in the data from the unfiltered to the filtered datasets – indicates a large overall reduction in average size

By applying the data to a volume-based population density function (method 2b; Figure 5-16), certain features become more obvious (remembering this distribution better represents the larger sized particles). Immediately clear is a large shift in the 2 peaks of the original data (see arrows in Figure 5-16). Effectively a narrowing of the PSD has taken place; evident by a shift in the modal particle sizes to higher probabilities (≈ 150 microns). Some of the narrowing has come as a result of a large change in the probability of observing a larger particle (>200 microns), which is now significantly lower in the new datasets. Arguably, some of the 'spikiness' (i.e. random large particles appearing in bins >200 microns) has also relaxed.

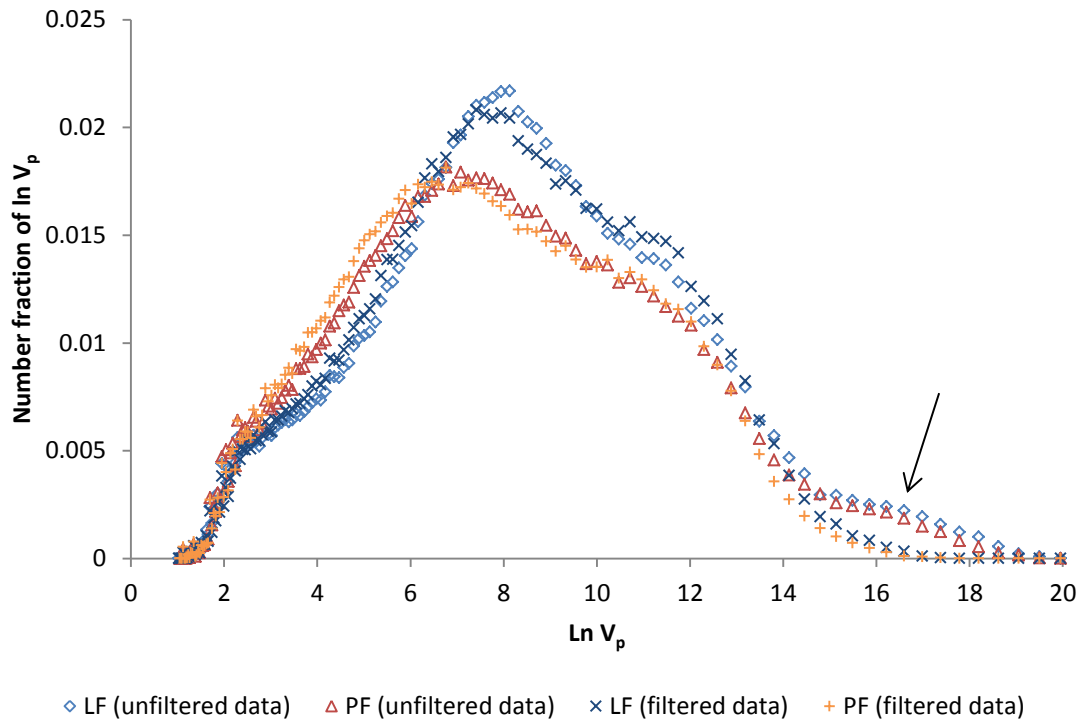


Figure 5-17: Filtered and unfiltered number-volume distribution data (method 3a) for beta-glutamic acid before and after percolation at 47.2 L/h

Finally in applying the new data filtering methods to the ‘shoe-box’ model, the previous assertions are also validated (Figure 5-17; method 3a). The major difference between the sets of plots is exemplified by the almost disappearance of the largest sized ‘particles’; which as can be inferred by now, are not actually particles, but agglomerates/particles resting on one another/fibrous material. Due to their large ‘containing boxes’ drawn by the G3 software, these objects appear to be much larger than they physically are. For a model in which lengths are taken with the square of the width, objects that are already oversized in dimensions (compared to say, their CE diameter) would have an even greater error in their assumed volume.

5.4.2.3 Automation of data filtering through computational scripting

As has been previously alluded to, manual drawing of the polygons to filter the data is subjected to operator bias and error (see example hand-drawn polygon in Figure 5-18). The method is also labour-intensive and would require large sums of time, seeing as the exporting, importing into spreadsheet and subsequent analysis of data is performed many times for each dataset (of which there are many). An automated solution is therefore sought.

Using *Python*, a piece of software has been written to process the exported ‘.txt’ data files into a filtered dataset akin to those of the manual polygon. In this way, multiple datasets at a time

can be selected and processed in a number of seconds, as opposed to the many minutes – hours it may have taken to perform this manually.

The filtering algorithm also sheds the unused data from the original data-file (e.g. the ‘magnification’ column, which is a column of static entries of ‘x5’ for however many particles are in the dataset; clearly unnecessary and consumes computer memory), making the new file smaller and cleaner for importing into the spreadsheet and later analysis.

The qualification for a particle to be entered into the filtered dataset is dictated by an updated set of values listed previously in Table 5-2, now represented by Figure 5-19.

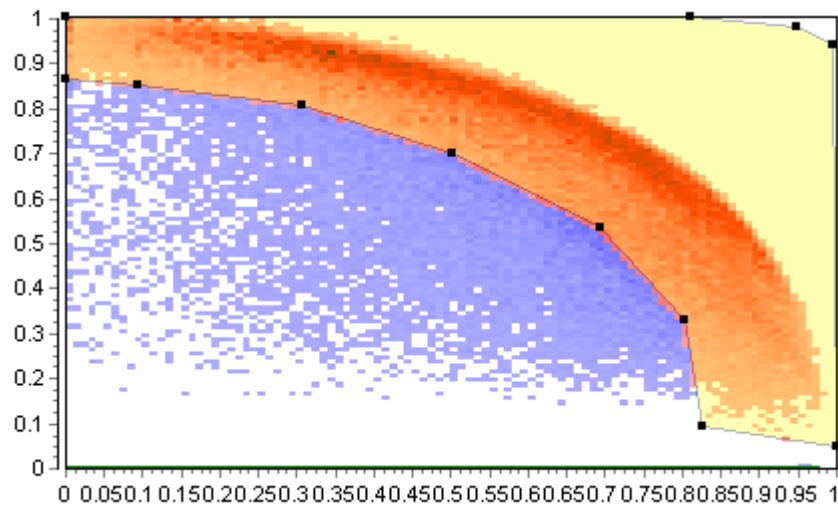


Figure 5-18: Example initial hand-drawn polygon overlaid onto a cloud plot of particles (screenshot within Morphologi G3 software GUI)

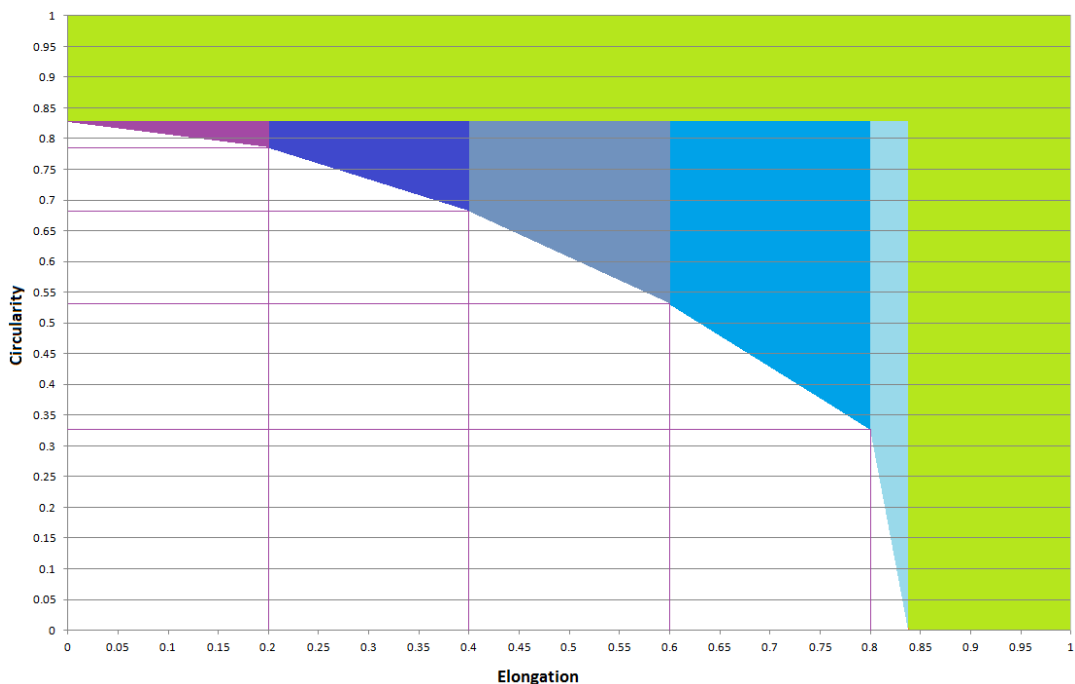


Figure 5-19: Updated polygon with boundaries dictating the extents of the filtering algorithm

The algorithm used by the software uses a set of decision logic to either place the particle into the new dataset, or bin the particle. If the particle lies within any of the coloured blocks within Figure 5-19, then it is added to the filtered dataset e.g. if the particle has elongation greater than 0.84, it is automatically added to the dataset; if the particle has elongation greater than 0.6 but circularity of 0.5, then it is binned. The pseudo-code for the algorithm is akin to:

```
import Morphologi-G3_data
for particle in Morphologi-G3_data:
    if circularity >= 0.84 or elongation >= 0.84:
        Append particle to list
    else:
        if circularity >= 0.83 and elongation >= 0.0825:
            Append particle to list
        else if circularity >= 0.82 and elongation >= 0.165:
            Append particle to list:
        ...
        # Repeat for decreasing circularity and increasing elongation
        ...
    else:
        # do not add particle to list

return list
```

The final result is a piece of software complete with GUI, capable of filtering a dataset of 10s of thousands of particles in a few seconds (Figure 5-20).

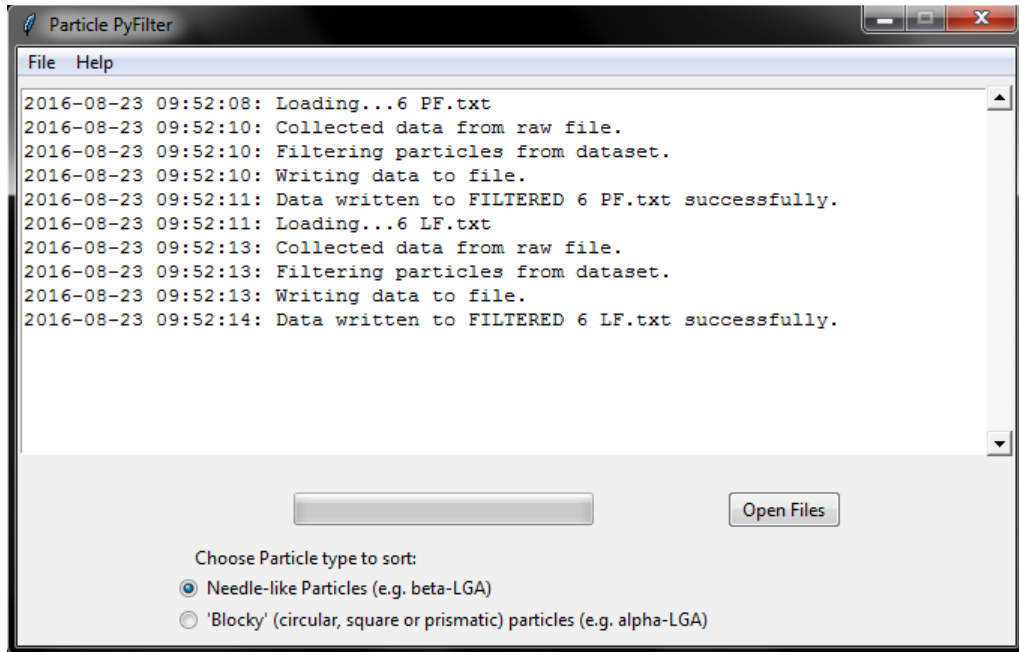


Figure 5-20: Screenshot of the 'Particle PyFilter' software GUI

The final test is to compare the result with that of the manual polygon (Figure 5-21). Subtle differences are observable (mainly around $12 \text{ Ln } V_p$), but these are to be expected as the 'polygon' utilised differs slightly from the original manual selection (i.e. criteria of circularity/elongation are altered slightly). The main finding is that the algorithm can accurately reproduce what the original manual method set out to perform, and hence is used to sort and filter all G3 datasets going forward.

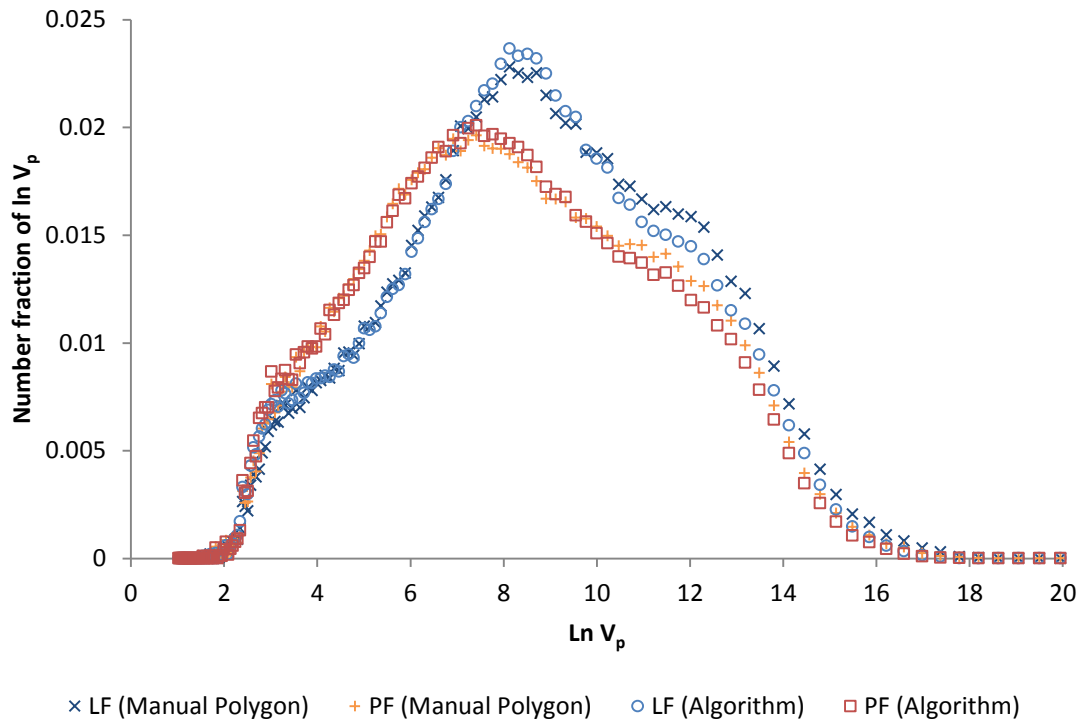


Figure 5-21: Comparison of manual-filtering of data with automatic filtering by software algorithm for beta-glutamic acid before and after percolation at 47.2 L/h

5.4.3 Reproducibility of measurement

Continuing with data validation, the reproducibility of the Morphologi G3 measurements must be evaluated. Due to the (relatively, e.g. compared with laser diffraction) low particle counts measured per sample run – somewhere in the region of 30,000-60,000 particles – the representativeness of the samples can be considered low compared to the total particles within the filter. Therefore for each sample taken (i.e. each LF, PF etc. for each experiment), multiple samples are tested with the Morphologi G3 to increase the representation. 3-4 different measurements are typically obtained; limited in part by the long analysis time of the instrument (approx. 1.5 hours per measurement).

Obtaining multiple distributions and plotting them together yields an indication of the ‘thickness’ of each distribution curve; i.e. the extent of y-axis variability. Data is displayed in Figure 5-22 and Figure 5-23; each individual analysis is given a label 1-4.

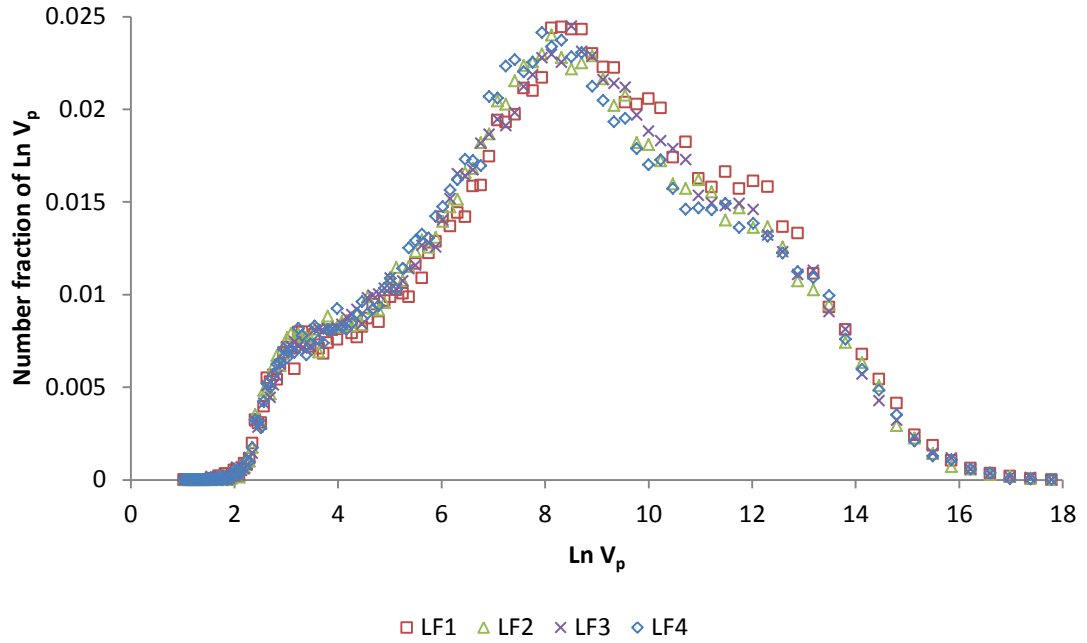


Figure 5-22: Results of a variability analysis for 4 separate measurements of LF samples of beta-glutamic acid (i.e. no percolation performed)

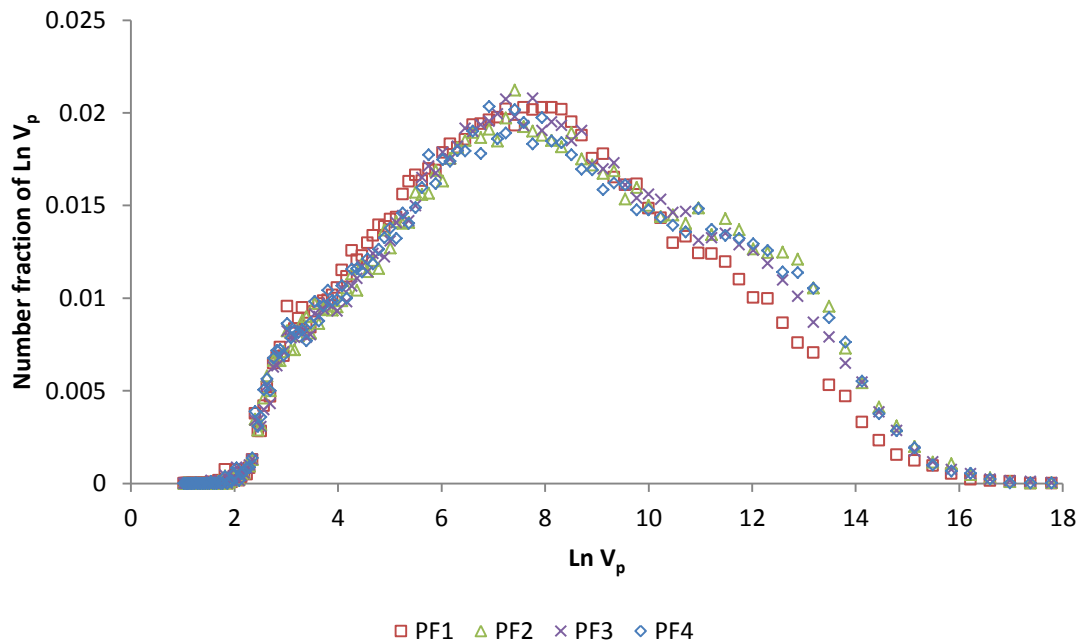


Figure 5-23: Results of a variability analysis for 4 separate measurements of PF samples of beta-glutamic acid (i.e. percolated at 47.2 L/h)

As is evident, the spread of data is not excessively large between the 4 samples. The largest deviations are represented by a single result in both cases; the 'LF1' and 'PF1' samples both display some disparity from the other 3 curves. Differences between these results are obviously reduced when mean data is taken into account as they effectively have only $\frac{1}{4}$ of the weight. Despite these 2 results however, the distributions display good agreement considering

the randomness of the sampling and therefore it can be concluded the individual samples are reproducible.

Taking the values of number fraction for each distribution and averaging them produces a mean result. The mean result is thus plot alongside the standard deviation for the 4 distributions in Figure 5-24, and distributions of the mean value + the standard deviation and the mean value – the standard deviation (i.e. 2 curves for each dataset) are plot in Figure 5-25.

Standard deviation for the curves is typically of the order of 10^{-5} - 10^{-4} for the low (2-6 $\text{Ln } V_p$) size ranges and rises to maximums of approximately 0.001 around the 12 $\text{Ln } V_p$ size ranges. This is expected as the low and medium size ranges are typically characterised by several thousand particles per bin, whilst the higher order sizes of the plot typically contain several hundred. The standard deviation is also skewed by the (*relatively* anomalous) LF1 and PF1 datasets.

Overall the result establishes an indication of the typical deviations to be encountered with measurement of size distribution. It does mean however, that distributions of pre and post-percolation size data should ideally be clearly separated from one-another in order to be sure of a statistically relevant result. This presents a problem; distributions in which the curves lie close to one-another are likely to indicate an inconclusive result statistically, yet these are expected for experiments performed under low levels of stress.

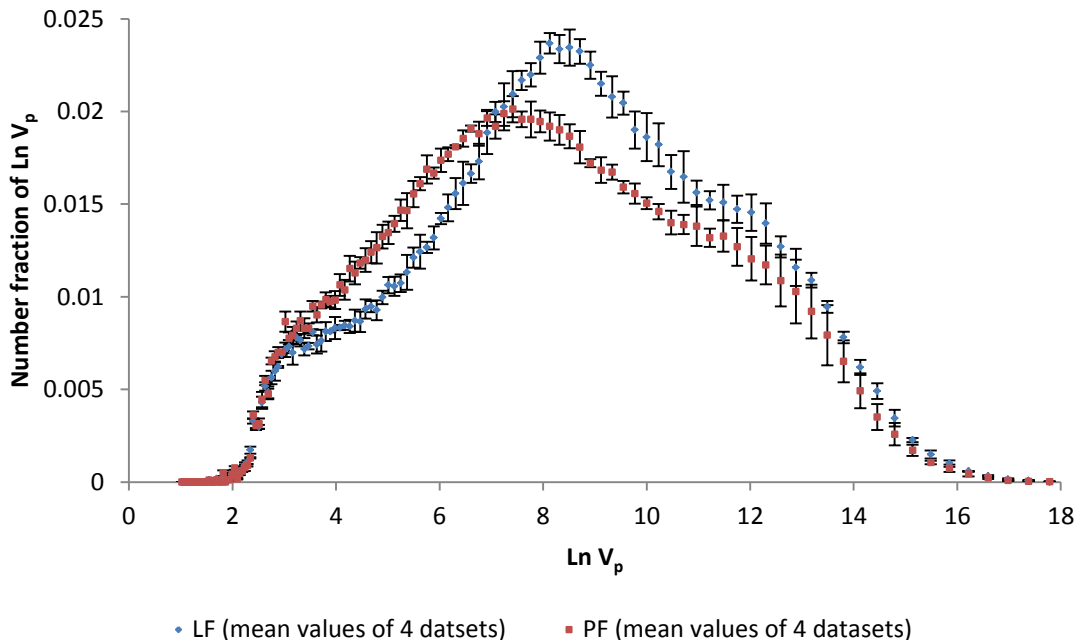


Figure 5-24: Mean values of number fraction of $\text{Ln } V_p$ for 4 separately measured samples with standard deviation; for beta-glutamic acid before and after percolation at 47.2 L/h. The ‘thickness’ of the distribution is therefore evident from the y-axis deviation in the results

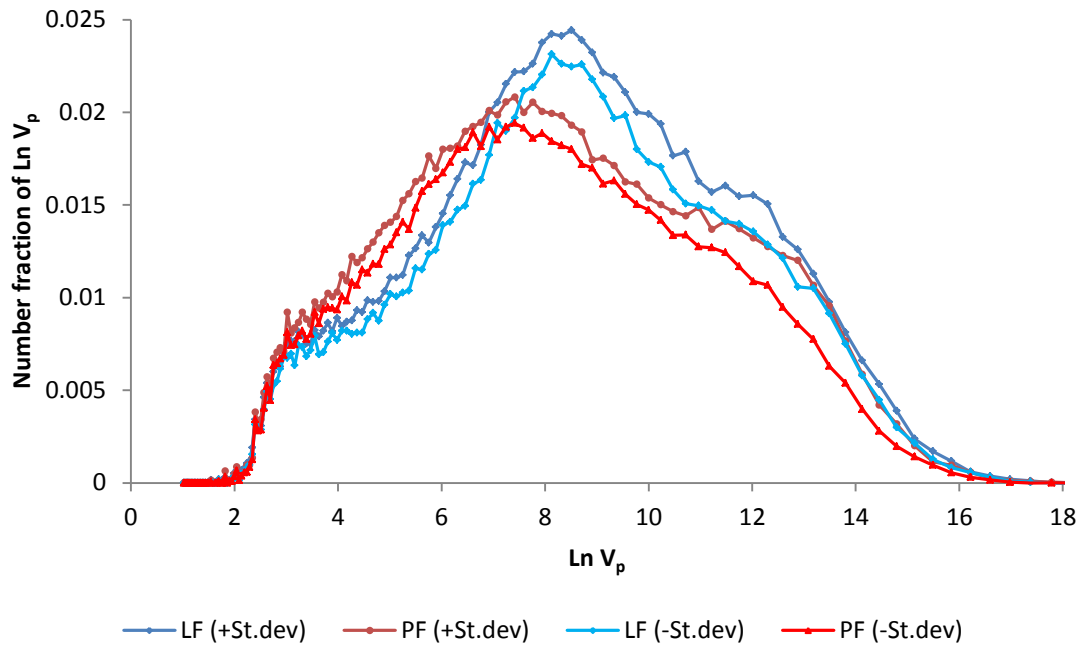


Figure 5-25: Curves of (mean value + standard deviation) and (mean value – standard deviation) for 4 separately measured samples of LF and PF powder samples of beta-glutamic acid before and after percolation at 47.2 L/h; number fraction vs. $\text{Ln } V_p$. Distribution ‘thickness’ is evident from the separation between each sample types’ curves

An alternative method of displaying the data is presented by re-thinking the way in which the measurements are conducted. If 4 measurements are considered as individual and separate, then theoretically any particle size analysis technique that counts a number of particles could be thought of as taking ($x \times$ numbers of measurements), where ‘ x ’ is a fraction of the total particles counted (e.g. in this case x is 0.25). For example a single laser diffraction sample might measure 1 million particles, but this is analogous to counting $10 \times$ samples of 100,000 particles each.

In this way, the 4 measurements obtained could actually be thought of as 4 fractions of the total sample – thus combining the 4 measurements provides a single sample with increased particle count (approx. 4 times the particle count). Thus the 4 LF and PF results examined previously are combined into a single dataset of approximately 120,000-200,000 particles and the results plot vs. the mean values as previously discussed.

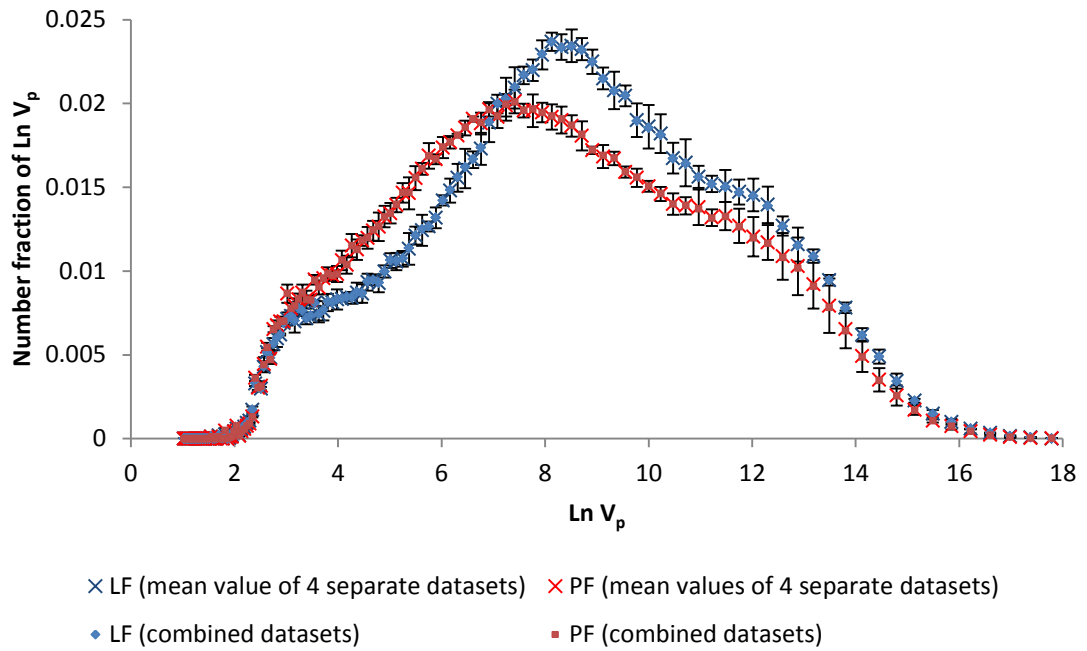


Figure 5-26: Mean values of $\text{Ln } V_p$ vs a single dataset containing all particles from samples 1-4 for each LF and PF sample set; for beta-glutamic acid before and after percolation at 47.2 L/h

The data in Figure 5-26 makes it evident that the differences to be encountered between assuming 4 separate measurements and a single dataset containing every particle within these 4 measurements are subtle. The minor changes to be noted are unfortunately so small that they are difficult to observe on the curve above; deviations around the values that display the largest standard deviations are noted however. Interestingly, this shows the combination result serves to dampen the effect of anomalous data; even if, again, the effect is minimal.

Overall the results show very good agreement, and even if no major changes are to be observed, the combination of particles into single datasets simplifies the data analysis process (which places high strain on the computer processor and memory due to the vast sizes of the datasets); thus the method is an acceptable one to carry forward to process the bulk of the experimental data.

5.5 Conclusions

The Morphologi G3 optical microscope is heavily employed in analysis due to its ability to gather detailed particle size properties from a vast number of particles. The instrument itself is still just a machine however; based on algorithms and lacking a human input, and like any analytical method it must be used with its limitations in mind.

The advantage of this instrument compared to other indiscriminate analysis methods is that the raw data is made available in full for human interpretation post-experiment (unlike e.g.

laser diffraction methods). This means that artefacts, non-particles, agglomerates, over/undersized particles etc. can be observed, criticised, removed, highlighted, given added weight etc. all based on the users preference and individual needs of their investigation; making it an incredibly powerful analytical tool.

Particle size distribution data has been extracted from the Morphologi G3 instrument and used to construct a series of differing size distribution representations. On the whole, size distributions generated from particle circle-equivalent diameters tend to minimise any differences between pre and post-stress sample changes; particularly the volume distribution.

A model is thus employed to make use of the measured particle length and width, in order to idealise particles as 3D cuboidal needles from their 2D projected areas, by assuming a particle height (that is a function of the particle width). The 'modelled volume' distributions depict a clearer picture of the changes in size occurring under percolation. Aspect ratio distributions also highlight the quite striking differences between the example data samples.

The validity of the data obtained is also critically analysed by deeper examination of the exact particle parameters measured by the Morphologi G3. It is found that a considerable number of touching, overlapping or 'non-particles' are scanned by the instrument. These can be removed from the measurement via filtering based on particle circularities and elongations; thereby increasing the relevancy of the result. This is a novel application of the Morphologi G3 data; many existing uses of the instrument in the literature do not critically assess the parameters obtained.

In addition to the data validation, an automated method of instrumenting the filtering is produced through the use of a scripted algorithm. The use of the automated software theoretically saves hundreds of hours of intensive labour if all datasets were to be manually filtered. Assessing and removing irregular particles by hand for a single dataset might take approx. 1-2 hours and the results would be subjective and inconsistent (and probably error-stricken!); multiply this by 4 datasets per sample; 2-4 samples per filtration...

Moving forward into experimental analysis, the modelled volume and aspect ratio distributions are to be used to characterise the particle size distributions of filter cake samples that have been subjected to pressure filtration/percolation; due to their superior ability to highlight changes. It is anticipated that changes in size distribution will at times be subtle (e.g. for low pressure/flowrate filtrations), hence it is important for the analysis method to distinguish between these subtle changes.

It should be noted however that these distributions could in fact be *over-estimating* changes in size distribution. There is nothing objective to show that these are the 'real' representations,

or that the CE diameter volume distribution isn't a true representation of the size changes (i.e. very few if any!). It is hoped however that evidence presented in the forthcoming chapter, that particle size reduction *is* occurring, will demonstrate these distributions to be the *truer* representations.

Chapter 6

6 Investigation into the Changes in Particle Size Distribution from Percolation of Liquid through a Packed Bed of Particles

6.1 Introduction

The aims of this section of work are to examine the changes in particle size distribution that occur during liquid filtration. This will be accomplished via the enactment of a new methodology to investigate the impact of continuous percolation through a bed of particles; the newly constructed continuous percolation rig (CPR).

As per the hypothesis, we propose that the stresses exerted on a bed of crystals subjected to percolation is expected to cause a certain amount of needle-shaped crystals to fracture. First and foremost it will be the aim to investigate whether this hypothesis is true, and if so, then what is the relationship between the levels of liquid flow/pressure on the corresponding crystal breakage.

Much of the analysis detailed in Chapter 5 is to be employed in determining the outcome of filtration on particle breakage.

Finally, as with any new methodologies, a conclusion on the validity of the percolation method will be sought. This is obtained through traditional batch filtration as a means of comparison, which in itself is a scaled-up experiment. Thus the ability to examine crystal breakage in particle beds using bench-top percolation is evaluated.

6.2 Use of the Continuous Percolation Rig to Investigate the Effects of Liquid Flowrate on Particle Size Reduction

6.2.1 Introduction

The objective of this section of work is to investigate the effect of liquid flow through particle beds; specifically how hydrodynamic stress impacts the particle size distribution of a filter cake. As we are interested in the effects of stress on particles, and not specifically in performing the most realistic filtration, the idea of a continuous percolation is proposed.

The proposal is simple; industrial filtrations typically last many hours (or days in extreme cases), during which the particles (typically fragile ones such as needles or plates) are subjected to stress. It is difficult to replicate these conditions in a small-scale laboratory test as lab-scale filtrations are typically completed in a few seconds (e.g. 5-60 seconds). Thus if a piece of equipment can subject a bed of particles to stress over a longer period of time then this has the ability to more realistically reproduce the conditions normally encountered in an industrial filtration.

The key premise is as follows: subject a bed of particles to a constant filtrate flow (hydrodynamic stress), keeping the particles 'wetted' in the process, and investigate the effects on the size and shape of the particles in the filter cake. Although of course many industrial filtrations are operated under constant pressure, it is envisioned that this test assumes a filtration that has approached the flow vs. time plateau, such that the bed has fully formed and flow rate with respect to time does not change.

The solution is a self-constructed rig in which a pump provides a controllable flow rate of liquor through the filter cake; the continuous percolation rig (CPR).

The system provides the capability of pumping up to approx. 160 L/hour of solvent through the 320 mL filter tube (filtration area of 962 mm²), in which the cake particles remain whilst the experiment is underway. A glass reservoir houses support for approximately 1 L of solvent, whilst a Julabo heater-chiller bath provides temperature control to the circulating liquid. A series of isolation valves also allow separate drying from a fume cupboard's N₂ supply.

The aim of the following experiments is to investigate the influence of fluid flow rate on the size reduction (if any) of the particles in the bed. A secondary aim (although technically inherent within the primary aim) is to evaluate the feasibility of the CPR itself; how effectively can the rig reproduce and/or simulate the findings of a 'real' filtration e.g. an industrial batch filtration. The findings here will be compared with those of the 2 Litre scale batch filtrations performed at AstraZeneca.

The case study compound utilised is that of the beta polymorph of glutamic acid. This needle-like crystal should provide an industrially relevant fragile crystal that is susceptible to particle breakage due to its morphology.

6.2.2 Data collection methods

For a full description of the methods and methodologies in use refer to the methodology section (Chapter 3). Particle sizing is performed by use of the Morphologi G3 optical microscope and software. Samples of 'lightly' filtered powder samples are obtained from a

post-crystallisation slurry, which is gently filtered under vacuum in a Buchner filter ('LF' sample). This provides the control sample for each experiment, such that the reference size distribution can be obtained. A sample that has been tested in the CPR ('PF' sample) provides the secondary size distribution from which conclusions about particle breakage can be inferred.

A temperature probe within the fluid reservoir provides a reading of solution temperature via a control interface written in Python; this enables the temperature of the solution to be monitored and controlled using the thermal jacket. The maintenance of solution temperature is essential when working with saturated solutions, particularly when subtle changes in size distribution are the target of investigations. Careful control is necessary to avoid temperature rising (could lead to dissolution/size reduction) or falling (could lead to particle growth/nucleation/size enlargement).

Fluid flow rate is controlled using the inverter (the pump speed control unit) frequency and calibrated such that flow rates are known (see Chapter 3). Pressure inside the system is read from a manual pressure gauge.

6.2.3 Results and discussion

6.2.3.1 Experimental outline

Experiments are labelled according to the pump inverter setting that they are operated under along with an alphabetic identifier (e.g. the 3rd experiment performed at 40 Hz is referred to as experiment '40c'). The pump inverter rating is directly tied to the flowrate and is more easily conveyed; hence this provides a simple and descriptive notation which is used henceforth to refer to individual experiments.

Peak pressures as measured by the pressure gauge are listed for posterity but during experimentation are subject to fluctuations and are thus often unreliable; hence these are to be used as an indication of approximate pressure and not taken as absolute. The flowrates listed have been calibrated and are reliable to a low standard deviation due to the reproducibility of the positive displacement pump.

Unless otherwise stated, experiments are conducted for a period of 1 hour at the peak flowrate i.e. this does not include time taken to ramp up to the peak rate. Crystallisations are all performed using water as the solvent. They are seeded with a number of seed batches; initial experiments were seeded using raw material (i.e. unprocessed material from the manufacturer) before 3 seed batches 'A', 'B' and 'C' were used for common experiments.

A full experiment using the maximum flowrate of 159.5 L/h, or a 50 Hz inverter setting, is only performed once due to the uncertainty of potential damage being suffered by the CPR (high flowrates exert strain on the rig structure). The experiment in this case (experiment 50a) is a pump calibration experiment in which the speed of the pump is ramped up to 159.5 L/h over the course of experimentation. Full flowrate is achieved for 20 minutes in which time sufficient calibration is obtained, after which the experiment is ended.

With these conditions in mind, the experimental information for the CPR is listed in Table 6-2; details on seeding material is listed in Table 6-1.

Table 6-1: Information on seed batches used for experimentation

Seed batch	Description
Raw material	As taken from supplier packaged bottle; used without further refinement
A	Ground seed taken from bulk solid from experiment '30a'
B	Ground seed taken from bulk solid from experiment '40b'
C	Ground seed taken from bulk solid from experiment '10a'
D	Ground seed taken from specifically crystallised batch of material (not experimented with); crystallised under same conditions as experimental material

Initially raw material is used to seed the batches for crystallisation. After the 1st round of experimentation, a ground batch of 'PF' material (dried material obtained from the crystals that are percolated within the CPR) is selected as the seed material for the next round of experimentation (seed 'A'), due to its favourable yield of glutamic acid shapes and sizes (from unreported crystallisations) when compared to raw material seed.

Once seed material of 'A' is empty a new batch of seed material is selected in a similar manner (B). However as this material produces unexpected variations in the final size distributions of the crystallised material, seed material is changed again to batch 'C'.

Experiments conducted off-site at AstraZeneca are performed with seed from a specially crystallised (i.e. a crystallisation not used for any filtration testing) batch of glutamic acid (seed 'D'). This seed material is also utilised for experimentation in the 2 L scale batch filter/dryer (section 6.3).

Table 6-2 lists the experiments conducted within the CPR, including the concentration of solid added to each crystallised slurry mass (the actual mass of solid within the CPR chamber is less than this and a function of the yield of the crystallisation – approximately 70%).

Table 6-2: Experiments performed with the percolation rig (500 mL crystallising solution volume)

Exp.	Crystallising Conc. (mg/ml)	Pump Inverter Hz	Max P (bar)	Flow-Rate (L/h)	Details
10a	40	10	0.5	31.1	Seeded with batch A
10b	40	10	0.2	31.1	Seeded with batch D
15a	25	15	1.5	47.2	Seeded with raw material
15b	40	15	0.8	47.2	Seeded with batch A
20a	40	20	1.2	63.2	Seeded with batch A
20b	40	20	1.0	63.2	Seeded with batch D
30a	25	30	3.5	95.3	Seeded with raw material
30b	40	30	4.2	95.3	Seeded with batch A
30c	40	30	1.6	95.3	Seeded with batch C
30d	40	30	2.0	95.3	Seeded with batch D
40a	25	40	5.5	127.5	Seeded with raw material
40b	40	40	2.0	127.5	Seeded with batch A
40c	40	40	4.2	127.5	Seeded with batch B; 5 minute percolation time
40d	40	40	4.5	127.5	Seeded with batch B; 2 hour percolation time
40e	40	40	2.5	127.5	Seeded with batch C
40f	40	40	3.0	127.5	Seeded with batch D
50a	40	50	4.0	159.5	Seeded with batch A; Pump calibration exp. - flowrate titrated from 31.1 - 159.5 L/h over 1h

6.2.3.2 Microscopic image analysis

Optical microscopy with the Morphologi G3 has resulted in a series of images which aim to characterise the difference between a crystal sample that has been stressed within the CPR and one that has not. As with any microscope image analysis, the inherent limitation is that the data is purely qualitative; not only is the material under the microscope a tiny fraction of the sample (itself a tiny fraction of the whole cake), but the images presented show an inherent bias of what the operator perceives as being important to display.

They do, however, present the advantage whereby a human can offer visual interpretation to a crystal sample where a computer algorithm can only think in terms of numbers i.e. certain agglomerates or particles resting on one another can be reasoned as such by a human. They also offer an opportunity to characterise any potential crystal breakage that is occurring before any numerical data is presented – this should lend weight to any future quantitative observations. The author has thus attempted to present a representative series of images that are believed to highlight the differences between the Buchner filtered (lightly vacuum filtered) and percolated (samples of crystals that were tested in the CPR). Unless otherwise stated, all data is acquired using a 5x zoom lens of the Morphologi G3 microscope, according to the methodology as described in Chapter 3.

Because it is impractical to display a representative series of images for each trial in this section of the thesis, a short comparative exhibition of 2 different experiments is presented – one performed with a low rate of percolation and one with a high rate of percolation.

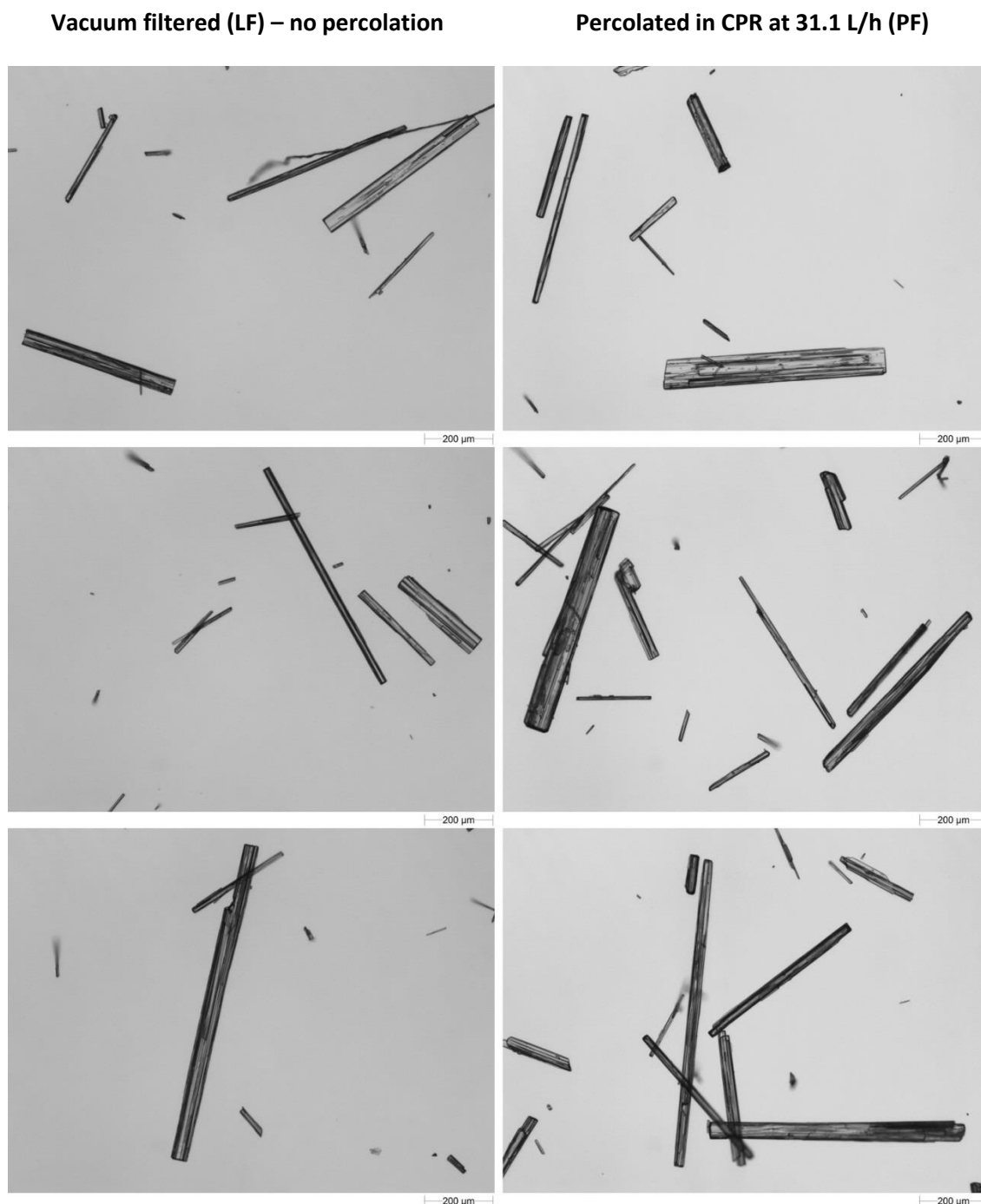


Figure 6-1: Microscopic images of beta-glutamic acid crystals before and after percolation at 31.1 L/h flow rate; left column: vacuum filtered samples (no percolation); right column: samples tested in CPR. Sample images obtained from experiment '10b' material. No significant difference is observed in the crystal morphology

Figure 6-1 depicts the outcome for a low flow rate percolation performed at 31.1 L/h. The crystals with and without subjection to percolation show few changes in their structure and elongation; the long needle shapes produced from the freshly crystallised material are also observed in the sample post-percolation.

There are several examples of what appear to be broken/fractured edges in the PF sample; however these are not the dominant crystal form in the images above and many long needles remain completely intact. Thus it can be concluded that the low flow rate percolation does not have a significant effect on the crystal morphology. An additional conclusion is drawn on the viability of the CPR itself – the action of transferring a batch of crystals into the rig and removing them (i.e. the ‘solids handling’ aspects of the experiment) evidently has little effect on the final morphology of the crystals. However in both cases quantitative data should be examined before firm conclusions are to be drawn.

The second examination is performed using a high flow rate percolation. This experiment is selected due to the additional data collected across the height of the solid cake, which is unique to this particular experiment. Hence in addition to the typical ‘LF’ and ‘PF’ samples being obtained, a sample from the top of the cake (‘PFT’) and from the bottom of the cake (‘PFB’), are also collected. The ‘PF’ sample is obtained in a random fashion from the bulk powder – the powder from the top and bottom of the cake is separated from the bulk powder before any sampling is performed; hence no overlap is assumed to occur between these height fractions.

The results of the microscopic image analysis are displayed in Figure 6-2 (LF and PF samples) and Figure 6-3 (PFT and PFB samples).

Major differences to note include the apparent density of particles across the image (great care is taken using the volumetric spatula to load an identical volume of sample for each sample dispersion); indicating that for similar sample volumes, the percolated sample volumes (PF, PFT, PFB) are more populated with fines (approx. <5-10 microns). Conversely, the ‘lightly’ filtered samples appear to have more free space between the particles, indicating an overall average larger particle size as fewer fines are evidently collected in the volumetric spatula (that determines the number of particles dispersed onto the microscope slide).

In addition to a general increase in the number of fines in the stressed samples, it is interesting to note the appearance of several larger, rectangular-shaped crystals (some examples of these are circled in red; Figure 6-2). These are of interest as it is known that glutamic acid will not usually grow into these shapes under normal circumstances – crystals will preferentially grow into long needles before thickening – hence it can be reasoned that these crystals were once much larger.

Comparing these rectangular crystals’ thicknesses to the long needle crystals observed in the LF sample (also circled) shows an apparent similarity in thickness. These ‘crystals’ in the

PF/PFT/PFB could be the fragmented remnants of particles as seen in a non-percolated sample. These crystal fragments are particularly evident in the PFB sample (Figure 6-3).

It is also interesting to note the 'sharp' and broken edges of many of the particles in the percolated samples (many of which are angled with respect to the normal of the crystals' lengths); which are largely absent from the LF sample. These also point to apparent breakage of needle-like crystals into 'stubbier' fragments. If present across the entire cake then this should be particularly evident in a large change in the aspect ratio distribution of the samples.

The differences across height of the percolated samples also point to variances in the extent of crystal breakage. It would be expected that particles at the top of the cake would suffer only from the force of liquid drag in the filter chamber, as few particles lie on top of these. Crystals at the bottom of the cake are also exposed to the weight of all particles stacked above them, hence are at risk of higher stresses. It would be expected that these would manifest as a greater likelihood of crystal breakage as the particles depth in the cake is increased.

It is therefore interesting to note the increased presence of small broken fragments in the PFB sample (and very few longer needles), and the presence of some longer needles still intact within the PFT sample (conversely with fewer broken fragments). This also seems to correlate with what is observed in the PF sample, where not quite as many fragments are observed as in the PFB, and not quite as many longer needles as in the PFT.

The evidence on the basis of the microscopic images therefore points to the breakage of the beta-glutamic acid needles into smaller, less elongated fragments. The extent of breakage seems to be heavily reliant on the flow rate of liquid passing through the static cake, and also somewhat reliant on the z-position (height) of the particle within the cake.

Vacuum filtered (LF) – no percolation

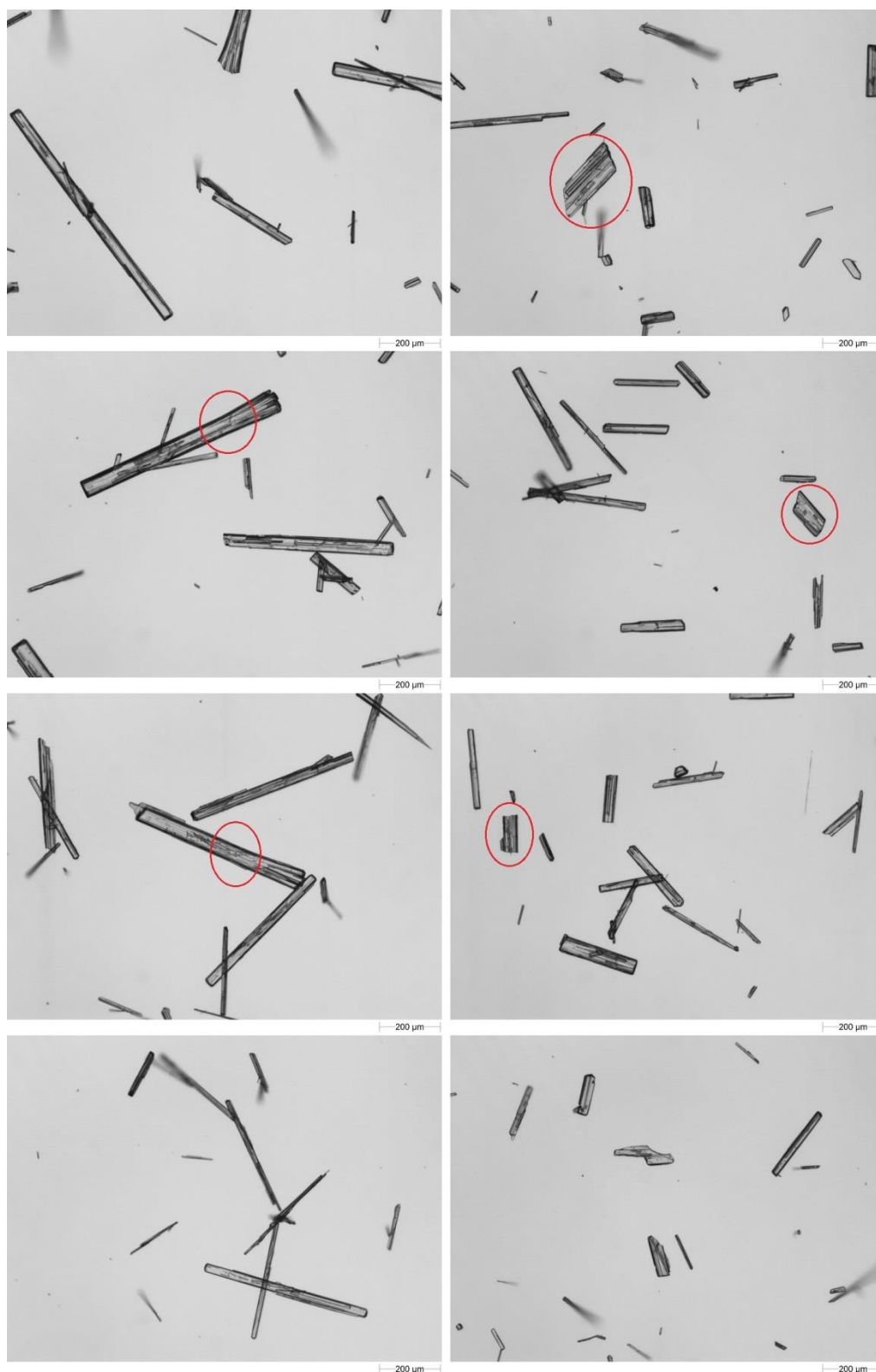
Percolated at 127.5 L/h – from **bulk** (PF)

Figure 6-2: Microscopic images of beta-glutamic acid crystals before and after percolation at 127.5 L/h flow rate; left column: vacuum filtered samples (no percolation); right column: samples percolated in CPR. Sample images obtained from experiment '40f' material. Significant changes in particle size are observed

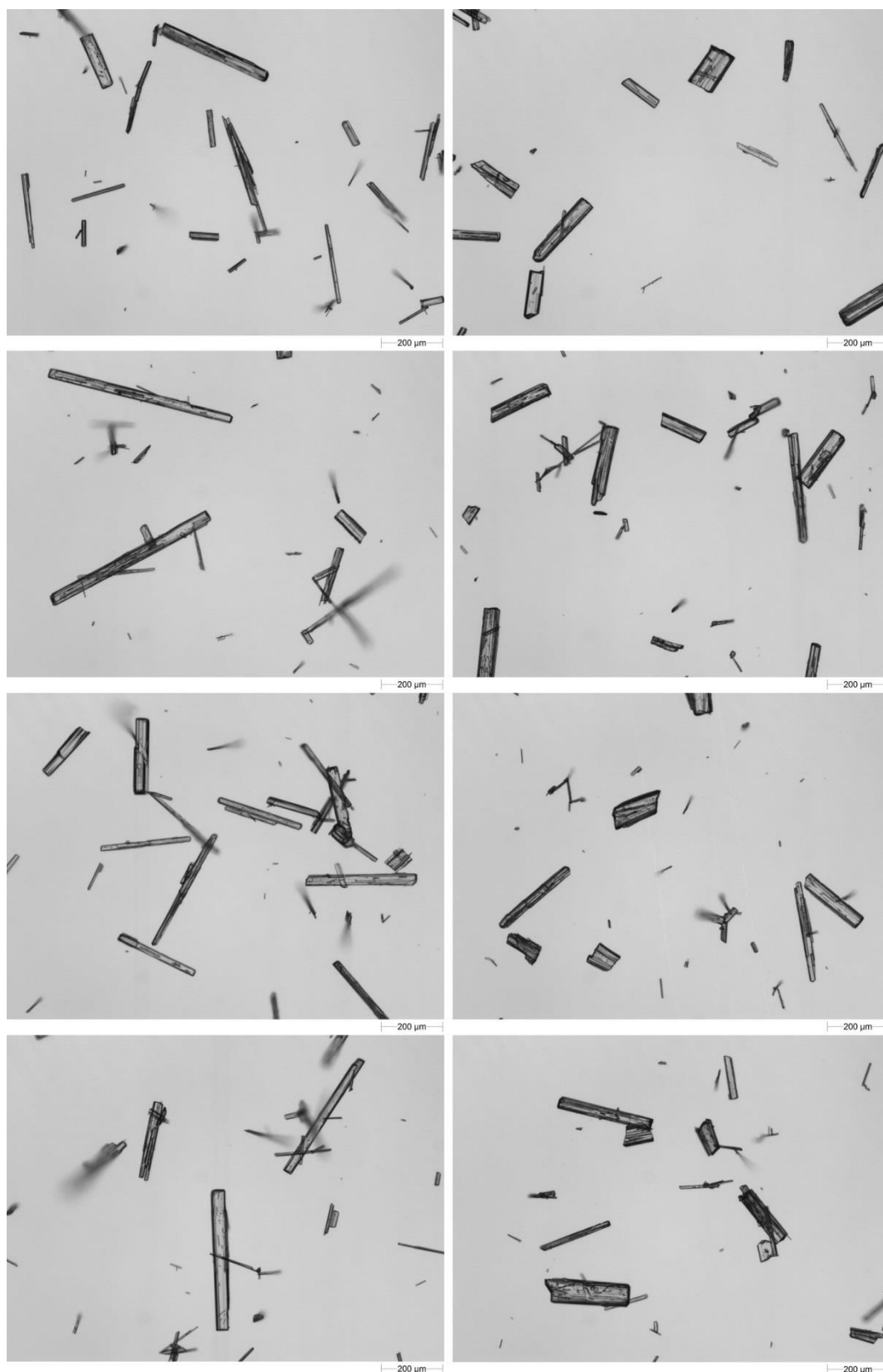
Percolated – from **top** of cake (PFT)Percolated – from **bottom** of cake (PFB)

Figure 6-3: Microscopic images of beta-glutamic acid crystals before and after percolation at 127.5 L/h flow rate; left column: samples tested in CPR from the TOP of the cake; right column: samples tested in CPR from the BOTTOM of the cake. Sample images obtained from experiment '40f' material. More breakage is evident in the PFB sample than in the PFT

6.2.3.3 Size and shape distribution analysis

Again, due to impracticalities with displaying a large numbers of graphs, 2 experiments are picked to highlight the process of analysis of the size distribution data. Following on from the microscopic analysis, experiment 10b is selected to highlight a low flowrate example, with experiment 40f chosen to represent a high flowrate dataset.

Morphologi G3 data is assembled into distributions based on the modelled volume of particles (calculated from particle length and width), with additional distributions generated from the number fractions of aspect ratios. The methodologies for the production of these distributions are described in Chapter 5.

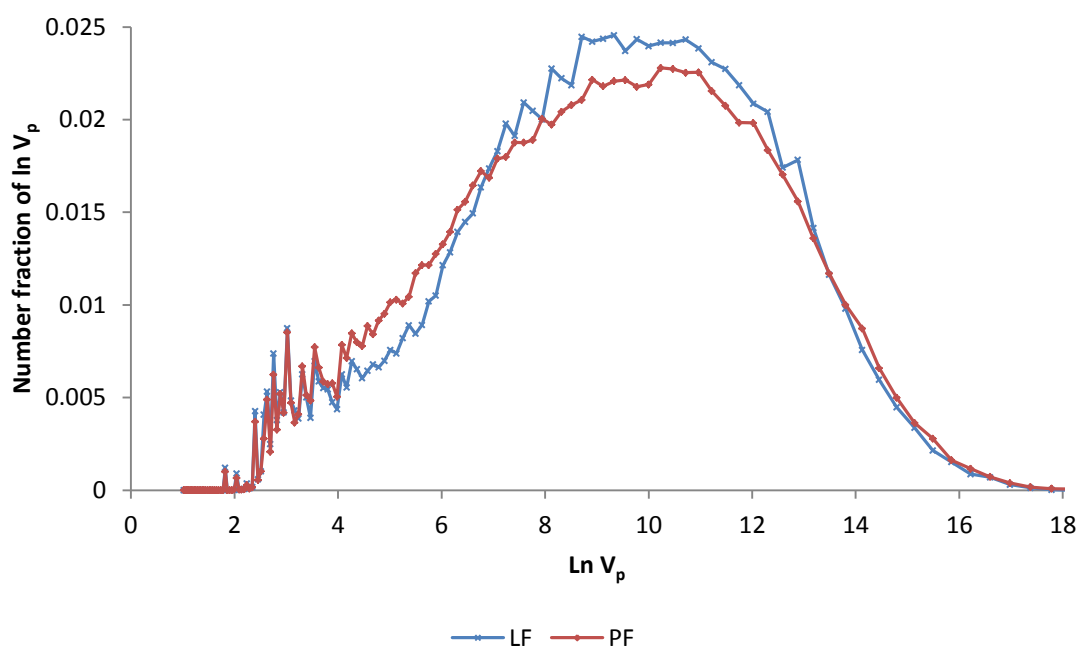


Figure 6-4: $l_p \cdot 0.5 \cdot w_p^2$ distribution for 31.1 L/h percolation of beta-glutamic acid (exp. 10b)

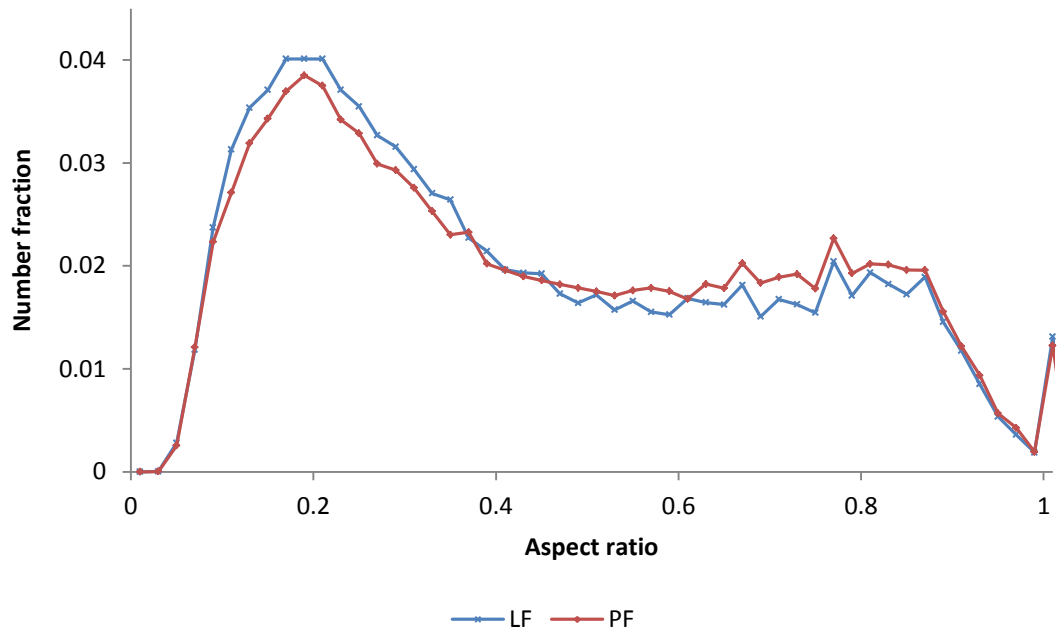


Figure 6-5: Aspect ratio distribution for 31.1 L/h percolation of beta-glutamic acid (exp. 10b)

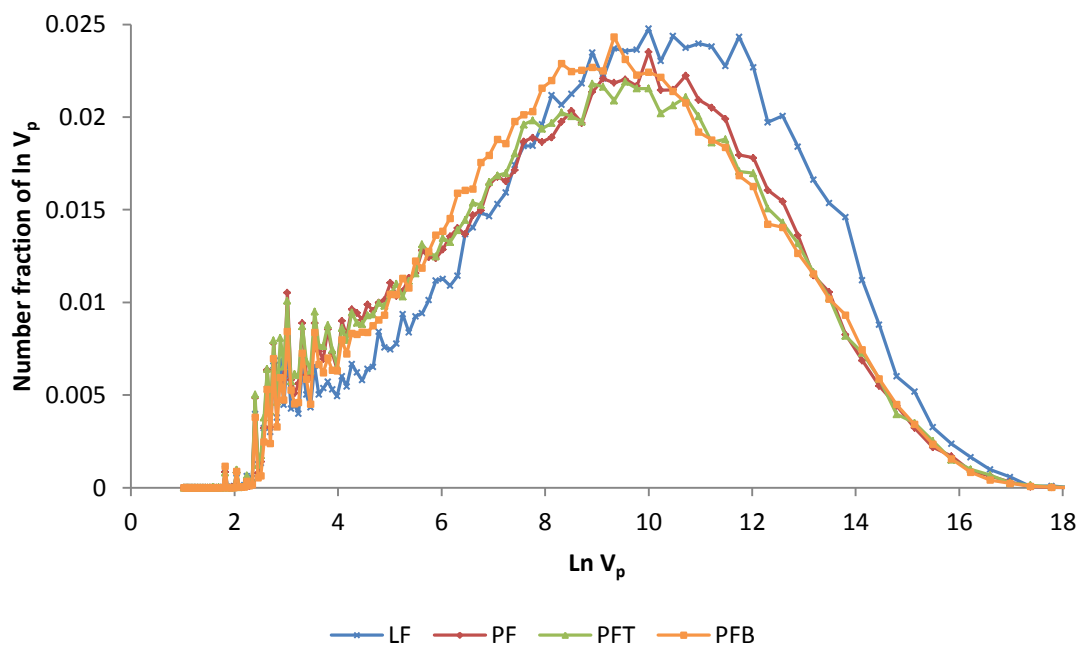


Figure 6-6: $l_p \cdot 0.5 \cdot w_p^2$ distribution for 127.5 L/h percolation of beta-glutamic acid (exp. 40f)

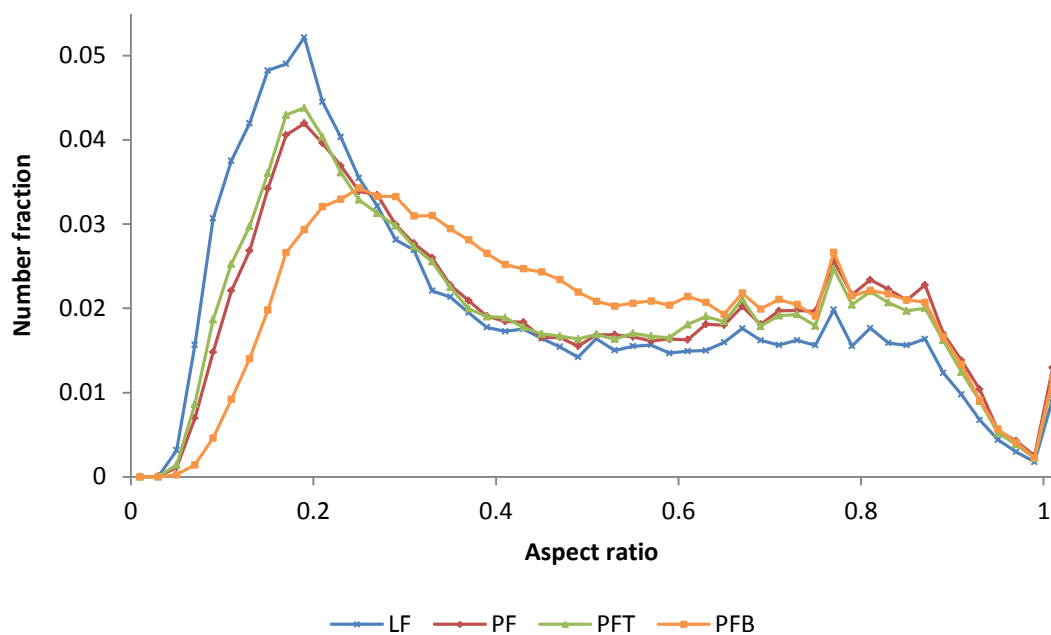


Figure 6-7: Aspect ratio distribution for 127.5 L/h percolation of beta-glutamic acid (exp. 40f)

Figure 6-4 and Figure 6-5 depict the distributions for the low flowrate percolation. As previously observed, microscopic analysis failed to highlight any significant changes between samples but the quantitative analysis depicts a subtle change in particle size distribution.

The modelled volume of particles does appear to point to a slightly reduced fraction of medium-sized particles (between approx. $7-13 \ln V_p$) under percolation, and an apparent manifestation of this is an increased fraction of small particles ($< 7 \ln V_p$). However the distributions are otherwise closely matched, particularly in the region of the largest particles.

Differences in the distribution of aspect ratios (Figure 6-5) also highlight the minimal change imparted to the crystals from percolation. Interestingly, there are few reductions observed with the most elongated particles (aspect ratio < 0.1) which would be expected to be the most likely to suffer breakage. A small change in the fraction of particles in the range of $0.1 - 0.3$ aspect ratio is evident; however the reduction is small e.g. when compared to reductions observed at higher flow rates (Figure 6-7).

Figure 6-6 displays the particle volume distribution for the higher flowrate percolation of 127.5 L/h. When compared to the data from the low rate percolation, the difference in size reduction from LF to PF (of any height fraction) is greatly increased. This is particularly evident in the medium-large size ranges ($> 10 V_p$).

The modelled particle volume of the post-percolation samples does not appear to be strongly dependent on bed height. Distributions from samples from the top, bottom and bulk all display similar size.

The limitations of this type of distribution are thus apparent when compared to the aspect ratio distribution (Figure 6-7), which displays a dramatic difference between the PF/PFT/PFB height fractions (in addition to the LF sample). The vacuum filtered LF sample is observed to have the most elongated particles as a fraction of the whole, with the PFT and PF displaying similar aspect ratios. The particles at the bottom of the cake (PFB) have suffered a significant reduction in their elongation compared to the other powder samples.

These observations are largely consistent with those evaluated from microscopic analysis, meaning it is highly likely that the cause of size reduction in the percolated samples can be attributed to the breakage of crystals. It is also evident that the level of breakage in the filter is related to the position of the particle within the bed; where particles in the bottom of the cake are more likely to undergo fracture than those in the remaining bulk.

An interesting point of note is the difference in the way the size distributions change at high and low flowrates. At a low flowrate, the majority of the change in size distribution (admittedly with reference to a smaller overall change) occurs in the medium and small sized particle ranges, whilst the most elongated crystals remain largely present in the post-percolation sample. Experimentation at high flow causes a major change in modelled volume in the large particle size range (in addition to the medium size range), whilst the fraction of highly elongated crystals (< 0.1 aspect ratio) reduces when percolating.

This could suggest that the mechanism by which breakage occurs at lower flowrates tends to favour the breakage of smaller (volume) particles. The very largest particles are by definition large due to their product of length and width; it is possible that the increased width/height of many of these particles provides them with additional resistance to fracture.

At higher flowrates the crystal breakage appears less dependent on particle size, with all sizes suffering losses due to the increased stresses present.

The observed changes in particle size can be envisioned by depicting the distributions as probability density functions and generating normalised curves to model the density functions. The underlying assumption is that the particle distributions are composed of a number of separate distributions, i.e. a distribution of small particles, a distribution of medium and a distribution of large particles. Therefore when the model curve is generated it is the sum of the

3 individual curves and thus shares characteristics of the 3 constituent curves; this is evident from the 3 peaks within these curves (see Figure 6-8 and Figure 6-9).

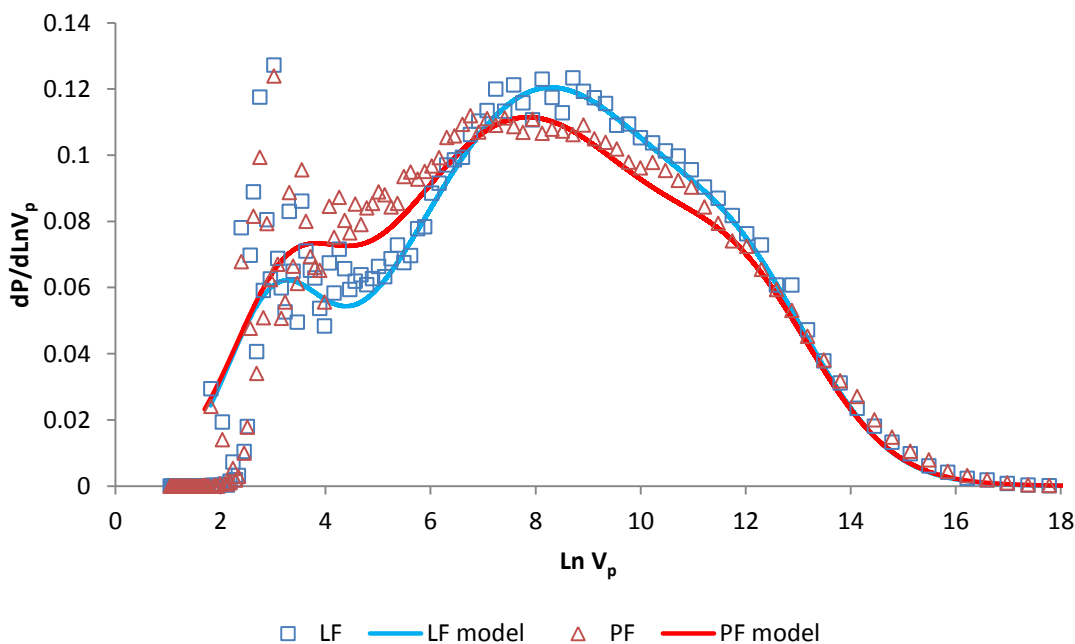


Figure 6-8: Normalised modelled particle volume changes at percolation flow of 31.1 L/h (exp. 10b)

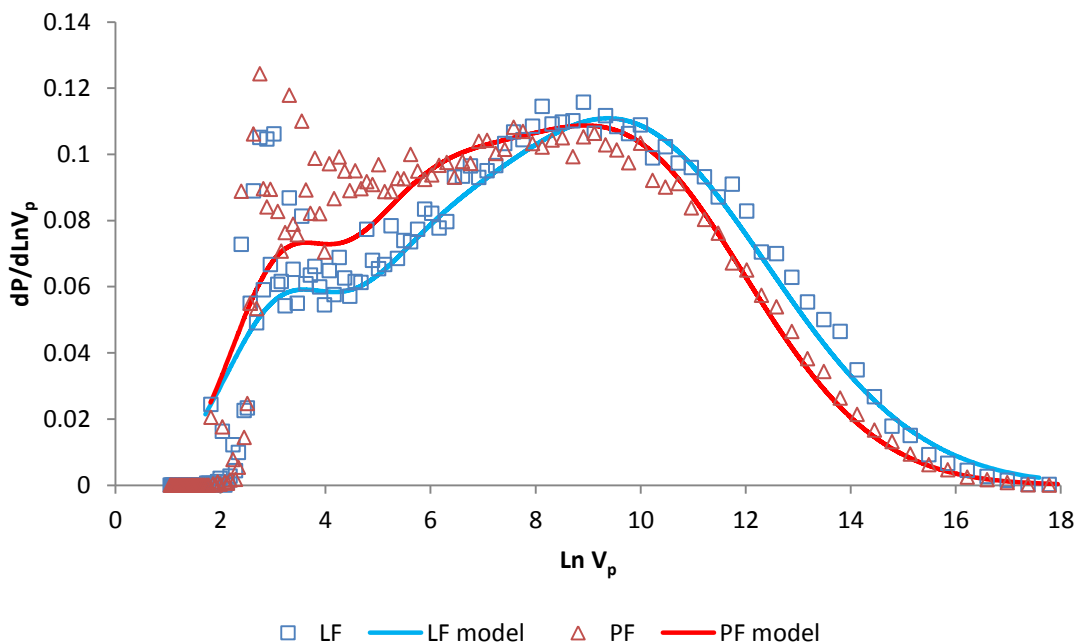


Figure 6-9: Normalised modelled particle volume changes at percolation flow of 127.5 L/h (exp. 40f)

Generating an optimal fit for the curves is somewhat of a balance; particularly within the low size regions ($<4 \ln V_p$) e.g. raising the probability of encountering a particle at $3 \ln V_p$ reduces the probability of encountering particles of $4-5 \ln V_p$. Overall the modelled curves show good

agreement for the experimental data and serve to highlight the changes in size distribution occurring under percolation.

6.2.3.4 Change in size and shape distribution across fluid flow rate

To examine the effects of percolation as a function of flowrate, the changes in size distribution can be examined by definition of the arbitrary fractions f_s , f_m and f_L referring to the fraction of small, medium and large particles, respectively. For the modelled volume distribution, the fraction of small particles is defined as those with particle volume less than $5 \ln V_p$ (5.011 to be precise). The fraction of large particles are defined by those larger than $10 \ln V_p$, whilst the 'medium' sized particles consist of those between these 2 defined values.

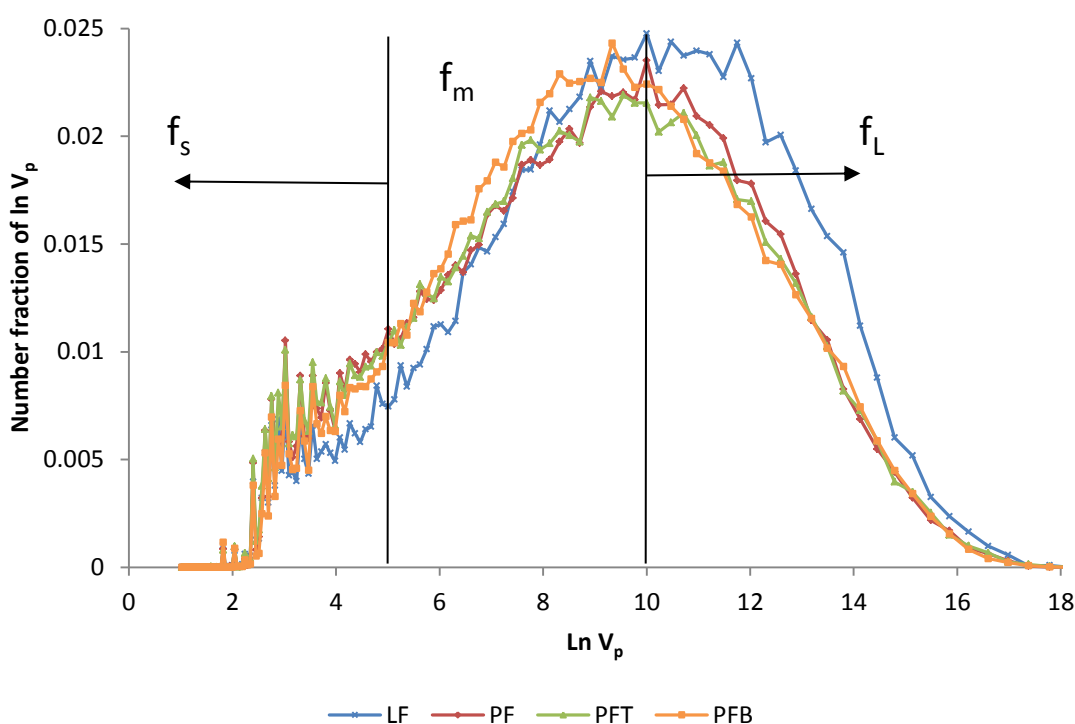


Figure 6-10: Graphical depictions of the fractions by which the particle modelled volume size distributions are divided by

It is idealised that the 'medium' sized particles are defined as roughly 50% of the distribution (i.e. 50% of the calculated volume of the powder sample resides in this arbitrary fraction). In any particular dataset, this therefore leaves the remaining 50% of particles to be defined as either 'large' or 'small'. The limits of 5.011 and $10 \ln V_p$ are found to fit this definition relatively satisfactorily (and are also precise bracket definitions within the spreadsheet).

As has been previously discussed (section 6.2.3.3), the assumed volume of particles can sometimes fail to highlight large changes in aspect ratio of the powder samples. For this reason the datasets are also examined by definition of 3 shape factor parameters; f_e , f_p and f_r , the

fraction 'elongated', 'prismatic' and 'rounded' particles respectively. In a similar manner to the size fractions, these shape fractions are also technically arbitrarily defined; but it is the opinion of the author that these fractions represent key areas of the distribution in which changes are likely to manifest.

The fraction 'elongated' is therefore defined as the fraction of particles with aspect ratio less than 0.21. The fraction 'rounded' consist of any particles with aspect ratio greater than 0.51, leaving the fraction 'prismatic' as any particle between these 2 limits. The result is an approximate 30:40:30 fractional split for a typical number distribution.

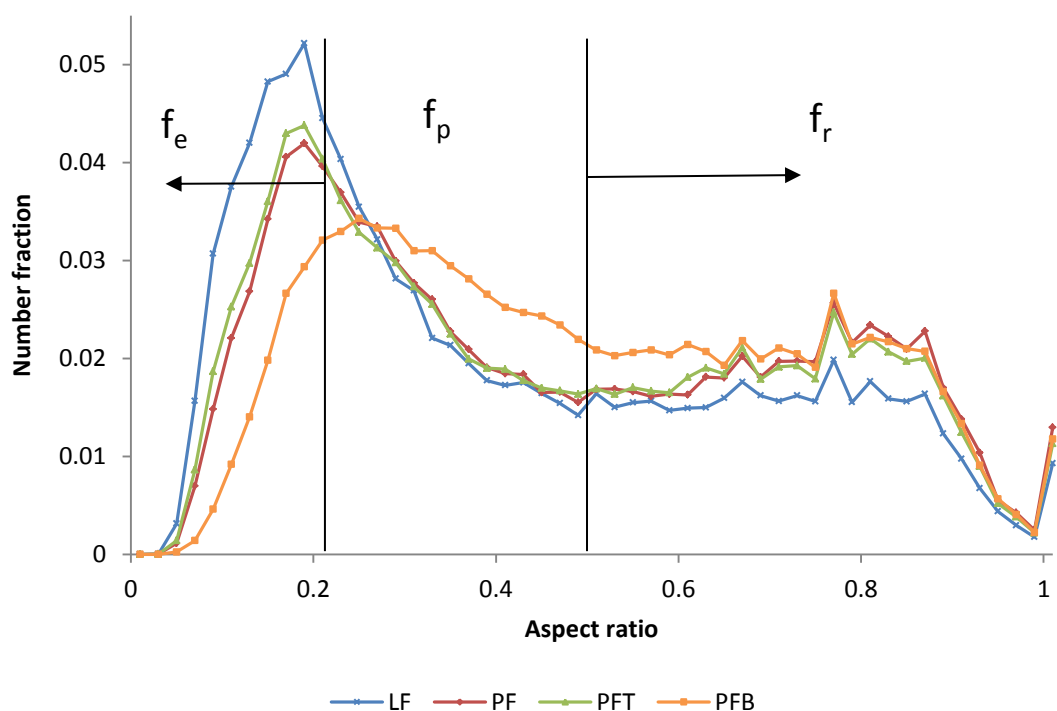


Figure 6-11: Graphical depictions of the fractions by which the aspect ratio size distributions are divided by

Although a particle just within the lower limit of f_r (i.e. its width is roughly half its length) could still be defined as an elongated crystal in most circumstances, many of the changes occurring in the aspect ratio distributions tend to manifest within the highly elongated ranges (between 0 – 0.3 aspect ratio; e.g. see Figure 6-7). Large fractions of the particles also exist with aspect ratio < 0.3 (as evidenced by the tall peaks). As such it is the author's opinion that these ranges should benefit from higher scrutiny.

Cumulative particle fractions are generated with respect to the LF and PF powder samples and the differentials in fractional contents calculated. The results are displayed in Table 6-3 and plot as a function of percolation flowrate in Figure 6-12.

The respective calculation is performed for the differentials in shape fractions of aspect ratio distribution and the results depicted in

Table 6-4 and Figure 6-13. The respective datasets are plot with mean and standard deviation in Figure 6-14 and Figure 6-15.

Table 6-3: Changes in size fractions f_s , f_m and f_L for LF and PF powder samples tested in the CPR across flowrates 31.1 – 159.5 L/h

Exp.	Flowrate (L/h)	LF			PF			$\Delta f = f_{LF} - f_{PF}$		
		f_s	f_m	f_L	f_s	f_m	f_L	Δf_s	Δf_m	Δf_L
10a	31.1	0.3257	0.5150	0.1592	0.3148	0.5395	0.1458	-0.0109	0.0245	-0.0134
10b	31.1	0.1770	0.5197	0.3033	0.1960	0.5142	0.2898	0.0190	-0.0055	-0.0135
15a	47.2	0.4161	0.4849	0.0989	0.4319	0.5035	0.0646	0.0158	0.0186	-0.0343
15b	47.2	0.2462	0.5411	0.2127	0.2929	0.5287	0.1785	0.0467	-0.0124	-0.0342
20a	63.2	0.2447	0.5269	0.2284	0.2437	0.5462	0.2101	-0.0010	0.0193	-0.0183
20b	63.2	0.1399	0.5336	0.3265	0.2090	0.5136	0.2775	0.0691	-0.0200	-0.0490
30a	95.3	0.3500	0.5003	0.1497	0.4110	0.5011	0.0879	0.0610	0.0008	-0.0618
30b	95.3	0.3475	0.4787	0.1738	0.3166	0.5371	0.1463	-0.0309	0.0584	-0.0275
30c	95.3	0.2899	0.4694	0.2407	0.2730	0.4881	0.2389	-0.0169	0.0187	-0.0018
30d	95.3	0.2159	0.4335	0.3506	0.2254	0.4981	0.2764	0.0095	0.0646	-0.0742
40a	127.5	0.3567	0.4573	0.1860	0.3790	0.5203	0.1007	0.0223	0.0630	-0.0853
40b	127.5	0.2248	0.4798	0.2955	0.2757	0.4883	0.2360	0.0509	0.0085	-0.0595
40c	127.5	0.2765	0.4703	0.2531	0.2639	0.5468	0.1893	-0.0126	0.0765	-0.0638
40d	127.5	0.2296	0.4905	0.2799	0.2307	0.5437	0.2256	0.0011	0.0532	-0.0543
40e	127.5	0.2876	0.4569	0.2555	0.2819	0.4869	0.2312	-0.0057	0.0300	-0.0243
40f	127.5	0.1787	0.4876	0.3336	0.2370	0.4995	0.2635	0.0583	0.0119	-0.0701
50a	159.5	0.2637	0.4459	0.2905	0.2849	0.5202	0.1949	0.0212	0.0743	-0.0956

Table 6-4: Changes in shape fractions f_e , f_p and f_r for LF and PF powder samples tested in the CPR across flowrates 31.1 – 159.5 L/h

Exp.	Flowrate (L/h)	LF			PF			$\Delta f = f_{LF} - f_{PF}$		
		f_e	f_p	f_r	f_e	f_p	f_r	Δf_e	Δf_p	Δf_r
10a	31.1	0.3402	0.4081	0.2517	0.3086	0.4124	0.2790	-0.0316	0.0043	0.0273
10b	31.1	0.2626	0.3730	0.3645	0.2433	0.3565	0.4003	-0.0193	-0.0165	0.0358
15a	47.2	0.2149	0.5033	0.2817	0.2038	0.5168	0.2794	-0.0111	0.0135	-0.0023
15b	47.2	0.3265	0.3893	0.2842	0.2598	0.3912	0.3470	-0.0667	0.0019	0.0628
20a	63.2	0.3618	0.4031	0.2352	0.3591	0.4120	0.2289	-0.0027	0.0089	-0.0063
20b	63.2	0.3058	0.3649	0.3293	0.2314	0.3611	0.4075	-0.0744	-0.0038	0.0782
30a	95.3	0.2912	0.5039	0.2049	0.2604	0.5018	0.2378	-0.0308	-0.0021	0.0329
30b	95.3	0.3567	0.4006	0.2427	0.2837	0.4344	0.2818	-0.0730	0.0338	0.0391
30c	95.3	0.4010	0.3666	0.2324	0.3588	0.3827	0.2585	-0.0422	0.0161	0.0261
30d	95.3	0.2851	0.3132	0.4012	0.2388	0.3460	0.4152	-0.0463	0.0328	0.0140
40a	127.5	0.2799	0.4850	0.2350	0.2616	0.4984	0.2400	-0.0183	0.0134	0.0050
40b	127.5	0.3497	0.3588	0.2915	0.2633	0.3964	0.3403	-0.0864	0.0376	0.0488
40c	127.5	0.3147	0.4169	0.2684	0.2158	0.4556	0.3286	-0.0989	0.0387	0.0602
40d	127.5	0.2680	0.4197	0.3123	0.2197	0.4256	0.3546	-0.0483	0.0059	0.0423
40e	127.5	0.4471	0.3533	0.1996	0.3529	0.3916	0.2555	-0.0942	0.0383	0.0559
40f	127.5	0.3230	0.3409	0.3360	0.2282	0.3530	0.4189	-0.0948	0.0121	0.0829
50a	159.5	0.4086	0.3289	0.2625	0.2071	0.4194	0.3735	-0.2015	0.0905	0.1110

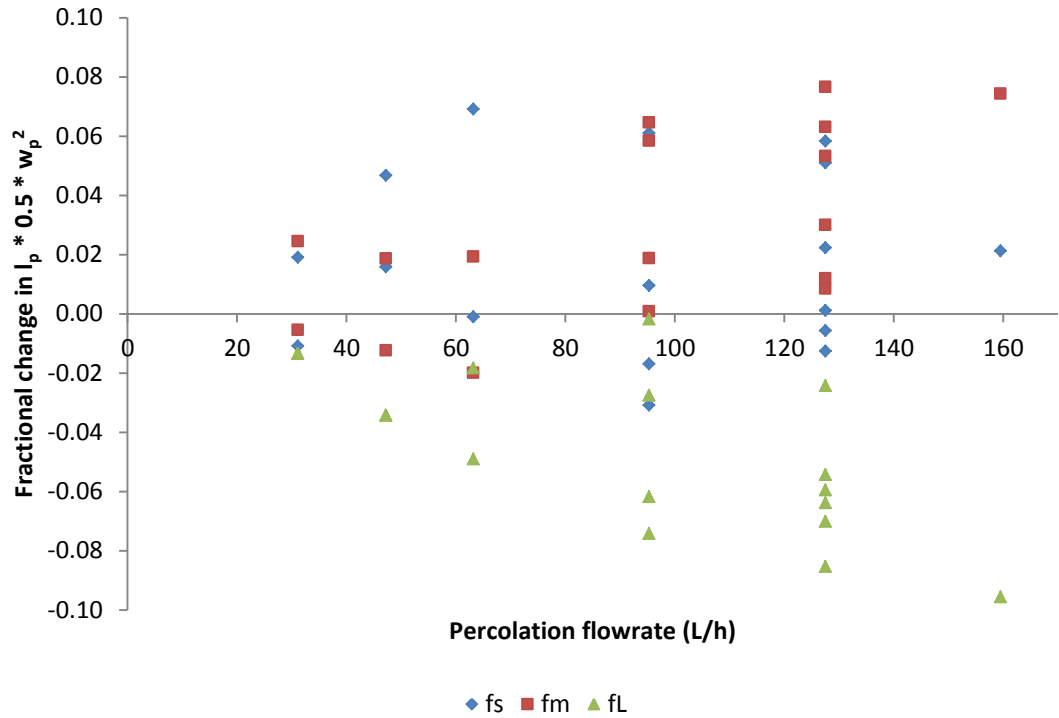


Figure 6-12: Changes in size fractions of modelled particle volume as a function of CPR flowrate, for beta-glutamic acid with and without percolation

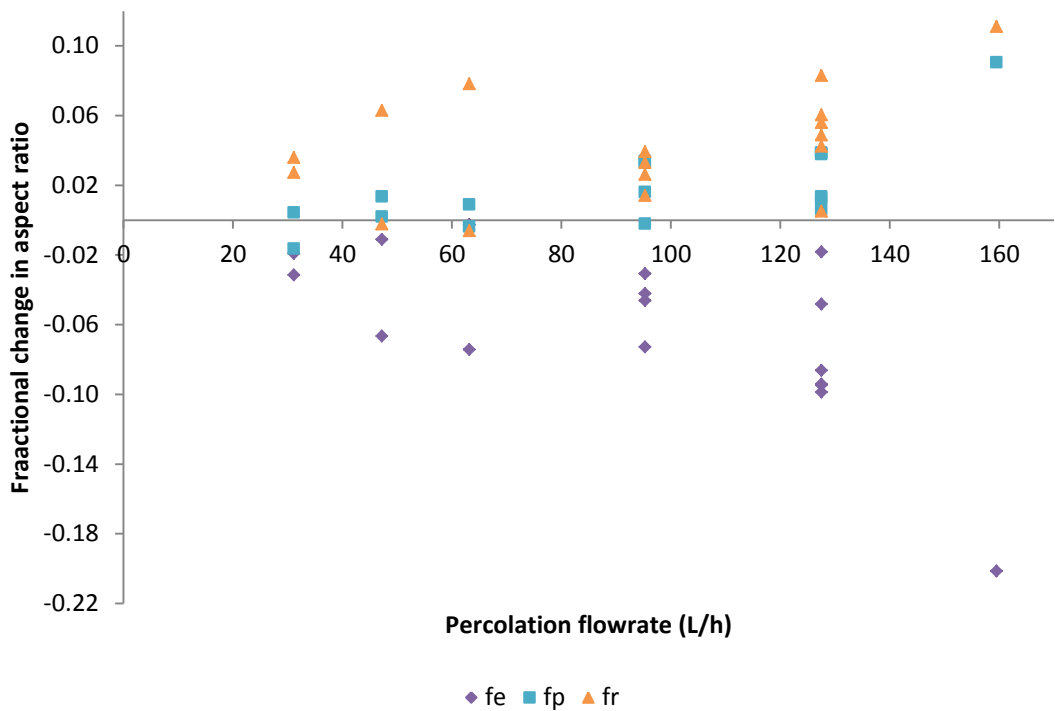


Figure 6-13: Changes in shape fractions of aspect ratio as a function of CPR flowrate, for beta-glutamic acid with and without percolation

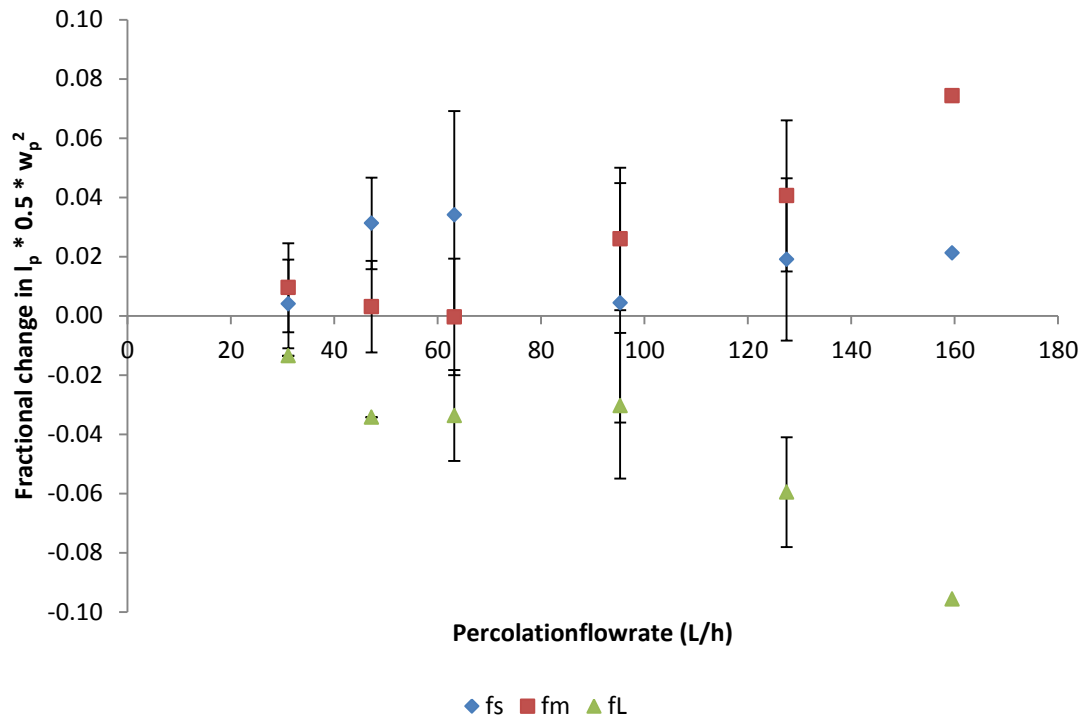


Figure 6-14: Mean changes in size fractions as a function of fluid flowrate, for beta-glutamic acid with and without percolation. Error bars represent standard deviation

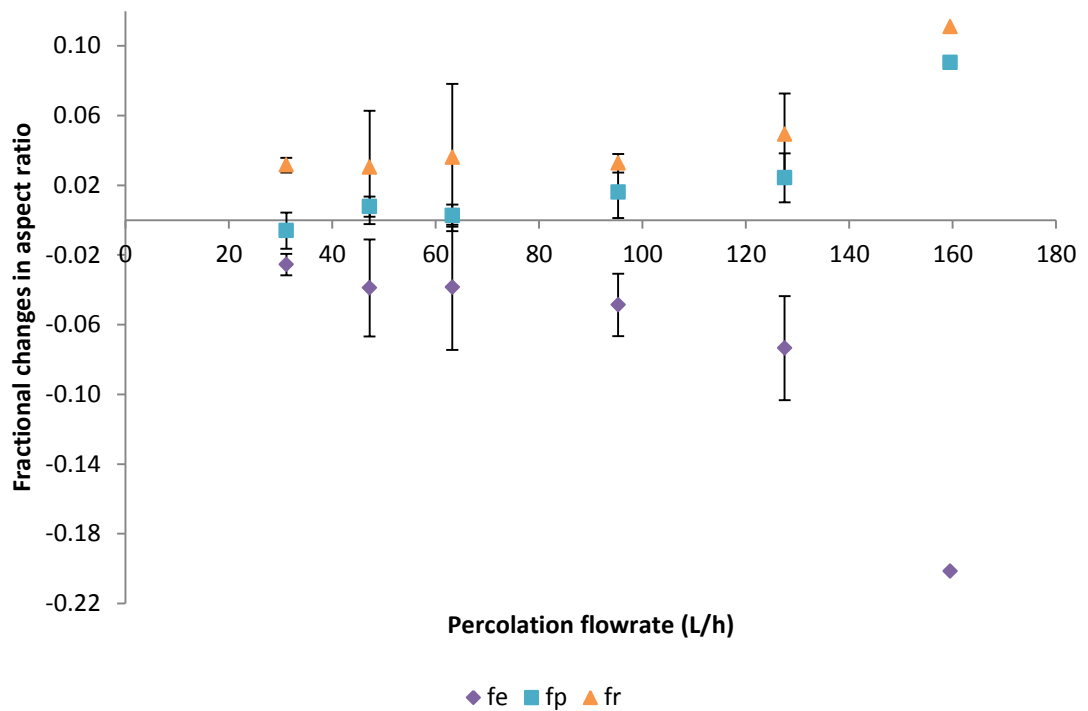


Figure 6-15: Mean changes in aspect ratio fractions as a function of fluid flowrate, for beta-glutamic acid with and without percolation. Error bars represent standard deviation

6.2.3.4.1 Analysis of size changes due to flowrate

Despite some anomalous data the trend overall is one of increasing size reduction and decreasing particle elongation with increasing flowrate; depicted by the plots in Figure 6-14 and Figure 6-15. The modelled particle length * width data suggest the largest particles reduce in fraction at an increasing rate as fluid flow rises; the result of this is an increase in the fractions of small and medium sized volume particles. On the whole the fraction of 'medium' sized particles grows at a greater rate than that of the 'small' particles.

The changes observed in sample aspect ratio also display a dependence on fluid flowrate, with an increasing percolation tied to a greater reduction in the fraction of elongated particles. Concurrently the fractions of prismatic and rounded particles rise with increasing flow. The fraction of rounded particles rises to a greater extent, indicating that the 'prismatic' crystals also suffer from breakage (which is not unexpected as these particles still display considerable ratios of width:length).

The reductions of the largest particles into predominantly medium sized particles, along with the general reductions in particle elongation lends weight to the proposed breakage mechanism; long, needle-like particles cleaving into fragments. This is in opposition to e.g. a crushing or total fracture mechanism or attritional breakage, in which the generation of a considerable portion of fines ('small' particles) would be expected.

It is not completely unexpected that some fines would be produced by a cleavage mechanism and as such the increase in fractions of small particles across all flowrates is a confirmation of this.

The analysis of fines however is subject to considerable uncertainty with the Morphologi G3; it is not uncommon to detect e.g. particles of dust that come to rest on the glass slide as being 'particles' in the distribution. As such it is better practice to lend more weight to the changes occurring with larger particles.

Looking further into the trends of the reductions in size and aspect ratio with increasing flowrate, it is evident that critical points exist in the data (these are highlighted with dotted lines in Figure 6-16); points at which breakage events appear to be occurring.

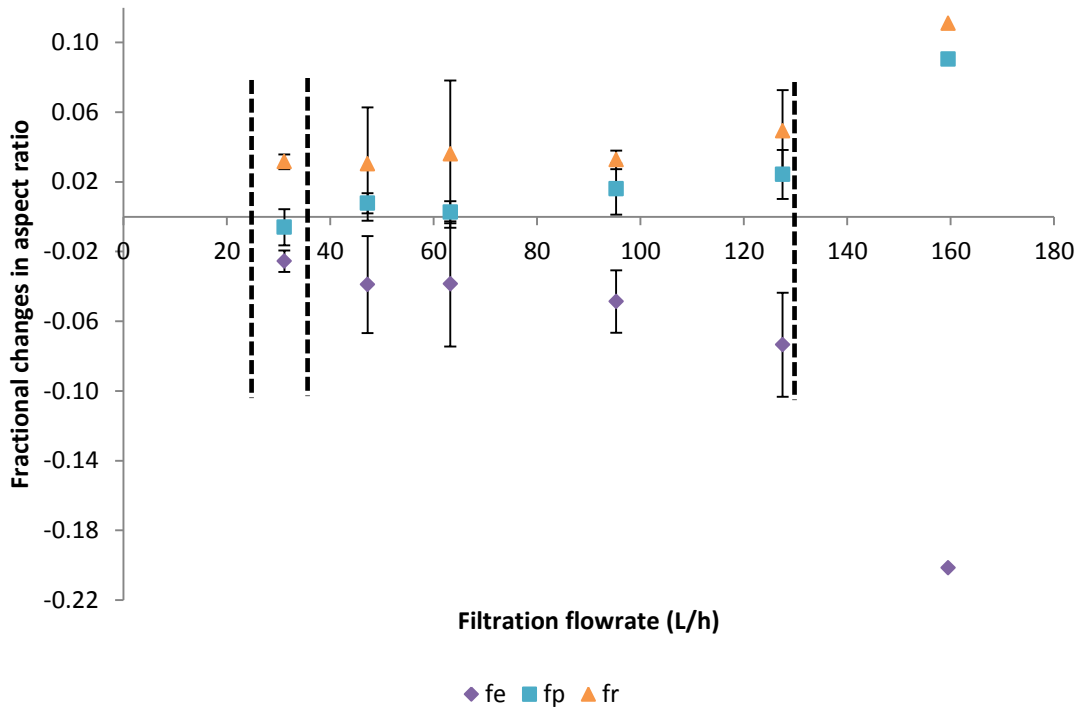


Figure 6-16: Critical points in the breakage of particles under percolation

At a point approximately equal to or before 30 L/h flowrate a small amount of primary breakage is evident; roughly 2% reductions are observed for both elongated and large particles. At a flowrate on or before 40 L/h another critical point is observed, and the level of size/elongation reduction jumps again to 5/6%. These initial critical points represent the initial stages of primary breakage, in which the particles most susceptible to breakage are likely to fracture i.e. the largest and most elongated particles.

Beyond this point, interestingly the reductions in the fraction of elongated particles are approximately constant. Reductions in the fractions of large particles are largely constant but with a mild linear trend. This signifies the point at which further breakage of particles is minimal; longer needles have largely been broken into smaller fragments, which we assume have higher resistances to breakage, thus the stagnation in reductions of elongated particles reflects this.

Between a flowrate of approximately 95 – 127 L/h another critical point is reached; at this point the reductions in the largest and most elongated particles jumps once more as a response to new breakage events. The particles now breaking are those with slightly higher resistances to breakage; taller/thicker particles and those of smaller dimensions.

As many of the largest particles are presumed to have broken already, this explains the greater reductions in elongated particles (20%) when compared to reductions in the large particles (10%); the compressive forces experienced are now high enough to break smaller needles with

breakage strengths. It is also possible that many of these smaller needles are existing particle fragments that have already suffered a fracture event, having undergone a period of reorganisation/movement within the bed as they broke.

6.2.3.4.2 Critical analysis of experimental methods and discussion of error

As is additionally evident from the data in Figure 6-12 and Figure 6-13 are that there is some considerable scatter with the data; this highlights the general inconsistency with the method. There are a number of factors that could have led to the spread in size/aspect ratio changes, particularly for higher flowrate percolations. These include poor experimental practice and sampling methods, of which are to be expected of the CPR method in its infancy.

The major problem concerns the transfer of material from the crystallising vessel into the filter tube, of which at present is a manual handling operation in which crystal material (separated from the mother liquor) is literally 'spooned' into the filter tube. This presents the possibility that material could suffer from breakage due to physical handling. It is possible that in future an automated method of transferring material (without it having to pass through the pump, of which it is inadvisable to pass larger particles through and which could cause damage itself) could be implemented into the rig.

An additional cause for concern is that agglomeration during drying. The nature of needle-like powder samples causes inter-twining of particles as they build filter cakes and thus come to rest in this state. During drying the evaporation of liquid bridging particles together can cause additional material to precipitate out, bonding particles together in weak networks.

Combined with the need to be gentle when handling the dried samples (to avoid causing breakage) it is possible that weakly bonded particles remain as agglomerates and are imaged as thus (as again the need to avoid possible breakage necessitates the use of low dispersion pressures e.g. with the Morphologi G3 to disperse particles for imaging). Filtering of particle data is likely to remove such agglomerates from the final result however, but the problem cannot be entirely eliminated if particle agglomerates coalesce into 'normal' looking particles (see Chapter 5).

A further problem relates to the identified heating effect of the diaphragm pump. The possibility that heating of the saturated solution could lead to dissolution seems to have been largely subdued by the addition of heat exchange methods (and as evidenced by the low flowrate percolations which tend to display similar pre/post experimental size distributions). However the possibility remains of local points of over/under cooling affecting the final result.

6.2.3.5 Effect of continuous percolation time on size distribution

As part of a brief examination into the effects of percolation time the results of a short, 5 minute percolation are compared with that of a 2 hour percolation. Both experiments are run at identical flowrates (127.5 L/h) and with similarly crystallised beta-glutamic acid material (i.e. both generated from the same seed batch). The modelled volume and aspect ratio distributions are displayed in the Figures below.

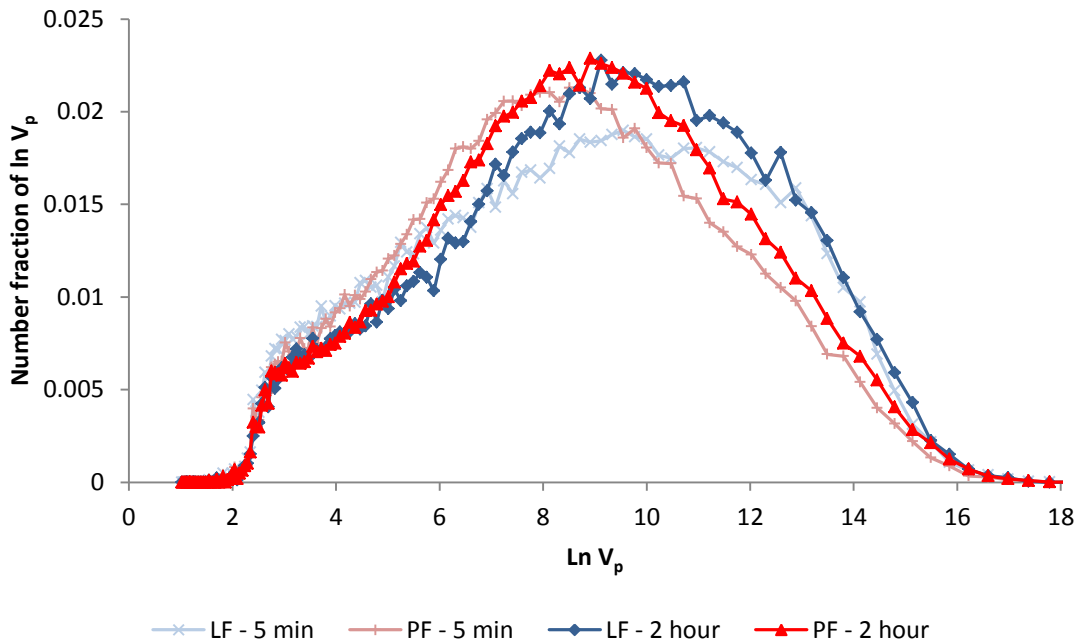


Figure 6-17: $I_p \cdot 0.5 \cdot w_p^2$ distribution for 127.5 L/h percolation of β -glutamic acid (exps. 40c and 40d)

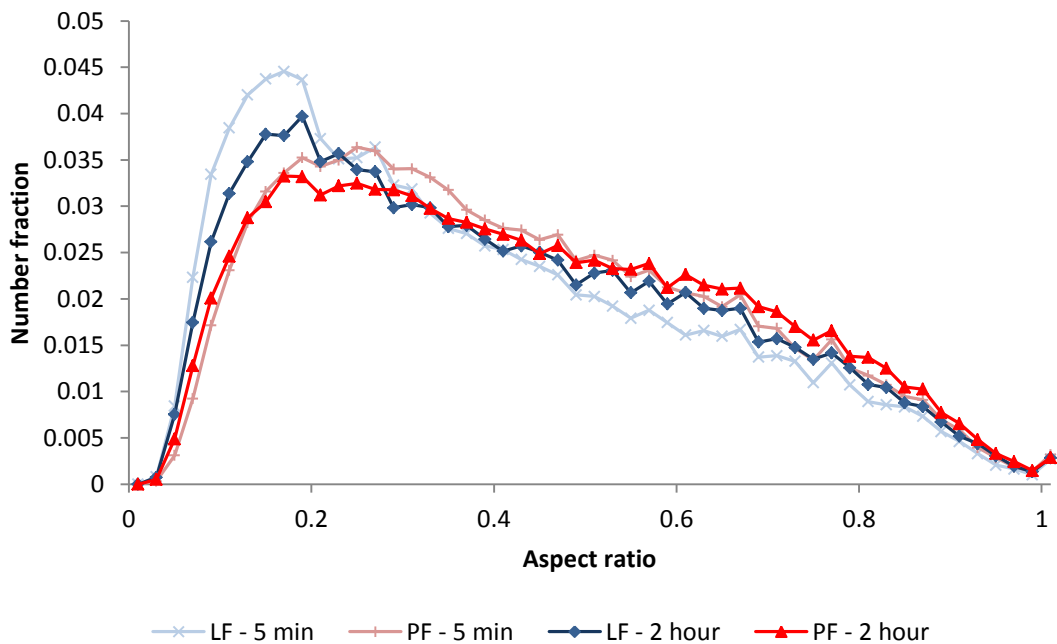


Figure 6-18: Aspect ratio distribution for 127.5 L/h percolation of β -glutamic acid (exps. 40c and 40d)

The results highlight the significant variation that is sometimes encountered when crystallising from solution; the respective vacuum filtered batches each display somewhat differing levels of size and aspect ratio distributions. Data is in fact already available in Table 6-3 and

Table 6-4:

Table 6-5: Changes in size and aspect ratio fractions for exps. 40c and 40d

Exp.	Duration	Δf_s	Δf_m	Δf_L	Δf_e	Δf_p	Δf_r
40c	5 mins	-0.0126	0.0765	-0.0638	-0.0989	0.0387	0.0602
40d	2 hours	0.0011	0.0532	-0.0543	-0.0483	0.0059	0.0423
Mean for 127.5 L/h		0.0191	0.0405	-0.0596	-0.0735	0.0243	0.0492

Post-percolation distributions are typically linked to the parent distribution, meaning the short percolation has experienced greater relative changes in size compared to the longer percolation, which can be seen from Table 6-5.

It is difficult to draw any firm conclusions as this is the result of only 2 experiments, both of which are subject to individual variation; however the lack of significantly higher than average size reduction in the 2 hour percolation combined with the significant reduction also observed in only 5 minutes of percolation points towards a time-independent process.

If such a statistically significant extent of crystal breakage is encountered in a 5 minute process it would suggest that breakage is enacted during the initial cake consolidation phase when the force of pressure is first levelled onto the particles. Evidently the stress imparted has little additive effect when applied for an additional 1 or 2 hours, thereby pointing to the fact that when stable and in equilibrium, little breakage is observed in the particle beds. Only critical points at which the force of pressure rises beyond the bed limit result in breakage; the bed then re-organises as new, more resistant, particle contacts are made and no further breakage is observed.

These findings agree with those of Cornehl et al who found that it is the peak pressure applied, not the duration of which it is applied for, that influences the extent of crystal breakage[10].

6.3 Batch Filtrations of Crystal Suspensions on a 2 Litre Scale

6.3.1 Introduction

The 2 litre scale pressure filter/dryer (8 cm filter diameter), situated at AstraZeneca's Macclesfield research and development site, provides a basis for conducting a study into the batch performance of crystal size reduction under filtration. The filter/dryer unit itself is a scaled-down replica of a pilot plant sized filter/dryer, also situated at the same site in

Macclesfield. Consequently, the interior geometry and vessel internals closely match those of existing industrial equipment, and therefore should provide relevant data on the filtration performance of industrial crystallisations.



Figure 6-19: The 2 L scale pressure filter/dryer

The filter unit is supplied with nitrogen via a pressure regulator. Although the pilot plant scale unit is limited to 1.6 bar of filtration pressure (due to safety), the 2 litre unit is capable of higher pressure differentials. The filter chamber is pressurised to a specific level with the regulator controlling this; during filtration the pressure is maintained at a constant level, thus resulting in a constant pressure filtration.

In addition to providing the driving force for filtration, the ability to pass nitrogen through the filter unit also aids in drying of the cake. A built-in pressure gauge gives an indication (albeit an analogue one) of the pressure inside the vessel, whilst a sight glass allows for visual inspection of the inner contents.

Material is charged into the filter via a $\frac{1}{2}$ " PTFE tube by vacuum.

The equipment also houses a pitched-blade impeller with z-axis control, allowing it to be raised and lowered in/out of the filter cake. As the focus of experimentation is on the breakage due to filtration, any additional disturbance of the cake is likely to affect the result; hence agitation

will not be employed at any stage of filtration/drying. Additionally, the vessel is equipped with a thermal jacket to aid drying, but this option is seen as surplus to requirements, as nitrogen alone is capable of drying the crystals sufficiently; hence will also not be employed.

A Hastelloy C22 finish on all surfaces exposed to chemical contamination and seals fabricated from PTFE yield excellent all-round chemical resistance.

The aim of this experimental trial will be that of data validation. The construction and operation of the continuous percolation system may have raised some scepticism with regards to its applicability to real industrial processes; this trial into traditional batch filtration aims to provide corroborating evidence of particle size reduction, and bring added validity to the CPR with regards to its industrial applicability.

The case study molecules that will be studied include the alpha and beta polymorphs of glutamic acid and the AstraZeneca compound Lesinurad (Zurampictm; for the treatment of gout). This will yield the opportunity to investigate the filtration behaviours of 3 compounds of differing size and morphology; specifically how the morphology influences particle size reduction, filtration rate and cake compressibility.

6.3.2 Data collection methods

The full SOP for the operation of the filter/dryer equipment can be found in the methodology section (see Chapter 3). Data on particle size is collected from 4 powder samples per each experiment that are taken in the form of a vacuum filtered sample ('LF' – i.e. a sample that is not filtered under excessive stress/pressure filtered), a sample from the top of the cake ('PFT'), from the bottom of the cake ('PFB') and from the remaining bulk of the pressure filtered sample ('PF').

Data on the filtrate flow rate is collected in the form of mass per unit time, as read by a Mettler-Toledo PG-S3000 analytical balance. Mass/time data is read with a Python script that returns a reading approximately every 0.12 seconds. This is an improvement over the existing software which yields a data point every 4 seconds. For filtrations that can complete in ~10-20 seconds, this is a significant increase in the output of data, and a therefore a considerable escalation in the volume of data is achieved (which helps to increase the accuracy of the calculated filter/cake resistance, which are identified from the mass/time data). Data is output in the form of a '.txt' file, which can be imported into a spreadsheet for further analysis.

Additional data collected include the filtration pressure in bar gauge, the cake height and mass (which therefore allows calculation of cake volume and bulk density) and the filtrate mass and volume.

Particle sizing is performed using the HELOS Sympatec laser diffraction measurement technique; the full SOP of which is described in Chapter 3. The use of an alternative particle size analysis technique will help to provide an alternative data source to the Morphologi G3. In addition, the sample masses (approx. 50 – 200 mg) used per measurement are far higher than those used by the G3 (approx. 11 mm³ or 3 mg per sample); the Sympatec taking in several hundred thousand–millions of particles as opposed to 10,000 – 50,000 with the G3. Thus the data obtained will be statistically significant.

Analogous to the use of batch filtrations to validate the performance of the percolation rig, laser diffraction provides a completely different method by which particles are imaged. Corroboration on this front will help to alleviate any potential bias in the methods of analysis provided by the Morphologi G3.

6.3.3 Calculation of filter resistances

Knowledge of the filtrate flow in volume per unit time can be plot as a linear trend to calculate the cake and filter medium resistances; from the gradient and y-intercept respectively. For a constant pressure filtration, the integrated filtration equation is[125]:

$$\frac{t}{V} = \frac{\alpha \cdot \mu \cdot K_m}{2A^2 \cdot \Delta P} \cdot V + \frac{\beta_m \mu}{A \Delta P} \quad \text{Equation 6-1}$$

Where α represents the filter cake resistance and β_m the filter medium resistance. K_m is a concentration factor representing the ratio of the mass of particles in the filter cake over the total volume of filtrate (i.e. a density). Taking the above equation in the form of 'y = m.x + c' and substituting yields:

$$\frac{t}{V} = m \cdot V + c \quad \text{Equation 6-2}$$

Hence the values of cake and medium resistance can be calculated from:

$$\alpha = m \frac{2A^2 \cdot \Delta P}{\mu \cdot K_m} \quad \text{Equation 6-3}$$

$$\beta_m = c \frac{A \cdot \Delta P}{\mu} \quad \text{Equation 6-4}$$

The resistance of the cake is a function of the ease of which liquid is able to pass through. A porous cake with many pores and channels to allow liquid droplets to pass through offers little resistance to flow. Conversely, tightly packed cakes with fewer routes for liquid to flow through provide high resistances to flow.

At the beginning of filtration i.e. where (theoretically) no particles are present on the filter medium to offer resistance to flow, the cake mass (represented above by the term ' K_m ') is assumed to be 0, hence the equation for the filter medium resistance is obtained.

For each experiment the final collected filtrate is weighed and the volume recorded using a measuring cylinder; this yields the filtrate density. Knowledge of the density allows translation of the recorded mass vs time data into volume vs time of collected filtrate. By plotting the volume collected against time, a plot typical of the following is produced:

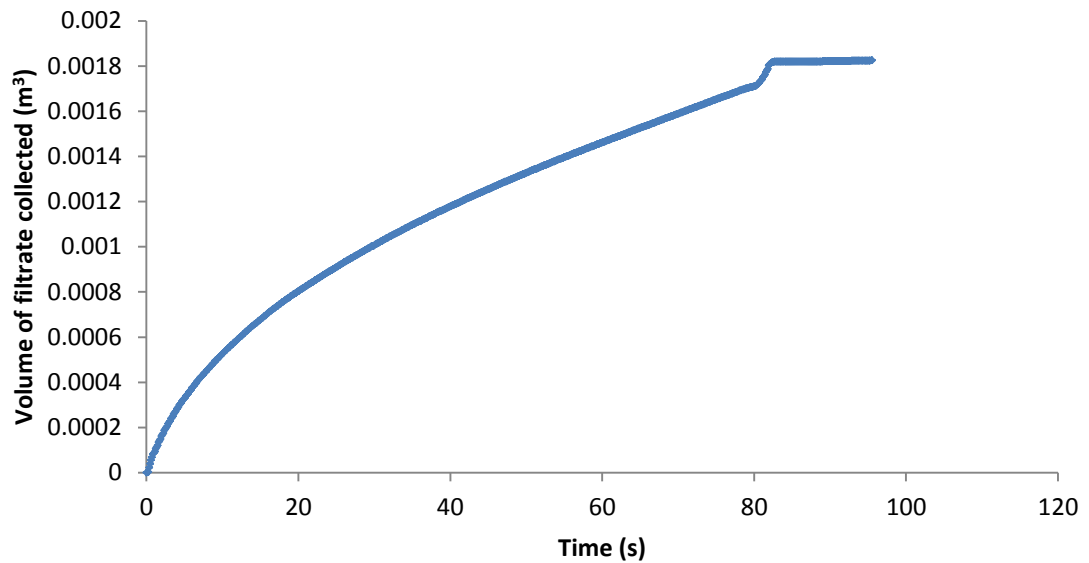


Figure 6-20: Plot of filtrate flow out of the 2 Litre pressure filter over time for Lesinurad at 1.6 bar pressure

The curve in the plot indicates a change in rate over time, and will be discussed later. The small upward jump in the plot (around 80 seconds) indicates the end of filtration, where the small volume of liquid remaining is ejected from the filter at high velocity, leading to a plateau in volume collected. To establish a trend akin to that predicted by Equation 6-2, the final plot requires calculation of values for ' t/V '; which are then plotted vs the volume of filtrate in order to yield a final graph:

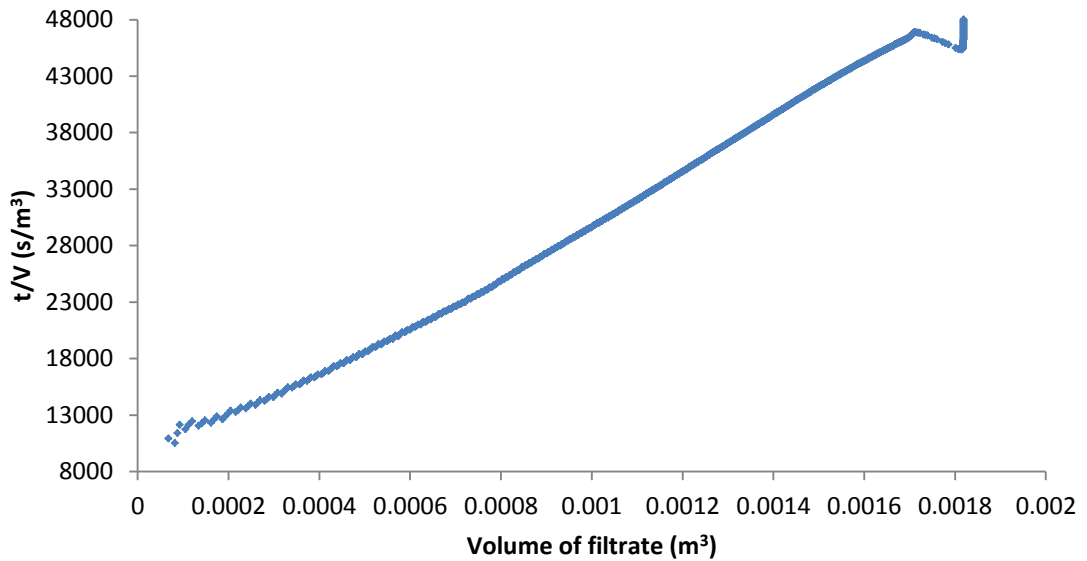


Figure 6-21: t/V vs volume of collected filtrate for Lesinurad at 1.6 bar filtration pressure

Taking the values of known constants and variables and substituting them into Equation 6-3 and Equation 6-4 yields the approximate cake and medium resistance, e.g. for the filtration of Lesinurad at 1.6 bar (Figure 6-21), the following table lists the values used in this calculation:

Table 6-6: Constants and variables used in the calculation of cake and medium resistances

μ	Dynamic viscosity	0.001	kg/m.s
A	Filter area	0.00503	m ²
ΔP	Pressure differential	160000	kg/m.s ²
K_m	Concentration factor	23.48	kg/m ³
m_c	Dry cake mass	0.0425	kg
V	Filtrate volume (total)	0.00181	m ³
a	y-intercept	8000	-
b	Gradient	21875000	-

Hence the filter resistances are as follows:

$$\alpha = 1.01 \times 10^{10} \text{ m/kg}$$

$$\beta_m = 6.02 \times 10^9 \text{ 1/m}$$

This process is repeated for each filtration to obtain a series of resistances with respect to the pressure drop. Results are discussed in section 6.3.4.3.

6.3.4 Results and discussion

6.3.4.1 Experimental outline

As part of experimentation with the 2 Litre pressure filter, 3 particle systems are selected for testing; 2 polymorphs of glutamic acid (α/β) and the AstraZeneca compound Lesinurad. This should aid in elucidating the differences between the differently shaped alpha and beta forms of glutamic acid, and compare these two (relatively easy to filter) particle types with the developmental compound Lesinurad, which is slow to filter.

3 different filtration pressures are selected for testing; 0.5 bar, 1.6 bar and 3.0 bar, as a low, standard and high pressure option. Each compound will be filtered at these 3 pressures (with an additional '0' bar filtration test for beta-glutamic acid, which will be explained in due course).

Table 6-7: Table of experiments conducted in the 2L crystallisation vessel and 2L pressure filter

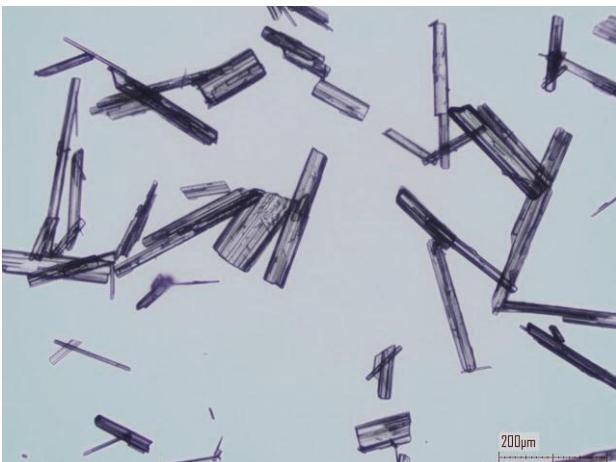
Exp. No	Compound	Conc. (mg/mL)	Solvent	Solvent Vol. (mL)	Solid added (g)	Pressure (bar)	Final Cake Height (cm)	Cake Mass (kg)	Filtrate Vol. Collected (L)	Cake Volume (m ³)	Bulk Density (kg/m ³)
1	β -Glutamic acid	40	Water	2000	80	0	5	0.05940	1.720	2.51E-04	236
2	β -Glutamic acid	40	Water	2000	80	0.5	3	0.05940	1.860	1.51E-04	394
3	β -Glutamic acid	40	Water	2000	80	1.6	2.3	0.05940	1.890	1.16E-04	514
4	β -Glutamic acid	40	Water	2000	80	3	2	0.05940	1.887	1.01E-04	591
5	α -Glutamic acid	40	Water	2000	80	0.5	1.45	0.05449	1.880	7.29E-05	748
6	α -Glutamic acid	40	Water	2000	80	1.6	1.5	0.05449	1.890	7.54E-05	723
7	α -Glutamic acid	40	Water	2000	80	3	1.5	0.05449	1.800	7.54E-05	723
8	Lesinurad	40	MeCN	2000	80	0.5	1.75	0.03335	1.810	8.80E-05	379
9	Lesinurad	40	MeCN	2000	80	1.6	1.2	0.03335	1.827	6.03E-05	553
10	Lesinurad	40	MeCN	2000	80	3	0.9	0.03335	1.810	4.52E-05	737

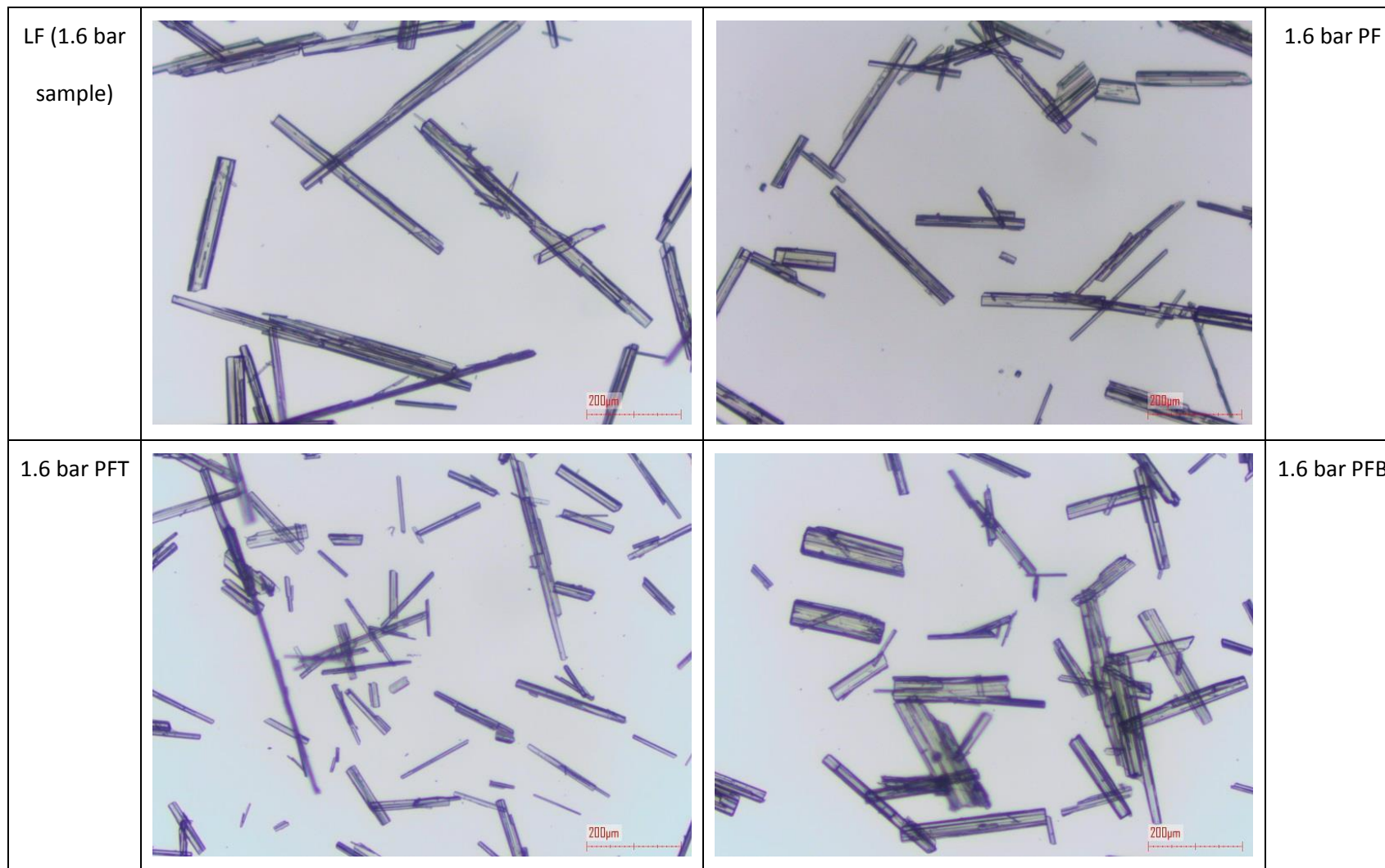
6.3.4.2 Microscopic image analysis

As microscopic analysis is qualitative and selective in the information it shows it displays a certain bias which cannot be completely ignored, but the investigator has attempted to collate images representative of the samples. The other problem is that of quantity of images; even displaying 1 image per sample yields 36 total images (4 samples per pressure across 3 systems). Even with that in mind however, the microscopic analysis yields vital information on the state of the particles before and after filtration, and thus a series of images is presented for each compound within the following tables.

Note – ‘LF’ samples are listed alongside the appropriate pressure as an experimental indicator only, not as an indication of any stress applied to the sample. E.g. ‘0.5 bar LF’ refers to the fact that this sample is taken from the same bulk slurry that is pressure filtered at 0.5 bar, BEFORE the pressure filtration takes place. No LF sample is ever subjected to experimentation beyond the light vacuum process to used isolate the solid.

Table 6-8: Microscopic images of beta-glutamic acid samples before and after filtration.

LF (0.5 bar sample)			0.5 bar PF
0.5 bar PFT			0.5 bar PFB



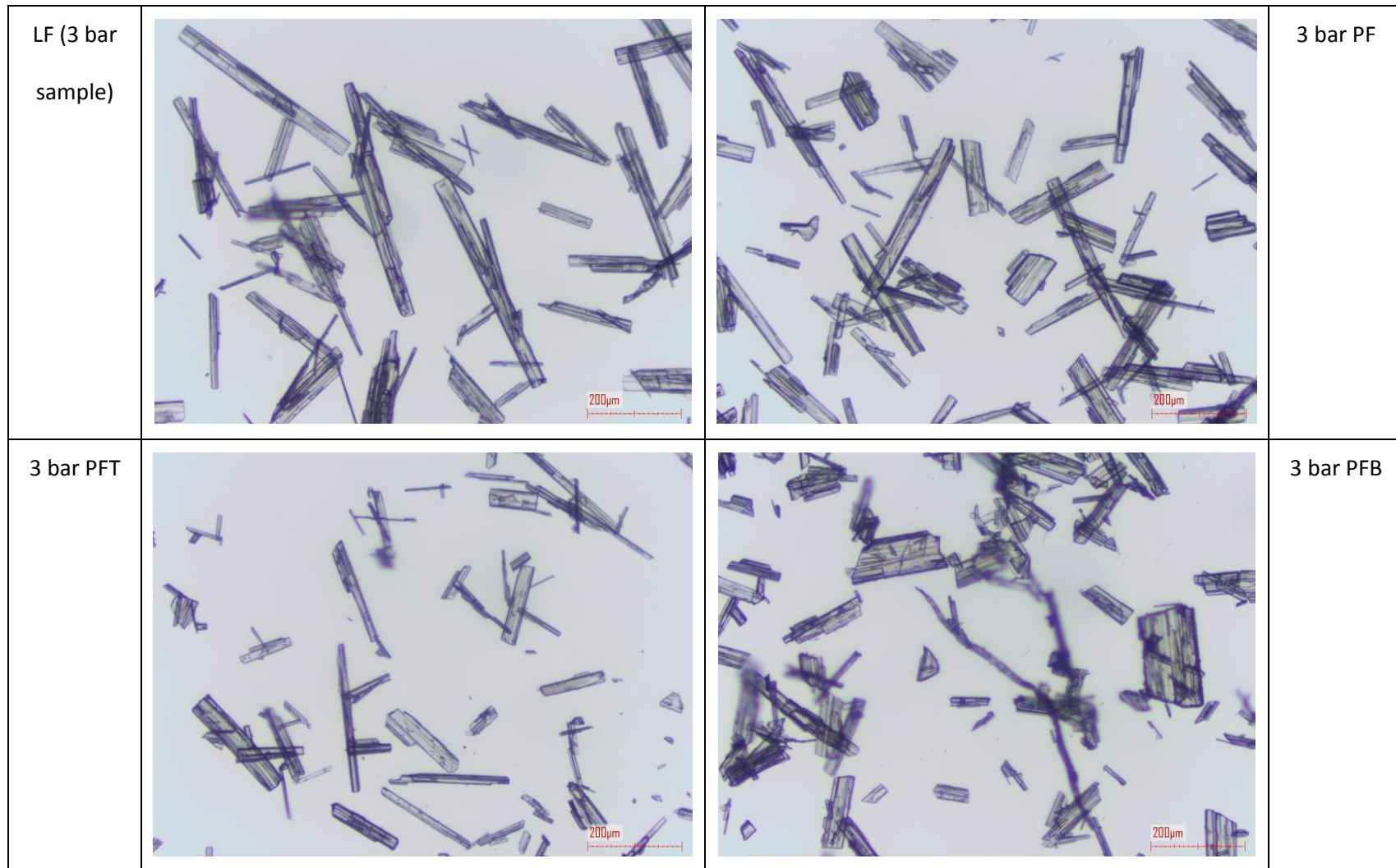
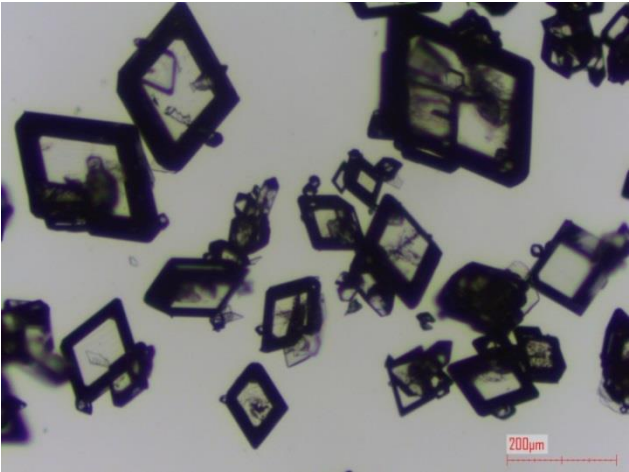
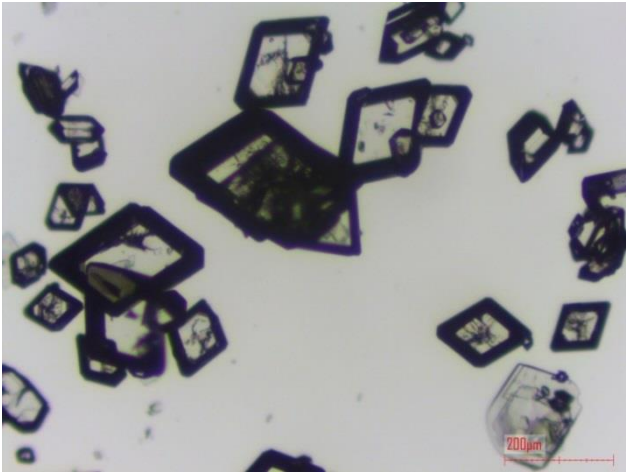
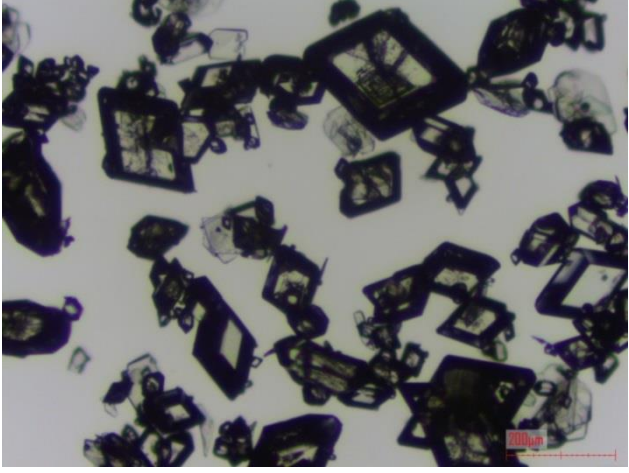
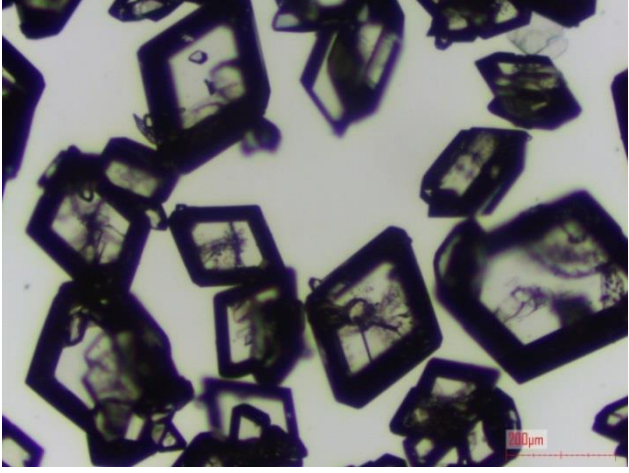
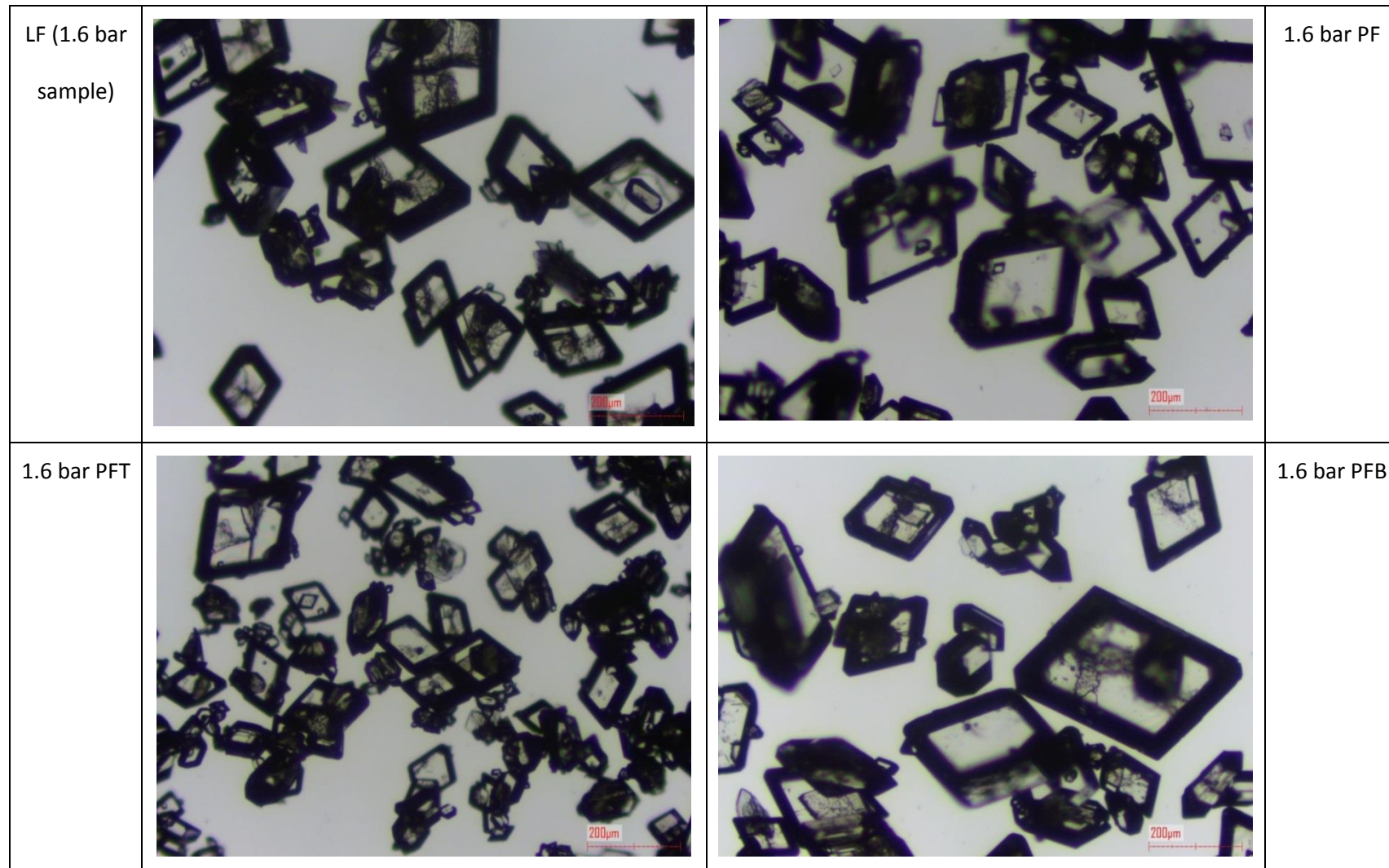


Table 6-9: Microscopic images of alpha-glutamic acid samples before and after filtration

LF (0.5 bar sample)			0.5 bar PF
0.5 bar PFT			0.5 bar PFB



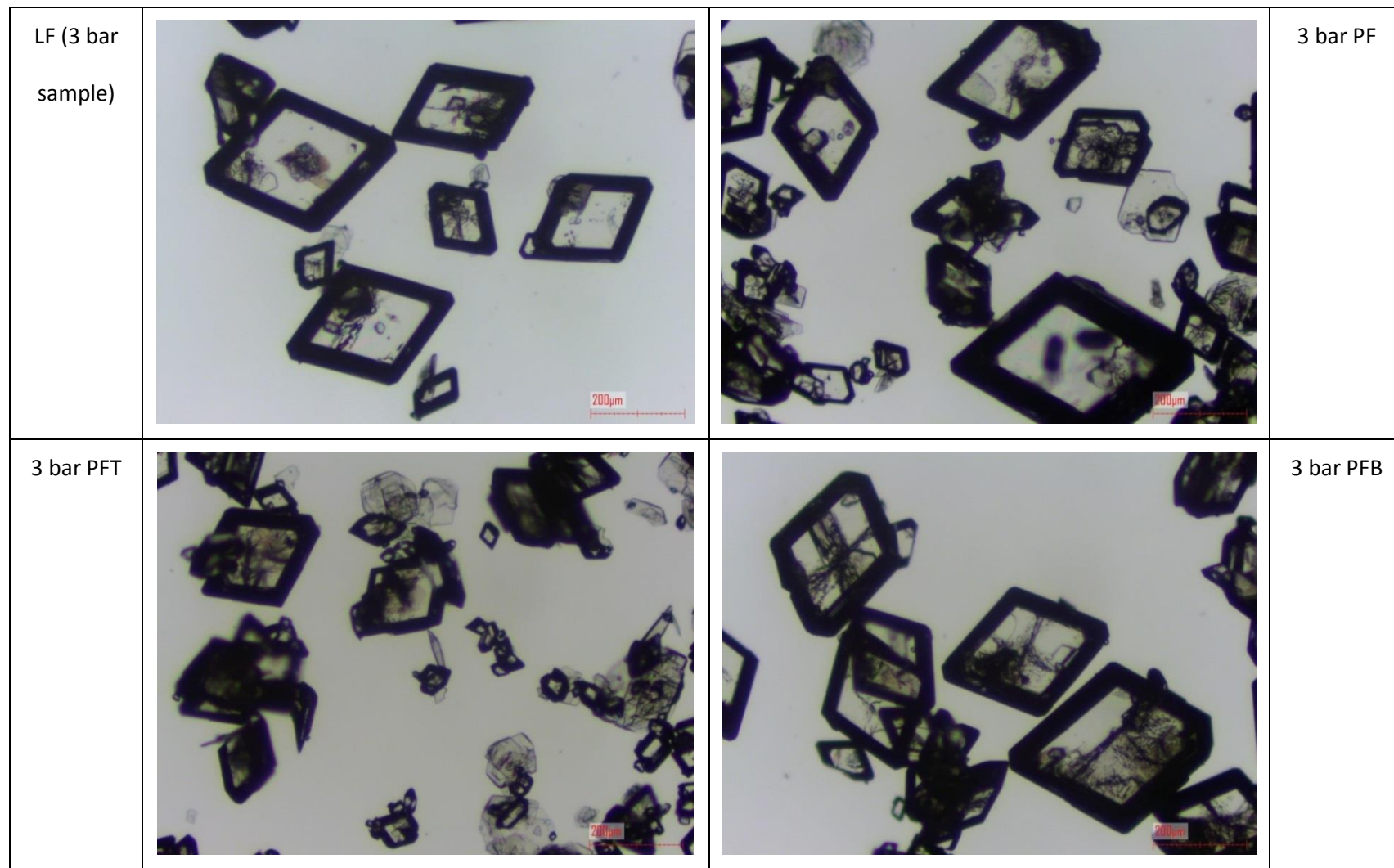
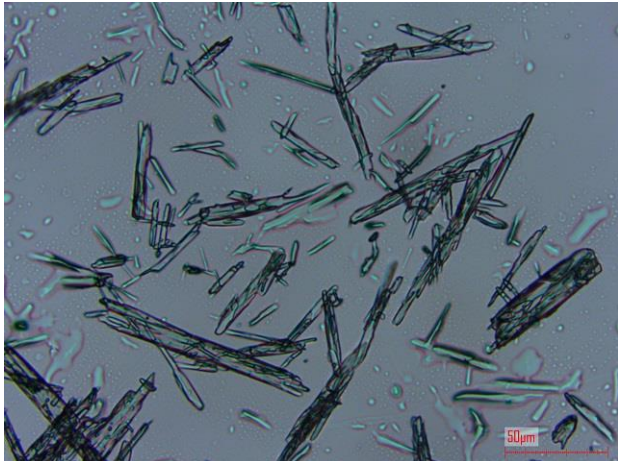
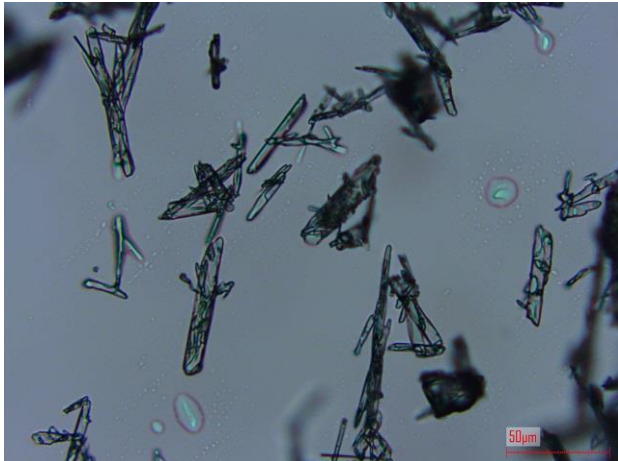
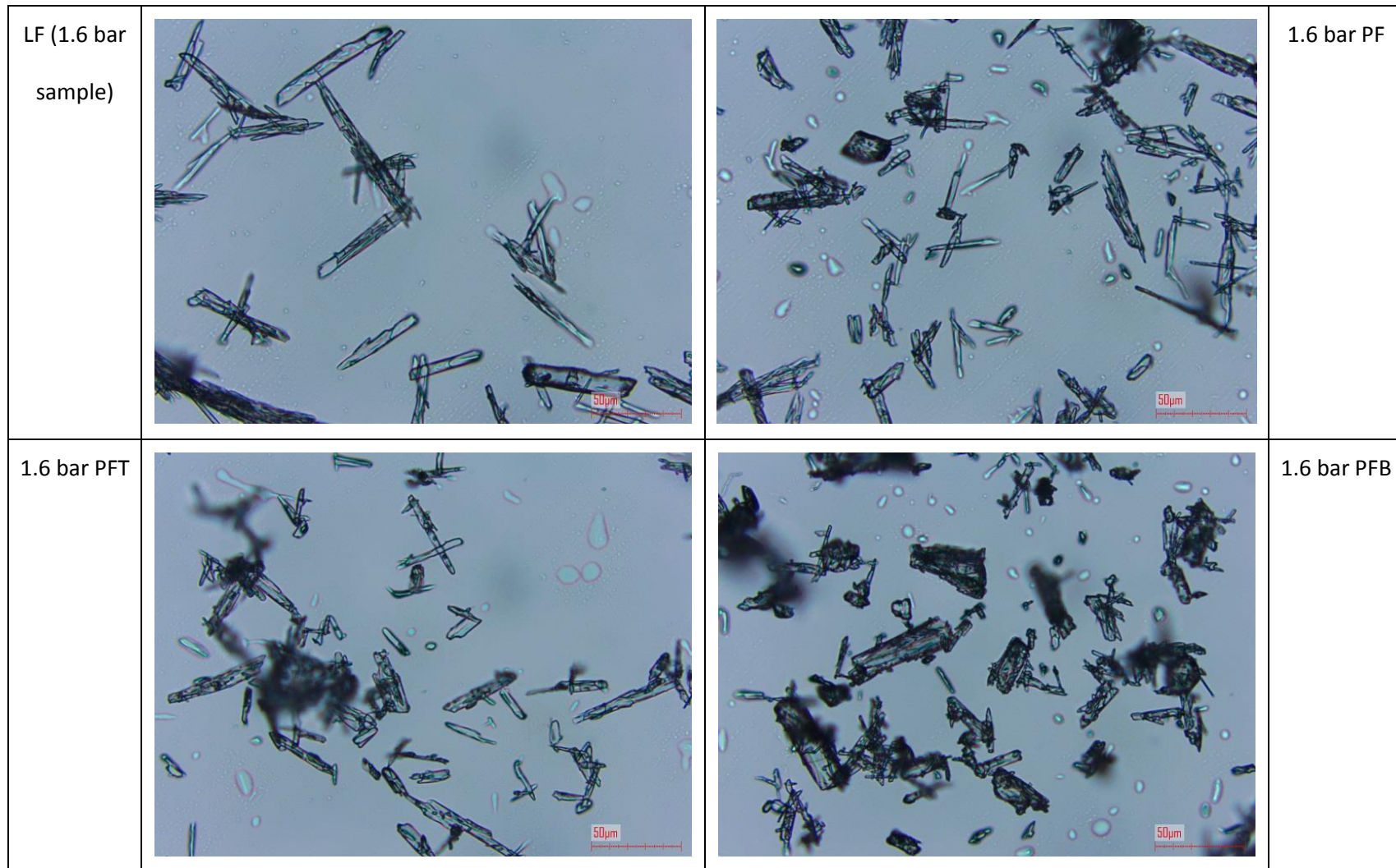
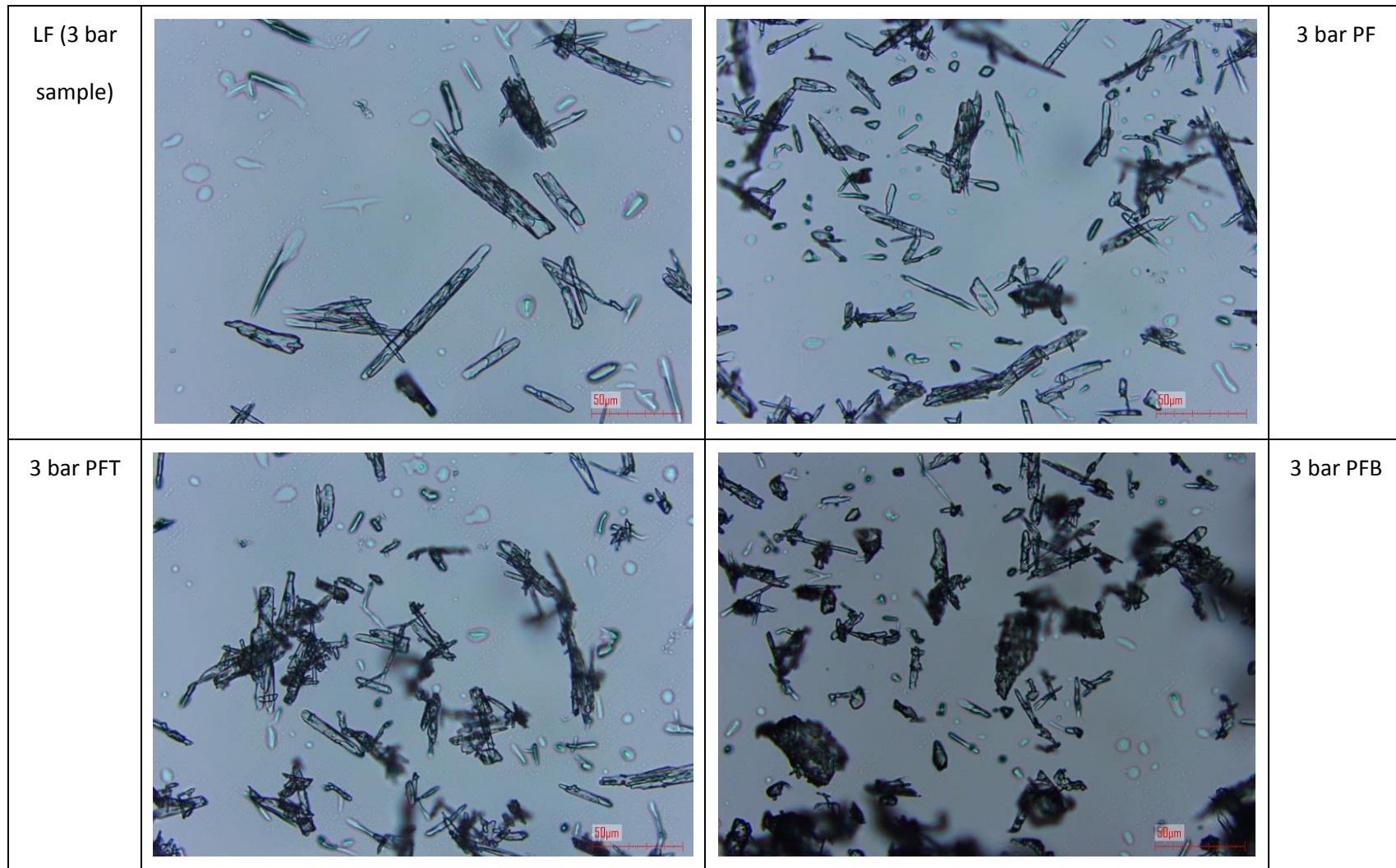


Table 6-10: Microscopic images of Lesinurad samples before and after filtration

LF (0.5 bar sample)			0.5 bar PF
0.5 bar PFT			0.5 bar PFB





The images in the preceding tables begin to elucidate some unexpected results. Observations that are most immediately evident include the presence of oversized and undersized particles within the PFB/PFT samples, respectively; this is particularly evident with the alpha-glutamic acid system. This is contrary to what is likely expected; i.e. if particle breakage in any particular region of the cake is dependent to a certain degree on the weight of particles above then it would be expected that particles at the bottom of the cake would contain some of the smallest particles (e.g. fines and other fragments), whilst particles at the top would be larger on average due to suffering less breakage. This is not the case.

Furthermore it appears, for the needle-like systems of beta-glutamic acid and Lesinurad at least, that the breakage of crystals is evident from the change from vacuum filtered – pressure filtered samples.

The change in crystals is most obvious when looking from the LF sample to the PFB; in fact the extent to which the 3 bar beta-glutamic acid PFB samples have been fragmented are simply not justified with a single image, therefore additional images are available within the appendices. As is obvious from all these images, there is barely an elongated crystal in sight (i.e. in reference to the high-aspect ratio crystals exhibited in the LF samples. This is also true of the Lesinurad needles.

These observations are not only confined to the PFB samples however, but all pressure filtered needle samples appear to display a reduced aspect ratio compared to the lightly filtered crystals. The difference in size reduction from 0.5 bar to 1.6 bar is subtle, whilst the 3 bar samples are slightly more evidently ‘broken’; this is evaluated with size distribution data (which is significantly more representative) in section 6.3.4.6.

The exception to this appears to be the alpha-glutamic samples, which do not appear to exhibit much of the particle breakage observed with the needle-like samples. Although this is expected due to their shape being less conducive to breakage, this does not explain the large reductions in size that vary with increasing filtration pressure, as observed in Figure 6-37 and Figure 6-42. There is some evidence of slight fragmentation and attrition in the 3 bar PFB sample, but not enough to explain such large reductions (reductions in size of alpha-glutamic acid were larger than both beta-glutamic acid and Lesinurad).

It is possible that the increased drag of the higher filtration pressures ‘pulls’ some of the smaller crystals down through the gaps in the bed, thus contributing to the observed size reduction, however more evidence is required to investigate this further.

6.3.4.3 Filtrate flow rate and cake compressibility

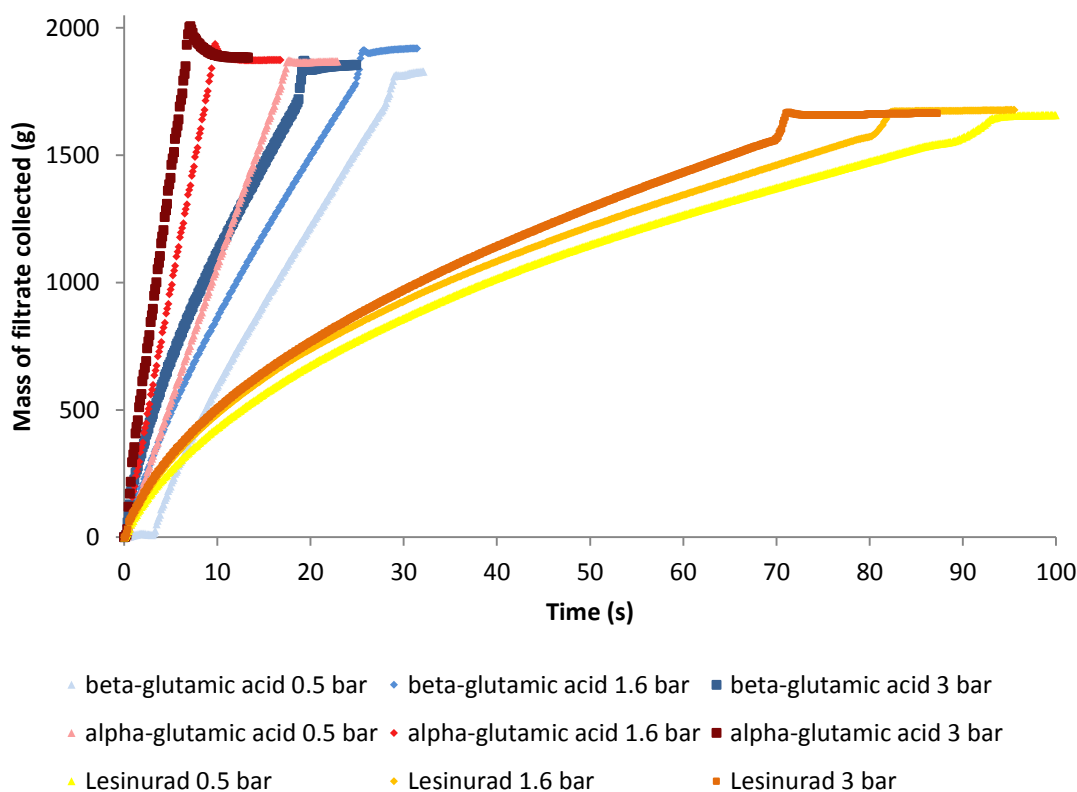


Figure 6-22: Filtrate mass flow over time for the 3 systems at filtration pressures of 0.5, 1.6 and 3 bar

Collection of the filtrate mass over time (Figure 6-22) reveals the differences in which the 3 crystal systems behave whilst under filtration (or percolation, depending on the system). It should first be noted that although 2 Litres of solvent is prepared and added to the crystallising vessel, hold-up of moisture in the cake itself explains the discrepancy between the final collected mass of solvent and the initial 2 Litre figure. Filtrate masses for Lesinurad are particularly low due to the lower density of acetonitrile which is used as a co-solvent in crystallisation.

The most apparent differences are in the rate at which the cake is de-wetted. The alpha-glutamic acid is dewatered at the fastest rate, even whilst subjected to the lowest pressure differential of 0.5 bar – for example at this pressure the cake is fully dewatered before the beta-glutamic acid cake at 3 bar.

It is unclear as to how much of this can be attributed to the particle shape, as particle sizes also differ between the 3 systems. Smaller sized particles are able to pack closer together and leave fewer/smaller channels for filtrate to pass through, thus affecting the rate at which liquid is able to pass through the cake. Lesinurad needles are typically 20 – 60 microns in length; compared to beta-glutamic acid needles which are commonly several hundred microns in

length. The Lesinurad rate of de-liquoring is thus the greatest due to its small average particle size.

The time taken for the cakes to fully de-liquor is also observed to increase with higher pressure differentials and this is true for each system. This is due to the rising driving force, thus producing an increase in the rate of flow through the cake. For a theoretically incompressible cake, the increase in pressure drop should produce a proportional rise in flow rate. Practically this does not occur, as almost all pharmaceutical-like substances have some degree of compressibility and thus tend to compact tighter with increasing pressure, reducing the flow of liquid. This produces disproportional rises in flow with increasing pressure differential.

The evolution of filtration behaviour over time is consistent across all pressures but does exhibit some variation with different systems. The rate of de-liquoring with alpha-glutamic acid is fairly constant (as evidenced by the apparent straight-line gradient of the mass v time trace), showing that the cake's resistance to flow is fairly constant over time. For the beta-glutamic acid and Lesinurad, the cake resistances (gradients) do change with time – both reducing as the filtration progresses – the change being more drastic with Lesinurad. For the needle systems, this is evidence of the filtration slowing over time as more material is compacted into a solid cake; reducing the channels available for liquid flow.

The integrated filtration equation data obtained from Equation 6-1 is depicted in Figure 6-23, Figure 6-24 and Figure 6-25. The data observable in these plots is confirmation of the previous assertions; the rate of change of alpha-glutamic acid filtration rate over time is minimal, whilst in Lesinurad and beta-glutamic acid (for pressures greater than 0.5 bar, at least) it is more significant.

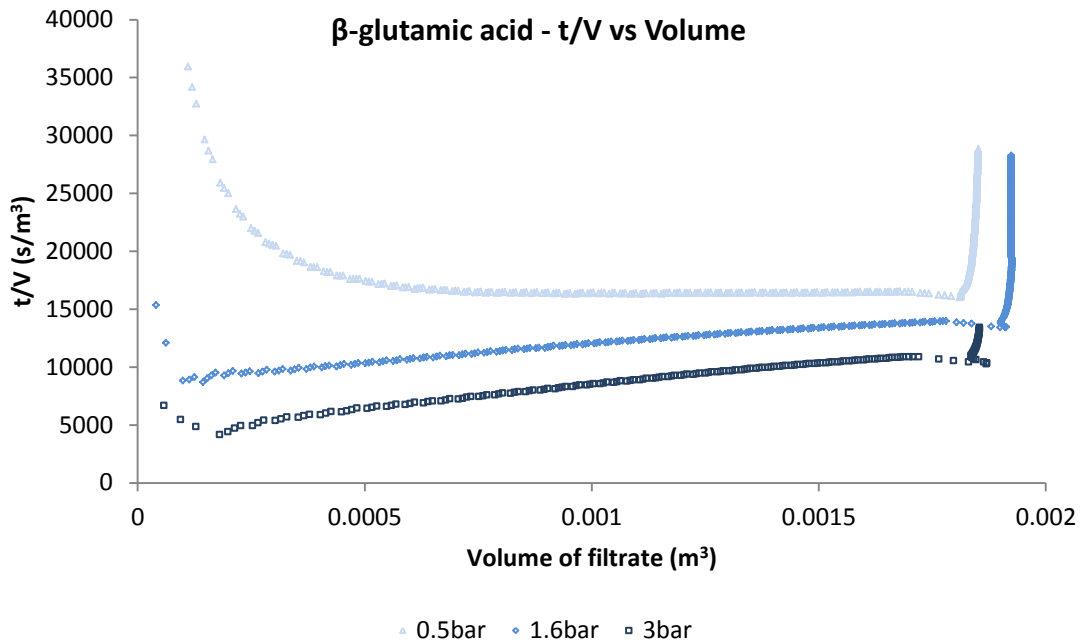


Figure 6-23: t/V against volume for β -glutamic acid filtered in 2 Litre pressure filter at 0.5, 1.6 and 3 bar

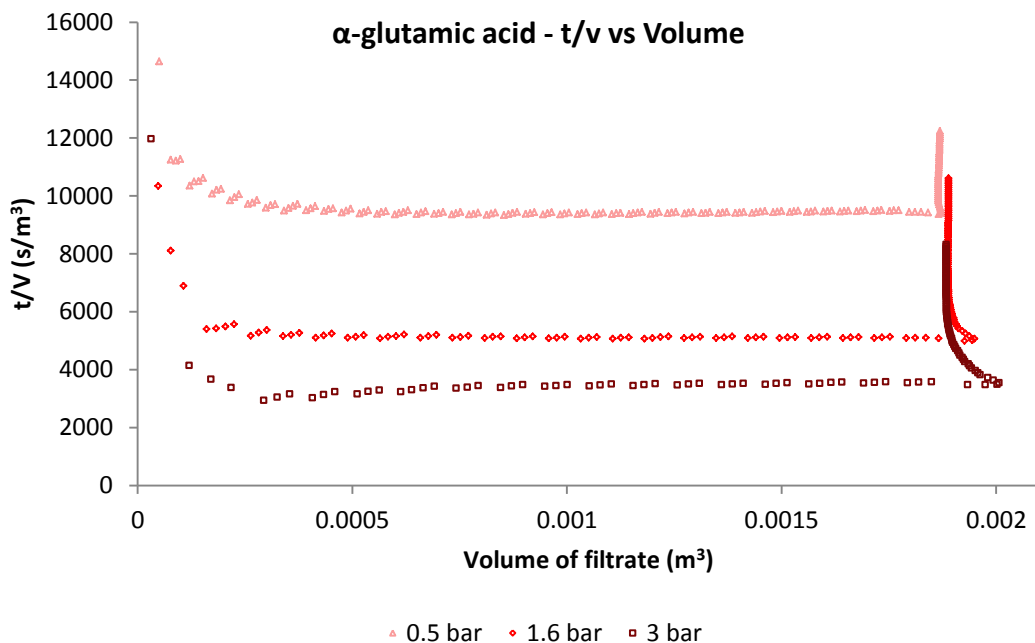


Figure 6-24: t/V against volume for α -glutamic acid filtered in 2 Litre pressure filter at 0.5, 1.6 and 3 bar

Note that the data in Figure 6-23 and Figure 6-24 display t/V vs. V data that is in most cases (i.e. all except for 1.6/3 bar beta-glutamic acid) indicative of fluid percolation, not filtration, as evidenced by the non-proportionality of the variables (i.e. virtually 'flat' lines of constant filtration rate). Filtration typically would decrease in rate over time due to the build-up of solid cake, yielding a proportional linear plot more indicative of those in Figure 6-25.

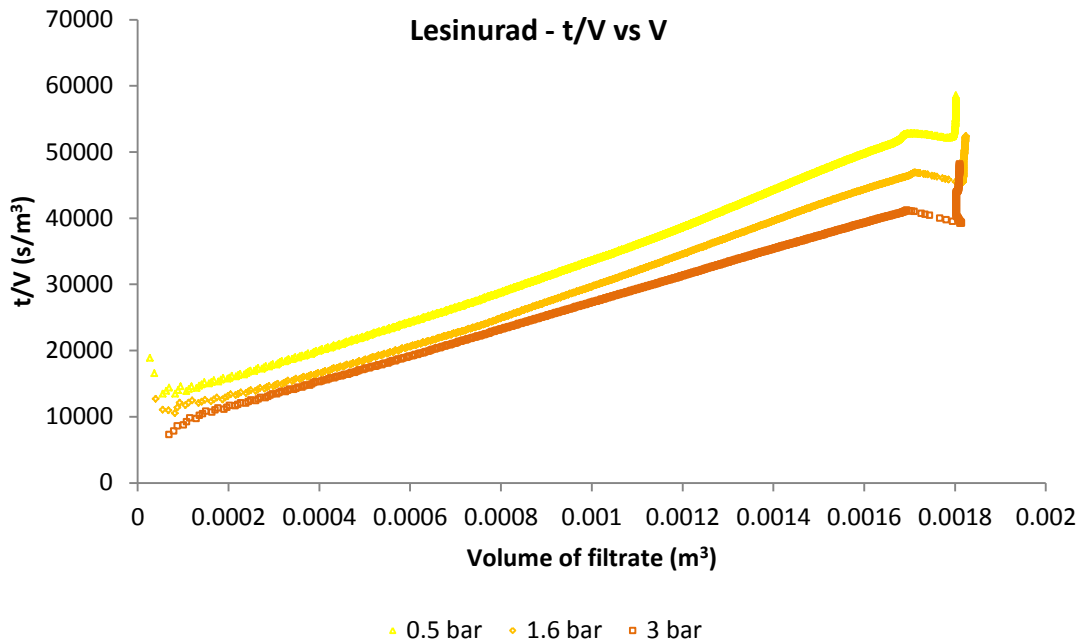


Figure 6-25: t/V against volume for Lesinurad filtered in 2 Litre pressure filter at 0.5, 1.6 and 3 bar

The cake resistance (α) can be calculated from the t/V data using Equation 6-3. It is a measure of the rate of change of filtration rate with respect to time, i.e. it is dependent on the gradients of the curves. Changes in the resistance of the cake with respect to pressure give an indication of the compressibility of the cake: the compressibility index 'n' is a measure of the extent to which cake resistance rises (or not) with increasing pressure drop. It is found from [26]:

$$\alpha = \alpha_0 \times P^n \quad \text{Equation 6-5}$$

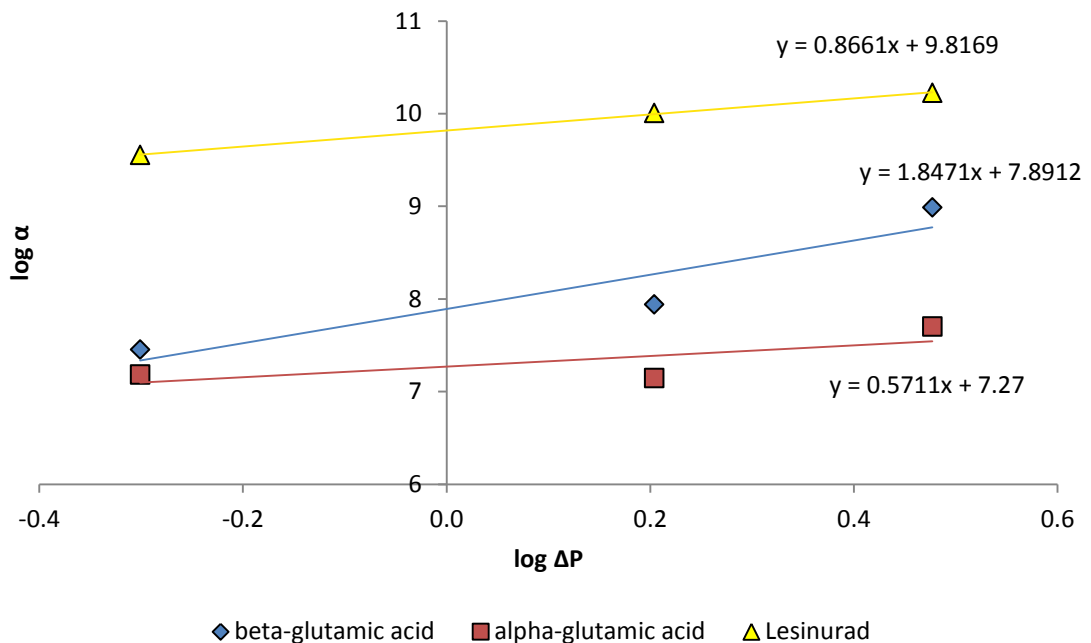
$$\log \alpha = n \log P + \log \alpha_0 \quad \text{Equation 6-6}$$

Hence the compressibility index 'n' can be found from the logarithmic plot of cake resistance vs. pressure drop. Any bed which displays a compressibility index > 0 is by definition somewhat compressible, i.e. the resistance to flow increases with pressure. A completely incompressible bed has an index of 0, whilst an index > 1 is likely to indicate a highly compressible bed.

Taking the cake resistances as calculated from the method outlined in section 0 and performing a further calculation to evaluate the compressibility yields the data in Table 6-11, and Figure 6-26:

Table 6-11: Cake resistance and log(cake resistance) for the 3 crystal systems

Filtration Pressure (bar)	0.5	1.6	3
α (beta-glutamic acid)	2.82E+07	8.72E+07	9.67E+08
α (alpha-glutamic acid)	1.52E+07	1.40E+07	5.00E+07
α (Lesinurad)	3.57E+09	1.01E+10	1.67E+10
Log P	-0.301	0.204	0.477
Log α (beta-glutamic acid)	7.450	7.940	8.985
Log α (alpha-glutamic acid)	7.183	7.146	7.699
Log α (Lesinurad)	9.552	10.004	10.223

Figure 6-26: log(α) against log(P) for calculation of compressibility indices

The variability of the cake resistance as the filtration pressure rises is an indication of a change in structure in the bed with respect to pressure; a key component of cake compressibility. Liquid channels and passages of flow are increasingly restricted as the cake compresses, thus slowing the rate at which liquid is able to pass through the cake as pressure is increased. Hence for these compressible cakes, a rise in pressure (increased driving force) does not produce a proportional rise in fluid flow, as the resistance to flow in the cake also rises.

From Table 6-7 the bed heights are observed to reduce with increasing pressure for the needle-like systems whilst the more blocky alpha-glutamic acid has a relatively stable bed height – a key indicator of compressibility being the collapse of voids at higher pressure drops. This is interesting as the cake resistance data shows that the alpha-glutamic acid is somewhat compressible (n of 0.57), meaning the result is in doubt.

The beta-glutamic acid displays an incredibly high compressibility of 1.8 (albeit the legitimacy of which is in doubt), yet from the mass-time data in Figure 6-22 there is no sudden plateau observed that would be typical of a highly compressible material. The Lesinurad displays the closest behaviour to a plateau in flowrate and even then the rate is still appreciable by the end of filtration; Lesinurad however only has a compressibility index of 0.87 (still very compressible).

Beck et al[41] found the cake resistance of needle-like glutamic acid to be in the region of $4-6 \times 10^8$ m/kg when filtering at 2, 4 and 6 bar pressure, with a compressibility index of 0.12; although the 'needles' they produced are more prismatic in nature than those crystallised in this project. It is therefore likely that the cake resistances of the 0.5 and 1.6 bar filtrations are severely undervalued.

The increased resistance observed at 3 bar pressure drop could also be due to the elevated levels of particle breakage observed under microscopy. The crystal breakage would serve to destroy any bed structures supported by networked needles and thus reduce the porosity of the cake as particles rearrange. This does not explain why the compressibility of the alpha-glutamic acid is so high however; having suffered much less particle breakage under filtration.

The alpha-glutamic acid rates may have been influenced by the rate of settling of the particles – the filtration rate model assumes at $t = 0$ a bed height of 0 (i.e. no particles yet exist in the cake), whilst in reality these particles are observed to settle before the operator has time to begin the pressure filtration (settling within a few seconds).

Overall the results must be treated with scepticism; Mahdi and Holdich note that constant pressure filtration tests are subject to inconsistencies, particularly with compressible cakes[126]. The alpha and beta-glutamic acid systems were typically subject to percolation (and not filtration) due to the high rates of liquid flow, which will have affected the results. A subsequent analysis would therefore take Darcy's Law into account where the analysis method may be more befitting of the process.

6.3.4.4 Dispersion pressure titration

Dispersion of a powder sample aids in particle sizing, as this helps to separate particles and loosen weak agglomerates; thus giving a 'truer' representation of the number and size of particles in the sample. The reaction of a powder sample to dispersion depends upon the extent of force, and hence the energy, imparted to the powder.

Lower dispersion pressures are preferable in this sense, as it helps to avoid unnecessary stresses being placed upon the particles (which could also lead to breakage through either particle-wall or particle-particle collisions).

With too little dispersion however, the particle size distribution becomes skewed with the appearance of additional peaks towards the higher end of the size range; a result of multiple particles being imaged as if it were a single crystal. Higher injection pressures provide a greater actual dispersion of the particles; and for systems in which agglomeration or electro-static binding of crystals is a particular problem, it may be necessary to raise the dispersion pressure in order to combat these.

A test is proposed in which each crystal system tested with the 2 litre filter is subjected to a 'pressure dispersion titration', i.e. a series of measurements of size distribution are taken for the same sample at varying dispersion pressures. The appearance of the size distribution is then analysed for positive and negative effects, with the idea being to identify an 'optimum' set of conditions to test the full range of samples for final results.

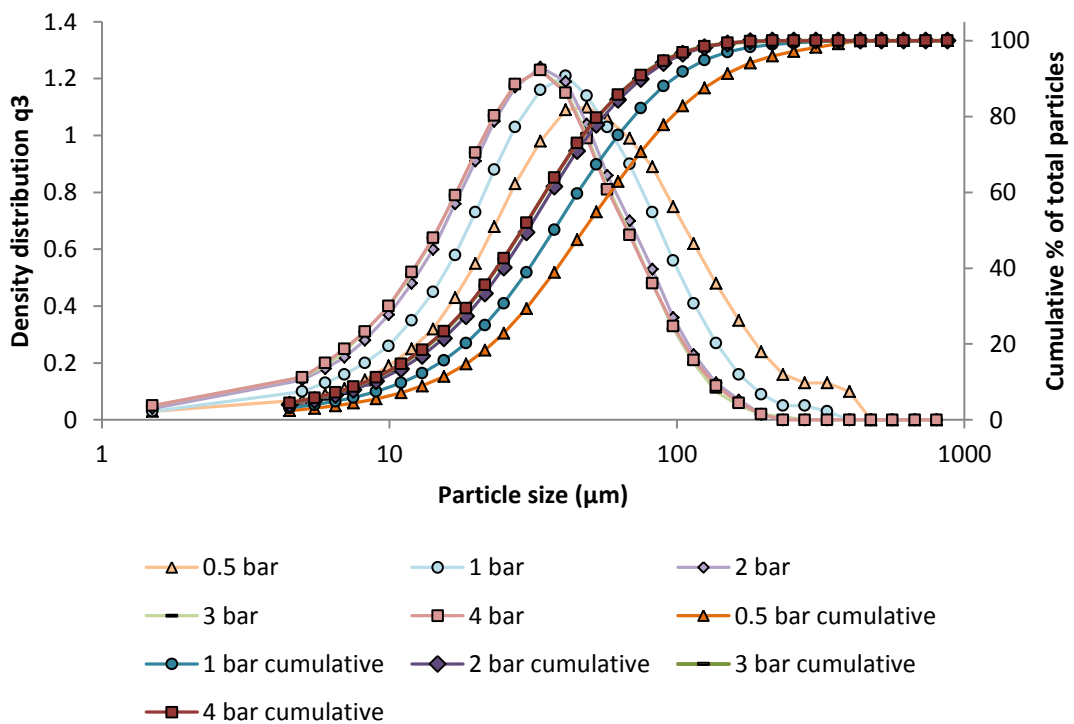


Figure 6-27: β -glutamic acid particle size distributions for pressure titration test from 0.5 – 4 bar dispersion

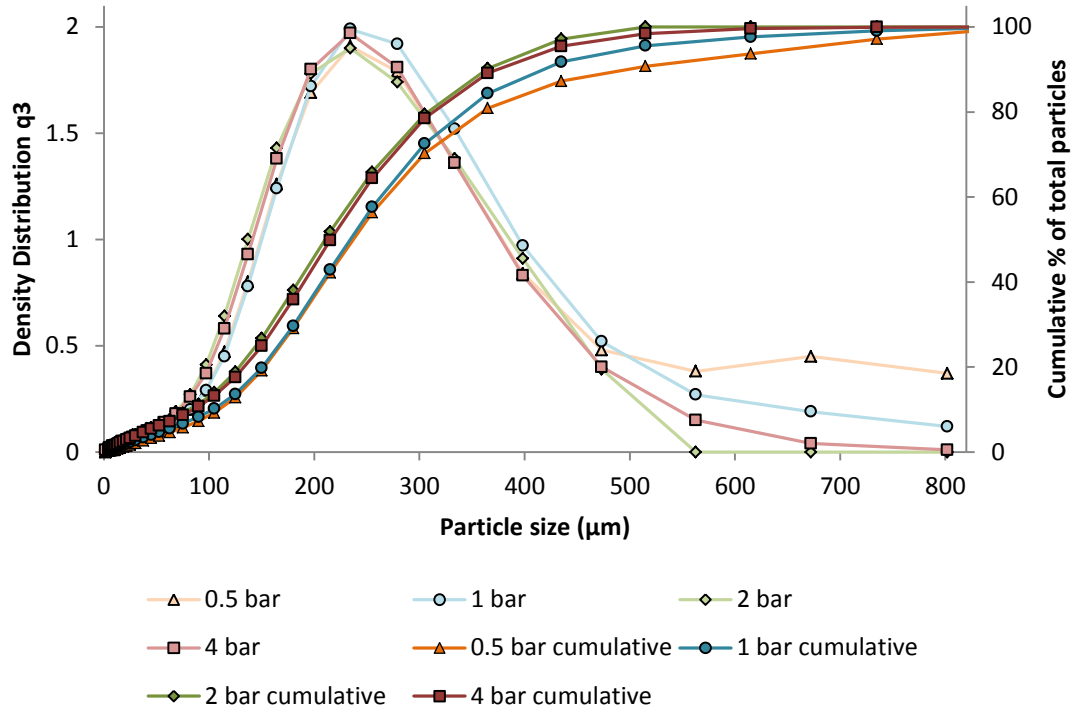


Figure 6-28: α -glutamic acid particle size distributions for pressure titration test from 0.5 – 4 bar dispersion

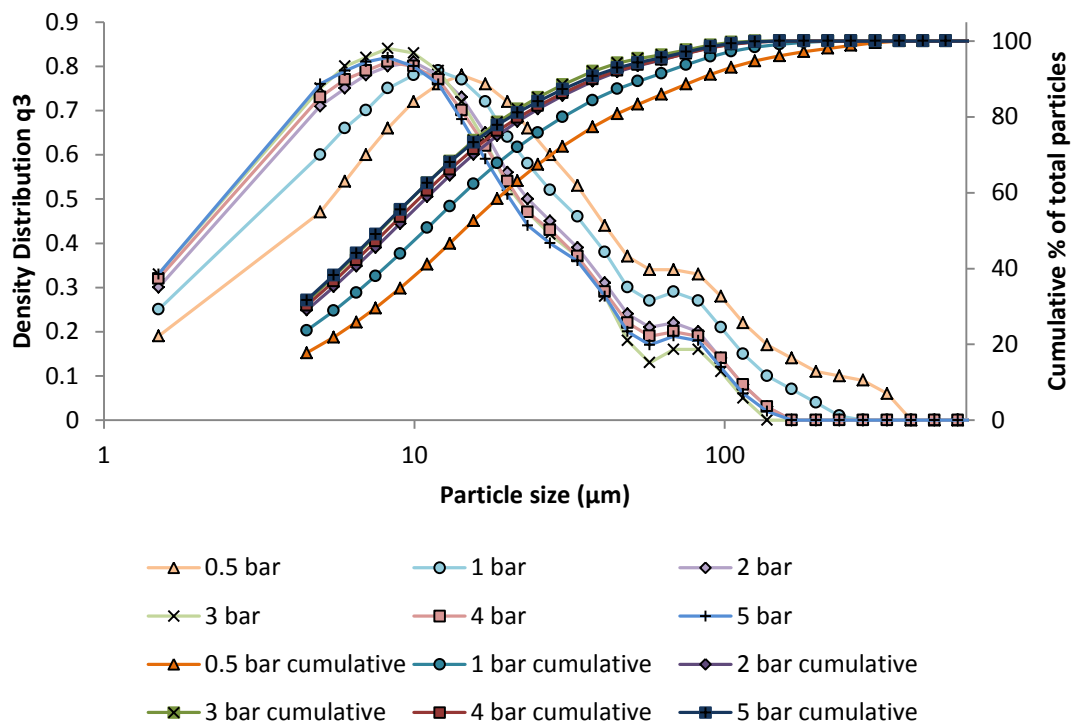


Figure 6-29: Lesinurad particle size distributions for pressure titration test from 0.5 – 5 bar dispersion

From Figure 6-27 to Figure 6-29, the data depicts the particle size distributions of the 3 different systems tested. The β -glutamic acid, predicted to be one of the more 'fragile' compounds due to its long needle habit, reacts typically to the dispersion titration; showing a

characteristic shift to the left of the curve. The effect is not hugely pronounced, but there is a definite 'reduction' in the measured size distribution when dispersing from 0.5 – 4 bar.

The greatest changes are observed when moving from 0.5 – 1 bar, and 1 bar – 2 bar; after which, increasing the dispersion pressure makes little difference to the size distribution i.e. a 'peak' effect is observed and further increases in dispersion are (largely) independent of the size observed. Incidentally, this effect is noted for the Lesinurad system (also a needle-like habit), but is less pronounced with the α -glutamic acid.

Particles (although it is likely some of these are agglomerates) in the higher size ranges ($> \sim 250 \mu\text{m}$) show a tendency to be under-dispersed; as is evidenced by the reduction in size of the 'bump' or peak appearing in this area of the curve when dispersing at pressures < 2 bar.

The α -polymorph samples (Figure 6-28) react differently. For particle sizes less than $\sim 500 \mu\text{m}$, the reductions in estimated particle size with increasing dispersion pressure are small. The largest particle sizes (above $500 \mu\text{m}$) however experience significant variations on increasing dispersion pressure. It is clear that some particles/agglomerates within the higher size ranges are not sufficiently dispersed at lower pressures (particularly 0.5 bar).

Lesinurad size data is available in Figure 6-29. Like the other crystal systems, the Lesinurad displays a trend of apparent size reduction in the range of pressures 0.5 – 5 bar. Unlike the other crystal systems however, crucially the variability of the Lesinurad size distributions are greater, or rather, the likelihood of a poorly dispersed sample measurement is much higher than with glutamic acid.

It should be noted however that the data in Figure 6-29 consists of the more well dispersed samples i.e. samples in which an excessive anomalous peak did not manifest within the large particle size ranges (data is omitted such that a fairer comparison can be made between size differences at all dispersion pressures – the distribution is weighted therefore anomalous peaks affect the entire distribution in all size ranges). These results are an uncommon phenomenon with the glutamic acid samples, but become increasingly likely with Lesinurad, particularly at the lower dispersion pressures of 0.5 – 1 bar. This is likely due to the small particle size causing the solid's tendency to be paste-like macroscopically.

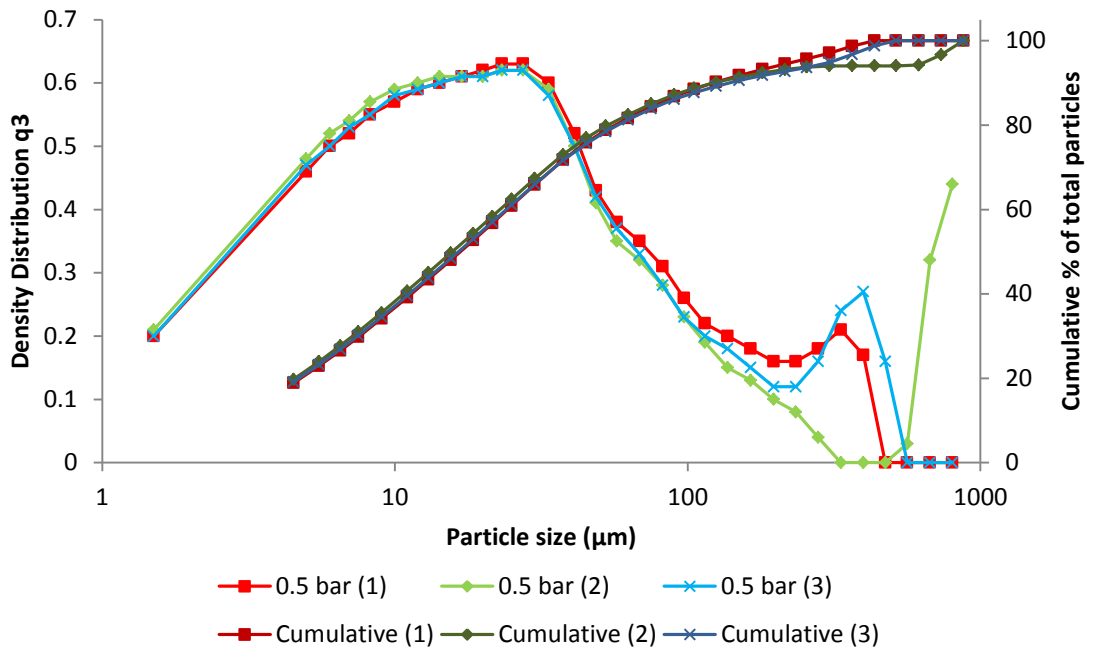


Figure 6-30: Lesinurad particle size distributions at 0.5 bar dispersion

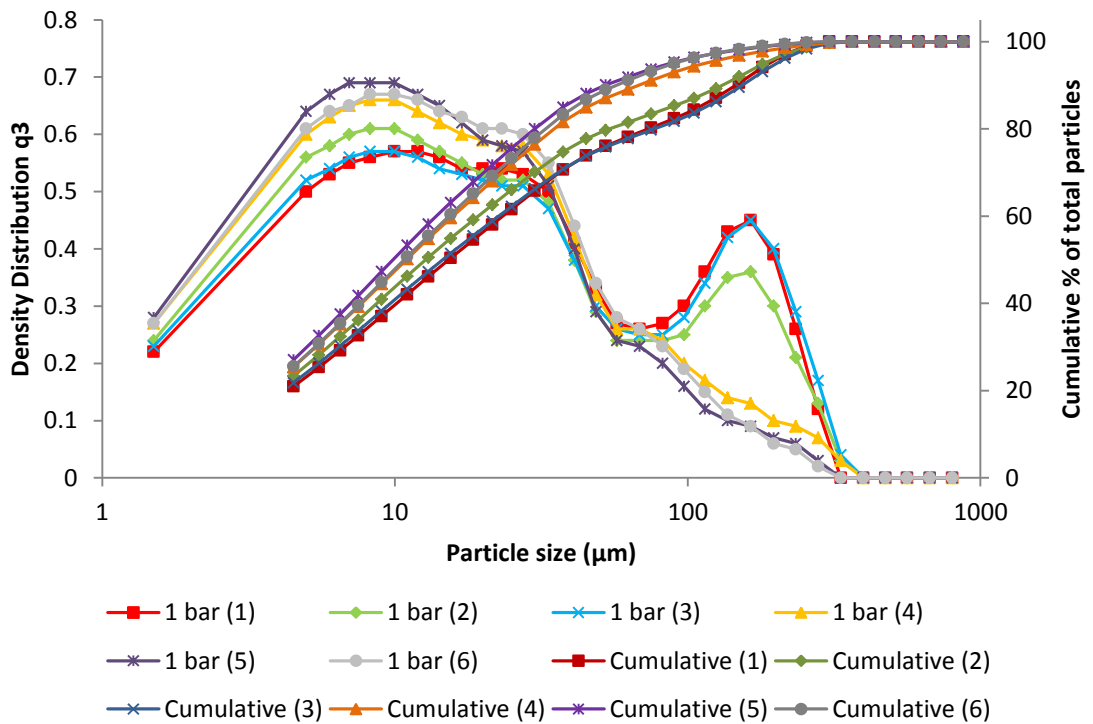


Figure 6-31: Lesinurad particle size distributions at 1 bar dispersion

As is evident from Figure 6-30 and Figure 6-31; a typical set of concurrent sample runs, the likelihood of an anomalous result is fairly high. This is particularly evident when dispersing at 0.5 bar, at which a properly dispersed result is very rare (~1 in 10).

This variability in using lower dispersion pressures is not only time consuming, but material consuming also. The HELOS Sympatec is a destructive analysis method (not theoretically; but it

would be practically impossible to retrieve sample material from the waste bin) and hence for samples in which limited material is available the risk of material loss is a significant factor.

The final dispersion pressures therefore are selected on the general rule of being the lowest possible pressure that will yield a consistent and well-dispersed result, whilst avoiding wasting of (in certain cases, precious) material. For β -glutamic acid, this is 0.5 bar. α -glutamic acid is too inconsistent at 0.5 bar, hence is dispersed at 1 bar. Lesinurad, as discussed, is too variable at 0.5 and 1 bar, hence is dispersed at 2 bar.

This does unfortunately make comparison of separate systems problematic (i.e. it is difficult to compare d50s or other numeric values), but relative trends such as extent of size distribution change can still be compared.

It should be noted that the feed rate at which the sample is injected into the chamber, and the mass of sample injected is also tested. These factors were not observed to have a large effect on the final distributions, but were mainly a function of the average particle size in the sample. For example the α -glutamic acid, with its average particle size being the largest of the 3, required a greater mass for each sample vial.

This is simply because accuracy of the result is dependent on the number of particles tested (more particles tested yields a more representative result), and with having a larger average particle size, more mass is required of the α -samples to increase the particle number. Conversely, the Lesinurad has a low typical particle size, and hence a lower mass of sample contained enough particles to yield a representative result.

These 2 parameters were mainly optimised via trial and error, along with attempting to gain a suitable 'optical concentration' (a variable recorded by the Sympatec software, which is a measure of the number of particles imaged in a sample).

The setting of a lens size is a typical operation in a microscopy operation, and is indicative of the range of particles sizes you expect to image. The 875 micron lens is chosen for glutamic acid; whilst the Lesinurad is imaged using the 350 micron (apparent from the loss of some data in the lower particle size ranges within the pressure titrations).

The final experimental settings are listed in Table 6-12 below:

Table 6-12: Experimental conditions for particle sizing of each compound

Compound	Dispersion P (bar)	Feed rate (mm/s)	Sample mass (mg)	Lens size (μm)
β -glutamic acid	0.5	60	100	875
α -glutamic acid	1.0	100	250	875
Lesinurad	2.0	50	50	350

6.3.4.5 Particle size analysis by Sympatec laser diffraction

6.3.4.5.1 Sample vial observations

Figure 6-32 displays 4 sample vials of Lesinurad powder ready to be inserted into the ASPIROS sample delivery system. Evident in this image are the relative packing heights of the samples; where LF samples pack to the greatest height, with the PFB particles only reaching a fraction of this height.

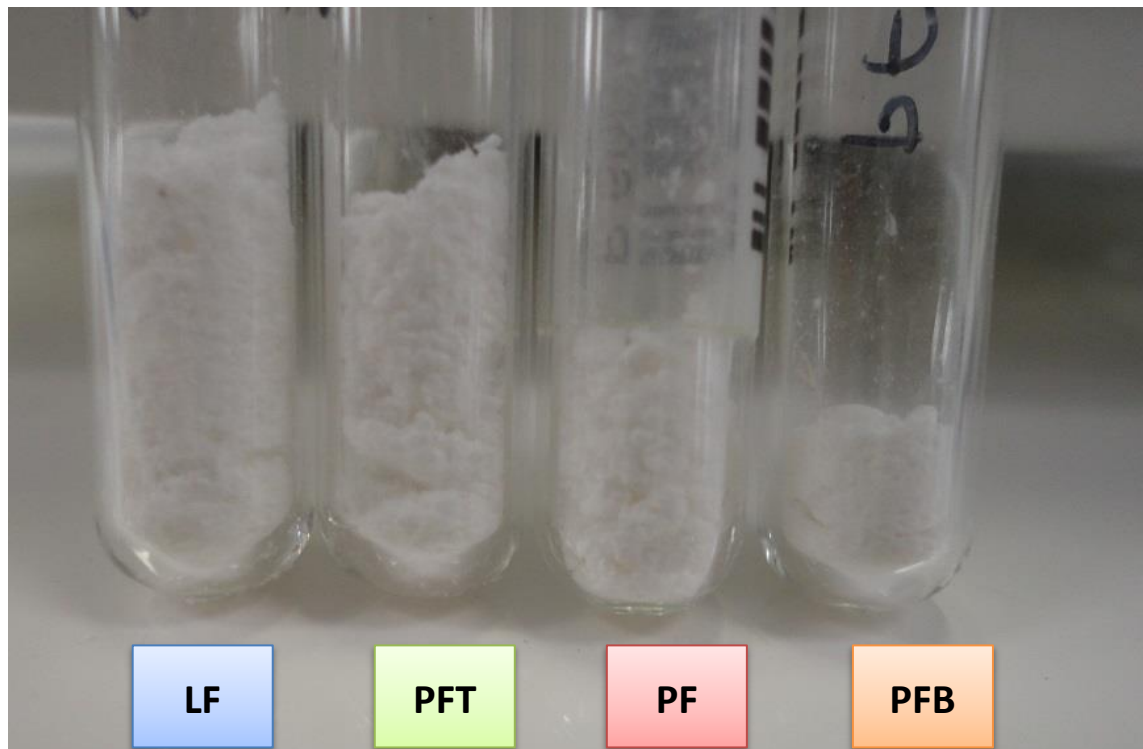


Figure 6-32: Sympatec HELOS sample vials containing Lesinurad powder filtered at 1.6 bar

This example of LF samples packing with the greatest height and PFB with the smallest is consistent across all samples and for all 3 systems. The PF/PFT samples are much more variable; for instance in this case the PF packs with greater density than the PFT, but for example with the beta-glutamic acid system these samples pack with roughly equal bulk density. Masses of all samples are constant, thus the bulk densities of these samples are variable.

It would be imagined that larger particles would pack with lower bulk density (due to larger voids between particles) and smaller particles would pack with the tightest configurations. It is possible that the bulk densities of the powders is related to the extent of breakage they have suffered under filtration. From image analysis, the PFT samples tended to display the least breakage of the pressure filtered samples, followed by the PF, then the PFB. This would imply that the more 'broken' crystals of e.g. the PFB samples would be able to pack in tighter configurations due the increased presence of fines.

The PFB samples, being under such great pressure, could be more compacted than other sources of sample material. This would seem to explain the difficulty in retrieving a well dispersed result for the PFB samples; many sample results are under-dispersed (and thus re-tested) and better dispersed samples tend to show greater variation. The PFT samples display very little under-dispersion and overall show greater consistency in their size distributions.

6.3.4.5.2 Particle size distributions

The following graphs are the result of taking the mean values for 4 samples run through the Sympatec particle sizing system i.e. 4 samples of LF material, 4 samples of PF material, 4 of PFT and 4 of PFB. The results are displayed firstly according to each filtration pressure examined:

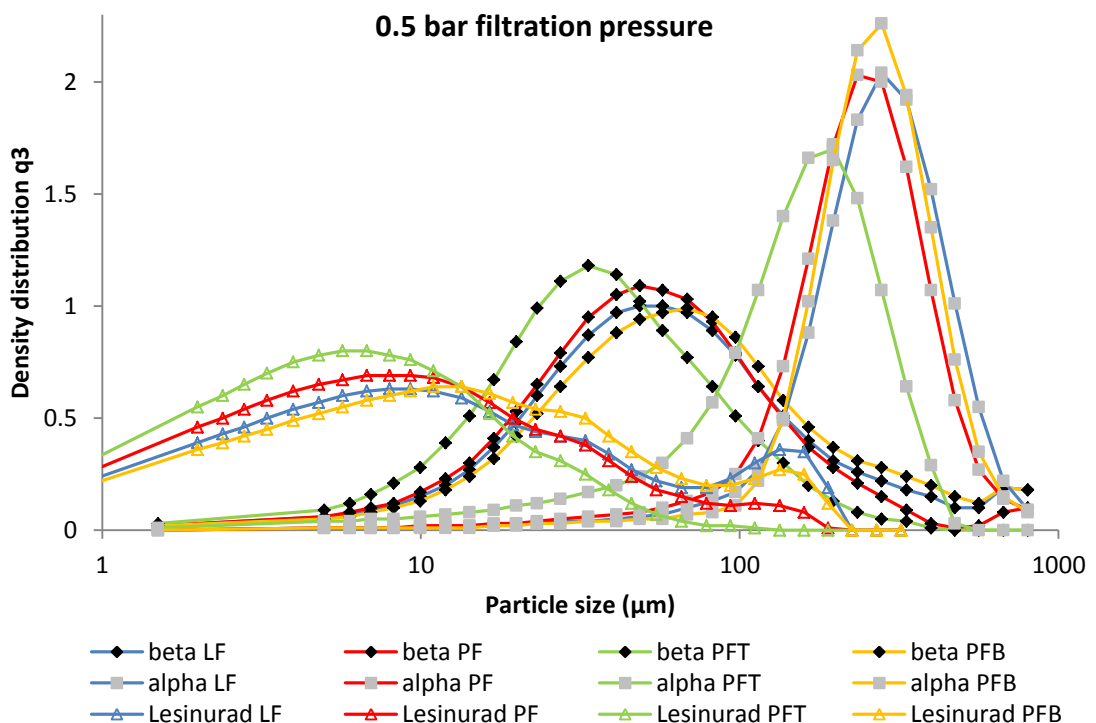


Figure 6-33: Particle size distributions for the 3 systems filtered at 0.5 bar

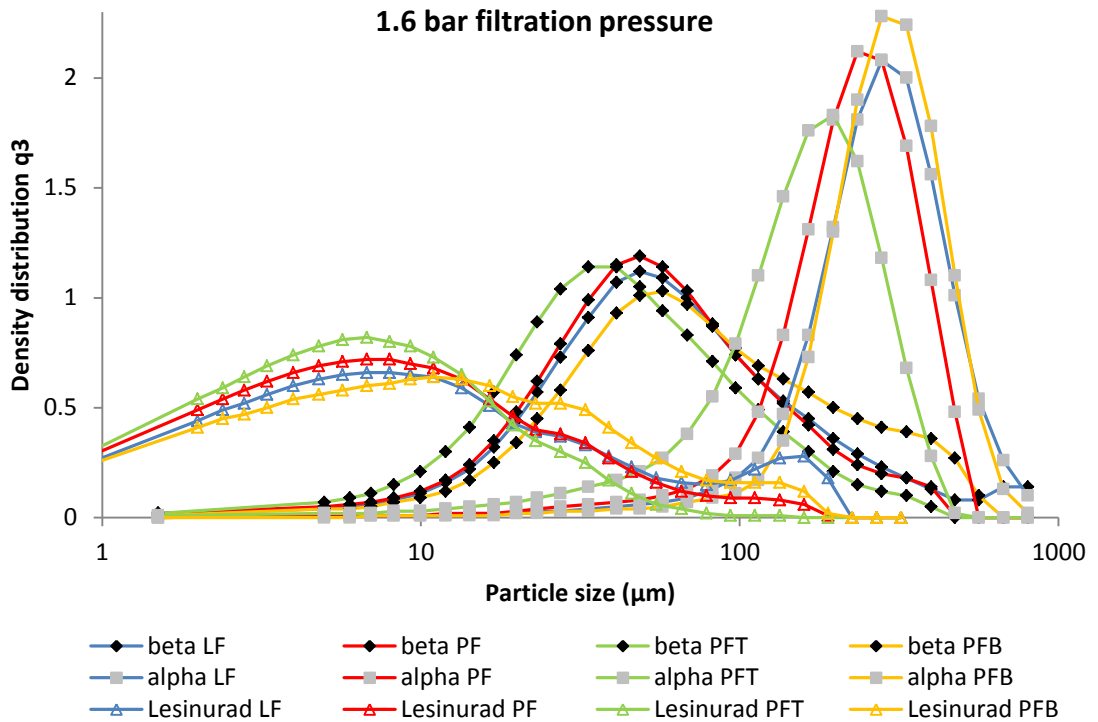


Figure 6-34: Particle size distributions for the 3 systems filtered at 1.6 bar

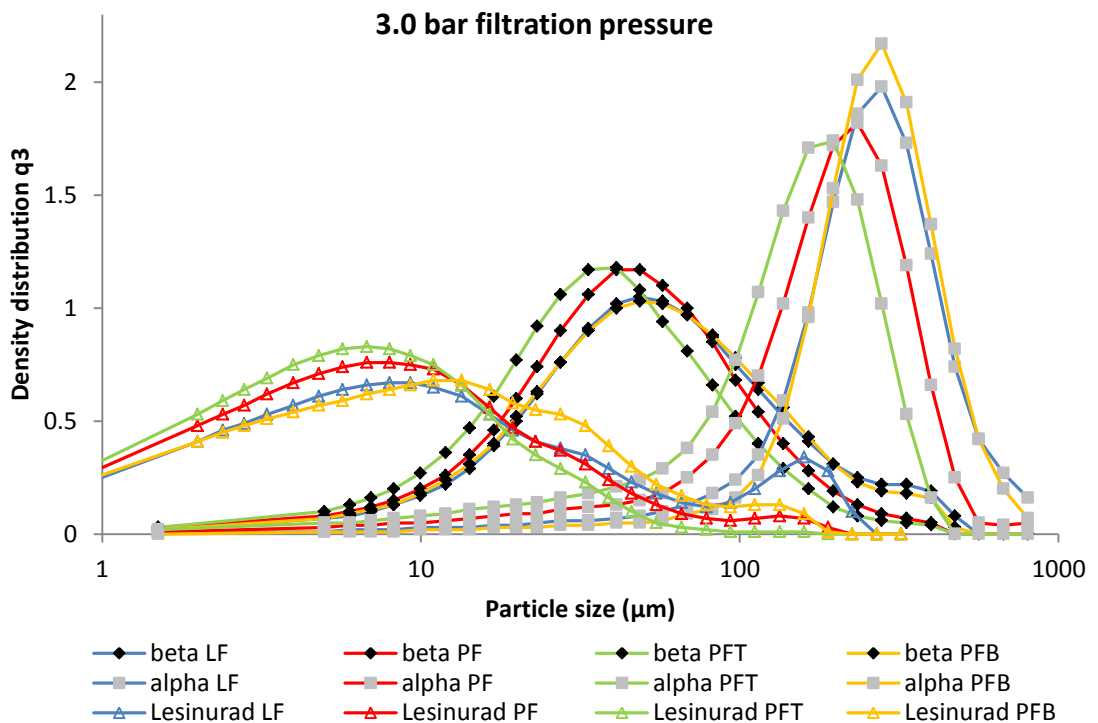


Figure 6-35: Particle size distributions for the 3 systems filtered at 3 bar

Figure 6-33, Figure 6-34 and Figure 6-35 highlight the differences in typical particle size between the compounds. Although not strictly of great importance to the particular study, it is

interesting to note the 'width' of the distributions, i.e. that alpha-glutamic acid has the narrowest distribution of sizes; the spread of particle sizes encountered are smaller than beta-glutamic acid, which in turn are smaller than for Lesinurad. This is likely due to the caking that occurs with Lesinurad; where small particles (which are more likely to agglomerate) can be imaged in the size analysis as larger particles than they truly are.

As the study set out to prove, it can be observed that for all 3 particle systems there is a reduction in size between the vacuum filtered LF samples and the pressure filtered PF samples. The reduction appears to be most evident at a filtration pressure of 3 bar, and is particularly noticeable with the alpha-glutamic acid. This is interesting to note, as this is not the typical particle morphology in which breakage is expected to be most pronounced; indeed microscopic image analysis did not allude to any particle breakage occurring.

One of the more surprising revelations concerns the size distribution of the particles at the top (PFT) and bottom (PFB) of the cake. If particle breakage were a significant factor in the outcome of the particle sizes, it would be expected that the particles at the bottom of cake, which are subjected to greater stresses due to the weight of particles above them, would experience more breakage, and thus would tend to be comprised of the smallest particles. Conversely, it would be expected that the particles at the top of the cake would be larger on average, due to them experiencing a lower stress.

What is observed is that the PFT samples are consistently the smallest of all 4 sample sources, whilst in some cases the PFB samples display larger sizes than even the reference point of the LF sample. Taking each system individually and plotting the distributions of all pressure filtered samples (PF, PFT, PFB) at all pressures yields the following figures:

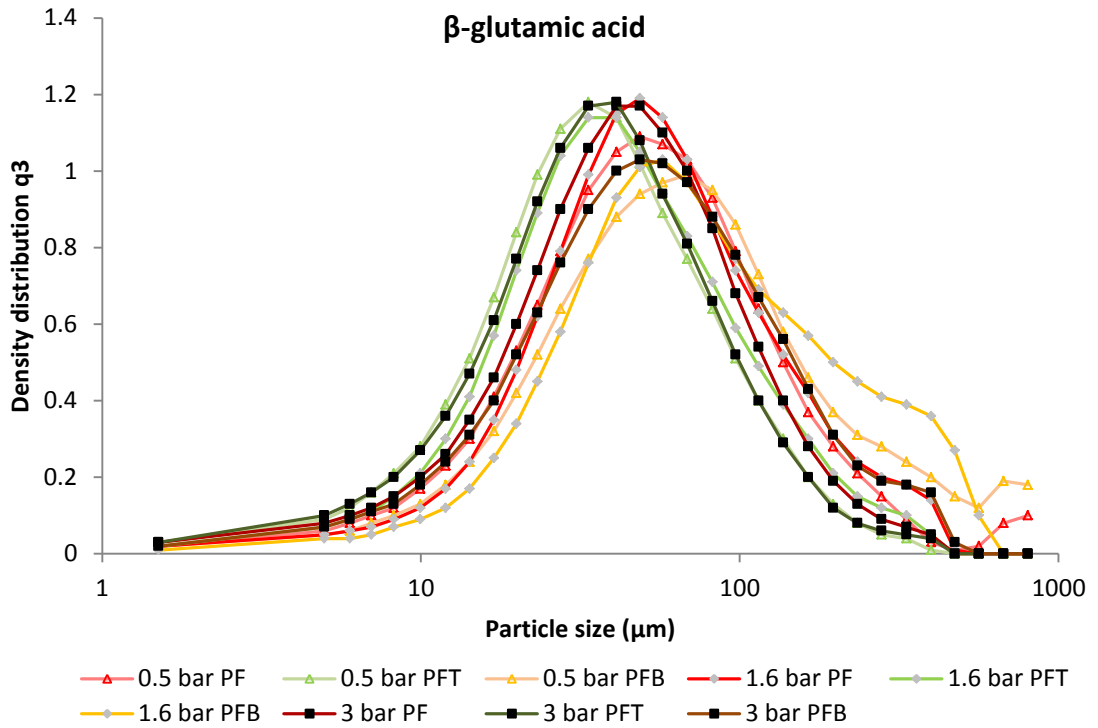


Figure 6-36: Size distributions of pressure filtered samples for beta-glutamic acid filtered at 0.5, 1.6 and 3 bar

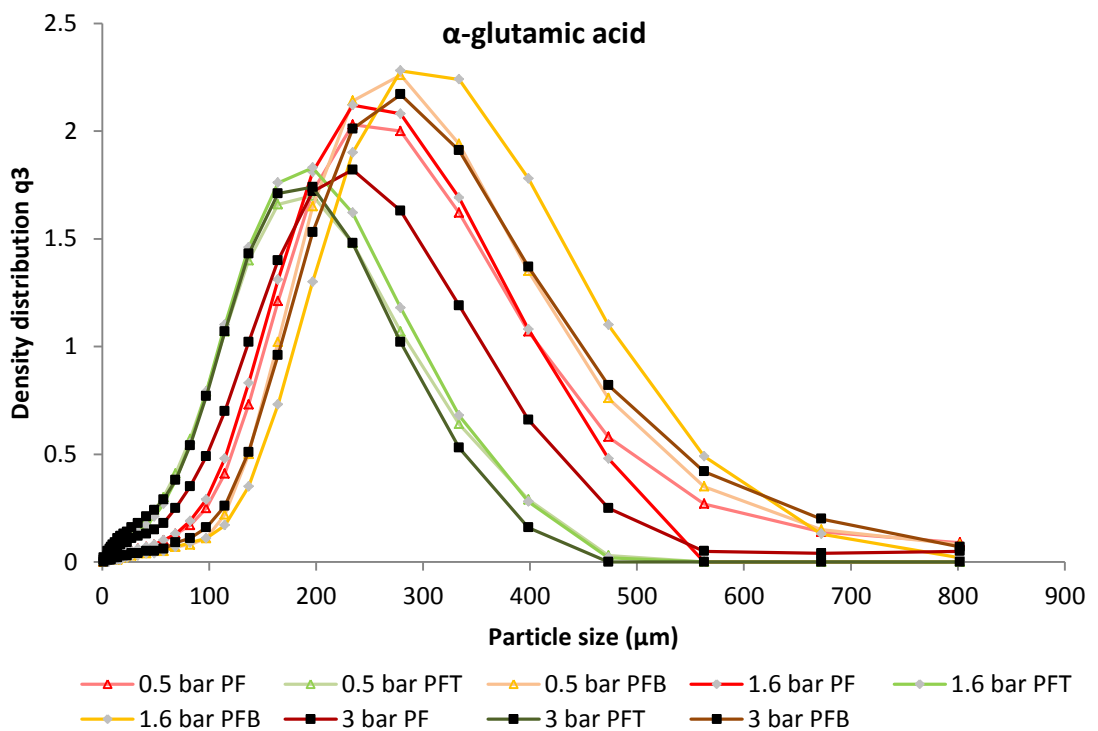


Figure 6-37: Size distributions of pressure filtered samples for alpha-glutamic acid filtered at 0.5, 1.6 and 3 bar

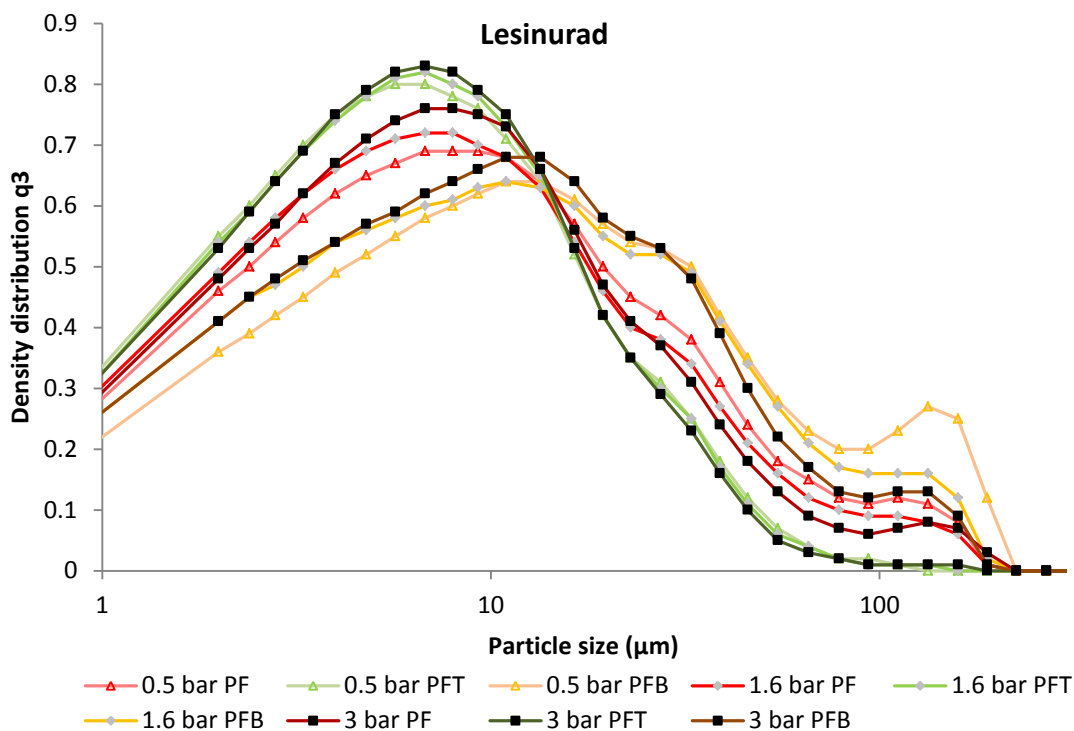


Figure 6-38: Size distributions of pressure filtered samples for Lesinurad filtered at 0.5, 1.6 and 3 bar

Observing Figure 6-36, Figure 6-37 and Figure 6-38, the changes to individual systems as a function of pressure is investigated. The PF samples of beta-glutamic acid, alpha-glutamic and Lesinurad all display a reduction in size as filtration pressure rises from 0.5 to 3 bar.

For beta-glutamic acid, the trend is weak from 0.5 → 1.6 bar, but strong overall when looking from 0.5 → 3 bar, although reductions in size are much more apparent in the smaller size ranges (< 100 microns). The 0.5 bar PF sample distribution is significantly larger in the higher size ranges (> 500 microns), although this could be the result of under-dispersion causing imaging of agglomerates, as discussed in section 6.3.4.4.

The alpha-glutamic acid displays a very clear trend of reduction between 0.5 → 1.6 → 3 bar, with a small trend in reduction in PFT with increasing pressure. The overall reduction in size of the PF samples is significant. With the exception of the 1.6 bar PFB sample which appears overly large, the sizes of the PFB particles are fairly independent of pressure (from 0.5 → 3 bar).

The Lesinurad samples, continuing the trend, also display a reduction in size that is apparent from 0.5 → 3 bar pressure; the reduction is apparent across all size ranges. The PFB samples also show significant size loss with increasing filtration pressure. The PFT distributions display the clearest trend yet of independence on pressure; particle sizes are almost completely identical across all size ranges.

For all 3 systems, the trend is clear – the PFB samples are larger than the PF which are larger than PFT. What is more interesting is the apparent independence of pressure of the PFT (and to a lesser extent the PFB) samples. It is possible that settling of the particles is the cause: as crystal suspensions are decanted from the crystallising vessel into the pressure filter, the particles have time to settle through the liquid before the filtration starts. For a particle in free-fall, its terminal velocity is dependent on the square of its diameter (this nominally applies to spheres but for low Reynolds numbers in which viscous effects are dominant the effect of particle shape is negligible)[15]:

$$v_t = \frac{d_p^2(\rho_p - \rho_f)g}{18\mu} \quad \text{Equation 6-7}$$

Hence larger particles will fall at higher velocities on average will be expected to settle on the bottom of the filter medium before smaller particles. This not only explains the unexpected result of the PFB particles being the largest and PFT being the smallest, but also explains the apparent independence of pressure on the size of the PFT particles. With a tendency for the PFB samples to show a slight dependence on pressure, and considering the microscopic image analysis, it is likely that breakage is still having an effect on these measured size distributions.

To test this theory, an additional experiment is proposed; a batch of beta-glutamic acid (priority given as it is the primary case study across this project) is filtered with the minimal possible head of nitrogen pressure (no filtration is experienced purely from natural gravitational forces in the pressure filter). The pressure regulator to the pressure filter is opened *very* slowly until liquid is observed to flow from the filter, at which point no further nitrogen is injected (this nitrogen flow is kept constant overnight for drying the cake).

The pressure inside is low enough that no movement on the pressure gauge dial is observed. For the purposes of notation this filtration is referred to as a '0' bar filtration, however the actual pressure is unknown. All that is certain is that the pressure is significantly less than that of the 0.5 bar filtration. Whilst a filtration at 0.5 bar pressure takes 30 seconds, this filtration is observed to last more than 6 minutes (the actual end-point is difficult to ascertain as the mass vs. time curve plateaus whilst liquid drops still flow out on occasion; timing is ceased at 8 minutes).

The aim of this experiment is to test the theories that the PFT and PFB samples are independent of pressure, whilst the PF sample is dependent on pressure (and thus that pressure directly impacts the size of particles). Figure 6-39 illustrates the particle size data for the 4 samples (which were obtained as normal).

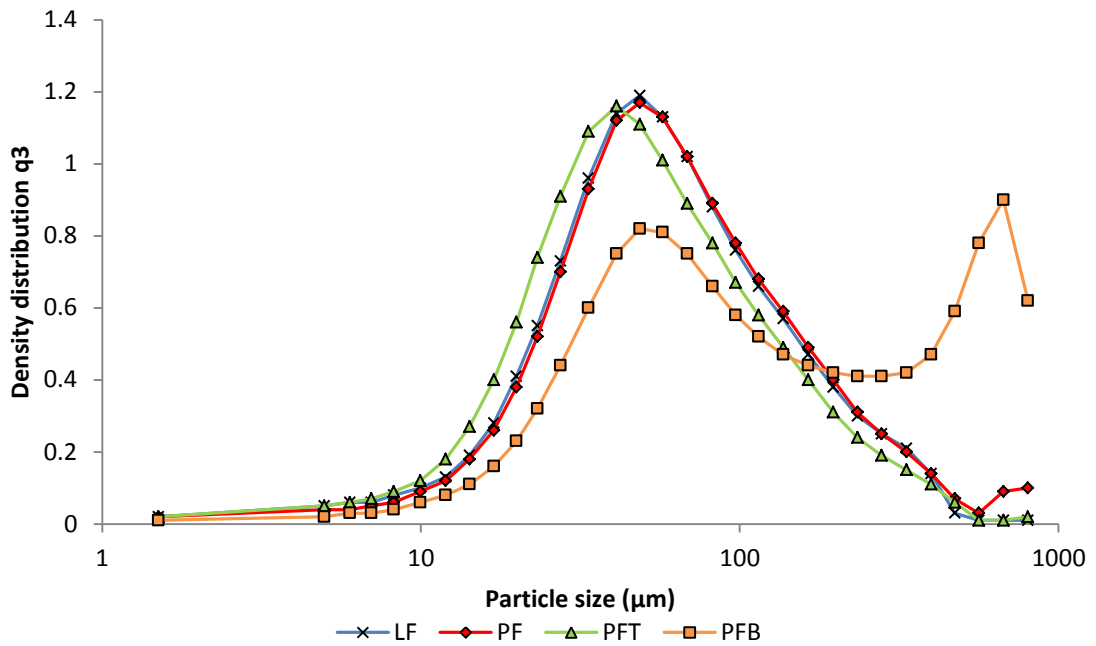


Figure 6-39: Particle size distributions for beta-glutamic tested with a minimal pressure ('0' bar) filtration

From the data the theory appears to hold; the LF and PF size distributions are similar in all size ranges, showing better correlation (and thus less size reduction) than even the 0.5 bar filtered LF/PF samples. The PF sample does appear to contain some oversized particles relative to the LF however, but again it is unclear if this is caused by under-dispersion.

The PFT sample is again significantly smaller across all size ranges, with the PFB sample concordantly displaying a greater size distribution. The bi-modal nature of the PFB distribution is likely due to some residual moisture remaining in the base of the cake after overnight drying (hence the pressure was low enough to not have even forced all liquid out of the cake), thus causing some agglomeration of sample material.

Whilst it can be argued that the PFB samples do show increased levels of crystal breakage (i.e. from microscopic images), the question remains why these particles are still consistently larger (sometimes even on par with the LF) in terms of size distribution.

The author believes that these microscopic image analysis reveal an answer to this paradox. Looking in particular to the needle systems and their PFB samples across all pressures, several very large fragmented crystals can be observed; some of these are highlighted in Figure 6-40.

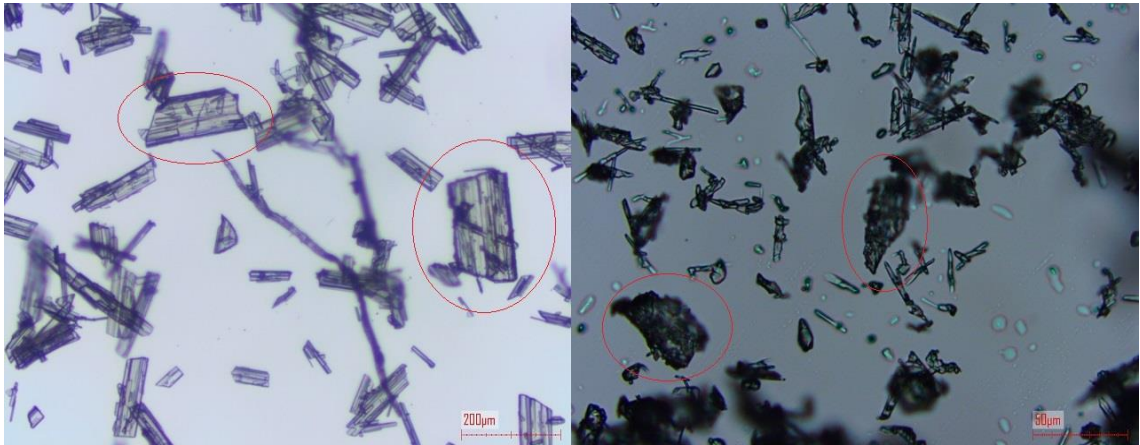


Figure 6-40: Large fragmented crystals in the 3 bar PFB samples of: (Left) beta-glutamic acid; (Right) Lesinurad

Even though these ‘stubs’ are clearly fragments (fractions of their original length), they are still among some of the largest particles in view; much larger than many of the typical particles observable in the PFT samples. One must remember that particles are imaged in 2 dimensions, and not classified in terms of aspect ratio. This means the projected area of a particle is much more important to determining its ‘size’ by laser diffraction.

Thus although these fragments may have equal or lesser length to needles in the PF or PFT samples, their significantly larger widths will contribute to their having greater overall imaged size. This does raise into question the legitimacy of using the Sympatec HELOS to detect particle breakage however.

Nonetheless, the reason behind the larger size distribution of the PFB samples is most likely a combination of the settling of larger particles to the bottom of the filter initially; followed by increased breakage with the large high-width fragments remaining in this region, where they are ultimately imaged as large particles.

The issue of aspect ratio is investigated further in section 6.3.4.6 by use of an alternative data source.

6.3.4.5.3 Changes in size fractions of the distribution

Qualitative analysis of the size distribution curves is followed with a quantitative analysis of the size changes occurring in the crystal beds. Numerical data from the distributions is used to define the fractions f_s , f_m and f_L , which are the fraction of ‘small’, ‘medium’ and ‘large’ sized particles in the distribution, respectively. As the typical sizes of the 3 case study systems differ (i.e. the distributions have different spreads), these are defined individually for each system. Each fraction is the ratio of the cumulative volume of particles within the size ranges defined to that of the total volume of all particles in the dataset.

It is idealised that the fractions are defined in the ratios 25:50:25; i.e. that 'f_s' is defined as the smallest 25% of particles of the 'LF' 0.5 bar distribution, as a reference point. The fractions 'f_m' and 'f_L' then make up the next 50 and 25% respectively, both still with respect to the 0.5 bar reference point. In reality the fractions are not exactly 25:50:25, but as close as possible as the data will allow (some overlap is experienced due to the small number of brackets that the data is organised in).

The ratio is also expected to change significantly across filtration pressures and for 'PF' sample data; this is intended of course, as this will highlight the physical changes occurring in the particle beds, and specifically in which size regions the changes occur.

For each particle system this results in a set of arbitrary particle sizes from which the fractions f_s, f_m and f_L are bound; these are listed in Table 6-13.

Table 6-13: Particle sizes binding the size fractions f_s, f_m, f_L

Compound	Particle size defining boundary (µm)		
	f _s	f _m	f _L
β-glutamic acid	27.39	57.28	114.56
α-glutamic acid	196.72	278.88	398.47
Lesinurad	4.78	10.95	32.86

The difference between the fraction of f_s, f_m and f_L of the LF samples and that of the PF samples is plot for each compound, with the full data available in Table 6-14.

Table 6-14: Calculated f_s, f_m, f_L, Δf_s, Δf_m and Δf_L for β-glutamic acid, α-glutamic acid and Lesinurad

P (bar)	LF f _s	PF f _s	LF f _m	PF f _m	LF f _L	PF f _L	Δf _s	Δf _m	Δf _L
β-glutamic acid									
0	0.2081	0.1914	0.5540	0.5479	0.2379	0.2607	-0.0167	-0.0061	0.0228
0.5	0.2448	0.2693	0.5035	0.5377	0.2517	0.1930	0.0245	0.0342	-0.0588
1.6	0.2181	0.2385	0.5296	0.5549	0.2523	0.2065	0.0204	0.0254	-0.0458
3	0.2619	0.3125	0.5160	0.5505	0.2220	0.1370	0.0505	0.0345	-0.0850
α-glutamic acid									
0.5	0.2955	0.3991	0.4444	0.4353	0.2602	0.1656	0.1036	-0.0091	-0.0945
1.6	0.2828	0.4282	0.4513	0.4520	0.2659	0.1197	0.1455	0.0007	-0.1462
3	0.3543	0.5596	0.4281	0.3591	0.2175	0.0813	0.2053	-0.0690	-0.1363
Lesinurad									
0.5	0.2664	0.3167	0.4740	0.5249	0.2596	0.1584	0.0503	0.0510	-0.1013
1.6	0.3043	0.3413	0.4826	0.5238	0.2130	0.1349	0.0369	0.0412	-0.0781
3	0.2844	0.3386	0.4880	0.5447	0.2277	0.1167	0.0542	0.0568	-0.1110

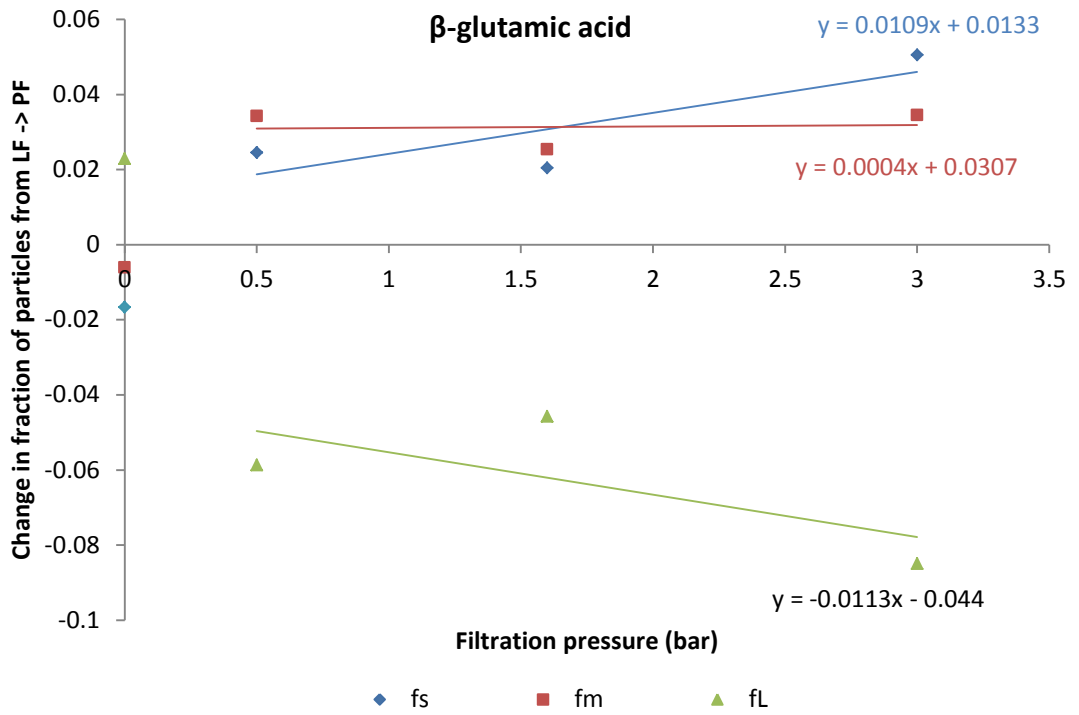


Figure 6-41: Changes in particle size of LF and PF samples of beta-glutamic acid

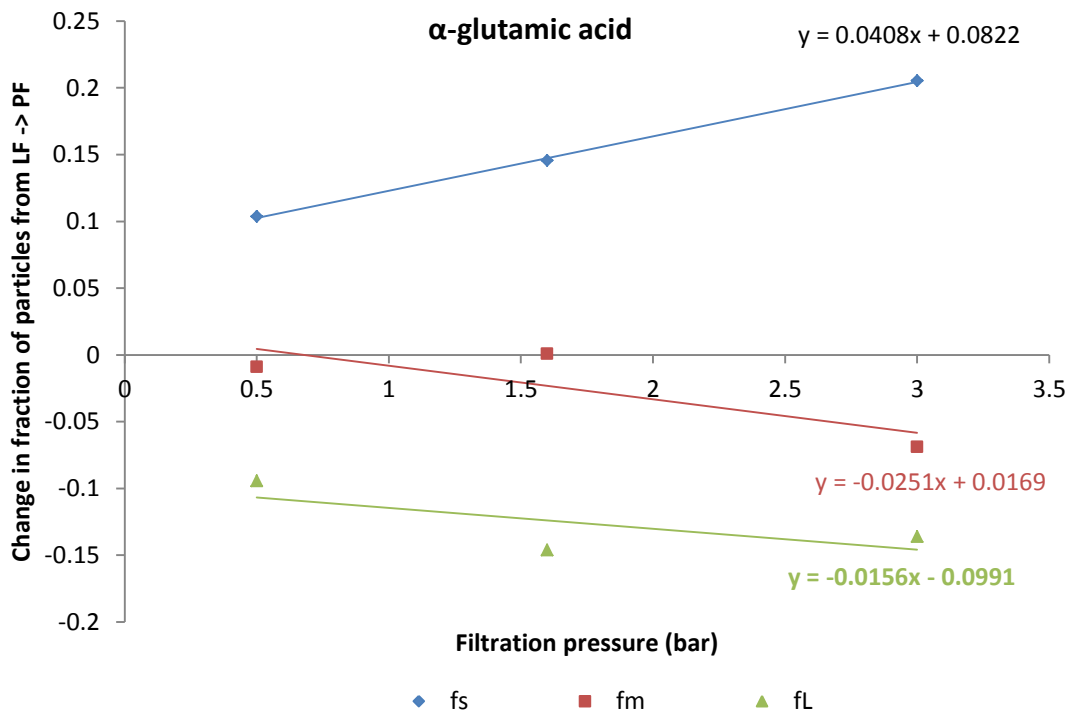


Figure 6-42: Changes in particle size of LF and PF samples of alpha-glutamic acid

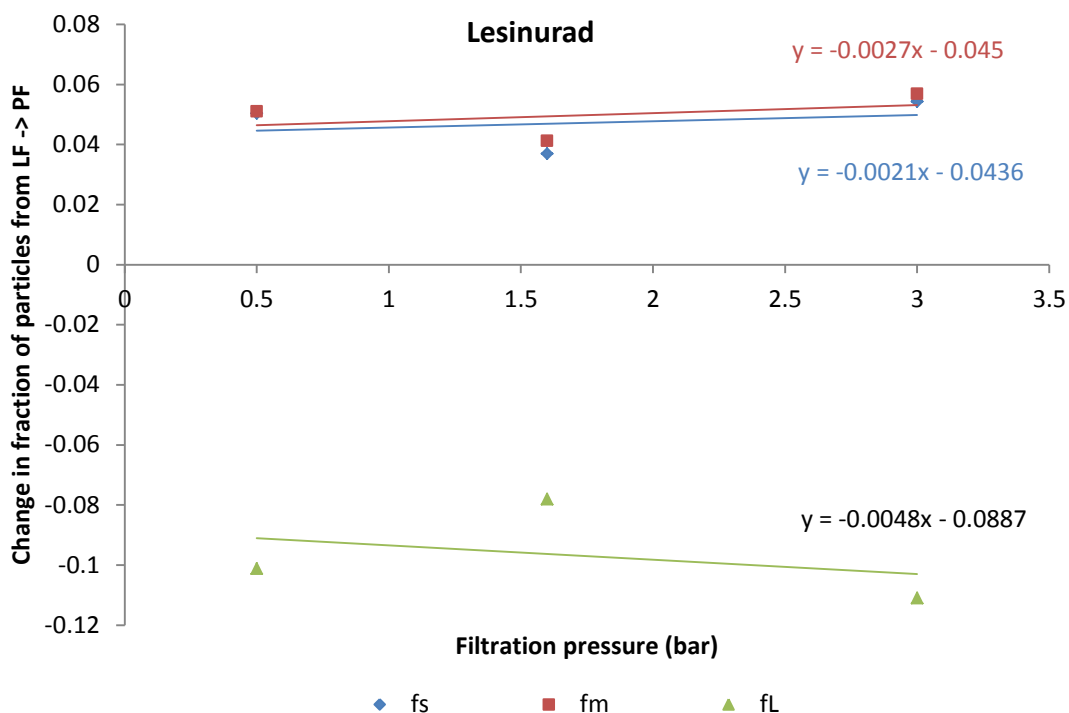


Figure 6-43: Changes in particle size of LF and PF samples of Lesinurad

The data in Figure 6-41, Figure 6-42 and Figure 6-43 illustrate quantitatively the findings observed from the particle size distributions; namely that particle size reduction occurs in the pressure filtered samples when compared to the 'lightly' vacuum filtered samples; this occurs in all 3 particle systems but are most pronounced with the alpha-glutamic acid and least so with Lesinurad (taking gradients of lines as indicators).

For the beta-glutamic acid the data from the '0' bar filtration is included for posterity, but does not appear to match the trends of filtrations at > 0 bar, although the general changes in size are less pronounced overall (i.e. all values are closer to 0, of which indicates no change), meaning these are more open to random fluctuations.

The change in fraction of 'medium' sized particles in this system appears less dependent on pressure but does increase consistently for all pressures tested. This could be an indication of the mechanism of fraction by which beta-glutamic acid crystals break; i.e. they would be expected to be more likely to cleave into 2 particles of roughly half the length of the parent particle, as opposed to any form of attritional breakage; hence the greater influence of pressure on the small and large particles. As seen from microscopic analysis, increasing pressure appears to produce more small fragments, meaning the extra energy imparted is likely going towards total fracture of the largest particles into fines.

The needle-cleavage mechanism would be in opposition to e.g. the alpha-glutamic mechanism, of which its prismatic crystals would be less expected to fracture into 2 or more fragments but

are more likely to suffer from attrition – this may explain why the fraction of small particles increases greatly whilst the fractions of medium and large particles both show decreases as a proportion of the total. Of the 3 systems only the alpha-glutamic acid displays a reduction in the fraction of the medium-sized particles.

The alpha-glutamic acid crystals are also much larger overall in nature and hence have larger exposed surface areas from which viscous drag from the down-flowing filtrate acts; therefore the forces experienced on the surfaces of these particles is likely to be higher and could be contributing to the increased levels of size reduction observed. Being such large particles however, the possibility of settling of the particles under suspension is much more likely.

Conversely the Lesinurad, being the smallest overall particles, display a very weak correlation of size reduction against pressure, perhaps showing that the increased viscous drag at higher pressures has less of an influence of these tiny crystals. They do however display fairly consistent levels of size reduction regardless of pressure, which could point to other mechanisms of size reduction, namely experimental procedure (breakage by retrieving the particles from the filter), which cannot be entirely ruled out.

This could also point to differences in bed structure – smaller particles being able to pack tighter are expected to have a greater number of particle-particle contact points, which would spread the forces experienced over a larger area, and thus contribute to reduced stresses on the particles.

6.3.4.6 Morphologi G3 data analysis

Numerical data from the beta-glutamic acid needles is obtained by use of the Morphologi G3 optical microscope. As a full complement of raw data is obtained from the instrument, this method allows quantification of the aspect ratios of the crystals, among other particle properties, which can be manipulated into the figures below; all plots are generated as described by the methods in Chapter 5. Technically although these distributions are histograms, they are plot as continuous distributions for ease of viewing.

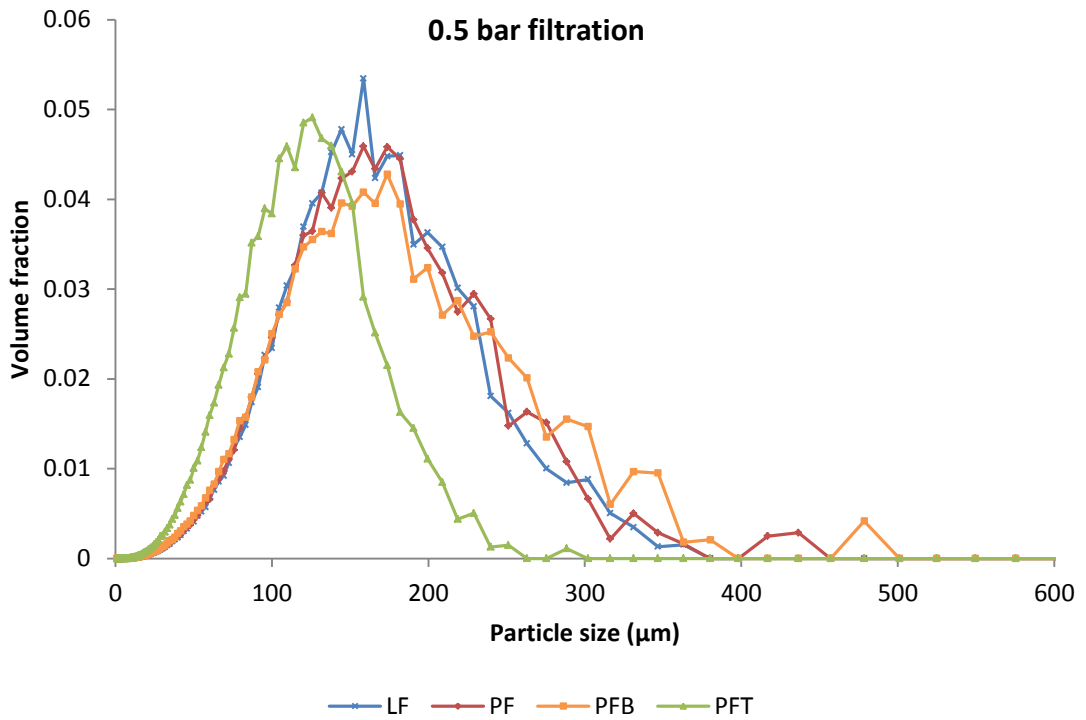


Figure 6-44: Volume distribution for 0.5 bar filtration of beta-glutamic acid

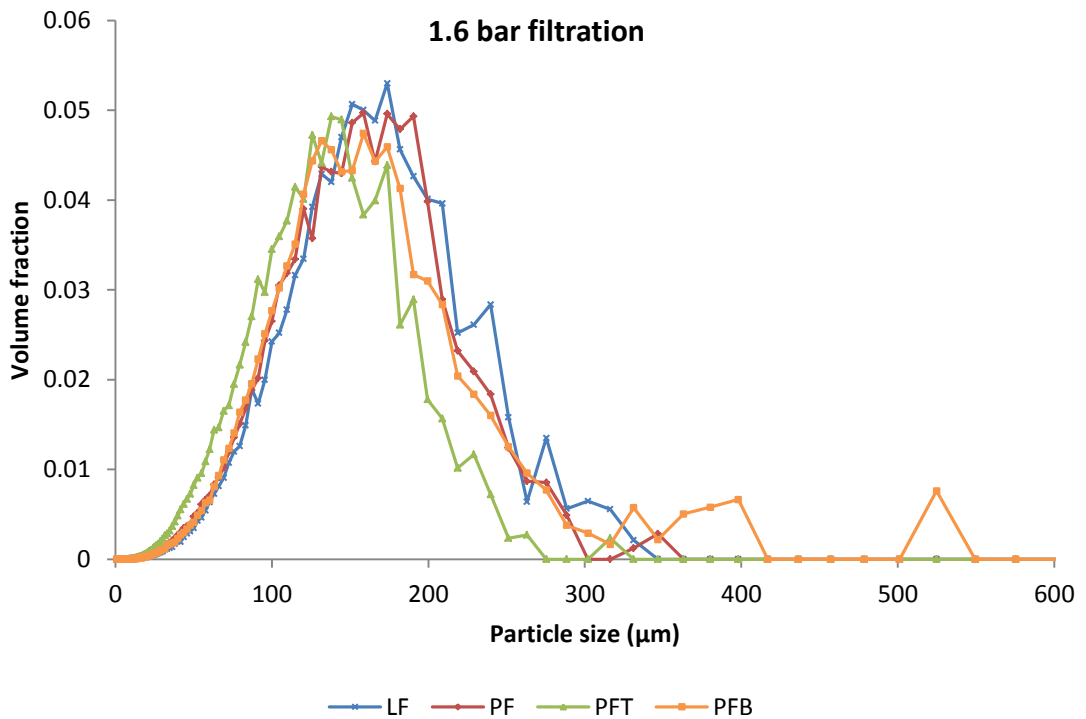


Figure 6-45: Volume distribution for 1.6 bar filtration of beta-glutamic acid

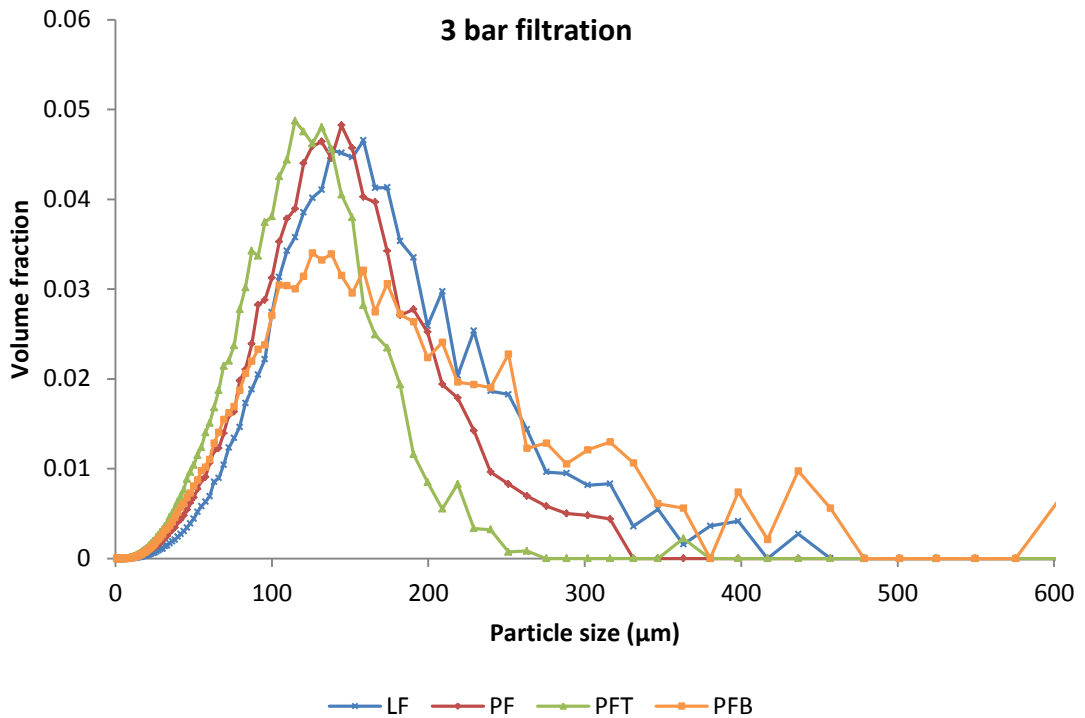


Figure 6-46: Volume distribution for 3 bar filtration of beta-glutamic acid

The volume distributions present the data in a similar method to that utilised by the HELOS laser diffraction instrument, hence the curves provide an indirect comparison to the performance of the equipment; although however the data in Figure 6-44, Figure 6-45 and Figure 6-46 have been subjected to ‘filtering’ of the data (see Chapter 5).

From observations of the figures, and as has been previously discussed, the size distributions of the PFT samples appear relatively constant whilst the differences in size between the LF and PF appear to diverge as filtration pressure rises. Again it is observed that the LF and PFB size distributions appear roughly equal in size, and the ‘widening’ of the PFB distribution as pressure rises is also apparent, even with filtering of ‘non-particles’ from the data. At 3 bar, the PFB distribution is particularly wide (indicated by the low peak height relative to the other curves, and the presence of large portions of volume in the large particle size ranges of 400+ microns).

The following figures depict the data with particles modelled as cuboidal boxes (particle length * particle width * 0.5 * particle width). These modelled distributions are displayed alongside the aspect ratio distributions of the particle data. Generation of these curves is possible with the particle properties measured by the Morphologi G3.

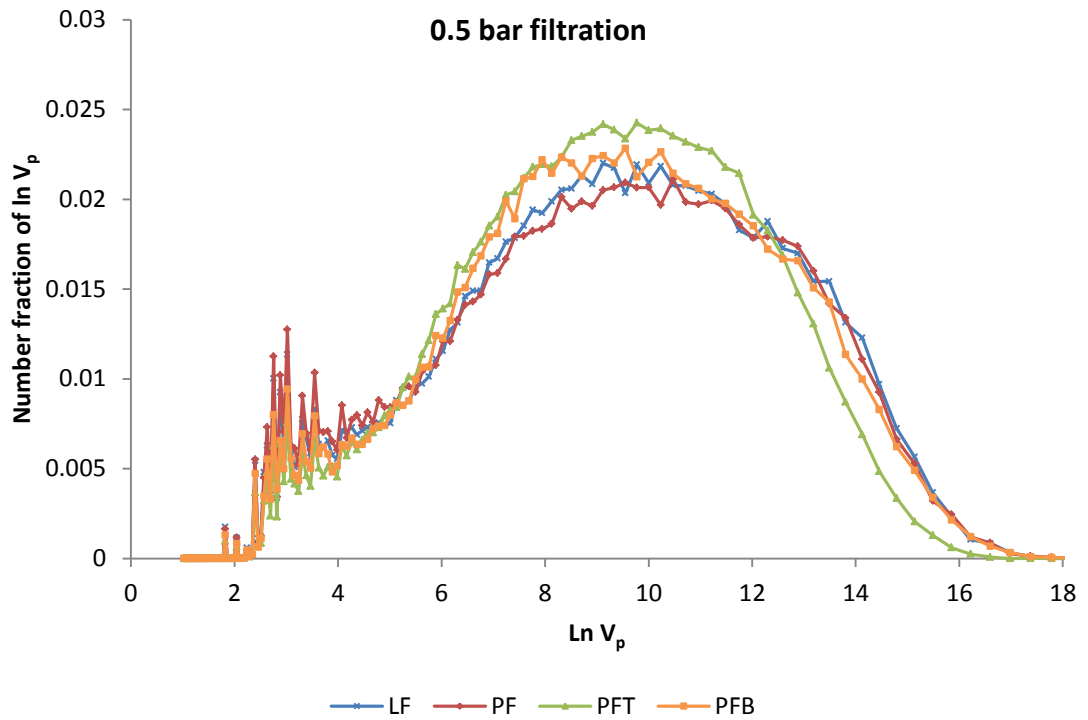


Figure 6-47: $I_p * 0.5 * w_p^2$ distribution for 1.6 bar filtration of glutamic acid

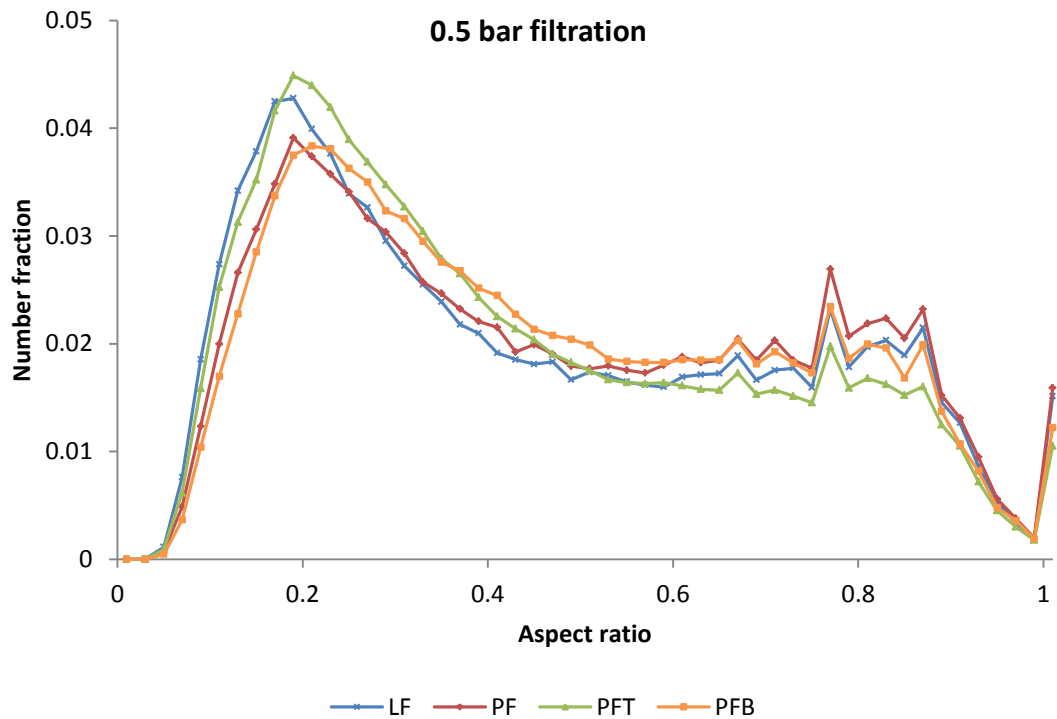


Figure 6-48: Aspect ratio distribution for 0.5 bar filtration of beta-glutamic acid

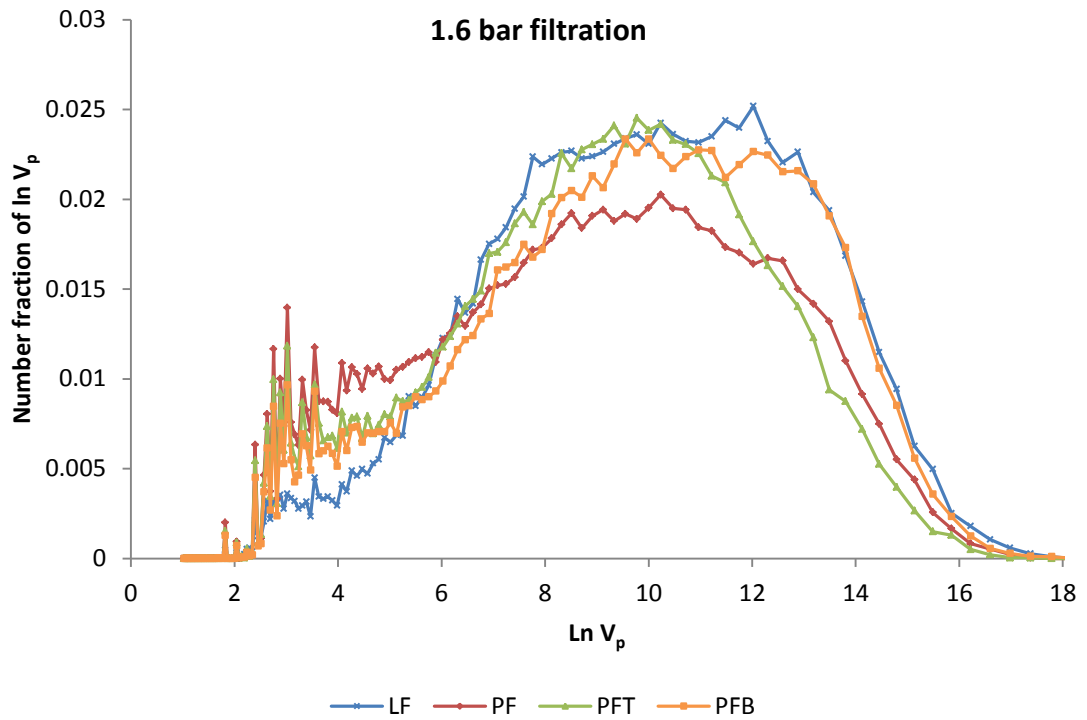


Figure 6-49: $I_p * 0.5 * w_p^2$ distribution for 1.6 bar filtration of glutamic acid

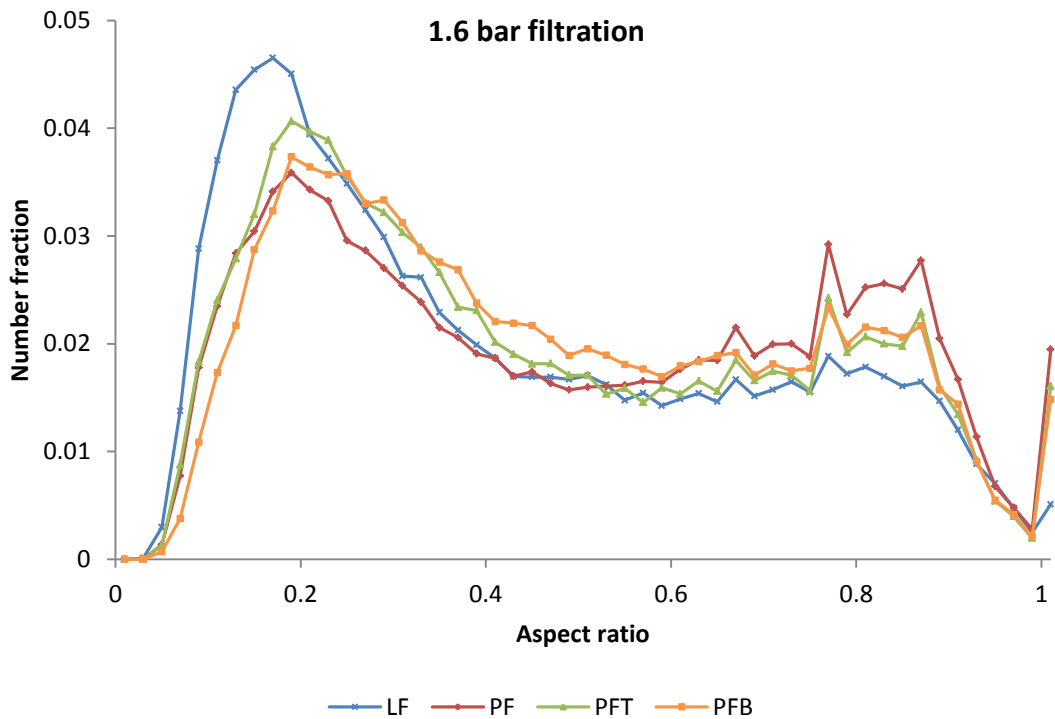


Figure 6-50: Aspect ratio distribution for 1.6 bar filtration of beta-glutamic acid

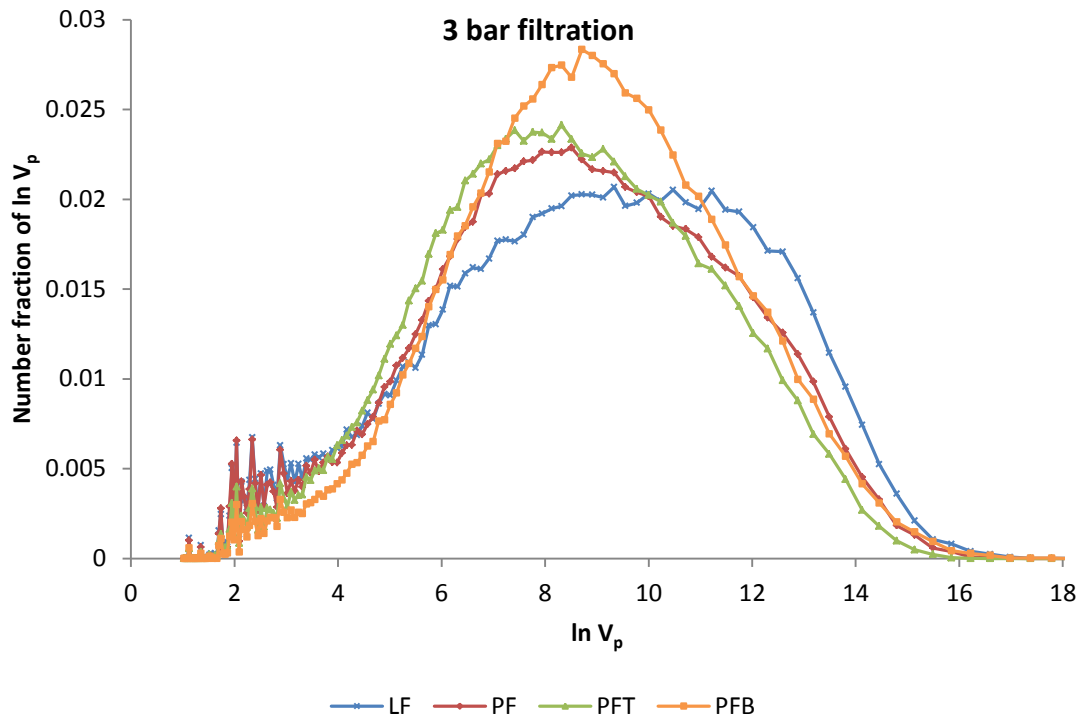


Figure 6-51: $I_p * 0.5 * w_p^2$ distribution for 3 bar filtration of glutamic acid

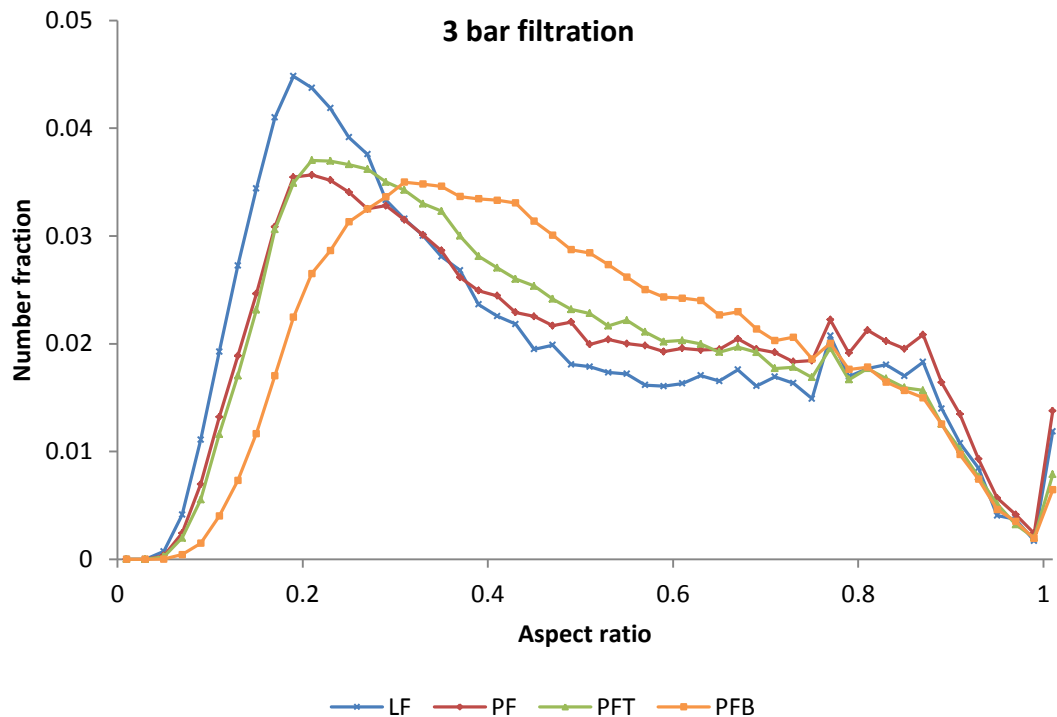


Figure 6-52: Aspect ratio distribution for 3 bar filtration of beta-glutamic acid

At 0.5 bar filtration pressure (Figure 6-47 and Figure 6-48) the modelled size distributions appear roughly equal (excluding the PFT samples which still display reduced size), whilst the aspect ratio distribution displays a clear difference between the LF/PFT and the PF/PFB samples. This is crucial as evidently the aspect ratio is not dependent on particle size; the PFT

sample shows clear reduction in size based on volume and modelled size distributions yet appears more elongated than the PF/PFB samples and roughly similar elongations to the unfiltered LF material.

This would appear to suggest that the LF and PFT samples have a greater proportion of their particles retaining their elongation under measurement.

The differences in aspect ratio highlight the importance of the additional particle properties measured by the G3; both the volume and modelled distributions display few differences for the LF, PF and PFB samples.

At 1.6 bar filtration pressure the differences become more apparent. The volume distribution (Figure 6-45) showed only subtle changes in size distribution for the LF and PF samples, yet the modelled distribution (Figure 6-49) highlights greater differences in size between the 2 samples. The PFB samples still appear roughly equal in size to the original LF samples, perhaps (as previously alluded to) due to measurement of the large fragments originating from this region of the bed.

The aspect ratio distribution (Figure 6-50) again highlights well the changes in particle elongation that are undergone during the pressure filtration. The vacuum filtered LF particles now display a clear difference in aspect ratios compared to all of the pressure filtered samples, indicating the effect of the increased pressure; even the particles at the top of the cake are now suffering from reduced elongation (although not as much as the PFB samples).

When filtering at 3 bar pressure, the modelled distribution (Figure 6-51) now displays a reduction in size for the PFB samples when compared to the LF. This indicates that the level of breakage is now at a stage in which the large fragments are breaking into smaller fragments, thus shifting the curve left to the smaller size ranges.

The aspect ratio distribution (Figure 6-52) correlates precisely to what is expected; the non-pressure filtered LF samples retain the highest proportions of elongation, followed by the pressure filtered PF and PFT samples. The PFB samples display a greatly reduced elongation compared even to the PF/PFT, as evidenced by the microscopic analysis in Table 6-8. Perhaps the only surprise is that there is no discernible difference between the PF and PFT (one might have expected slightly reduced breakage at the top of the cake); however the microscope images did not elude to any significant differences thus it should not be considered an unexpected result.

6.4 Conclusions

A series of experiments have been conducted in both continuous (a new method) and batch (traditional) filtration. Corresponding analysis methods have also been developed in order to characterise the particle size reduction and verify the validity of the particle data (Chapter 5).

The findings of size reduction under filtration, although difficult to quantify between differing crystallisation and analysis methods, agree with those of Macleod and Muller[9], and to a lesser extent with Hamilton et al[5]. Hamilton et al observed low levels of size reduction under filtration but only filtered at 0.5 bar pressure; under which it is shown in this work that levels of breakage are low. However it is difficult to make comparisons as the authors did not include images of the crystal morphology (they reported high aspect ratio needles).

Particle breakage is observed for all flowrates (CPR) and pressures (2 L), although the extent of breakage at low flow/pressure is minimal. This has been confirmed with optical microscopy of powder samples. Levels of size reduction are shown to increase approximately linearly with rising driving force, although evidence for alternative modes has been presented.

The breakage of glutamic acid has been studied extensively in both continuous (percolation) and batch mode. Evidence from continuous operation has revealed the critical points of breakage that are evident from increasing the driving force of filtration (compressive forces); thus it is apparent that large and elongated particles are much more likely to break than smaller and/or more rounded particles. This is predicted by beam bending theory and is thus a validation of that theorem to these needle-like particles.

Another key aspect of particle breakage concerns the time scales of operation; both from batch filtration (time scale of 10s of seconds to a few minutes) and short-term percolation (5 minutes), both of which display considerable size reduction when compressive forces are high. Percolation over longer timescales (2 hours) display no additional breakage when compared to short-term percolation. Thus it can be concluded that particle breakage for beta-glutamic acid is a time-independent process, and is only dependent on the peak forces of compression that are imparted to the bed. This finding agrees with that of Cornehl et al[10].

Under batch filtration the extent of particle size reduction is obscured by the settling of particles before the beginning of filtration; this is apparent due to the consistency of particle size in the samples taken from height fractions in the cake. These observations are not observed in the CPR samples which are not given the opportunity to settle.

Size reductions in alpha-glutamic acid beds appear to be greater than those of the needle-like beta-glutamic acid and Lesinurad systems. This is unexpected as the alpha-polymorph displays

less obvious breakage under microscopy – although attritional breakage of these particles is likely the predominant cause. More experimentation is required in this area to elucidate the filtration and breakage mechanisms associated with the blocky alpha-glutamic acid.

In terms of instrumentation the Sympatec HELOS particle sizer provides a statistically relevant confirmation of particle size reduction, but the data is lacking in depth. Conversely the Morphologi G3 supplies a much greater depth of data, allowing for manipulation of individually measured particle properties, but lacks the statistical strength of the laser diffraction method; additionally the method is highly labour intensive and sample times can range from 40 – 90 minutes (compared to several milliseconds for laser diffraction). Ideally both techniques are used in complement to one another. The size distributions observed in the Sympatec and Morphologi instruments provide a good match on the whole.

Chapter 7

7 Investigation into the Centrifugal Settling Behaviour of Crystal Beds

7.1 Introduction

The LUMiSizer, manufactured by LUM GmbH, is a temperature controlled bench-top centrifuge for the comprehensive characterisation of emulsions and suspensions. The unit comprises a centrifuge disk capable of rotating up to 12 samples at speeds of up to 4000 rpm.



Figure 7-1: The LUMiSizer benchtop centrifuge

By imparting a centrifugal force to the liquor contained within a sample cell, pressure is applied to the material inside, not unlike how a pressure filtration applies pressure to static crystal beds. The pressure at any point can be calculated from the relationship between the force of centrifugal acceleration and the static pressure in the fluid, thus providing a degree of comparability to a standard filtration of any particular pressure drop.

Samples are illuminated with near-IR radiation (865 nm beam) from the top-down. The detector lies beneath the centrifuge disk, meaning any radiation that is received must pass through the cell in order to reach the detector. The polymer sample cells are transparent to this radiation, whilst solid particles block the light from reaching the detector; this produces a high-low output (high: radiation received by the detector by passing through the cell; low: little or no radiation is received by the detector as it has been absorbed by the solid contents).

The signal received by the detector varies with cell height (or radial distance from the centrifuge), meaning the LUMiSizer can be used to determine the spatial extents to which the solid particles occupy within the sample (Figure 7-2).

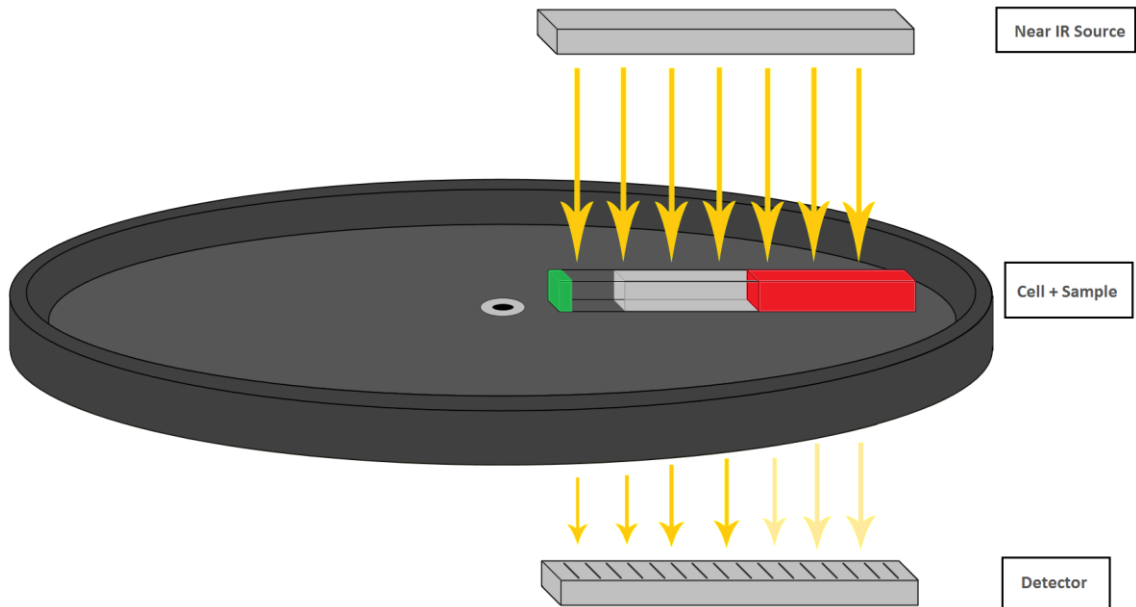


Figure 7-2: LUMiSizer measurement technique; IR source produces radiation which is either transmitted or scattered by the sample contents (Reproduced from LUM GmbH)[127]

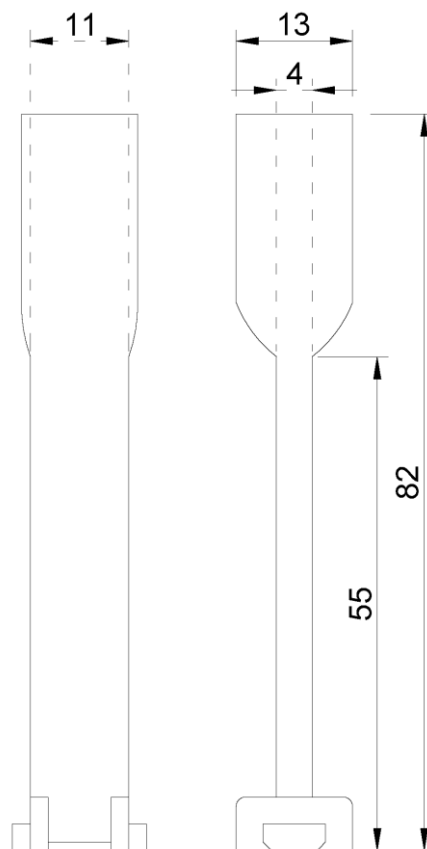


Figure 7-3: Schematic of LUMiSizer polymer sample cell (dimensions in mm)

Sample cells (Figure 7-3) lay flat on their sides (as in Figure 7-2); their longest dimension; meaning under rotation material is forced along a radial path towards the outer edges of the centrifuge disk. The faster the centrifuge rotates, the greater the centrifugal force, hence the crystal bed is subjected to greater stresses.

By recording the transmitted light over time the limits of the crystal bed can be tracked, as more/less light is able to pass through the sample due to structural changes. Clear liquid solvent provides a degree of transparency for radiation to pass through to the detector. If the level of solid in the bed falls over time due to bed consolidation, then the ratio of [liquid:solid] volume fraction within the sample cell increases, hence the amount of radiation passing through the cell unimpeded rises. If the height of solid increases, e.g. due to relaxation of the bed when the centrifugal force is reduced, then similarly the ratio of [liquid:solid] volume fraction falls, and hence a lower proportion of incident radiation is received by the radial detector (see Figure 7-4).

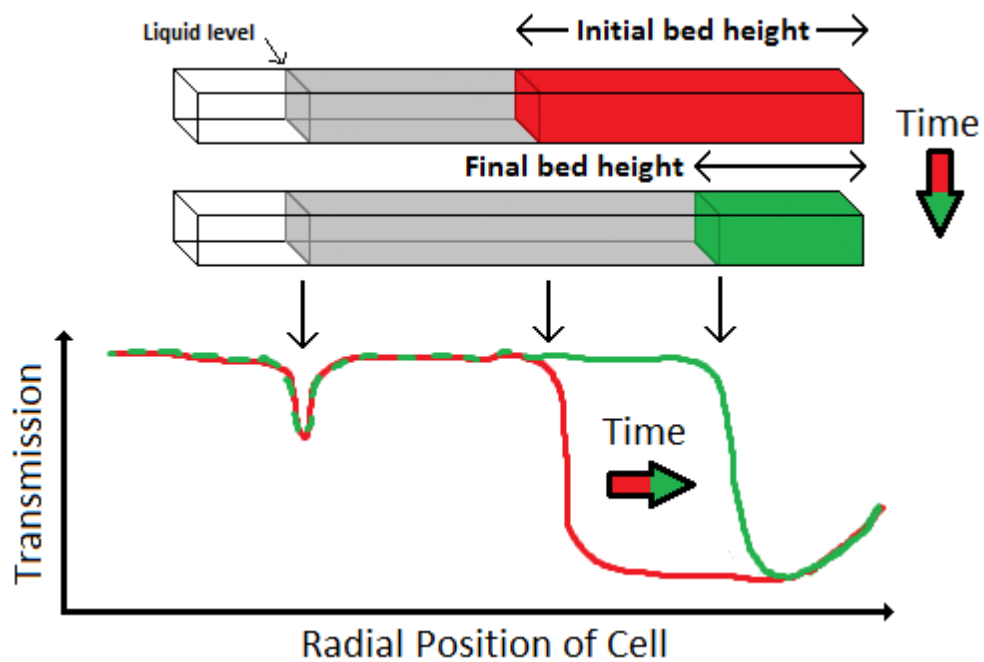


Figure 7-4: LUMiSizer bed height can be tracked through monitoring of transmitted radiation over time (Reproduced from LUM GmbH)[127]

As the radiation received along the length of the detector is indicative of the liquid:solid ratio, the end result is a unit capable of measuring the 'height' of the crystal bed over time.

The result can be compared with larger scale pressure filtrations due to the similarity of the forces acting on the bed. The particles are still compressed under a certain pressure, with the weight of its neighbouring particles also acting on it. A particle is either supported by the filter medium, or the cell base; both provide the solid surface with which the particle bed is compressed into.

Particles remain in the mother liquor throughout the centrifugation; hence the result is more applicable to slow filtrations, or those at large scales, for which the particles also stay wet for extended periods under pressure.

The LUMiSizer cells however, obviously cannot allow liquid to pass through their base, hence the usual forces imparted by viscous drag of filtrate flow through the particle bed is here replaced by the centrifugal force imparted by rotation.

The LUMiSizer therefore presents an opportunity for the study of small-scale 'crystal beds' and their reaction to the force of centrifugal acceleration.

7.2 Literature Review

7.2.1 Background

A centrifuge is in some respects similar in operation to a pressure filter; both involve the application of a driving force to a solid-liquid suspension in order to mechanically separate the phases. Centrifuges find wide application in the field of sedimentation, where they essentially provide the same function of large gravitational settling tanks (e.g. for water clarification) but with a much greater settling power (and therefore greater rate/throughput). As the form factor is much smaller than that of settling tanks (which are typically characterised by their surface area available for sedimentation), they are a popular choice as their power per unit area is so small[128].

The rate of settling of particles in a fluid is normally (with sufficiently low solid fraction) governed by Stokes laws i.e. settling is proportional to the relative particle density in the fluid and the square of the particle diameter, and inversely proportional to the fluid viscosity. At higher solid fractions settling is termed 'hindered'[128].

'Hindered settling' refers to the mechanism by which the descent of the particles through the fluid, which would otherwise be governed by the Stokes velocity, is affected by particle-particle and particle-fluid interactions[129, 130]. This is dependent on 2 factors: the extent of displacement of fluid by the falling particles (which causes a back-flow of fluid through the inter-particle voids), and an increase in particle drag caused by the interaction between neighbouring particles' velocity fields[15].

Of course with centrifugal operation, the rate of settling is also dependent on the rotational acceleration, not gravity. This is discussed with a derivation of the appropriate models in section 7.4.

Initial stages of centrifugation concern the 'free-fall' state of particles as they settle through the fluid. At this early stage, weak networks begin to develop between the particles in contact with one-another. As the particles are in free-fall however, the effect of weight felt from particles above, even those within the network, is minimal. Particles nearest the bottom of the centrifugal chamber begin to consolidate as they approach the limits of the vessel[131].

As bed consolidation continues the volume fraction of solids approaches a critical value, where the network of particle contacts assumes the properties of a solid structure. At this point compressive stresses are transmitted throughout the structure via the networked contacts and the bed is able to offer some form of resistance to compressive forces[132].

If the strength of the network is high enough the bed is able to resist collapse from the strength of the inter-particle bonding and the upward drag of liquid that is displaced from the structure. This liquid drag acts to partially balance the effects of the compressive stress; hence this explains the slow collapse of the structure over a period of time. As sedimentation continues the height of bed increases until a point of equilibrium is reached, at which point the forces are balanced and no further consolidation occurs[129].

Up until this point, the network of particles is able to absorb compressive pressure in the form of elastic strain energy, and any compaction due to pressure can theoretically be reversed by withdrawal of the compressive force. As pressure is further increased, a critical point is reached at which the bed network yields and a period of collapse is initiated via the breakage or rearrangement of particle-particle contacts; this results in an irreversible compaction[132].

It can therefore be inferred that the bed possesses an elastic limit; below which the bed is able to return to its original state, and beyond which the bed behaves plastically and thus permanent deformation results in a higher solids concentration structure[131].

7.2.2 Use of the LUMiSizer

In terms of existing literature on the use of the LUMiSizer for investigation of pharmaceutical compounds is very limited. This is not unexpected of course, as the instrument finds its primary use in the analysis of colloidal and inorganic material, of which the effectiveness of suspensions and their propensity to sediment is of great concern.

Lerche and Sobisch used the LUMiSizer instrument to investigate the sedimentation of differing suspensions of mineralogical nanoparticles, finding the sedimentation behaviour to predict colloidal stability with good agreement[133]. Palhares et al also studied sedimentation behaviour but investigated the effects of adding a citric acid dispersant to suspensions of slate,

showing that by varying the concentration of the dispersant they could either improve the stability of the suspension or induce flocculation[134].

Loginov et al evaluated the compression-permeability characteristics of calcium carbonate suspensions in the LUMiSizer by analogy to the method of constant pressure filtration[135]. In later work Loginov et al used modified sample cells that contained a membrane in order to study percolation and dewatering of mineral and biological suspensions whilst under centrifugation. They developed a method for the analysis of cake resistance that agreed with experimental cake resistance obtained from traditional pressure filtration[136].

Knoll et al have interestingly constructed a centrifuge with built-in optical microscopy, enabling on-line image analysis (via computer software) of the sample as it rotates. They then compared the adhesion potential of polystyrene particles attached onto a glass substrate by rotating the substrate and counting the ratio of ejected particles to those remaining. In comparing the results to those obtained with the LUMiSizer, the authors found good agreement with small (19 μm) particles, but large deviations with their self-constructed centrifuge with 90 μm particles. They claim the minimum rotational speed of the LUMiSizer was too high and thus most particles detached under rotation[137].

7.3 LUMiSizer Measurement Technique

The LUMiSizer relies on the Beer-Lambert relationship to measure the ratio between the intensity of radiation leaving the source and radiation received by the detector. The two differ due to the scattering and absorbance of light radiation as it passes through the sample[138]:

$$I = I_0 e^{-\epsilon_x \alpha_v l} \quad \text{Equation 7-1}$$

Where I_0 is the incident intensity and I the transmitted intensity.

The LUMiSizer feeds intensity data into the SEPView software, which uses a method known as ‘front tracking’ to analyse the peak bed height over time. In time periods specified by the user, an instantaneous ‘snapshot’ of the transmission profile over the cell is recorded. These profiles sum to provide a multi-dimensional record of the sample’s transmissivity vs. its height (See Figure 7-5).

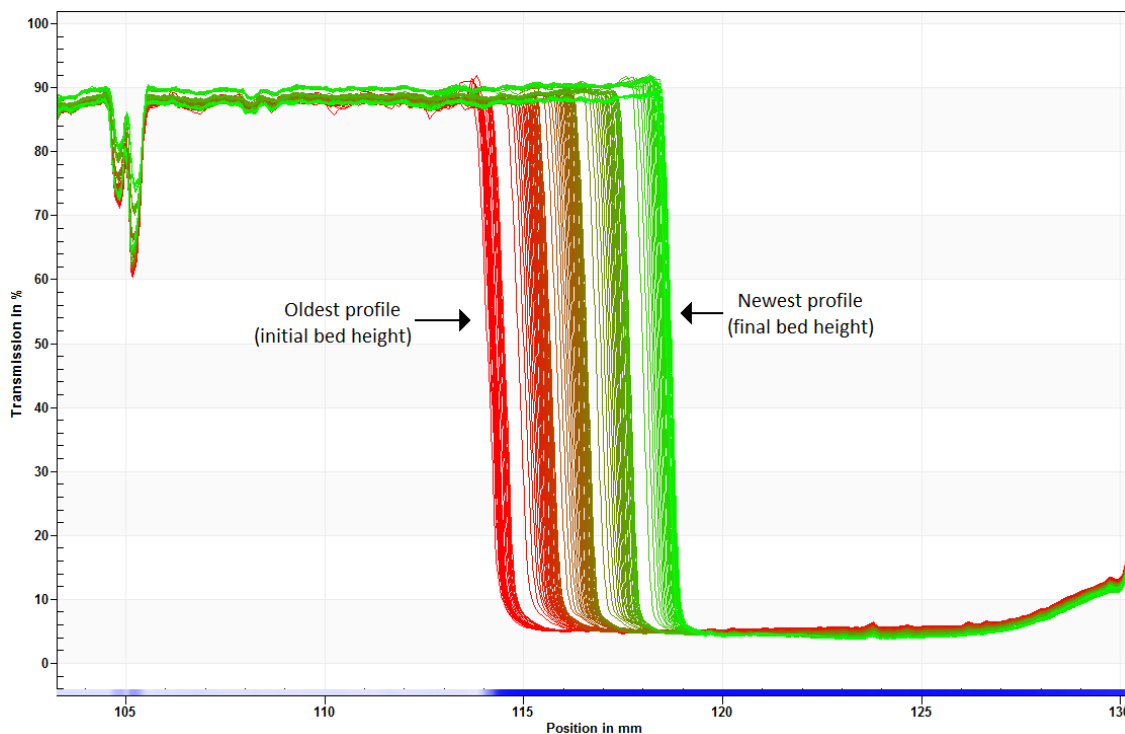


Figure 7-5: LUMiSizer raw data as displayed on SEPView software - sample transmissivity vs. height for Urea particles in saturated mother liquor (MeOH) after 34 hours

In Figure 7-5, the data for a Urea-MeOH centrifuged sample is displayed; more recent profiles are coloured green, whilst older profiles are coloured in red (i.e. profiles in-between are coloured with a shaded gradient of green to red). The 'brightest', 'greenest' profile therefore signals the final height of the crystal bed at the close of the experimental period, whilst the deepest red colour indicates the initial bed height.

A complete description of the experimental methodology is available in Chapter 3. All data is obtained from the internal measurements recorded by the LUMiSizer instrument.

Exported data is plot graphically with bed heights and the centrifuge rpm on opposing y-axes, and time along the x-axis. The SOP is visualised by following the trace of the instrument's centrifuge rpm as it varies with time.

7.4 A Model for the Calculation of Compressive Pressure Forces within a Bed of Particles

7.4.1 Pressure drop over the bed

The SEPView software is used to generate a standard operating procedure with which to operate the LUMiSizer. In addition to setting the number of samples to be run, the speed of rotation and measurement frequency for each time period is set. The user cannot explicitly

input a particular 'G-force' or pressure to apply to the sample; the rpm of the centrifuge is specified instead.

The actual force and pressure imparted to the sample requires calculation, based on a model derived below. This is derived on the basis that a bed of particles is a series of layers of solid weight, accelerated downwards towards the bottom of the vessel. Compressive pressure is applied to the particles in the layers beneath from the force of the weight of particles above.

The angular velocity is the speed at which a rotating object (i.e. the centrifuge contents) travels in a circular path:

$$\omega = 2\pi f \quad \text{Equation 7-2}$$

Where 'f' is the frequency of rotation i.e. when there is 1 revolution per second ($f = 1$), the angular velocity is 2π radians per second (or $360^\circ/\text{s}$). Angular velocity can also be defined by dividing the linear velocity of an object by the radius of its rotation:

$$\omega = \frac{v}{r} \quad \text{Equation 7-3}$$

Squaring both sides:

$$\omega^2 = \frac{v^2}{r^2} \quad \text{Equation 7-4}$$

Multiplying by 'r', the radial distance of the object from the centre of rotation:

$$\omega^2 \cdot r = \frac{v^2}{r} \quad \text{Equation 7-5}$$

Centrifugal acceleration is thus the change in radian-metres travelled per second per second (rad.m/s^2) i.e. the change in angular velocity over time:

$$a = \frac{v^2}{r} = \omega^2 \cdot r \quad \text{Equation 7-6}$$

The combinative forces of compressive pressure enacted upon and by a bed of particles can be calculated using a method similar to that of Curvers et al, who derived a model based on the forces placed upon particles under centrifugal acceleration[139]. Starting from Newton's 3rd law, the force enacted upon a particle is a function of its mass and the acceleration it is placed under:

$$F = m_p \times a \quad \text{Equation 7-7}$$

Substituting the relation for centrifugal acceleration from Equation 7-6:

$$F = m_p \times \omega^2 \cdot r \quad \text{Equation 7-8}$$

Where r is the distance from the centre point of centrifugal rotation. By knowledge of the disk size within the LUMiSizer – 0.13 m – the radial distance of any particular point in the particle bed can be calculated from:

$$r = 0.13 - \text{bed height} \quad \text{Equation 7-9}$$

If a differential volume of height dr is considered as a slice fraction of the bed of particles (Figure 7-6), the differential mass of particles within this layer is a function of the difference in particle/fluid density, the solids fraction, the slice cross-sectional area and the slice height dr :

$$dW_s = (\rho_p - \rho_f) \cdot \phi \cdot A \cdot dr \quad \text{Equation 7-10}$$

The solids fraction is assumed to be constant throughout the height of the bed (in reality it will increase with increasing compressive pressure).

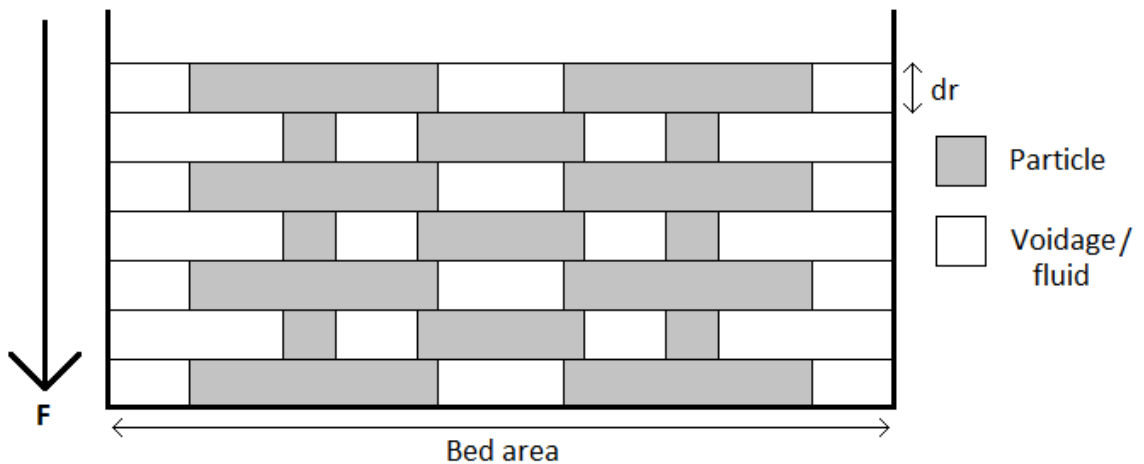


Figure 7-6: Schematic of particle bed separated into slices of height dr ; compressive force is imparted towards the base by the weight of particles above each slice

The total downward force exerted by the slice dr is therefore:

$$dF = \omega^2 \cdot r \cdot (\rho_p - \rho_f) \cdot \phi \cdot A \cdot dr \quad \text{Equation 7-11}$$

Dividing by the cross-sectional area yields the solids pressure exerted per slice dr :

$$\frac{dF}{A} = \omega^2 \cdot r \cdot (\rho_p - \rho_f) \cdot \phi \cdot dr \quad \text{Equation 7-12}$$

Therefore the total pressure drop over the particle bed is the integral of the slice forces from the top to the bottom of the bed:

$$\Delta P = \int_{r_{top}}^{r_{base}} \omega^2 \cdot r \cdot (\rho_p - \rho_f) \cdot \varphi \, dr \quad \text{Equation 7-13}$$

$$\Delta P = \frac{1}{2} (r_{base}^2 - r_{top}^2) \times \omega^2 \cdot (\rho_p - \rho_f) \cdot \varphi \quad \text{Equation 7-14}$$

Equation 7-14 is therefore the total pressure drop over the bed.

7.4.2 Model results

Table 7-1: Data from calculation of the total integrated compressive pressure acting over a bed of beta-glutamic acid particles

Centrifuge rpm	350	780	1100	1560	2200
Angular velocity ω (rad/s)	36.65	81.68	115.19	163.36	230.38
Initial mean cake height (m)	0.0162	0.0138	0.0131	0.0118	0.0104
Slice thickness dr (m)	8.12E-04	6.88E-04	6.54E-04	5.88E-04	5.22E-04
Ave bulk density (kg/m ³)	134.47	158.80	167.02	185.67	209.24
Solids fraction (Φ)	0.087	0.103	0.108	0.121	0.136
Void fraction (ϵ)	0.913	0.897	0.892	0.879	0.864
Radius of bed from centre (top of cake) (m)	0.1138	0.1162	0.1169	0.1182	0.1196
Radius of bed from centre (bottom of cake) (m)	0.13	0.13	0.13	0.13	0.13
Total integrated compressive pressure (Pa)	125.40	629.17	1254.74	2537.01	5072.61

Example data is available for beta-glutamic acid in Table 7-1. An example of integrated solid compressive pressure is plot against the centrifuge rpm in Figure 7-7; indicating a power law relationship of pressure imparted being dependent on the square of the centrifuge rpm.

A key point of note is the low solids pressure calculated over the bed of particles; 5000 Pa is roughly equal to 0.05 bar i.e. a very low pressure filtration. This is the most extreme case; i.e. for a centrifugation at 2200 rpm. It should also be noted that pressure throughout the upper layers of the bed is significantly lower than this; only particles at the base of the cell (and thus furthest away from the centre of centrifugal rotation) will feel the effect of 0.05 bar from the particles above them in the bed.

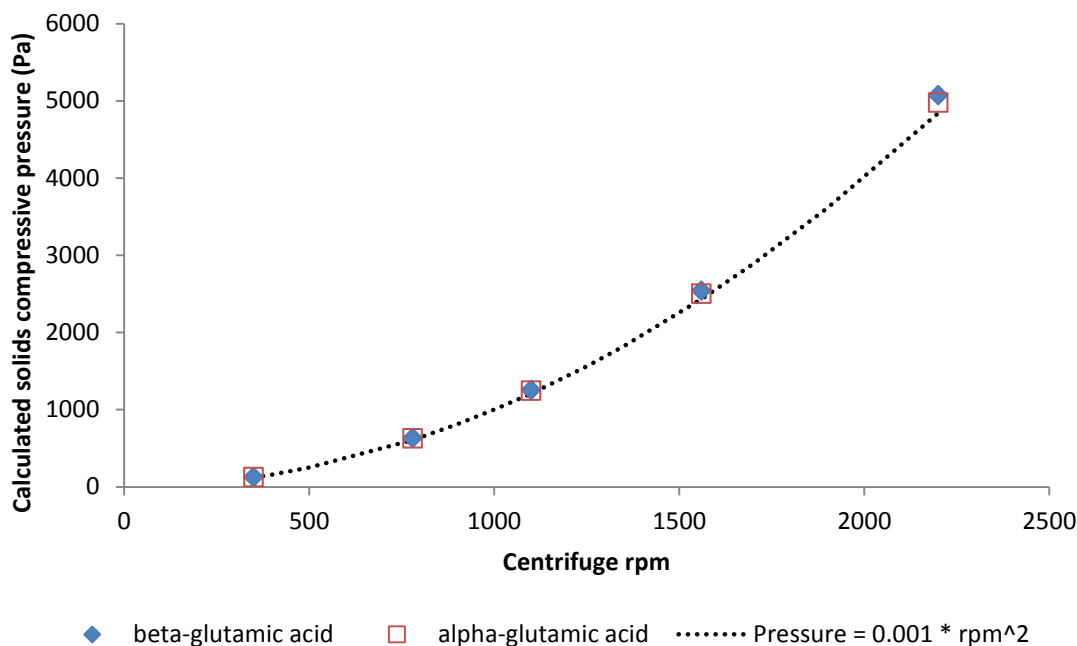


Figure 7-7: Total compressive pressure drop over a bed of particles situated in a LUMiSizer cell; for alpha and beta-glutamic acid. Other systems evaluated display similar power-law trends in pressure with rising centrifugal rotational speeds

Compressive pressure for both polymorphs of glutamic acid is approximately similar. The pressure drop in the cell is dependent on the solids fraction and bed height (distance from the centre of rotation) which both differ in these cases. The lower average solids fraction (less solid present; therefore less weight directed downwards to lower regions of the bed) of beta-glutamic acid compared to alpha is balanced by the increased bed height (more layers of solid with which to impart force). This means an inverse proportionality relationship exists with glutamic acid; as the solids fraction of alpha glutamic acid rises, the bed height drops; meaning the compressive pressure remains roughly constant.

A similar effect is noted with urea and urea-biuret systems (see Table 7-2); the urea having lower solids fraction but larger bed height; urea-biuret is an opposing case with higher solids fraction and lower bed height. The result is a largely coincidentally similarity in compressive pressure over the bed.

Table 7-2: Total compressive pressure over the particle beds for the systems investigated

System	Total Pressure drop (Pa)
Beta (β)-glutamic acid	5072.6
Alpha (α)-glutamic acid	4976.1
Urea	6078.5
Urea + biuret (6%)	6153.4
Lesinurad	3722.7

As evidenced with the beta-glutamic acid system, the pressure drops over the beds are all of low magnitude. Although this is a key finding this does limit the method in its applications for the study of high pressure crystal breakage; nonetheless, findings can still be correlated with those of lower pressure filtrations (see section 7.5.4). It does however have ramifications for the use of centrifugation as a method of filtration; if compressive pressures are low, then theoretically the levels of particle breakage will be also be low, meaning the method has applications for industrial filtrations in which crystal breakage is a serious concern.

7.5 Experimental Results and Discussion

7.5.1 Experimental outline

The SOP is designed according to the approximate pressures to be generated at the base of the sample cells. The initial step is a low-pressure (350 rpm roughly corresponds to 0.1 bar) pre-consolidation stage in order to allow for initial packed bed formation[135, 136] and thus to gain a baseline reading for the bed height.

Large voids will collapse during this stage, but no permanent damage to the crystals is anticipated at ~0.1 bar. This essentially performs the same process as a gravitational settling stage would (but obviously this is not possible as the sample vials rest horizontally – perpendicular to the force of gravity).

As certain materials are known to undergo elastic expansion when the centrifugal force of rotation is released[140], this highlights the importance of measuring the bed height during and after each centrifugal rotation stage, such that the compressed and ‘relaxed’ bed heights are recorded.

The ability of a particle bed to compress and ‘relax’ (i.e. re-gain height) implies that for any particular system there should be a theoretical tensile ‘elastic limit’, below which the bed will return to normal, and above which the bed will undergo consolidation/rearrangement (and in some cases, particle breakage) into a higher density structure[131].

This should give an indication of the bed’s elasticity; high ‘relaxation’ indicates an elastic bed (i.e. not permanently deformed), whilst low relaxation could indicate potential breakage of crystals (due to permanent deformation and failure of the bed’s structure).

Upon completion of the bed formation stage, the centrifuge rotation is increased, first to 780 rpm (~0.5 bar) for 6 hours, followed by a reduction back to the baseline rotation. This allows for any elastic relaxation of the bed to occur. Following this, additional stages of 1100, 1560 and 2200 rpm rotations are performed, each with an intermediary 350 rpm ‘relaxation’ stage.

A table of experiments is depicted in Table 7-3, listing the particle systems examined in the LUMiSizer. Detailed information on particle bed heights and calculated bulk densities of the beds are listed in Table 7-4.

Table 7-3: Table of systems investigated

Experiment	Solid	Solvent
1	Beta (β)-glutamic acid	Water
2	Alpha (α)-glutamic acid	Water
3	Urea	MeOH
4	Urea + biuret (6%)	MeOH
5	Lesinurad	MeCN

Table 7-4: Experimental bed heights and bulk density as a function of centrifugal rpm

β-glutamic acid					
Centrifuge rpm	350	780	1100	1560	2200
Mean bed height (mm)	16.24	13.75	13.08	11.76	10.44
St.dev (bed height)	1.28	0.58	0.54	0.33	0.30
Bulk density (kg/m ³)	134.47	158.80	167.02	185.67	209.24
α-glutamic acid					
Centrifuge rpm	350	780	1100	1560	2200
Mean bed height (mm)	3.96	3.13	3.10	3.03	2.96
St.dev (bed height)	0.78	0.37	0.38	0.37	0.38
Bulk density (kg/m ³)	525.36	664.53	671.13	686.74	703.94
Urea					
Centrifuge rpm	350	780	1100	1560	2200
Mean bed height (mm)	13.07	11.89	11.26	10.39	9.57
St.dev (bed height)	1.95	1.81	1.66	1.56	1.46
Bulk density (kg/m ³)	174.94	192.29	203.08	220.04	238.96
Urea-biuret					
Centrifuge rpm	350	780	1100	1560	2200
Mean bed height (mm)	11.16	8.04	7.60	6.98	6.48
St.dev (bed height)	0.89	1.12	0.95	1.08	0.97
Bulk density (kg/m ³)	204.82	284.40	300.75	327.53	352.83
Lesinurad					
Centrifuge rpm	350	780	1100	1560	2200
Mean bed height (mm)	11.04	10.68	9.61	7.66	6.98
St.dev (bed height)	0.80	0.82	1.04	0.58	0.50
Bulk density (kg/m ³)	111.55	115.32	128.10	160.63	176.34

A common trait among all samples is the compression of the particle bed when under centrifugal force. When the final samples are removed from the instrument they display a reduced cake height when compared to their initial (pre-experimental) height (e.g. see Figure 7-8).

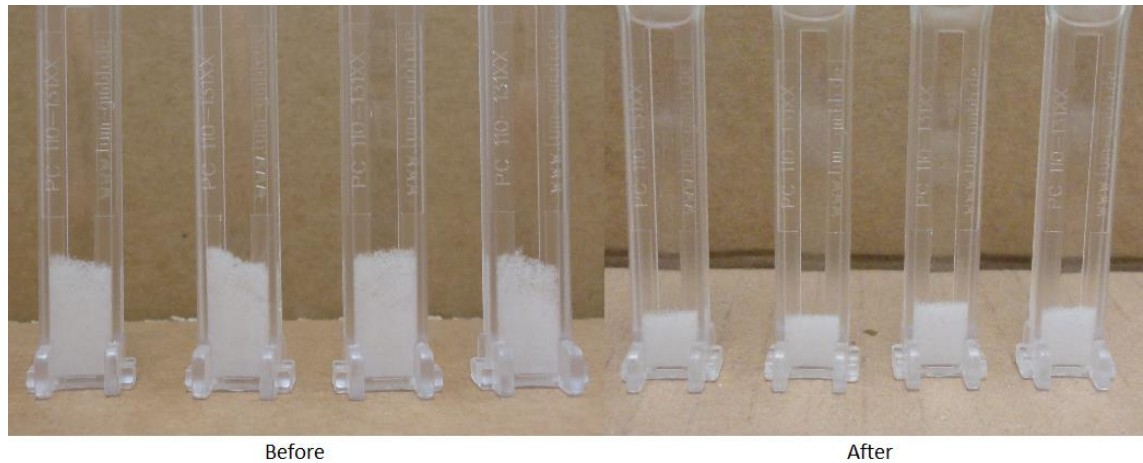


Figure 7-8: LUMiSizer sample cells containing urea; before and after centrifugation

This is reflected in the calculated bulk densities which universally rise as centrifugation rate increases; this translates to a consolidation of the cakes due to the compressive stress exerted during centrifugation. Bulk densities of the needle systems are universally lower than those of the 'blocky' (alpha-glutamic acid/urea-biuret) systems; this is to be expected as the bulk density is directly tied to the mean bed height, which is a function of the packing characteristics. This shows the needle-like particle beds pack with greater porosities than the blocky particle beds, which has subsequent effects on the extent to which these beds can compress under additional force (i.e. more voids exist, therefore there is more potential for collapse of these voids).

Bulk densities are typically much lower than those measured for particle beds under pressure filtration (i.e. for glutamic acid and Lesinurad under 2 Litre batch filtration - see Chapter 6). Bulk density is the mass per unit volume, and volume is dependent on the packing characteristics of the bed. Packing is in turn dependent on the compressive pressure applied to the bed; thus it can be concluded that the beds under centrifugation are being compressed to a lower extent than under large scale filtration. This is backed up by the calculated compressive pressures (section 7.4.2).

For beta-glutamic acid, for example, the pressure drop over a bed at 2200 rpm is roughly equivalent to 0.05 bar. The solids fraction at this rotation is approximately 0.14 (Table 7-1). The solids fraction for a 2 Litre scale batch filtration of beta-glutamic acid at negligible pressure is approximately equal to 0.15 (see Chapter 6); meaning these beds are consolidated to a similar extent.

7.5.2 Traces of sediment bed height over time whilst under centrifugation

7.5.2.1 Glutamic acid

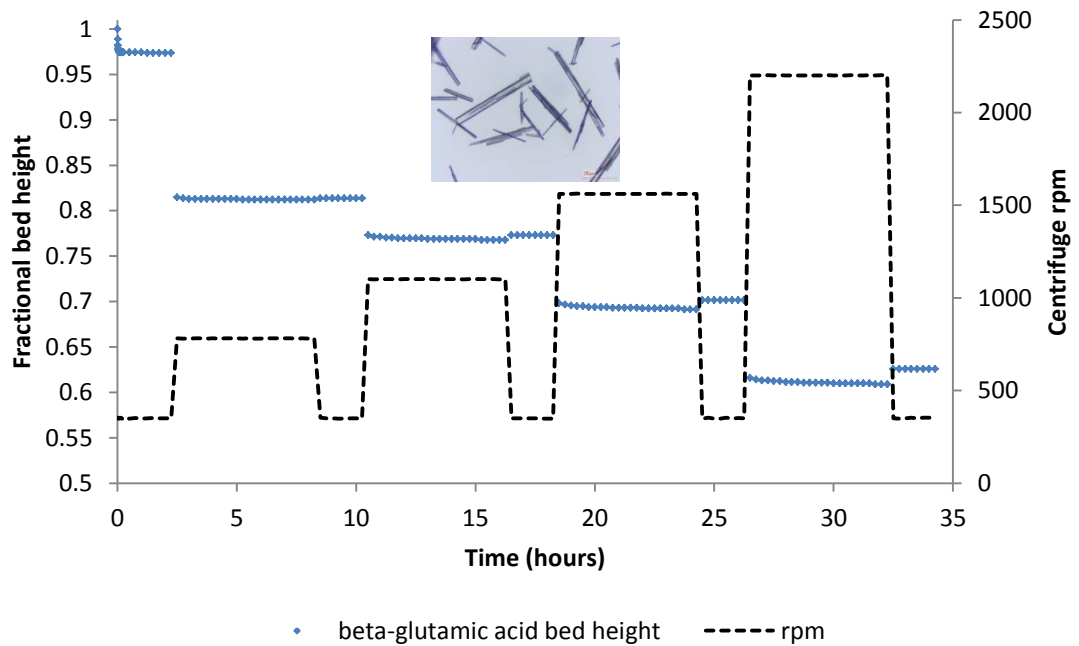


Figure 7-9: Fractional bed height vs time for beta-glutamic acid over 34 hours

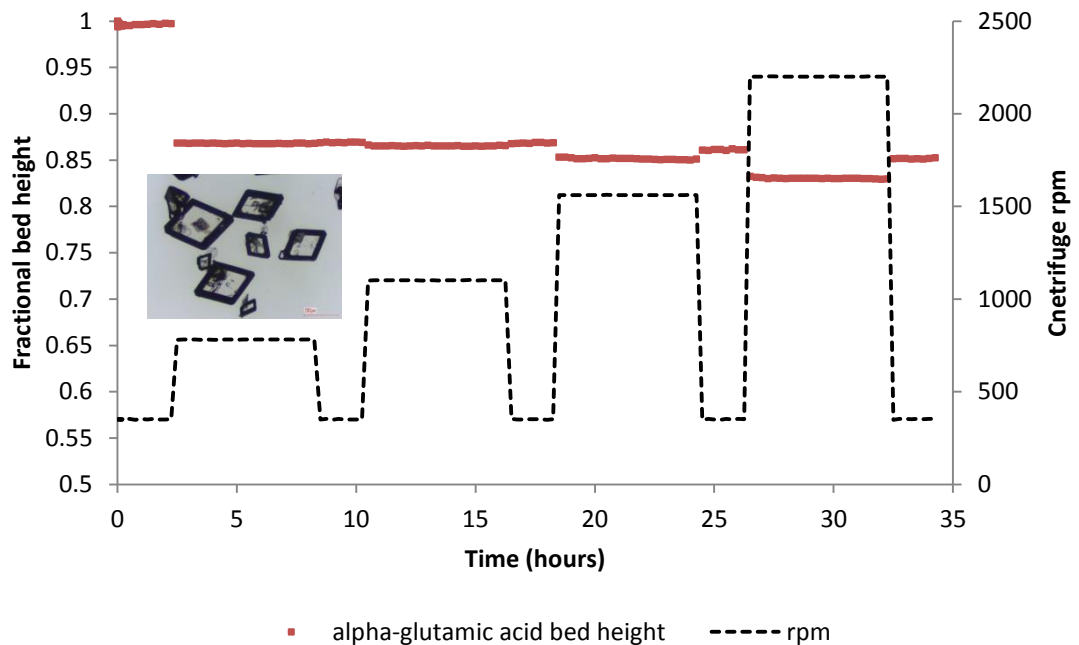


Figure 7-10: Fractional bed height vs time for alpha-LGA over 34 hours

The data in Figure 7-9 and Figure 7-10 display the centrifugation of 2 differing morphologies of glutamic acid: beta and alpha, respectively. The 2 polymorphs exhibit highly variable centrifugation behaviour; which can be ascribed to the variance in shape and packing characteristics that arise from particle morphology.

The major characteristic difference between the 2 morphologies is the reaction of the particle bed to the SOP plan i.e. ramping up the rpm causes the bed to react in differing ways.

The beta polymorph (Figure 7-10) bed tends to display a steady and gradual decline in bed height over the course of the experiment, and reaches a minimum bed height roughly 60% of that of the original (350 rpm). The alpha polymorph however displays comparatively much less bed compression, with minimum bed heights approximately 80% of the height of the maximum.

This highlights the extent to which the differing particle morphologies arrange and re-arrange within the bed. The beta polymorph mean initial bed height is over 16 mm, whilst the alpha polymorph is just under 4 mm. This shows how the initial packings differ greatly in bed density – the needle-like beta polymorph packs with many voids which are subsequently reduced in volume with each increase in centrifugal acceleration. As the bed yields under the compressive stress, particle contacts are severed and a period of particle re-arrangement occurs in which voids are collapsed; the result is a higher bed density.

The large, blocky alpha polymorph packs tightly even under the initial bed consolidation stage, so the potential for the collapse of bed voids is much lower. It should be noted however that the lack of alpha glutamic acid bed height is also likely affected by the lower initial mass of solid deposited into the sample cells. This is most likely as a result of the difficulty in transferring slurry material from the crystallised solution into the sample cells. Even using the largest bore needles available, this physically limits the amount of large alpha-glutamic acid crystals that are able to be drawn into the syringe. Material can also become lodged within the syringe which further limits the transfer of solid into the sample cells.

Another point of note is the relaxations of the particle beds. As higher forces are exhibited on the bed, the extent of relaxation rises slightly (i.e. the bed relaxes to a greater extent when decelerating from ~2200 rpm to ~350 rpm than when switching from ~780 rpm to ~350 rpm). This is due to the extra strain energy imparted to the crystal beds at higher rotational speeds.

The compression of the beds to differing structures is also evidenced by the relaxation. Needle-like beta crystals display small relaxations evident of permanent and drastic increases in bed density, and lower elasticity of the particle beds. Larger bed relaxations are evident in the blocky alpha particles, meaning not only is there less of a permanent consolidation in the bed structure, but that the bed is more elastic – i.e. it is able to store and release more energy than the needle-like system, resulting in the bed ‘bouncing back’ to a greater degree.

7.5.2.2 Urea and urea-biuret

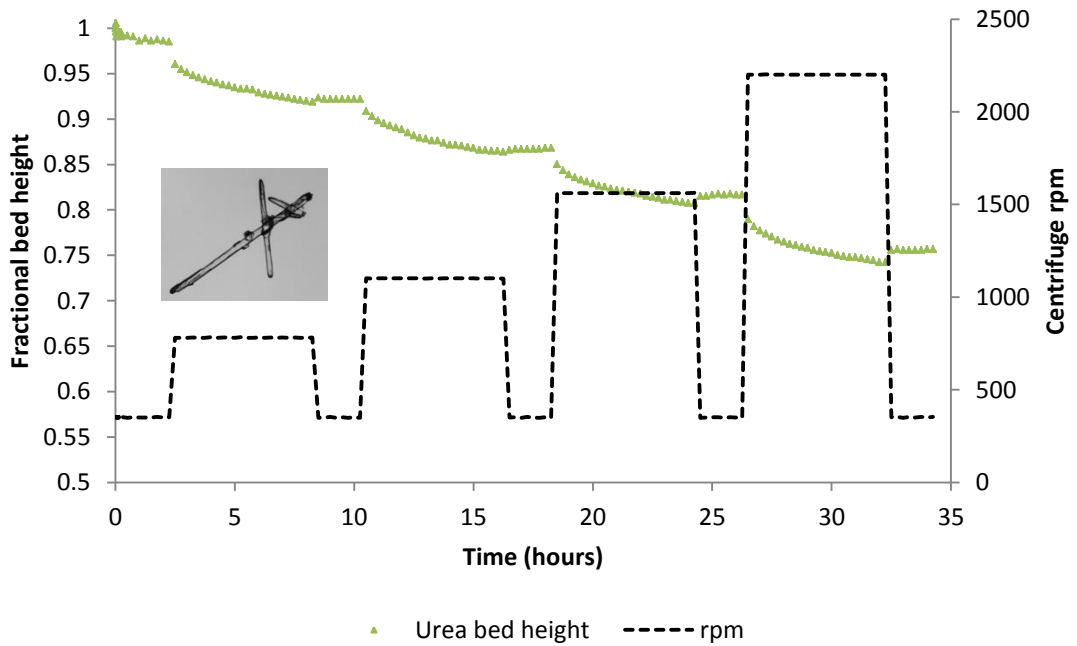


Figure 7-11: Fractional bed height vs time for urea over 34 hours

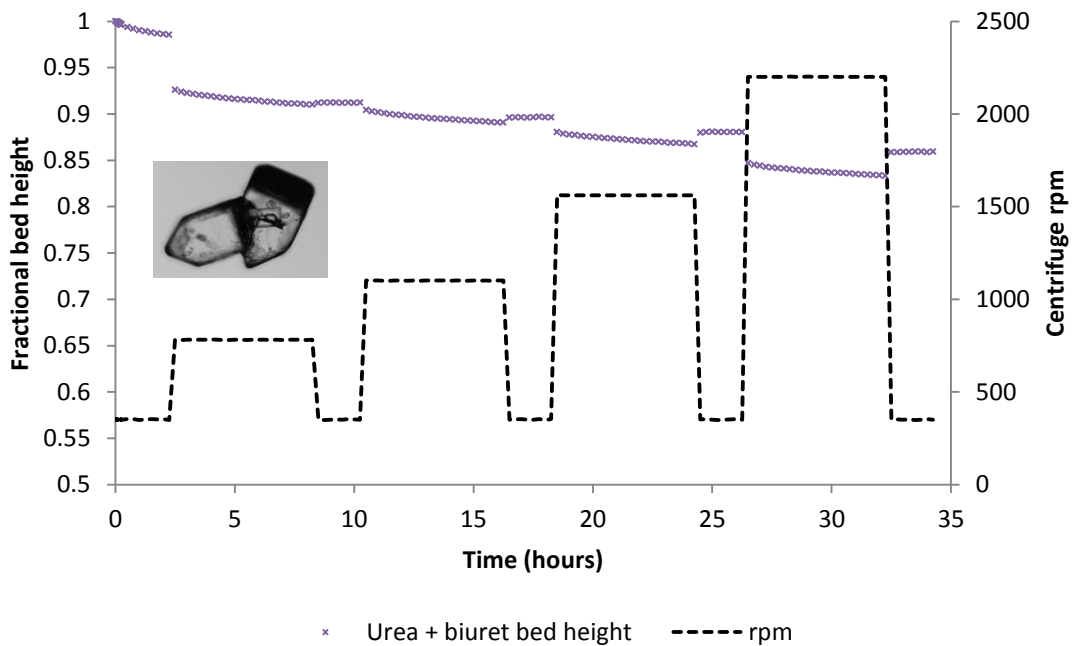


Figure 7-12: Fractional bed height vs time for urea + biuret over 34 hours

The urea samples show differing consolidation behaviour to the glutamic acid samples, and are hindered in their compression/settling. This is observable from the long durations required to compress the bed to an equilibrium height, versus for example the alpha/beta glutamic acid systems, in which bed collapses occur almost instantly upon raising the centrifugal force.

The time periods required (~6 hours) show the urea (pure in particular) beds have considerable resistance to structural deformation; 6 hours would make for a considerable filtration time even at larger scales. This is evidence of high structural strength of the crystal bed networks; networks that are able to resist deformation under compressive pressure.

As has been alluded to in Chapter 4, Urea, due to its high solubility in MeOH (~150 mg/mL at 20°C), is known to form solid bridges as it crystallises, with large fractions of solute molecules becoming entrained within the cake and solidifying the structure. Recent work by Kirsch has shown that the tensile strength of a dry solid bridge is found to increase with storage time; however these were tested over longer time periods (up to 16 days). They do however confirm that considerable strength is attained over minimum periods of 30 minutes, which is a fraction of the 34 hours these samples are centrifuged for [105, 141].

The urea samples remained wet throughout the experimental period, therefore it is likely that solid bridges are providing considerable strength to the structure of the cake; hence resisting collapse even at centrifugal speeds of 2200 rpm.

Similarly to the glutamic acid system, the high elongation pure urea crystals display higher initial bed heights and increased consolidation overall relative to the more rounded urea-biuret crystals. This shows again that the needle-like bed structures form with greater void fractions and thus are open to higher degrees of collapse when bonds are broken under compressive stress and re-arrangement of bed structure occurs.

7.5.2.3 Lesinurad

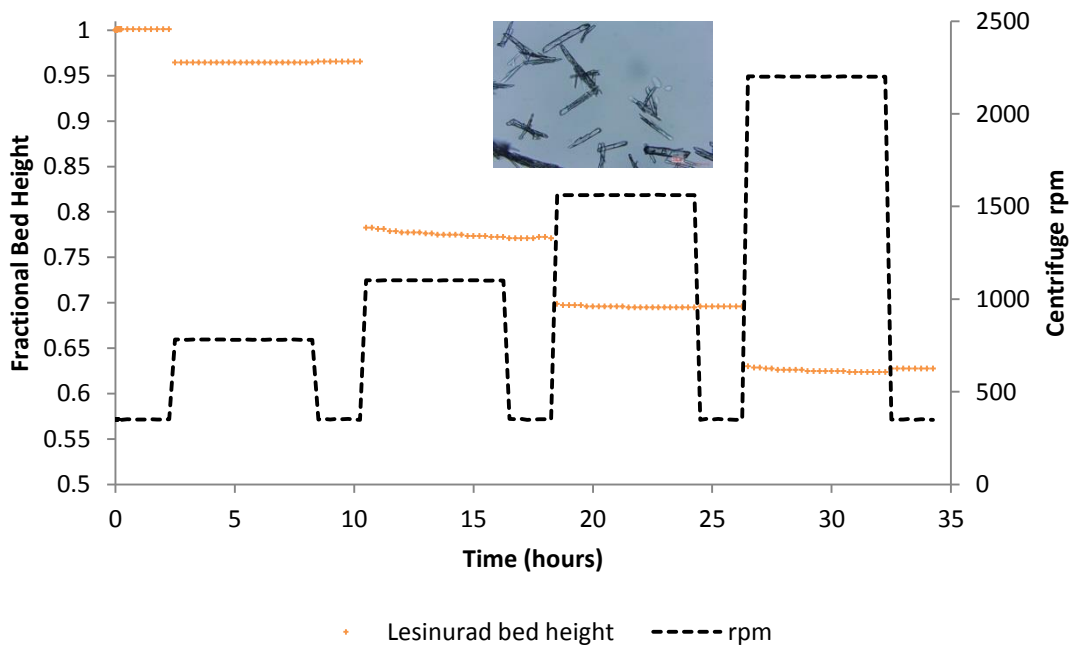


Figure 7-13: Fractional bed height vs time for Lesinurad over 34 hours

The Lesinurad system performs similarly to the other needle systems, particularly beta-glutamic acid. The data in Figure 7-13 displays the characteristic high reduction in fractional bed height with response to centrifugal force – both samples lose about 40% of their total initial height over the course of the experiment. This is interesting to note as the particle aspect ratios/shapes are similar and hence these systems would be expected to pack in a comparable way.

With the average Lesinurad particle size being considerably lower than that of beta-glutamic acid (20-60 microns for Lesinurad compared to several hundred microns for glutamic acid), this is evidence of a similar packing structure that is formed irrespective of particle size, although admittedly the differences in fractional bed height could be a factor of particle breakage strength or frictional forces between particles as they rearrange.

It is also clear that bed relaxation is particularly low with Lesinurad, indicating poor elasticity in response to cake deformation. Bed relaxations are examined in further detail in the proceeding section (7.5.3).

7.5.3 Bed Relaxation

By analysing the extent of relaxation in the beds after each drop-off in centrifuge velocity, a measure of elasticity in the bed can be gleaned. Elastic strain is a measure of the extent to which a solid can deform its shape under a force and regain its original shape when the force is

released; this can be applied to the heights of the power beds to determine their elastic performance.

The bed relaxation is calculated by taking the positional shift in the bed height when moving from a 'high-rotation' stage, to a 'low-rotation' stage i.e.

$$\text{relaxation} = \text{fractional bed height at 350 rpm} - \text{fractional bed height at 780 rpm}$$

The raw data is depicted in Table 7-5:

Table 7-5: Bed relaxations for each particle system at a range of centrifugal decelerations

System	Bed relaxation (%)			
	780 → 350 rpm	1100 → 350 rpm	1560 → 350 rpm	2200 → 350 rpm
β-glutamic acid	0.17%	0.51%	1.02%	1.70%
α-glutamic acid	0.06%	0.23%	0.97%	2.20%
Urea	0.34%	0.39%	1.01%	1.46%
Urea-biuret	0.19%	0.52%	1.22%	2.54%
Lesinurad	0.13%	0.13%	0.13%	0.38%

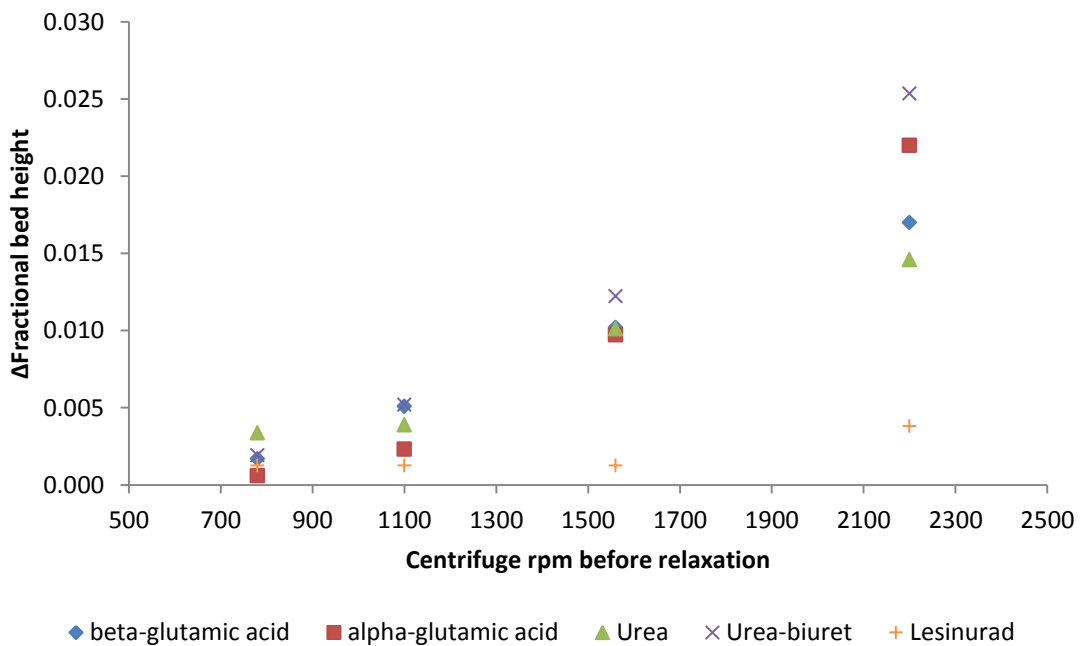


Figure 7-14: Bed relaxations (Δ fractional bed height) upon changing from high to low centrifugation

Figure 7-14 displays the bed relaxations for all particle systems, indicating the differing behaviour between the needle and rounded/blocky systems; needle system bed relaxations are lower, particularly at higher centrifugation accelerations. This indicates the overall reduced elasticity that these systems display; i.e. they are less able to absorb and release the strain energy imparted to the beds from the force of compressive stress; the result is a lower

'bounce-back' of the top of the bed when centrifugal force is backed off. The Lesinurad system is particularly inelastic.

Looking in more detail at the alpha-glutamic acid and urea-biuret systems (Figure 7-15), it can be observed that the relaxations appear to follow a power law, which is fitted to the data. This again highlights the extent to which these beds are able to store and release energy: proportional to the rate at which it is provided to the bed; as dictated by the compressive pressure drop imparted to the bed (see Figure 7-7)

Combined with the data showing that these beds do not vary drastically in bed height, it is clear that energy input into the system is not largely spent on rearrangement/breakage of particle contacts or collapsing of voids; rather it is more easily elastically transmitted through the bed network, stored and released.

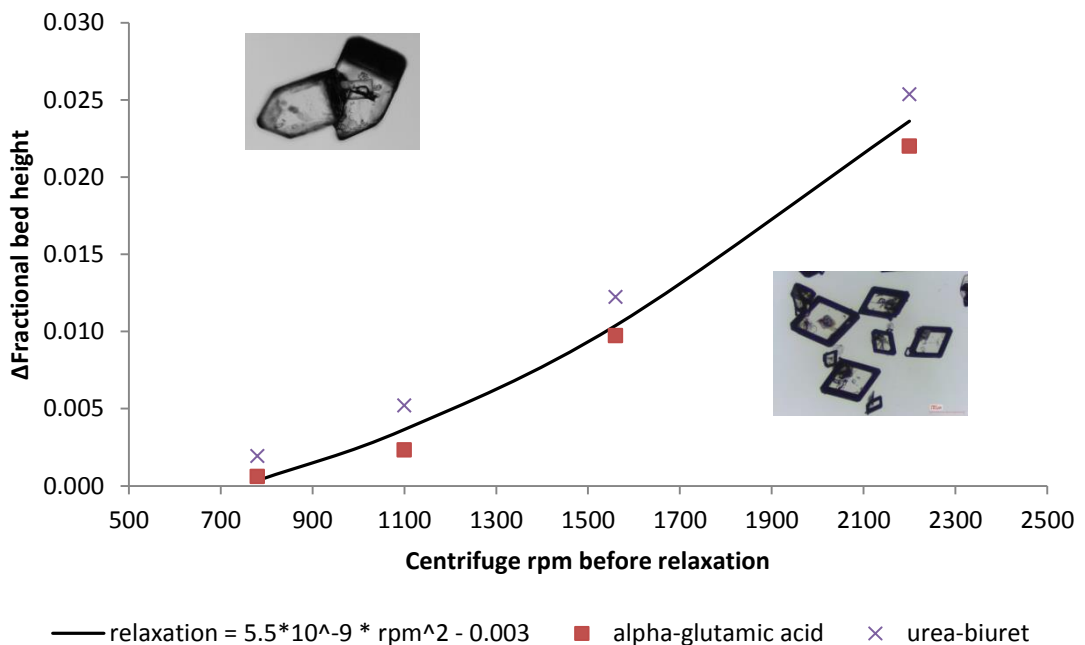


Figure 7-15: Bed relaxations vs centrifuge rpm for α -glutamic acid and urea-biuret

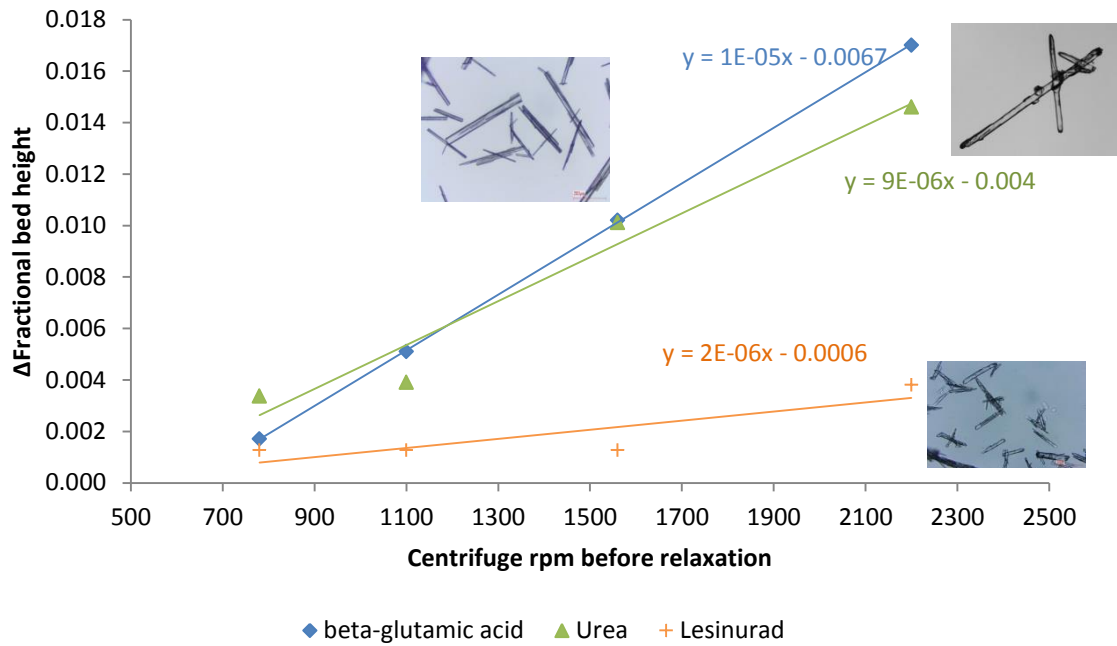


Figure 7-16: Bed relaxations vs centrifuge rpm for needle-like systems

The needle-like beds however display differing relaxation behaviour with increasing centrifugal acceleration (Figure 7-16), with roughly linear trends. Compared with the blocky systems, this shows that part of the elastic strain energy imparted to the beds is lost under compression. Clearly part of this energy is spent in the collapsing of bed voids and rearrangement of particles (as shown by the greater reductions in fractional bed height of these systems).

Assuming that random scatter is not responsible (which is admittedly a possibility), the urea and Lesinurad systems also display apparent critical points at 1100 and 1560 rpm relaxation, respectively. Prior to these points, bed relaxations are roughly constant; after which relaxations increase linearly. This could point to aforementioned collapses and rearrangements occurring to greater extents, as this would explain the apparent loss in energy relative to the centrifugal rotation.

It is interesting to note the similarity in relaxations with the beta-glutamic acid and urea systems, considering the differences in bed height over time and settling behaviour. The solid bridge network structure within the urea system clearly has similar capabilities in the storage and release of energy compared to the glutamic acid.

The Lesinurad bed however displays vastly reduced relaxations at all centrifugal speeds, which could be influenced by the particle size. Because of their smaller sizes, the particles within the Lesinurad bed should be able to rearrange more often and compact in tighter formations, which is likely the reason for the apparent loss in elastic energy. This should however have

been reflected in the bed height trace (which showed Lesinurad and beta-glutamic acid both pack to roughly 60% of the original bed height), thus the result is somewhat inconclusive.

7.5.4 Particle Image and Size Analysis

Part of the objective is to use the LUMiSizer as a representative tool for the comparative study of pressure filtration performance; hence the analysis of pressure filtered beds is required. The needle-like glutamic acid system is taken forward as a case study for further analysis as sufficient larger scale data exists (i.e. data from the continuous percolation rig and 2 Litre filtrations).

In a similar regime to the performance testing of the percolation rig, the particle size distribution (PSD) of the beta-glutamic acid crystals is tested after having been subjected to different processing types. A sample is taken after crystallisation (i.e. lightly filtered with a Buchner vacuum flask) (termed 'LF') and after percolation ('PF'), with a final comparative sample taken from the material in the LUMiSizer cells post-centrifugation. The continuous percolation rig (CPR) experiment in question in experiment '30c' (see Chapter 6); hence this should correspond to a percolation flowrate of 95 L/h.

As the physical amount of material in each cell is limited, multiple cells' crystal masses are collectively filtered and combined into a single 'post-centrifugation' ('CF') sample.

All samples are tested using the Morphologi G3 particle sizer, with the optical microscope also used to collect images of the crystal masses.

Figure 7-17 depicts several images of each sample taken on the G3 microscope (from top to bottom; vacuum filtered, percolated, centrifuged). It is difficult to draw any real conclusions from several images as they merely highlight a tiny, disproportionate area of a sample, but there are some aspects of note worth mentioning.

The vacuum/lightly filtered sample ('LF' sample) appears to have a lower average area-density of crystals on the microscope slide when compared to the percolated and centrifuged samples. This is observable from the general amount of free space that surrounds the crystals. Conversely the PF and CF samples both have greater densities of crystals that rest on the microscope slide; although this is partially attributable to the increased presence of smaller fragments and assorted crystal fines (more so with the PF sample), the levels of breakage observed are well below those typically encountered under high pressure filtrations (e.g. see Chapter 6; appendices for examples of high levels of breakage).

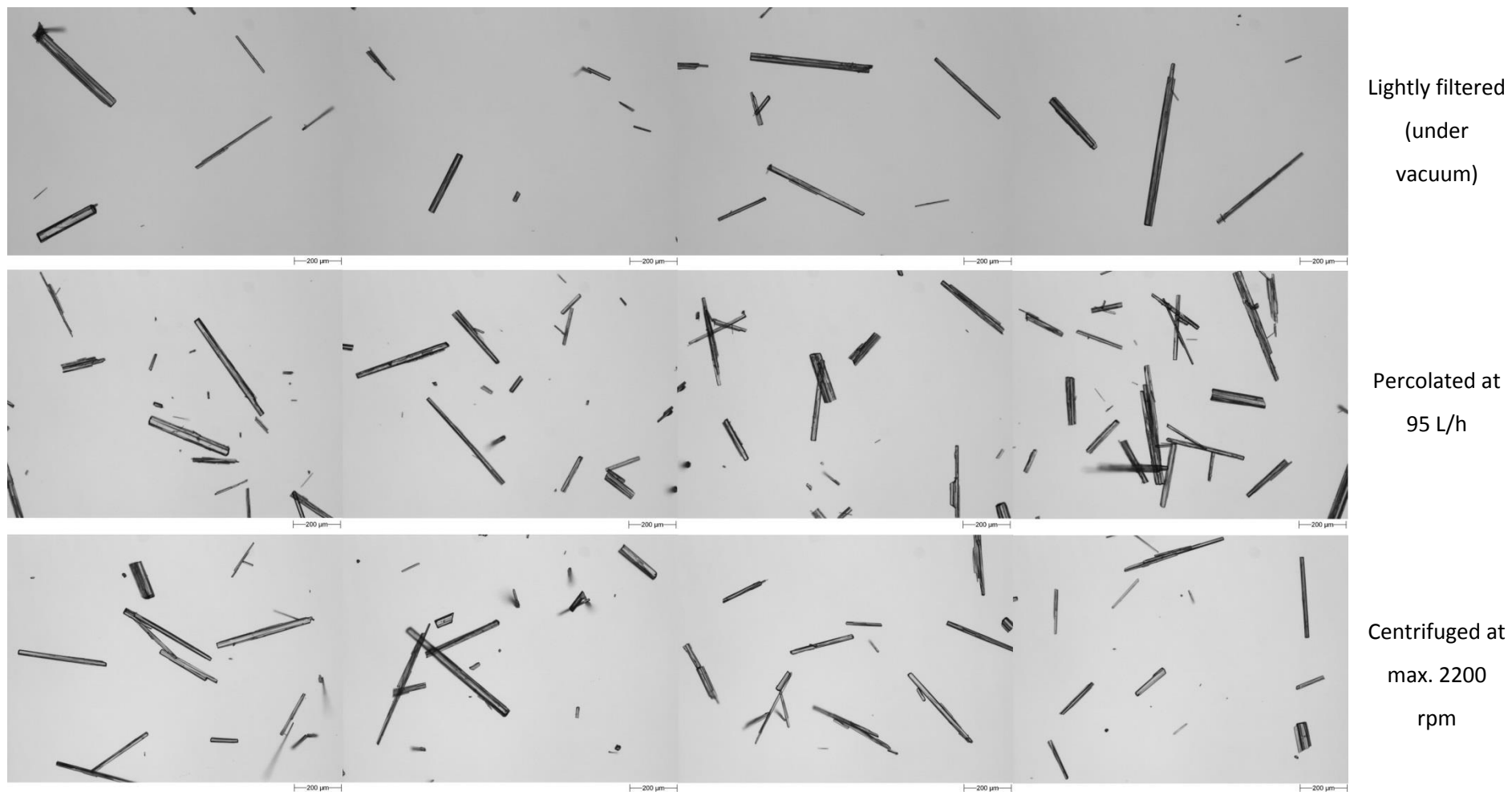


Figure 7-17: Optical microscope images of beta-glutamic acid needles after vacuum-filtration (top), continuous percolation at 95L/h (middle), and after centrifugation for 34 hours in the LUMiSizer (max rpm of 2200) (bottom)

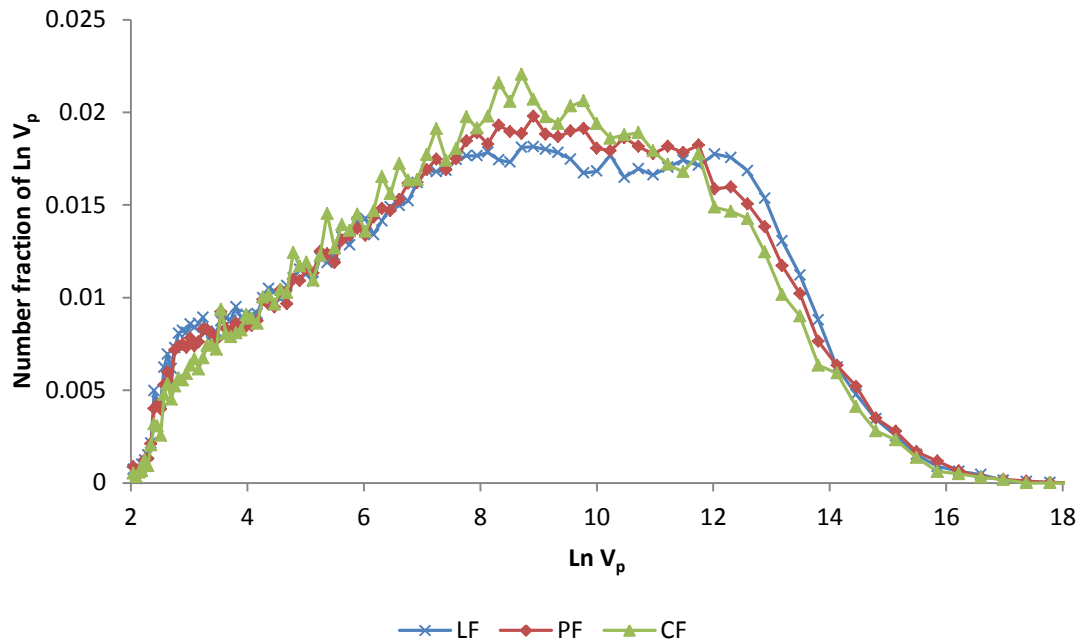


Figure 7-18: Modelled volume ($L_p * 0.5 * w_p^2$) size distributions of vacuum/lightly filtered (LF), percolated (PF) and LUMiSizer-centrifuged (CF) samples of beta-glutamic acid

The quantitative data from the G3 (Figure 7-18; Figure 7-19) appears to lend weight to these microscopic observations. The size distribution data in Figure 7-18 models the particles as ‘shoe-box’ like entities and calculates an assumed volume based on the particle dimensions (see Chapter 5 for explanation).

The greatest differences between the profiles is evident where a section of medium-large sized particles in the LF sample outsize the PF and CF samples (observable at approx. 12-14 $\ln V_p$). Apart from this instance, there are few differences between the 3 curves. This is of note as previous evidence has shown much of the differences in size distribution to be evident in the larger particle size ranges (i.e. larger particles are likely to break).

Here the centrifuged sample displays a change in the fraction of ‘large’ particles (defined as particles in the dataset with modelled volume $> 10 \ln V_p$ – see Chapter 6 for explanation) of 0.015; roughly corresponding to the mean change in large particles for a 31.1 L/h percolation (0.014). For comparison the highest flowrates and pressures display reductions in the fraction of large particles anywhere from 0.06 (127.5 L/h) to 0.1 (159.5 L/h).

In addition it should be noted that the percolation experiment (exp. 30c) conducted is not particularly indicative of a typical percolation conducted at 95 L/h; values of particle size change observed (reduction in fraction of large particles of 0.002) are well below those of the mean for this flowrate (reduction of 0.03); hence the similarity between this distribution and centrifuged size distribution is additional evidence of low levels of breakage.

In such situations of ambiguity however, it is helpful to appreciate the entire range of particle properties as output by the Morphologi G3, as these can often highlight features not ordinarily observed. In this instance, the distribution of particle aspect ratios is displayed in Figure 7-19.

Aspect ratio is another important gauge in the determination of changes in particle morphology, particularly for the case of needles. As needles break and split into smaller fragments, the ratio of their width/length changes i.e. a needle snapped in half doubles its aspect ratio. Hence for any breakage events one would anticipate an increase in the overall distribution of aspect ratios.

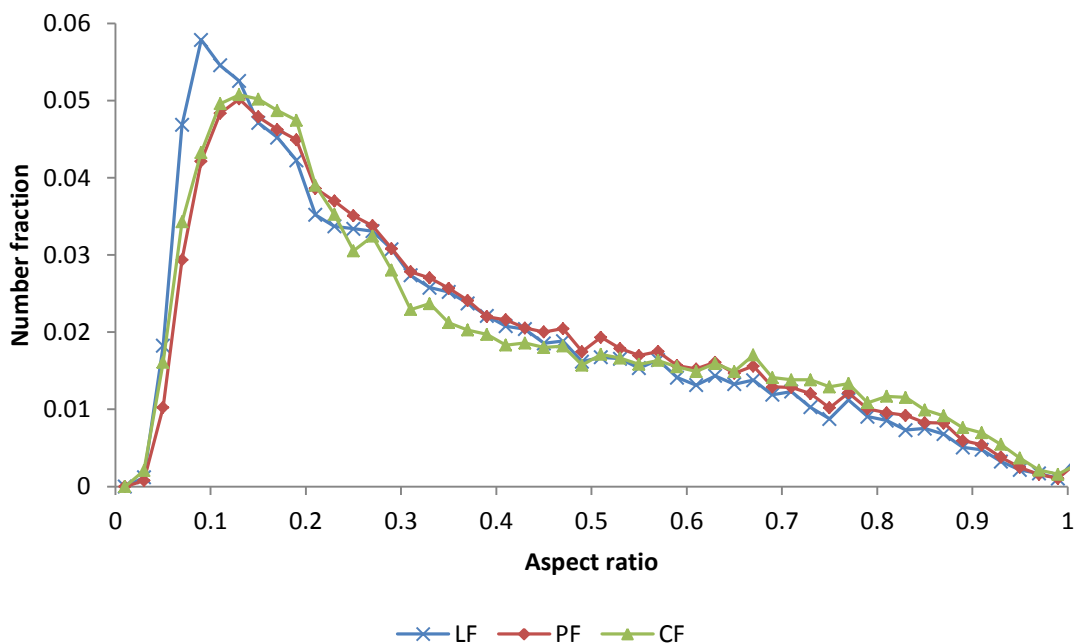


Figure 7-19: Aspect ratio distributions of LF, PF and CF (centrifuged) samples of beta-glutamic acid

The aspect ratio distribution does highlight a negative change in particle elongation (i.e. distributions shift downwards and to the right), but again the change is evidently small for both of these experiments. For example a change in the fraction of elongated particles (i.e. particles with an aspect ratio of < 0.21 before and after percolation) of 0.02 is observed under centrifugation; this is lower than the mean change observed under a percolation flowrate of 31.1 L/h – 0.025 (see Chapter 6). For comparison a high-rate percolation may experience a reduction in the fraction of elongated particles of 0.07 (127.5 L/h) to 0.2 (159.5 L/h).

Overall the centrifuged particles do display some levels of size and shape change, but this is presumably attributable to the solids handling process (i.e. disruption of crystals in retrieving them from the sample cells) and the size measurement, as the pressures experienced under centrifugation are not significant compared to larger scale experimental filtrations as examined in Chapter 6.

7.6 Conclusions

The major conclusions to be drawn are the difference in compression behaviour between the needle-like particles of beta-glutamic acid, urea and Lesinurad, and less elongated ('blocky'/rounded) particles of alpha-glutamic acid and urea-biuret. Crucially, the difference in compression with urea-biuret is almost certainly due to the differences in particle shape, as the urea-biuret is not an alternate polymorph or co-crystal. Similarly with the glutamic acid based systems, the change in shape leads to a large variance in compression behaviour under pressure.

The largest reductions in bed height appear to occur at lower centrifugal velocities, with diminishing reductions as acceleration is increased; as would be expected of a bed undergoing compression and elimination of its voids – larger voids less supported by the particles around them will tend to collapse first as they are the point of least resistance. The needle-like systems each show steady and gradual decline in bed height; indicative of a porous bed structure.

The relaxation (elasticity performance) of these systems is also highly dependent on shape; the lower elongation particle beds exhibit much greater elasticity and relax after compressive force is released in line with the strain energy imparted to them. Needle-like systems tend to display lower elasticity, implying that the cake structure is plastically deformed and strain energy is lost to rearrangement and breakage of particle-particle contacts.

Breakage or disruption of the packing network under load would permanently (plastically) deform the particle bed, meaning that once the force is released the bed would not return to its original height. The lower aspect ratio particles are expected to suffer a lesser degree of consolidation due to their inherent shapes being less conducive to bed rearrangement, which may explain the large degree of relaxation of the beds.

The urea system displays interesting settling behaviour in that it exhibits considerable resistance to the deformation of its cake structure; 6 hours of constant acceleration at 2200 rpm rotation is not sufficient to reach an equilibrium bed height, such is the strength of the solid network of bonds within the cake.

In terms of comparison to filtration methods, the sample of beta- glutamic acid taken from a centrifuged sample showed a similar particle size and aspect ratio distribution to that of a percolated sample. However this sample is known to display below average particle size reduction relative to other percolations at similar flow rates. Overall the levels of breakage experienced in the particles in the centrifuge is low; meaning much of the bed consolidation

and rearrangement is due to the collapse of voids and disruption of particle contacts within the bed, and not due to actual particle fracture. This is reinforced by a model of solids compressive pressure which calculates that peak pressure drops experienced across the beds within the sample cells is low (approx. 0.03-0.06 bar).

The LUMiSizer thus presents an interesting tool for the study of particle beds at small scales. The low material requirements and sealed environment make the tool ideal for the analysis of expensive or dangerous materials, of which pharmaceutical material typically is. The settling and bed relaxation behaviour is, on the basis of the data obtained thus far, a good indication of the 'filterability' of the particle systems tested; for example blocky systems in which filtration is typically a straightforward operation display small reductions in bed height relative to the original and relaxations proportional to the square of the centrifuge rpm. Needle-like systems, typically poor to filter at scale, display significant reductions in original bed height and relaxations that vary linearly with centrifuge rotational speed.

Chapter 8

8 Modelling of Breakage and Needle Particle Beds

8.1 Introduction

As far as industrial filtrations are concerned, the characterisation of bulk bed properties is typically the desired outcome. This has been the subject of much of the work presented thus far. A key part of experimentation however is the application of mathematical equations to model data and predict outcomes based on the variables that are input. The construction of theoretical and heuristic models has a significant basis in the scale-up of laboratory based experimentation.

The aims of this chapter are to build and evaluate the prospects of models of needle particle breakage and the ways in which needle-like beds are formed. Experimental data obtained in the CPR and the batch 2 L scale filtrations is modelled to predict the extent of breakage based on the filtration pressure, using a fracture model of needle breakage.

Additionally, a bed construction model is utilised to generate theoretical beds of needle particles and outcomes are compared to experimental data of bulk density and particle contacts; this is used to evaluate the applicability of the method in which particles are placed into the bed.

8.2 Literature Review

The breakage of particles within a bed is dependent on a number of factors; notably the position and orientation of the particles (determines the number of contact points), the particle strength (and their elastic limits), particle size/shape (determines breakage mechanism i.e. attrition or fracture) and the inter-particle friction (impacts transmission of forces through the bed)[13].

Extensive work has been undertaken into the modelling and simulation of particle (bed) breakage, however much of the work is directed at so called 'ideal' cases (as is typically the case with modelling); i.e. spherical, mono-sized distributions of particles. There are some cases of the modelling of needle-like particles in the literature however.

For instance, significant work has been performed by Grof and Štěpánek, among others. Grof, Kohout and Štěpánek created a DEM model in which needle-like particles are generated by

linking spheres together with rigid bonds in order to form long chains. These are then subjected to compaction and subsequent breakage[13].

The authors found that longer particles tend to fragment at lower compaction ratios than smaller particles, due in part to them being less able to rearrange themselves to fill space in the bed; thus were exposed to higher unavoidable stress. They also noted that the needles tended to break approximately in the middle regardless of their size; an important confirmation of a commonly assumed mechanism[13]. Like many DEM simulations (due to computational efficiency requirements) the raw number of 'particles' tested is low (several hundred), and the method lacks industrial relevance due to the absence of a distribution of particle sizes.

Further work by Grof et al concentrated on using the spherical-needle constructs to simulate the effects of breakage under crystallisation. They correlated experimental data of a needle-like pharmaceutical compound with that of computation simulations of die-compacted needles, finding that levels of breakage tend to plateau with increasing compaction force; suggesting a practical limit to the extent of breakage under compression[142].

More recent analysis by Grof and Štěpánek investigated the effect of random vs. ordered packing characteristics for needle-like (rigid spherical-beam) particles, finding for similar applied stresses the randomly packed particle suffer increased breakage. This is due to the increased average number of contact points between the particles when packed in regular (uniaxial) structures. The forces experienced are spread over a larger number of contacts and hence the experienced stress per contact (the determining factor in breakage) is lower[143]. A reduction in needle breakage can be achieved through the addition of filler granules to powder mixtures to increase the number of contact points[144].

This finding is similar to that of Golchert et al, who also performed DEM simulations but on granular agglomerates of a varying particle size distribution. The authors found that the contact point network has a significant effect on the breakage of the agglomerate; more so than the shape of the structure[145]. Interestingly the authors were able to integrate a range of particle sizes into the simulation, providing an element of real-system applicability.

Sato et al performed a 2D population balance on a needle system to simulate the effects on particle size reduction during crystallisation. The authors note that the crystals tend to break only above a certain limiting aspect ratio (i.e. longer crystals experienced far more breakage). Crystals were found to break along the axis perpendicular to their lengths[146].

The investigation of single crystal properties is also of use in the development of bulk models, as these provide much of the micro scale data that can be used to develop interactions that

affect larger scale properties. Recent work into the manipulation of micro scale objects under the use of the atomic force microscope (AFM) has provided insight into the mechanical properties of single crystals.

For example Namazu et al have performed bending tests on single crystal wafers of silicon. Crystals were suspended between 2 fixed points and a pressure applied to the centre of the wafers using the AFM probe tip, causing the silicon to bend until brittle fracture is observed. The authors also tested micron and millimetre scale silicon wafers by analogous use of hardness testing instruments. Their key finding was that of a strong dependence of breakage strength on the size of the silicon wafer. Nanometre scale wafers displayed tensile strengths 2-5 times larger than those typical of the micrometre scale wafers, and roughly 40 times larger than those of the millimetre scale wafers[147].

A new methodology for the investigation of single crystal properties has recently been developed, also through use of the AFM, and is directly tied to this project. Unpublished work performed at the University of Leeds[148] has investigated the breakage strengths of crystals of beta-glutamic acid by subjecting them to bending forces until brittle fracture is observed.

Crystals are arranged overhanging a glass slide perpendicular to the edge and secured in place using cyanoacrylate glue. A stiff AFM cantilever probe is then made to contact the overhanging crystals and provide a bending moment. Crystals are then subjected to increasing forces until fracture is observed, with the resultant tensile strengths of the needles calculated by measurement of the crystal dimensions; assuming a Euler-Bernoulli beam bending model[9].

Forces required for glutamic acid needle breakage range from 0.92-1.46 mN, and by taking the crystal dimensions into account (measured using optical microscopy), tensile strengths for beta-glutamic acid are found to be in the range of 5-28 MPa. The method is still new and requires considerable development and repeat testing (to date only 5 crystals have managed to be assembled and broken) but preliminary results suggest a dependence of crystal tensile strength on the inverse of the square of the particle height[148].

8.3 Modelling of Experimental Filtration Data and Predictions of Breakage

8.3.1 Model structure

The basis of this model is used to predict the changes in aspect ratio from a freshly crystallised batch of beta-glutamic acid as it undergoes pressure filtration. As the major breakages are to be found in particles at the base of the filter bed, these will be the basis of calculation (except

for a single case which is detailed in section 8.3.2). Experimental observations from the 2 L scale batch filtrations and the CPR are used to test the validity of the model to real systems, hence the model compound in all cases is that of beta-glutamic acid.

A Python simulation is built in which a full dataset of particle parameters can be imported. The particle lengths and widths are used to calculate a probability of breakage based upon 2 factors: the particle aspect ratio (of which a more elongated particle has a higher probability of breakage), and the particle size (of which larger particles are more likely to break). In addition the filtration pressure is used to modify the probability of a particle breaking, as it has been observed that higher pressures lead to an increase in particle breakage.

The following equations are listed alongside heuristic constants that have been identified on the basis of their applicability to the final distributions they tend to produce i.e. they have been fit empirically through a trial and error basis. The following equations are a form of Weibull analysis[149].

The probability of breakage based on particle aspect ratio is:

$$Probability_{Aspect\ Ratio} = e^{k_{asp} \left(\frac{w_p}{L_p}\right)^2} \quad \text{Equation 8-1}$$

Where the constant k_{asp} is equal to -5. The value of a particle's width to length ratio is given added weight in the model by raising it to the power 2, as it is known that the particles' aspect ratio has a large effect on the likelihood of resultant breakage. Thus particles with aspect ratios close to 0 (i.e. ratio of width:length is low) are more likely to break over particles with aspect ratio close to 1.

The probability of breakage based on particle size is:

$$Probability_{Size} = 1 - e^{k(0.5 \times L_p \times w_p^2)} \quad \text{Equation 8-2}$$

Where the constant k_{size} is equal to -0.00035; probability then depends on the size of the particle in terms of the modelled cuboidal volume (see Chapter 5). Larger particles are more likely to break over smaller ones.

The modification factor based on a linear trend of filtration pressure is:

$$Probability_{Pressure} = k_{pres.1} \times \Delta P + k_{pres.2} \quad \text{Equation 8-3}$$

Where $k_{pres.1}$ is equal to 0.232 and $k_{pres.2}$ is equal to 0.292; where the probability of breakage rises with increasing pressure (increasing compressive forces).

For each particle in the distribution, the final probability of breakage is calculated as ('1-' the product of these 3 factors:

$$\text{Probability of breakage} = 1 - (\text{prob}_{asp} \times \text{prob}_{vol} \times \text{prob}_{pressure})$$

A random number generator is then introduced to determine whether the particle breaks or not. If the particle is found to break, it is split into 2 separate particles of equal width but lengths half that of the parent particle length, as such:

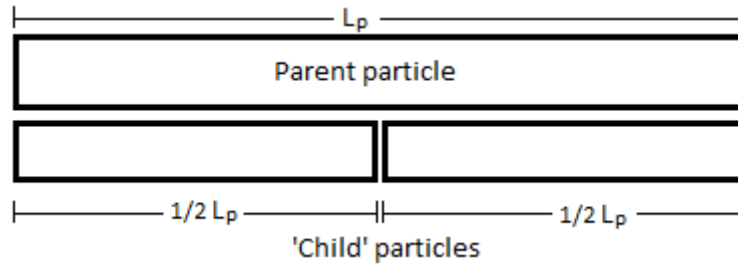


Figure 8-1: Parent needle particle breaking into 2 'child' particles

This is based on the empirical assumption that particles break approximately in the middle regardless of their absolute size[13], in addition to current experimental observations of this occurring (see Chapter 6). Particles, broken or not, are then counted; their shape is evaluated and a number-based distribution of the particle aspect ratios is calculated as per the method detailed in Chapter 5.

Only a single series of breakage events is modelled, i.e. once a particle has broken the fragments are assumed not to break a second time.

8.3.1.1 Calculation of estimated pressure drop for experiments in the CPR

As per the breakage model, the percolation pressure drop is a factor in determining the probability of particle breakage. Experiments performed in the CPR are characterised by their flowrate and by an approximate pressure reading which is subject to considerable fluctuation. As an additional means of characterisation the theoretical pressure drop predicted by the Ergun equation can be used to correlate experimental values of pressure to test their validity. As additional data is available the pressure drop can be modelled with greater certainty:

Table 8-1: List of values used to estimate fluid flow through a packed bed of diameter 3.5 cm

Parameter	Symbol	Value	Units
Superficial Velocity	u_i	Variable	m.s^{-1}
Bed Height	H	Variable	m
Particle Diameter	d_p	0.00003	m
Fluid Density	ρ_f	998.2	kg.m^{-3}
Fluid Viscosity	μ	0.001	$\text{kg.m}^{-1}.\text{s}^{-1}$
Porosity	ϵ	Variable	-
Bed Area	A	0.000962	m^2

Values of superficial velocity are obtained from the calibrated P200 pump flowrates, whilst a revised Sauter mean diameter of 30 microns is obtained from laser diffraction measurements.

Bed porosity values can also be approximated and input on the basis of a variable cake height (which varies as a function of filtration pressure). These are taken from approximation of bulk density relative to the true density of glutamic acid, taken from 2 L filtration measurements. It is therefore assumed that bed porosities at 2 L scale are similar to those encountered in the CPR. The true density of glutamic acid is 1540 kg/m^3 [150].

Data is modelled for a low flowrate operation experiment (experiment 10b) and a high flowrate experiment (experiment 40f) – see Chapter 6 for more details on these experiments.

Table 8-2: List of values used to estimate fluid flow through a packed bed at a flowrate of 31.1 L/h

Parameter	Symbol	Value	Units
Superficial Velocity	u_i	0.0147	m.s^{-1}
Bed Height	H	0.05	m
Porosity	ϵ	0.74	-
Est. ΔP from Ergun		0.171	bar
ΔP (experimental)		0.2	bar
Error		14%	-

Table 8-3: List of values used to estimate fluid flow through a packed bed at a flowrate of 127.5 L/h

Parameter	Symbol	Value	Units
Superficial Velocity	u_i	0.0497	m.s^{-1}
Bed Height	H	0.03	m
Porosity	ϵ	0.61	-
Est. ΔP from Ergun		2.131	bar
ΔP (experimental)		3	bar
Error		29%	-

The estimated ΔP values offer a good match at low flowrates but poor correlation at high flowrates, due to turbulent effects in the fluid.

8.3.2 Model results

8.3.2.1 Probability factors

The range of probability factors for a selected range of example particle dimensions is presented in the tables below, based on Equation 8-1, Equation 8-2 and Equation 8-3.

Table 8-4: Probability factors for particles of a particular aspect ratio

Aspect Ratio	Probability Factor
0.1	0.951
0.15	0.894
0.2	0.819
0.25	0.732
0.3	0.638
0.35	0.542
0.4	0.449
0.45	0.363
0.5	0.287
0.6	0.165
0.7	0.086
0.8	0.041
0.9	0.017
1	0.007

Table 8-5: Probability factors for a selection of particles based on their size (modelled volume)

Length (μm)	Width (μm)	$L_p * 0.5 * w_p^2 (\mu\text{m}^3)$	Probability Factor
500	50	625000	1.0
400	40	320000	1.0
300	30	135000	1.0
200	20	40000	1.0
100	10	5000	0.826
50	5	625	0.196
10	1	5	0.002
500	10	25000	1.0
400	10	20000	0.999
300	10	15000	0.995
200	10	10000	0.970
100	10	5000	0.826
50	10	2500	0.583
10	10	500	0.161

Table 8-6: Probability factors for a range of filtration pressures

Pressure (bar)	Probability Factor
0	0
0.18	0.14
0.5	0.41
1.6	0.66
3	0.99
3.7	1.15

The results of the 2 L scale batch filtrations are able to be fit to the model with a linear dependence with solid agreement. Extrapolating this trend to a point at which the continuous percolation rig (CPR) 'high flowrate' (approx. 127 L/h) experimental results fit the model for breakage yields an apparent 'pressure' of 3.7 bar (in reality this is just a value that must be input into the linear trend in order to yield the appropriate probability factor). The result is interesting nonetheless as this indicates that the continuous percolation at 127 L/h flowrate imparts higher forces and thus increased levels of particle breakage compared to the 3 bar batch filtration.

It should be noted that in order for data to fit the results of the CPR 'low flowrate' (approximately 31 L/h) experiment an additional linear dependence of pressure is formulated between pressures of 0 and 0.5 bar. This in fact agrees with experimental evidence (presented in Chapter 6) that low flowrates suffer a greatly reduced level of breakage compared to the higher order flowrates. In addition a sample of particles from the bottom of the cake is not available for this data; a bulk percolated 'PF' sample is used instead. This is acceptable for the low flowrate as breakage is significantly reduced at lower pressures/flowrates and thus the distributions of height fractions tend to converge closer to one another.

With this in mind the trends can be visualised in Figure 8-2 below.

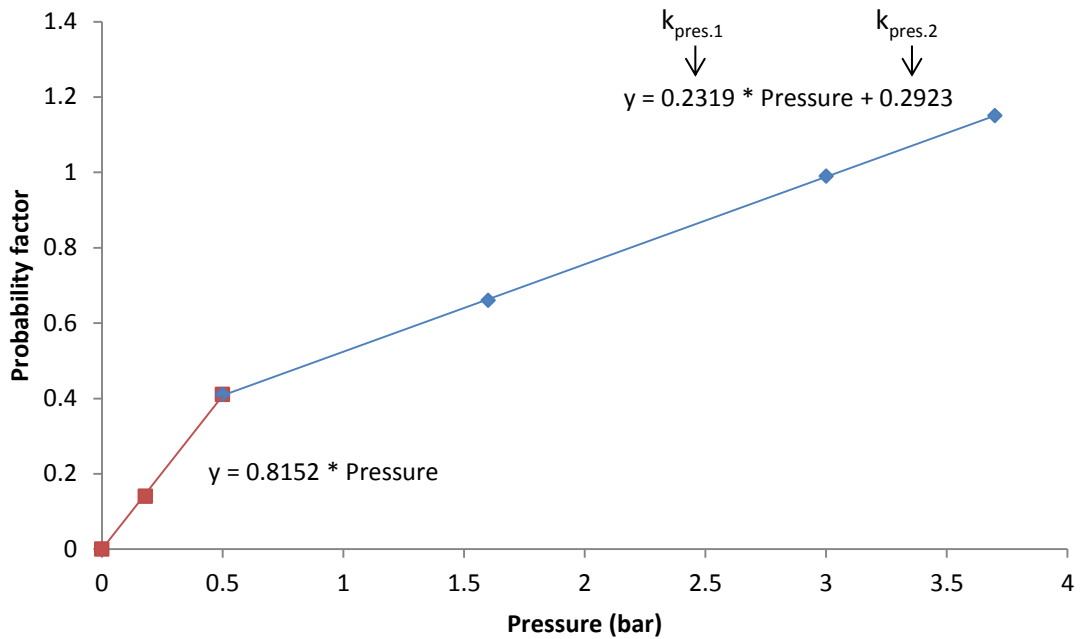


Figure 8-2: Probability factor as a function of filtration pressure (the identification of Equation 8-3 constants from the linear equation are exemplified)

It can now be observed that the calculated pressure drops according to the Ergun equation (Table 8-2 and Table 8-3) show good agreement at low flowrates but poor agreement at high flowrates. With low flowrates the Ergun equation predicts a pressure drop of 0.17 bar, experimentally this is observed as 0.2 bar, whilst to fit the data a pressure of 0.18 bar is required. At high flow, Ergun predicts a pressure of 2.13 bar, experimentally a pressure of 3 bar is read from the gauge and to fit the data a pressure of 3.7 bar is predicted. The considerable error in the high flowrate pressures are not unexpected; it is well known that predictions of flow suffer with increased levels of turbulence in the system.

8.3.2.2 Predicted size distributions and commentary on model fit

The predicted particle size distributions produced by feeding particle data into the algorithm is available to view in 5 Figures, starting with Figure 8-3.

The primary aim when looking for good fit of the model is to accurately reproduce the high-elongation regions of the curves (<0.2 aspect ratio). These represent the most important areas of the distribution, as this is the region where the most needle-like (fragile) particles are represented; thus it is of paramount importance to model the breakage of these highly elongated needles accurately. The 5 datasets presented all show good fit of the modelled distributions compared to the PFB in these regions.

Limitations result from the lack of predictive power of the model itself. On the whole, the constants in the probability modifier equations can be modified to yield better fits of either the low aspect ratio regions (<0.2) and poor fits of the remaining regions, or better fits of the medium-high aspect ratio regions and poor fits of the <0.2 region.

This paradoxical fitting is possibly influenced by to the lack of multiple breakage events within the model. A single breakage event fits well with reducing the initial <0.2 aspect ratio LF curve, as clearly almost all of these particles are among the first (and most likely) to suffer breakage. However in a real system a pair of broken particle fragments (particularly large and still relatively elongated ones) would still be likely to break under increased compressive stress.

Furthermore the modelling of attritional breakage is not considered and this likely has an effect on the resultant distributions; however it appears that the lack of attrition does not significantly affect the final result. It would be expected that attritional breakage would produce small fragments and fines that are likely to have very high aspect ratios. The highest aspect ratio regions (~0.95-1) are actually a region in which the model typically overestimates the breakage of particles and thus overshoots the fit of the PFB curve; hence it can be concluded that attrition does not have a large effect on the overall result.

Additional limitations of the model are clear within the high flowrate (127.5 L/h) CPR data, which displays the most significant deviations in the 0.2-0.8 aspect ratio regions. This is likely due to the distribution not being influenced by the settling of particles (where the batch filtrations are). Settling of larger particles is observed under batch filtration (see Chapter 6) and the presence of larger particles within the PFB sample influences the size distributions. The batch filtrations are seen as the primary target for fitting model parameters as these are more representative of industrial filtrations, so this is an acceptable error.

Data fit for the low flowrate (31.1 L/h) CPR is acceptable with the addition of a 2nd pressure probability trend into the model; save for the 0.2-0.4 aspect ratio regions, as with the other data sets.

Overall the model provides good fit for the breakage of needles on the basis of a fracture of parent particles into 2 child particles of equal length (length half that of the parent particle). Limitations are evident in the mid and high aspect ratio ranges; the distributions are typically slightly overestimated in the mid-aspect ratio regions thus it is likely that initial breakage propensity for mid-level size/elongation particles is too high. Future work would therefore concentrate on the addition of a more realistic set of breakage rules that takes into account multiple breakage opportunities for the particles and an overall reduced likelihood of initial breakage.

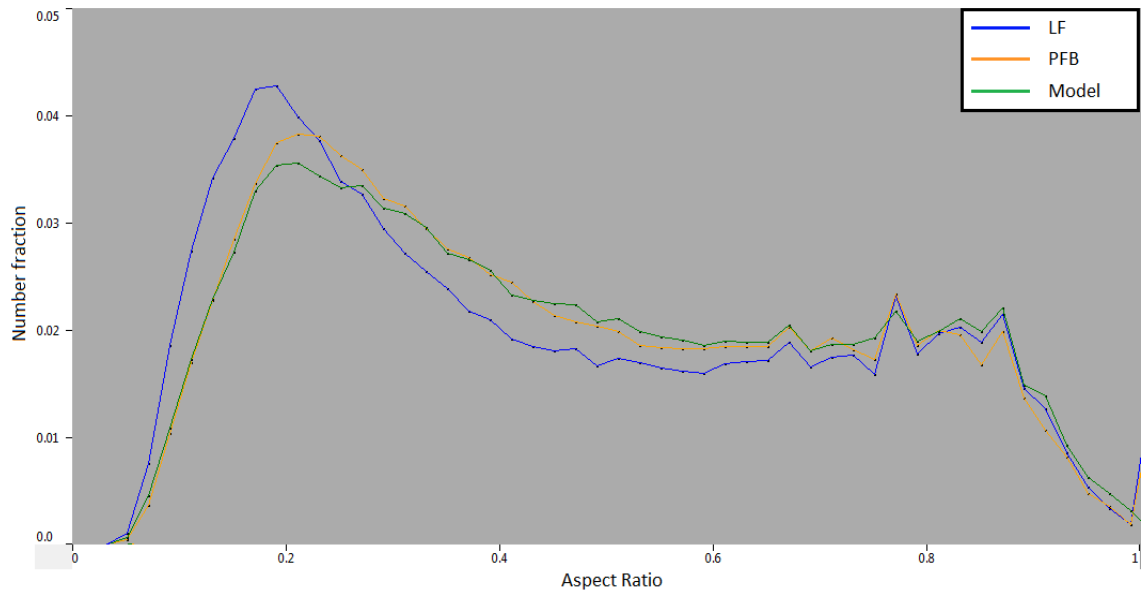


Figure 8-3: Modelled distribution for 0.5 bar batch 2 Litre pressure filtration of beta-glutamic acid – fraction of broken particles relative to total = 0.137

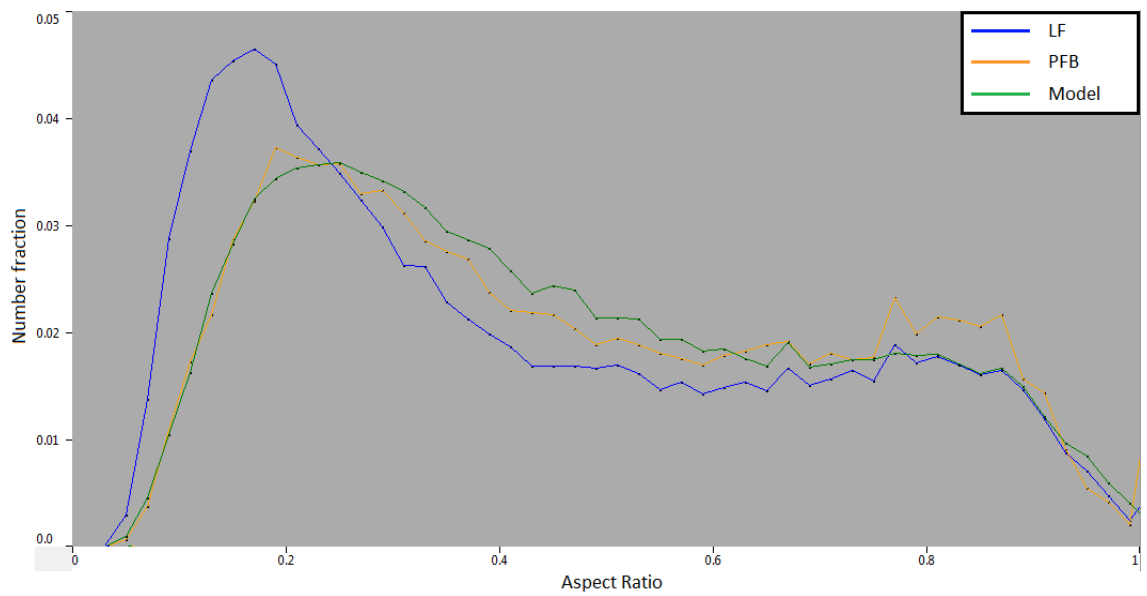


Figure 8-4: Modelled distribution for 1.6 bar batch 2 Litre pressure filtration for beta-glutamic acid – fraction of broken particles relative to total = 0.256

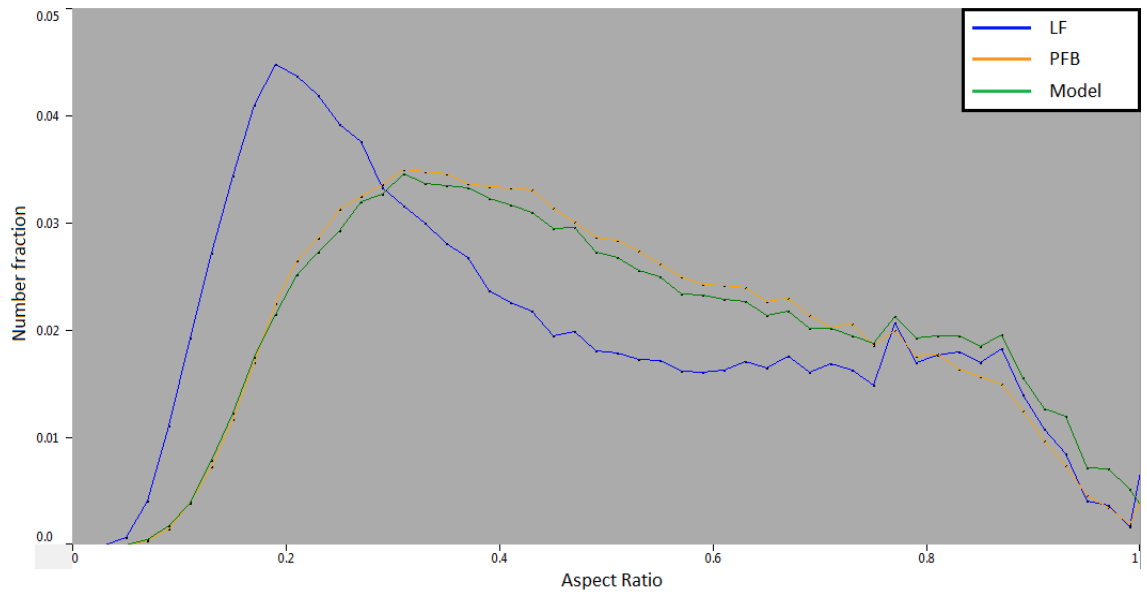


Figure 8-5: Modelled distribution for 3 bar batch 2 Litre pressure filtration for beta-glutamic acid – fraction of broken particles relative to total = 0.328

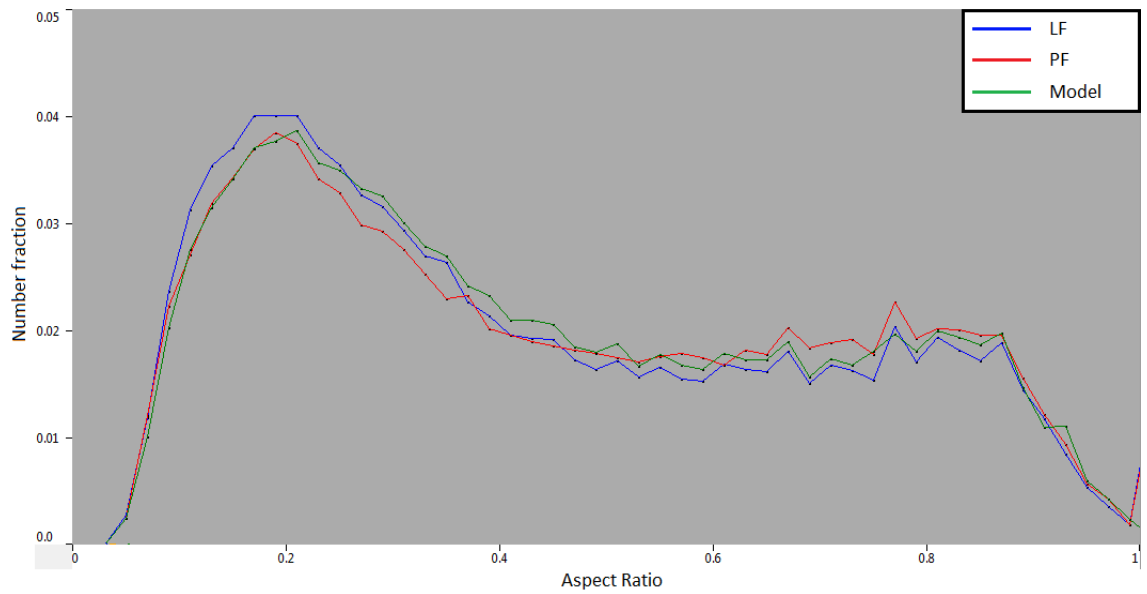


Figure 8-6: Modelled distribution for 31.1 L/h flowrate percolation of beta-glutamic acid (note modelled distribution is compared to the 'PF' distribution as data for particles from the base of the cake is not available) – fraction of broken particles relative to total = 0.05

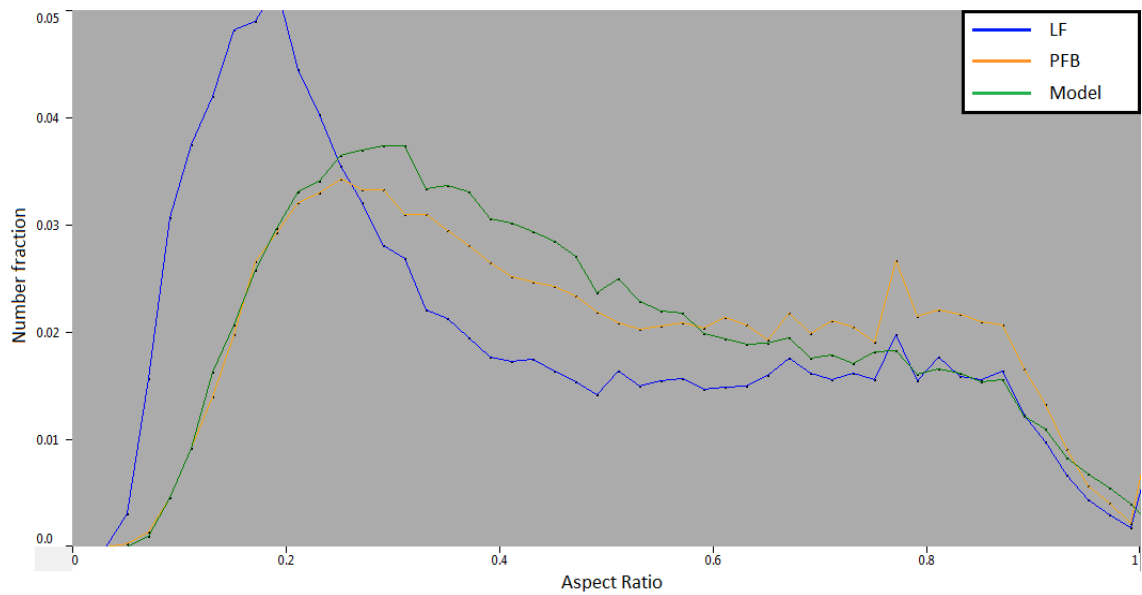


Figure 8-7: Modelled distribution for 127.5 L/h flowrate percolation of beta-glutamic acid– fraction of broken particles relative to total = 0.427

8.4 Modelling of Needle-like Crystal Beds

8.4.1 Introduction and experimental input to the model

Modelling of particles is typically conducted using a rigorous method such as discrete element modelling (DEM), due to its high precision and depth. The scope of DEM is typically limited to lower numbers of particles however, due to the intense computing requirements for calculation of particle interactions. Using simple scripting with a traditional programming language a model can be developed that is capable of processing tens of thousands of particles within a much shorter time period.

A model is envisioned in which a bed of needle-like particles is constructed by ‘dropping’ particles onto a 2-dimensional grid. When a ‘falling’ particle contacts an existing particle in the bed it comes to rest on top of the existing particle, causing the height of the bed to grow as more crystals are added. The resultant crystal stack is reminiscent of a bed of needles.

In order to retain as much relevancy as possible to the experimental filtrations, particle length data obtained from the Morphologi G3 is used to determine the particle dimensions of the simulated needles being placed in the stack. The particle addition order is randomised using a simple algorithm not detailed here. 4 sample measurements worth of particle data is input into the model, yielding a total of 101,189 particles with which to build the particle bed.

Particles are modelled as 1-dimensional beams of infinite stiffness and friction; as such once placed in the bed they remain static. No contact mechanics are simulated. Particle width is

negated, whilst particle heights are assumed constant at 1 'height unit' – equivalent to 25 microns.

The area over which the particles are dropped is confined to a sufficiently small space such that appreciable building of the bed will occur, but significant particles will avoid contacting the 'walls' of the simulation space. A standard bed size of 300 pixels is selected, with a scaling factor of 1 pixel = 10 microns; i.e. the total bed diameter is equal to 3000 microns or 0.003 m. At this scale a 100 pixel length particle would be equivalent to a 1000 micron particle; a 10 micron length particle would be 1 pixel long on the canvas.

8.4.2 Model structure

8.4.2.1 Object oriented programming and the 'particle object'

Python is an object-oriented language and thus enables the construction of 'objects'. An object is a data-structure that encapsulates different data types and functions into a kind of 'blueprint', which can then be used to reproduce identical forms of the original, all with access to the same properties and functions[151] (it is helpful to think of manufacturing processes here – plastic bottles are 'objects' that are created with a mould – they were all created from the same mould and each share the same properties but are all unique entities!). In this way, thousands or even millions of objects can be generated and modified in a similar and generic manor.

Functions or methods are simply procedures that perform the same task, such that sequences of code that are required to run multiple times do not have to be physically written tens or thousands of times over; one would simply 'call' the function as many times as necessary.

The particle object, or blueprint, includes a number of data *attributes* (i.e. variables that refer to some form of data) that are common to all the particles e.g. floating point integer values represent its (x_1, y_1, z_1) and (x_2, y_2, z_2) coordinates in 3d space. In this way, the particles' position in the bed can be inferred by accessing and retrieving these values. A method to calculate the particles' 3D length is also common to all particles, and again can be accessed by calling the relevant method with the *argument* (i.e. the input data to the function) as the particle in question.

Additional attributes of the particle object include an integer ID (a simple unique reference for each particle), floating point integer values to represent the particles' gradient and y-intercept in 2D space (see section 8.4.2.3), and a multi-dimensional array structure that stores the

physical contact points of each particle; with an (x, y, z) coordinate of the actual contact as well as a reference to the particle ID to which it is contacting.

Methods common to all particle objects include procedures for calculating the particles' gradient/y-intercept, finding the particles' 'sector' or position on the canvas (see section 8.4.2.4) and others such as calculating the particles' 3D length or registering contacts.

8.4.2.2 Particle generation and legality

The cake area (or canvas) is displayed on-screen as a circular area representing a plan-view of the cake. Particles are generated incrementally by first selecting random x and y coordinates for one end of the particle. A random orientation for the particle is then calculated using a Pythagorean method (Figure 8-8); where the roots of the horizontal and vertical particle components (dx; dy) sum to the total particle length (i.e. the particle length is the hypotenuse of this theoretical triangle).

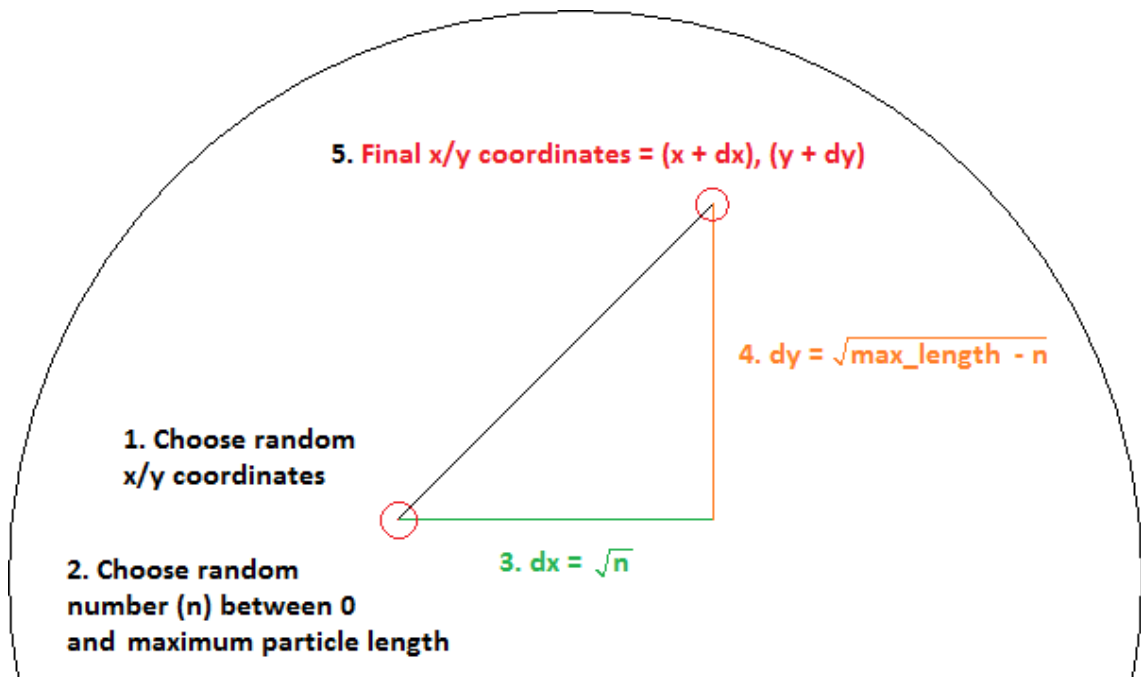


Figure 8-8: Plan view schematic of particle placement on the canvas (not to scale)

By knowledge of the fact that the particles may extend at any angle from vertically up (180° ; $n = 0$) to horizontally across (90° ; $n = \text{max. particle length}$) a random orientation can be applied to the particle by multiplying 'dx' or 'dy' by 1 or -1.

To check if the newly generated particle is legal and lies within the boundaries of the circle (bed) area, the following equation is used:

$$(x_i - x_c)^2 + (y_i - x_c)^2 \leq r_c^2$$

Equation 8-4

Where 'x_i' and 'y_i' apply to both the initial and final x and y coordinates of the particle (hence the verification is run twice), and the subscript 'c' applies to the coordinates of the centre of the circle. The radius of the circle is denoted by 'r_c'.

8.4.2.3 Evaluation of particle contacts in 2D space

As additional particles are generated and added to the bed model, the likelihood that a particle will fall over an area which is already occupied by a particle increases. At this point, the particles will contact and the newly generated 'falling' particle must be placed on top of the existing resting particle.

To determine whether particles have contacted or not (in 2D space; 3D placement builds on this algorithm); this requires solving the linear equations that are associated with the particles. Each generated particle has a particular set of x and y coordinates on the canvas, when viewed from the top-down perspective (from the z-axis). Using these coordinates it is possible to calculate a gradient and y-intercept for the theoretical lines as they exist in 2D space, with the equation of the line in the form:

$$y_i = m \times x_i + c \quad \text{Equation 8-5}$$

The intersection of 2 lines is by definition a point at which their x and y coordinates are both identical. Thus, the equations can be solved by setting them equal to each other:

$$m_1 \times x_1 + c_1 = m_2 \times x_1 + c_1 \quad \text{Equation 8-6}$$

The result yields the y-coordinate of intersection; the x-coordinate is found by substitution back into either of the original linear equations.

Almost all of the lines (particles) will intersect at a certain point in space (most somewhere outside the bed area); the crucial aspect being whether these lines intersect within the boundaries of the actual 'particle'. For example, the schematic in Figure 8-9 displays a series of particles on the canvas; all existing lines contact with 'particle a', either directly or by extrapolation. The difference between lines 'c-e' and line 'b' is that the (x, y) coordinates of contact for 'particle b' lie within the bounds of the particle itself:

$$x_{1; \text{line } b} < x_{\text{contact}; \text{line } b} < x_{2; \text{line } b} \quad \text{Equation 8-7}$$

And:

$$y_{1; \text{line } b} > y_{\text{contact}; \text{line } b} > y_{2; \text{line } b} \quad \text{Equation 8-8}$$

Whereas for lines 'c-e' this is not true:

$$x_{1; \text{line } e} \text{ and } x_{2; \text{line } e} < x_{\text{contact}; \text{line } e} \quad \text{Equation 8-9}$$

This obviously must also apply for line 'a' for the contact to be valid.

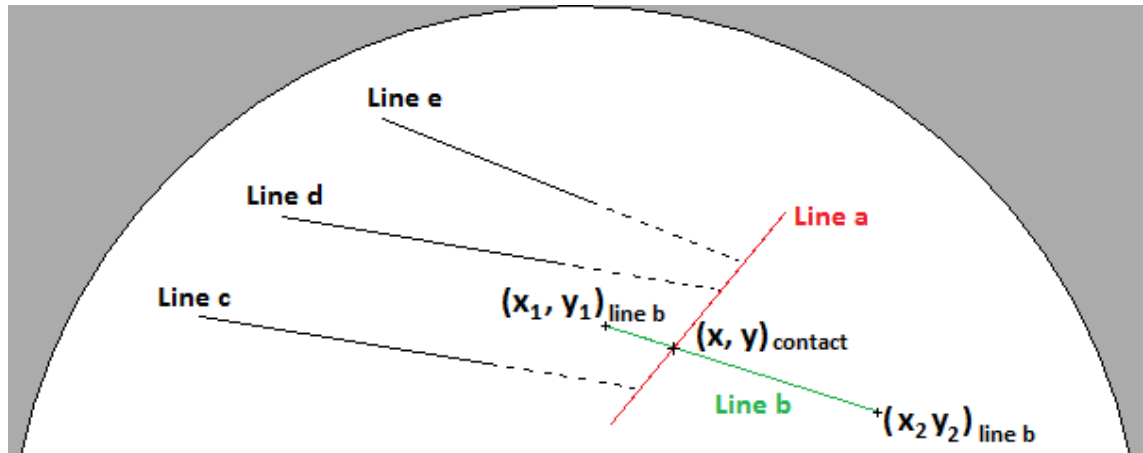


Figure 8-9: Plan-view schematic for the method of solving particle-particle interactions (not to scale)

8.4.2.4 Data structure – 'sectors' to narrow search for contacts

To increase the scalability of the model, a data structure is generated to increase the efficiency of contact searching. As particles are generated, they are placed into a specific 'sector' (or a number of sectors if the particle overlaps these). A simple division of the bed with horizontal and vertical lines defines a grid, with each separate area of the grid a discrete sector. In this way, when searching for potential contacts for each particle, only particles within the sectors that the potential 'falling' particle encompasses are evaluated for 2D contact; thus avoiding the wasted evaluation of tens of thousands of lines per particle generation cycle.

8.4.2.5 Placement of particles in 3d space

To place particles onto the canvas and begin building the bed, the 'potential' contacts for the particle must be evaluated first. These are existing particles that have already been placed and thus have already been assigned a 3D vector, including height coordinates of z_1 and z_2 . The algorithm is to scan through all the existing 'placed' particles (only if they reside in the current particles' 'searchable sectors' – section 8.4.2.4) by solving equations of lines in 2D (section 8.4.2.3).

Several possible outcomes result from the algorithm; either the particle has no (0) potential contacts, 1 potential contact, 2 potential contacts or more than 2 potential contacts. Each situation is evaluated separately in the following sections.

It should be noted that in 3D space particles are assumed to have a height unit of '1'; this is not absolute and can be scaled along with the heights of all particles at any stage. It does mean however that particles will come to rest with a height differential of +1 relative to any contact height, e.g. a particle resting on the base is defined as having a height of 1, whilst a particle resting in an identical position directly on top of this will have a height of 2, as its contact height will be 1.

It should also be noted that particle friction is assumed to be infinite; i.e. particles will not slip after contacting or slide into different conformations in the bed.

8.4.2.5.1 Placement with 0 contacts

This is the simplest of outcomes; a particle with 0 potential contacts exists in clear space and will thus come to reside flat on the base of the bed. The particle $z_1 = z_2$ which equals 1, and x/y coordinates do not change. This outcome obviously becomes less likely as more particles are generated and the bed fills up.

8.4.2.5.2 Evaluation of particle/contact height

For all other outcomes (potential contacts > 0), the height of potential contact must be evaluated in order to calculate the height at which the new particle will rest at. The simplest outcome involves the potential contact particle having been placed on the base, in which case the particle would come to rest on top of this particle: the contact height would equal 1. Similarly if the 'placed' particle is already resting horizontally ($z_1 = z_2$) then the contact height is z_1 (or z_2).

For all other eventualities, the 'placed' particle will have $z_1 \neq z_2$ and thus the contact height will lie at a point along the vector representing the particle. From a 2D perspective, this can be calculated using the law of similar triangles if the particle's position is envisaged as a right-angled triangle (Figure 8-10).

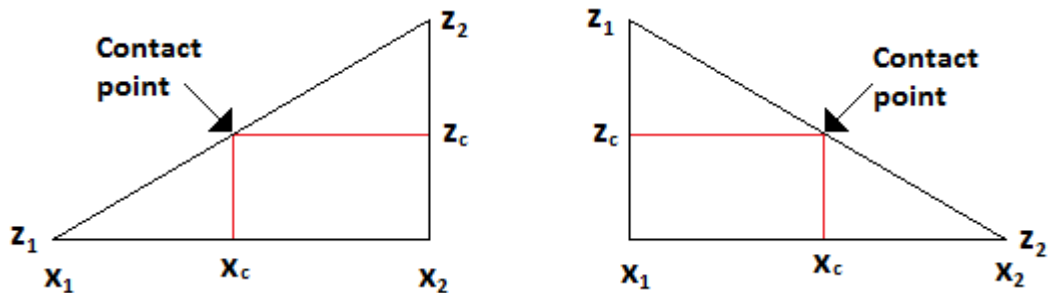


Figure 8-10: Calculation of contact height (c_z) by law of similar triangles

If the existing particle has coordinates of (x_1, z_1) to (x_2, z_2) then a right-angled triangle may be formed by connection of the coordinates in 2 dimensions. Then, depending on whether the particles' z_1 or z_2 is higher (whether the particle points 'up' or 'down'), the contact height c_z can be evaluated from:

$$\frac{c_x - x_1}{x_2 - x_1} = \frac{c_z - z_1}{z_2 - z_1} \rightarrow c_z = z_1 + \left((z_2 - z_1) \times \frac{c_x - x_1}{x_2 - x_1} \right) \quad \text{Equation 8-10}$$

Or:

$$\frac{x_2 - c_x}{x_2 - x_1} = \frac{c_z - z_2}{z_1 - z_2} \rightarrow c_z = z_2 + \left((z_1 - z_2) \times \frac{x_2 - c_x}{x_2 - x_1} \right) \quad \text{Equation 8-11}$$

Where c_x has been found from solving equations of the lines in 2D. If the particle is resting in a horizontal plane ($x_1 = x_2$) then x values can be substituted with the y coordinates of the particle and evaluated using the same method.

8.4.2.5.3 Placement with 1 contact

Where a single contact is identified for the particle, then the particle must also be resting on the base (except in the case of a particle 'balancing' which will be discussed). Assuming first that the particle will rest with one end supported by the base of the bed and the other supported by an existing particle, the 'lean' of the particle needs to be evaluated; this is performed using Pythagoras' theorem (Figure 8-11; top):

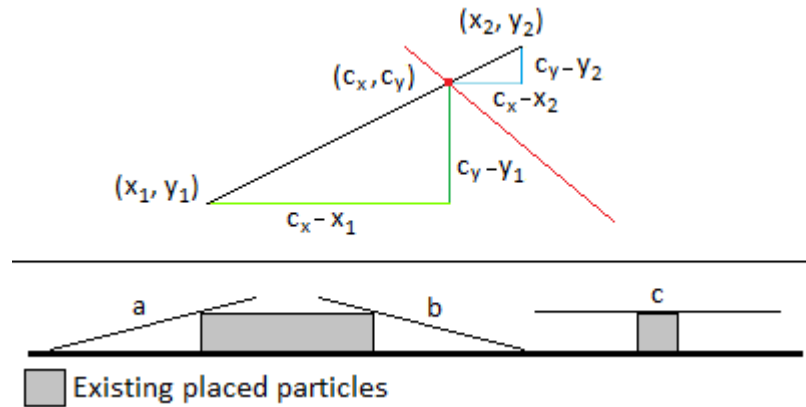


Figure 8-11: Finding particle lean from Pythagoras' theorem

It is assumed that the end of the particle that will be raised higher is dependent on the distance from this end from the contact point. In the example in Figure 8-11, the distances are the hypotenuses $(x_1, y_1) \rightarrow (c_x, c_y)$ and $(c_x, c_y) \rightarrow (x_2, y_2)$, which are calculated from Pythagoras' theorem:

$$\begin{aligned} \text{hypotenuse}_1 &= (c_x - x_1)^2 + (c_y - y_1)^2 \quad \text{and} \quad \text{hypotenuse}_2 \\ &= (c_x - x_2)^2 + (c_y - y_2)^2 \end{aligned} \quad \text{Equation 8-12}$$

In this example, as hypotenuse_1 is greater than hypotenuse_2 , the particle will rest with the point (x_2, y_2) higher than that of (x_1, y_1) , as particle 'a' does in Figure 8-11; bottom. If the reverse is true, then the particle rests as particle 'b' in Figure 8-11; bottom. If the hypotenuses are identical, then the particle is assumed to balance with equal z_1 and z_2 , as illustrated by particle 'c' in Figure 8-11; bottom, and no further calculation is necessary to 'place' the particle on the bed.

Assuming the particle leans with unequal z_1 and z_2 , then 2 fixed points in 3D space are known to exist; the point at which the particle contacts the base and the point of contact with the other particle. A 3D vector between these 2 points can be calculated from (following equation assumes particle leans 'up' as for particle 'a'; Figure 8-11; bottom):

$$\text{hypotenuse}_{3D} = \sqrt{x^2 + y^2 + z^2} = \sqrt{(c_x - x_1)^2 + (c_y - y_1)^2 + (c_z - z_1)^2} \quad \text{Equation 8-13}$$

Again 3 possibilities result from the calculated length of the vector; either the vector is less than the legal particle length limit, the particle is precisely equal to the legal limit (no further calculation required; coordinates are final) or the vector between the 2 points is greater than the legal limit; the legal limit in this case being the original particle length provided from experimental data. In the latter case, the particle is rejected as illegal and is not placed within

the bed; this avoids the generation of overly large particles that can result from close contacts with high z-distance between them.

If the particle is within size limits then the ratio of the vector between the $[(x_1, y_1, z_1): (c_x, c_y, c_z)]$ and $[(x_1, y_1, z_1): (x_2, y_2, z_2)]$ can be used to enlarge the vector up to the legal particle size and find the coordinates of (x_2, y_2, z_2) , e.g.

$$x_2 = \frac{(c_x - x_1)}{ratio} + x_1 \quad \text{Equation 8-14}$$

The 'x' terms in Equation 8-14 are replaced with equivalent 'y' and 'z' terms to find the remaining coordinates.

8.4.2.5.4 Placement with 2 contacts

For placement on 2 identified contacts the particle is assumed to rest between the 2 known fixed points in space, as a bridge would between the fixed points of land on either side. As always the simplest potential outcome is that of 2 contacts of equal height, in which case the particle will rest also with equal height. For all other outcomes the vector between the 2 contacts must be evaluated using Equation 8-13.

If the 3D vector distance between the 2 contacts is equal to the legal particle size limit, then no further calculation is necessary and the particle is placed on the bed. If the vector is greater, then placement is illegal and thus a new random set of coordinates are generated to re-place the particle in a differing random position. If the particle is within length limits but either of the extrapolated z_1 or z_2 heights are less than 0 (i.e. the particle encroaches on the base of the bed) then the placement is also illegal and therefore rejected.

If the particle is still legal then it is assigned extra length to return it to the original particle length. The (x_1, y_1, z_1) coordinates of the particle are evaluated using a method to similar to that outlined in section 8.4.2.5.2 (rule of similar triangles). With known starting point and intermediary vector coordinates (i.e. the contacts) the particle can thus be extended to full length using vector ratios, as with Equation 8-14.

8.4.2.5.5 Placement with more than 2 contacts

As model processing time increments and more particles are added to the bed, it becomes increasingly likely that more than 2 potential contacts are identified for the particle. Typically these contacts are below the present top (maximum height) of the particle bed, and thus placement on these particles is not acceptable and would prevent the bed from 'growing' in

height. A method is thus needed to evaluate the appropriate contacts on which the particle would theoretically truly rest on.

Although implicit in the placement for any number of contacts but not explicitly stated until now, the particles are assumed as though they are ‘dropped’ from an arbitrary height and fall with equal z_1/z_2 until contact with another particle is made, at which point they theoretically rotate around the fixed pivot of contact until finding another immovable surface (either the base or another particle). This process is illustrated in Figure 8-12.

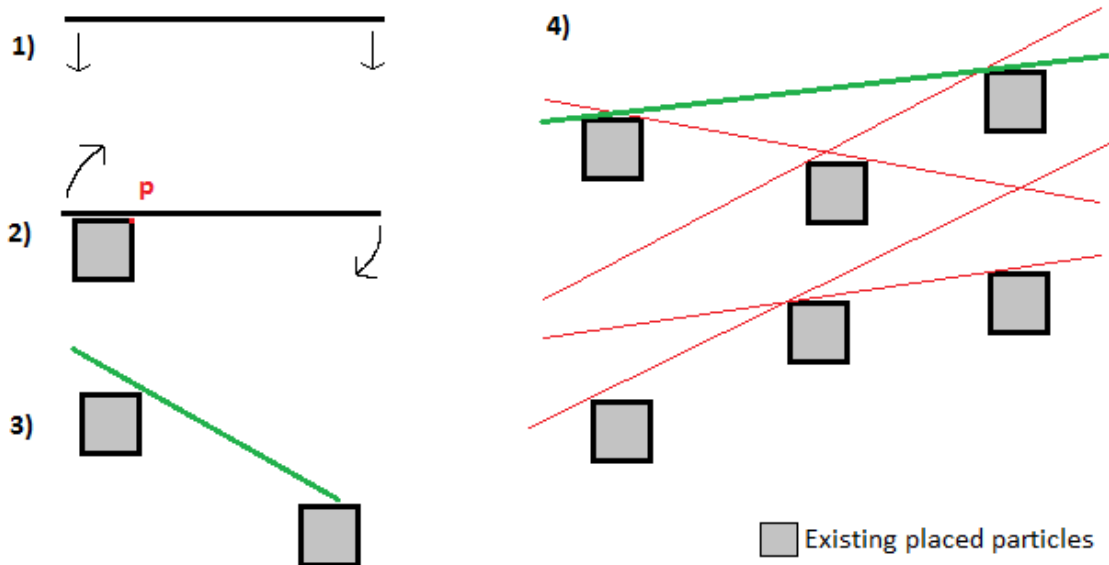


Figure 8-12: Placement of particles over multiple contacts; 1) Particle falls from arbitrary height with equal z_1, z_2 ; 2) Particle meets contact and begins to rotate around fixed pivot ‘p’; 3) Particle stops rotation and is successfully ‘placed’ when another surface is encountered; 4) When multiple contacts are encountered, a falling particle would come to rest on the 2 highest contact points (i.e. placement as the green line depicts; red lines depict illegal resting points)

This process is now pertinent in the evaluation of multiple potential contacts; as is envisioned in Figure 8-12; 4), any number of particle placement configurations are possible, but the model assumes a particle dropping until 2 points of contact are made (theoretically 3 or more contacts could line up in a vector but is unlikely with 8 decimal points of precision as used in the calculation of coordinates). Assuming this, the particle would come to rest on the 2 highest existing points of contact before even encountering any other contact points.

A simple algorithm to evaluate the highest contact points within the array of potential contacts thus enables the particle to be placed as with any other 2-contact particle; the method is as in section 8.4.2.5.4.

For 3 or more contacts all of equal height, then the particle is ‘placed’ to balance on these particles with equal height coordinates. This becomes increasingly unlikely as simulation time progresses, but is an eventuality with multiple particles all resting on the base.

8.4.2.6 Assignment, determination and calculation of various bed properties

The canvas (bed) size, as previously mentioned, is 300 pixels on-screen; thus corresponding to 3000 microns assuming a scaling factor of 10 microns per pixel. This yields a total bed area of:

$$A = \frac{\pi D^2}{4} = \frac{\pi \times 0.003^2}{4} = 7.07 \times 10^{-6} m^2 \quad \text{Equation 8-15}$$

The bed area is constant, but bed height varies with the extent of vertical particle building that occurs. The bed height is defined by the maximum height of the highest particle in the bed.

The bulk density is the mass per unit volume. The mass of the particle bed can be approximated using some additional experimental data.

Dry vacuum filtered beta-glutamic acid powder from the 0.5 bar 2 Litre batch pressure filtration test (pre-filtration 'LF' material) is measured out onto a mass balance using the 11 mm³ Morphologi G3 spatula; hence a known volume of powder is collected for each measurement. The mass of each sample is very low however, thus a cumulative mass is recorded after each sample is weighed, and the mean differential calculated thereafter to reduce error in the measurement. 20 samples are weighed in all, with the results in Table 8-7.

Table 8-7: Masses of 11 mm³ vacuum filtered beta-glutamic acid samples

Sample No.	Cumulative mass (mg)	Differential (mg)
1	1.6	1.6
2	4.8	3.2
3	7.6	2.8
4	9.9	2.3
5	12.3	2.4
6	15.3	3
7	17.9	2.6
8	20.6	2.7
9	23.5	2.9
10	26.8	3.3
11	29.8	3
12	33.3	3.5
13	36.7	3.4
14	39.3	2.6
15	42.4	3.1
16	45.9	3.5
17	49.5	3.6
18	52.5	3
19	56.2	3.7
20	59.3	3.1
Mean	2.97	mg
St.Dev.	0.50	mg
Max	3.7	mg
Min	1.6	mg

The mean mass of material per spatula of beta-glutamic acid powder is thus approx. 3 mg. As it is known that the input data (i.e. the particle length data used to generate the particles in the model) contains 4 sample volumes, it is assumed that the total mass of the particles within the simulation is:

$$4 \times 2.97 = 11.86 \text{ mg} = 0.00001186 \text{ kg} \quad \text{Equation 8-16}$$

4 samples of powder from the 11 mm³ Morphologi G3 spatula yield an approximate volume of:

$$4 \times 11 \text{ mm}^3 = 44 \text{ mm}^3 = 4.4 \times 10^{-8} \text{ m}^3 \quad \text{Equation 8-17}$$

Meaning the approximate bulk density of the sampled powder is:

$$\frac{0.00001186 \text{ kg}}{4.4 \times 10^{-8} \text{ m}^3} = 269.55 \frac{\text{kg}}{\text{m}^3} \quad \text{Equation 8-18}$$

Which roughly corresponds to a bulk density of a particle bed of glutamic acid under negligible filtration pressure (see Chapter 6) of 236 kg/m³. As the simulated bed is also built assuming negligible pressure acting on the particles, this value is a *target average* bulk density for the simulation. Differential bulk densities are obtained by taking differential 'slices' of d (bed height) and calculating the mass occupying these slices.

Returning to the sample mass; the average mass per crystal can be approximated from:

$$\frac{0.00001186 \text{ kg}}{101,189 \text{ particles}} = 1.172 \times 10^{-10} \text{ kg/particle} \quad \text{Equation 8-19}$$

A simulation that places every particle has a known fixed mass (Equation 8-16); whilst for partial simulation or testing purposes a different figure is utilised to calculate a more accurate mass. As particles are added in a random fashion and each particle has its own length, this means the mass of the particle should vary according to its size. A value of particle mass per micron of length allows calculation of individual masses on a particle-by-particle basis. Assuming an average particle length of 76 microns, then the sum of the lengths of all 101,189 particles multiplied by the mass per particle per micron approximately yields the original total mass for example particles of lengths 2 and 714 microns contribute masses of:

$$2 \mu\text{m} \times 1.542 \times 10^{-12} \frac{\text{kg}}{\text{particle} \cdot \mu\text{m}} = 3.08 \times 10^{-12} \text{ kg} \quad \text{Equation 8-20}$$

$$714 \mu\text{m} \times 1.542 \times 10^{-12} \frac{\text{kg}}{\text{particle} \cdot \mu\text{m}} = 1.1 \times 10^{-9} \text{ kg} \quad \text{Equation 8-21}$$

Thus the total particle masses can be obtained more accurately than e.g. assuming a particle volume and multiplying by the particle true density – which produces an order of magnitude error in particle mass compared to the experimentally obtained masses in Table 8-7.

8.4.3 Model output and discussion of data

Table 8-8: Mean bulk bed properties for the simulation ran with differing particle input counts

Particle Count	Total Particle Mass (kg)	Bed Height (units)	Est. Bed Height (m)	Bed Volume (m ³)	Ave. bulk density (kg/m ³)	Ave. Contacts per particle
5000	5.89E-07	15.614	0.000390	2.76E-09	216.15	1.254
10000	1.17E-06	29.764	0.000744	5.26E-09	224.18	1.608
15000	1.74E-06	47.654	0.001191	8.42E-09	207.96	1.796
20000	2.32E-06	69.437	0.001736	1.23E-08	190.43	1.927
30000	3.49E-06	98.625	0.002466	1.74E-08	201.65	2.110
40000	4.68E-06	123.682	0.003092	2.19E-08	215.16	2.237
50000	5.86E-06	140.170	0.003504	2.48E-08	237.04	2.329
75000	8.84E-06	219.954	0.005499	3.89E-08	228.33	2.495
101189	1.18E-05	289.926	0.007248	5.12E-08	233.20	2.622

Bulk properties of the bed are listed in Table 8-8 (additional simulation data including standard deviation are listed in the appendices). Overall the model shows good progression as increasing the particle count yields roughly linear increases in the bed height, whilst bulk density remains approximately constant. Typical average bulk densities also show good agreement with experimental observations. Bulk densities are however slightly lower than might be expected due to the increased likelihood of particles to find a resting position within the centre confines of the bed, as opposed to the outer areas (see Figure 8-13), meaning there is a fair amount of volume that remains empty.

The model displays good reproducibility for repeat simulations. A full listing of obtained data with standard deviation is listed in the appendices. Average contacts per particle shows the greatest reproducibility. As particle count increases, in general deviations in bulk density and average contacts per particle decrease (i.e. it is expected that larger particle counts produce finer averages); whilst deviations in bed height rise, as would be expected due to the random nature of building e.g. from large particles bridging over gaps and introducing large voids to the bed.

8.4.3.1 Visual bed structure

The bed constructed by the model can be viewed from multiple dimensions by drawing the particles in the x, y and z-planes (Figure 8-13). The result is depicted as a particle contact ‘heat map’, where particles are coloured according to the number of contacts they share with other

particles – particles with 0-2 contacts are black-grey; 3-8 are green-yellow; 9-18 are orange-red-magenta; 19-25 are cyan-blue and particles with greater than 25 contacts are coloured dark blue. Additional images for all particle counts tested are available in the appendices.

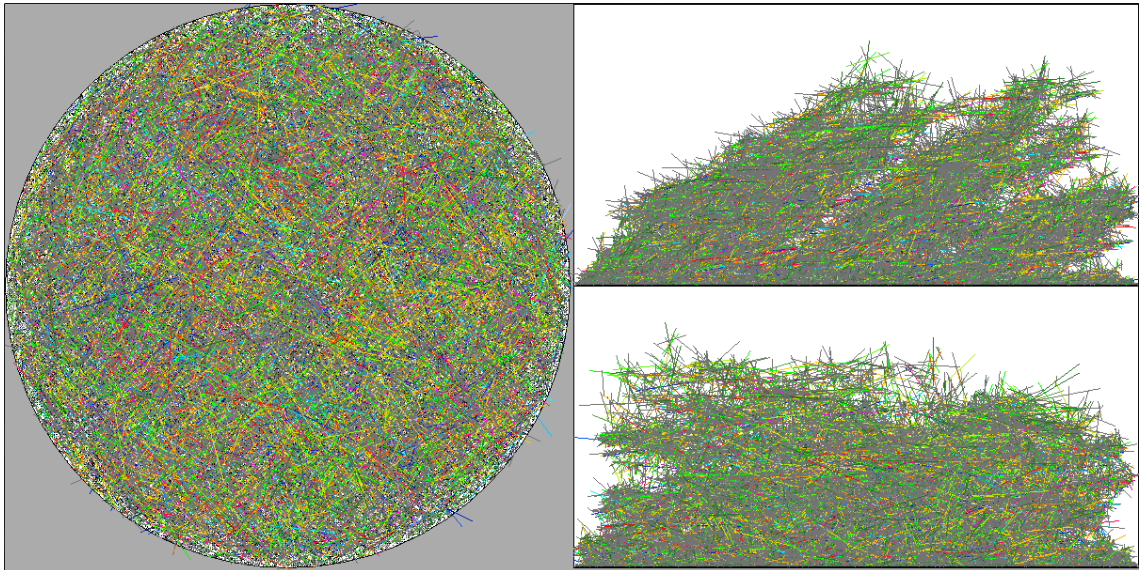


Figure 8-13: Example of model visual data output for simulation of 101,189 particles; left – z-axis view of particle bed; right (top) – x-axis view of particle bed; right (bottom) – y-axis view of particle bed. Particles are coloured according to number of particle contacts

From the visual data output, and as discussed previously, it is clear that the limits imposed by the model tend to favour the placement of particles within the centre-confines of the bed. This is a natural limitation of the simplistic nature of the model; the model needs boundaries and thus increasing the area of the bed would only serve to reduce this effect (i.e. the outer areas of the circle would reduce as a fraction of the total bed area), but not eliminate it entirely.

It should be noted that several particles exit the confines of the 2D bed when calculating the 3D placement. The effect is minimal (over the course of 100,000 particles) and thus does not significantly affect the result.

The visualisation does however provide a good indication that the simulation is performing adequately; for example natural voids in the bed can be observed from the x and y-axis views, and a range of 3D orientations are exhibited by the needles as they fall not just horizontally but also at a range of vertical angles.

8.4.3.2 Bed bulk density

By sorting particles by their average 3D heights and grouping them into differential height fractions of the bed, the mass within each height fraction can be calculated on the basis of the particle length. Knowing that each fraction has a constant height and area allows calculation of

each slice volume, which allows subsequent calculation of the bulk density of the slice. Figure 8-14 is a visual representation of the change in bulk density as a function of bed height.

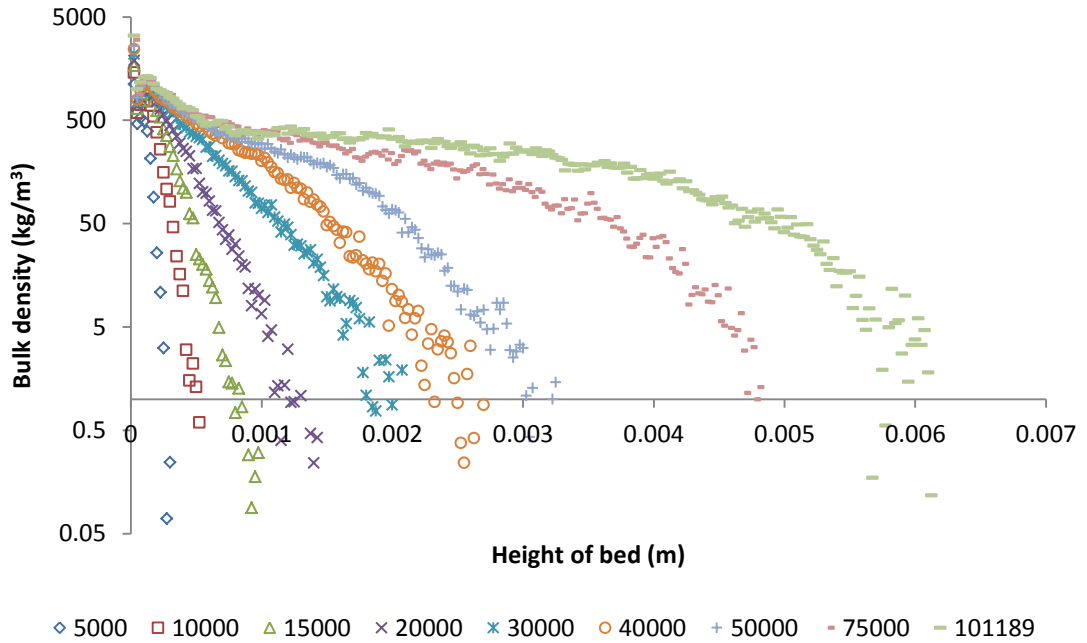


Figure 8-14: Bulk density of differential height fractions of the bed as a function of bed height for simulations of differing particle counts

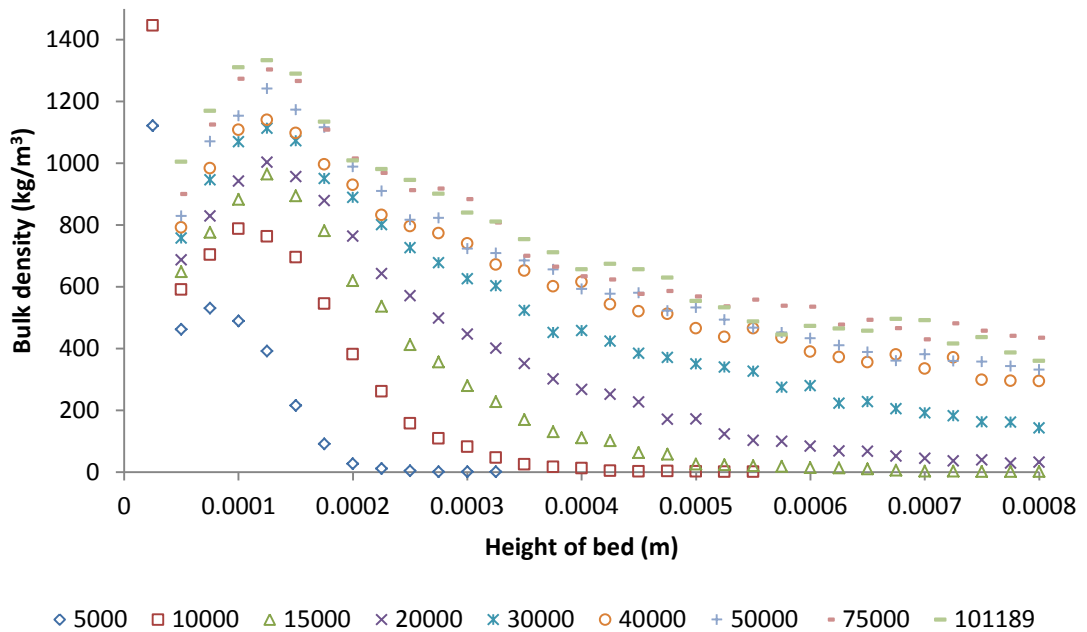


Figure 8-15: Bulk density of differential height fractions of the bed as a function of bed height for simulations of differing particle counts (with focus on data around bed heights of 0 – 0.0008 m)

The bulk density displays a local maximum at the base of the bed ($H = 1$) where a large number of particles are placed directly onto the flat canvas (more easily observed in Figure 8-15). A secondary maximum is then observed after 2-5 height units (i.e. data points). Differential bulk

densities then largely follow logarithmic trends, i.e. the log of the bulk density decreases roughly linearly with the height of the bed.

The primary and secondary maxima of bulk density both increasing with simulation count is evidence of the effect of small particles ‘falling’ through the bed to reach the lower regions. The smallest gaps in the bed are susceptible to small particles being placed within them due the lack of any particle width.

A real system would have a practical limit to the extent to which smaller particles could traverse their way through the voids between the larger particles; the simulation however is limited due to the 1-dimensional nature of the particles. This means as simulation count rises, increasing numbers of smaller particles are placed into lower height fractions and higher concentration of mass results, particularly in the base height fraction.

The primary/secondary maxima are also influenced by the type of bed building that is carried out. In the initial stages of bed construction, the needle particles are more likely to lie horizontally (or nearly so) with a preferential orientation, meaning more of their mass is concentrated in the lower height fractions. As bed building progresses and increasingly particles are placed at high angles, the concentration of their mass (dependent on the average of the min. and max. particle height coordinates) tends to be more randomly distributed throughout a number of differing height fractions.

Bulk densities dropping off with bed height is likely caused partly by the convex shape of the needle stack, i.e. the peak bed height is highest in the centre of the bed and lowest at the edges; with a slight curve in-between. This means as the volume of the bed increases (which is dependent on the maximum height), the mass contained within the bed is increasingly concentrated only within the centre of the bed. It is also affected by smaller particles being concentrated near the bottom of the stack, instead of being more evenly distributed throughout the bed.

The bulk density as predicted by the differential heights is therefore not as reliable as it could be, and the bed construction would benefit largely from the incorporation of particle width into the model (or at the least a method of halting the depth penetration of smaller particles).

8.4.3.3 Particle contact points

Analogous to bulk density, the contact points between particles can be plot as a function of bed height; this is displayed in Figure 8-16. The prediction of particle counts presumably suffers from the same limitations as the bulk density, i.e. this must be affected in some way by the concentration of smaller particles in the lower regions of the bed, but the results appear to

show an independence of average particle contacts on bed height (excluding the top of the bed).

It is clear from the data in Figure 8-16 that for a typical particle within the cake, assuming it is buried beneath a sufficient number of particles, that the average number of contacts for the particle is approximately 3.5 – 4 i.e. for particles within the bulk of the bed. As would be expected, the average number of particle contacts tails off towards the top of the bed as the exposure limits the number of particles in close proximity.

This is particularly evident with higher particle count simulations, as random fluctuations begin to dictate the entire height fraction i.e. this occurs when a small number of large needles come to rest pointing directly upwards and thus skew the result.

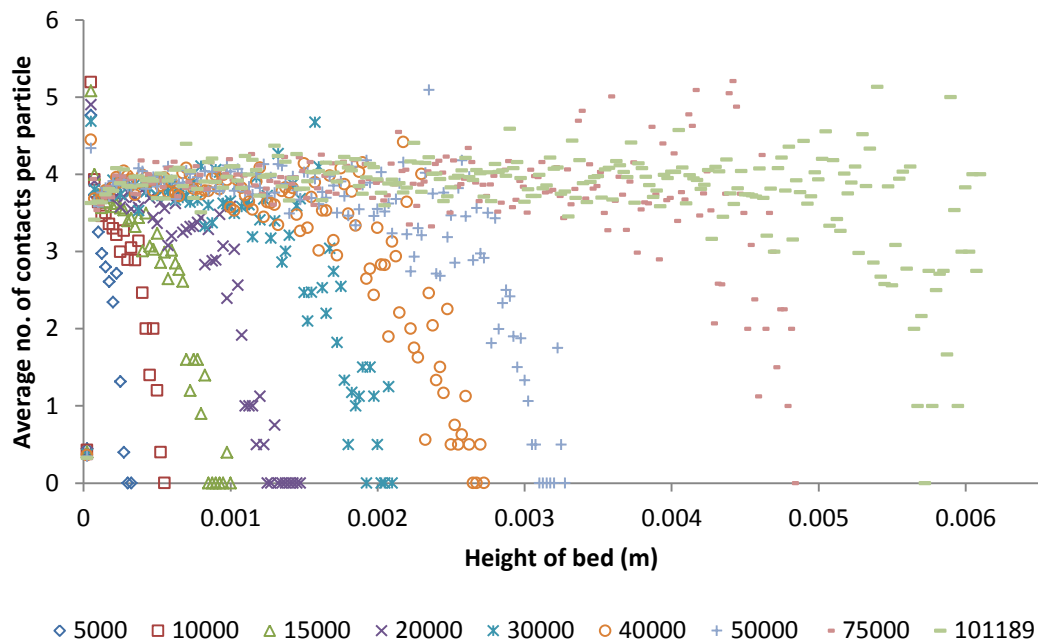


Figure 8-16: Average number of contact points per particle as a function of bed height

As is evident from the visual output (Figure 8-13), there are particles within the bed with significantly more contacts than the average (25+). Number of contacts can be plot as a function of particle length; as is displayed in Figure 8-17.

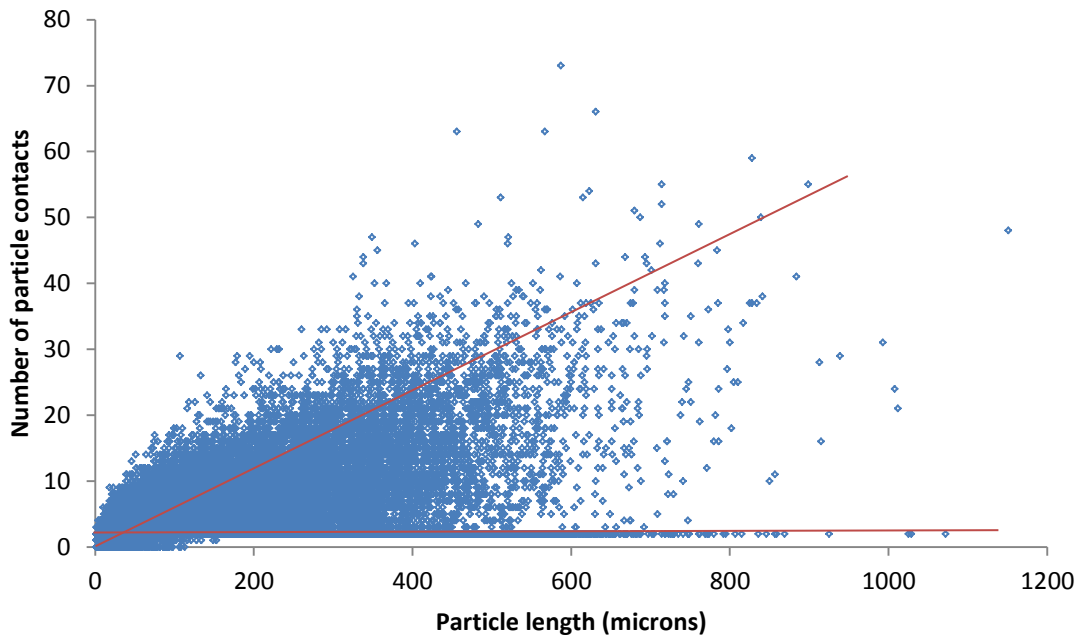


Figure 8-17: Number of contacts vs particle length for a simulation of 101,189 particles

A reasonable linear correlation is evident between the particle length and the number of particle contacts. This is to be expected as larger particles cover a wider range within the bed. Of the particles with zero contacts (and thus little or no influence on the structure of the bed), almost all of these are particles below 50 microns in length, with the largest being a particle of 113 micron length. Similarly the number of particles with a single contact is dominated by particles < 75 microns in length, with a maximum of 153 microns. Particles with 2 contacts are the most common within the bed, with particle size relatively independent on the numbers of these particles; meaning these particles provide significant structure to the bed.

As particle length increases, the average number of contacts rises, with many large particles in contact with significant numbers of others (e.g. from up to 20-70). This provides confirmation that the larger particles within the bed are the dominant structural entities; supporting the majority of the contacts equates to supporting the majority of the force transmitted through the bed. Their large size also contributes more to addition of height to the bed; smaller particles tend to 'fall' down to the base of the bed and are thus able to fit into tighter voids (increasing bed density but not significantly 'growing' the height of the bed).

8.4.4 Discussion of model applicability and limitations

As previously discussed, modelled bulk densities show fair correlation with experimental values. Although there is certainly some error in the averaged and differential values (missing mass at edges of the bed and smaller particles disproportionately falling to the bottom of the

bed, respectively), they are at least within the approximate experimental ranges (i.e. no order of magnitude errors for example). Thus the actual simplicity in which particles are 'placed' into the bed shows applicability to real systems.

Per the model rules, particle placements are rendered illegal if the particle drastically exits the bed area; thus longer needles are more likely to come to rest at higher angles. This is not unlike a real system, in which the wall of the vessel limits the extent to which a long needle would be able lie horizontally.

This simple assumption combined with the modelled bed building could explain why (relatively) uncompressed bulk densities in the LUMiSizer cells are so low (see Chapter 7) compared to experimental beds in the 2 Litre batch filtrations (Chapter 6) – approx. 134 kg/m^3 at 350 rpm rotation compared to 236 kg/m^3 at negligible pressure. With the dimensions of the LUMiSizer cells being 2 mm x 7 mm, the vessel geometry is roughly 2-4x – 7-14x the size of the larger particles in the distribution, assuming 500 – 1000 micron needles. This means many of these larger particles would find it difficult to come to rest with a horizontal (and thus conducive to high bulk density) resting position, and are more likely to lie at high angles and thus add more height to the bed (this is conducive to lower bulk densities).

The major limitations of the model include the lack of rigour, scalability and limited randomness. The model is simple in its application of particle placement; particles are assumed as rigid, massless 1-dimensional lines with infinite friction between them, meaning no re-arrangement of the particles is possible after they have been placed (this is in part a combination between the limited time-scale in which this simulation was built in and the aim to model a subset of real particle data).

The highly complicated and processor-intensive requirements for particle movement would make this unrealistic to achieve with a relatively slow interpreted language such as Python, thus it is likely that any future model taking this into account would be built using a more rigorous DEM software package or a language that can be compiled (compiled programming languages run much faster than interpreted languages).

The lack of model rigour leads to unrealistic bed building, particularly as the particle count moves above 50,000, where fibrous networks are formed that have significant 'overhang' as they are suspended in mid-air above the rest of the bed. In a more rigorous system, the build-up of mass would eventually lead to collapse of these structures, much as a particularly heavy branch of a tree might alter the centre of mass of the tree and cause it to lean. It should be noted however that the 'overhang' is not a phenomenon completely absent from real needle particle beds, but the unlimited extent to which these can infinitely build is.

Future implementations would also take into account the particle width; this would provide a more realistic 3D structure of the bed by preventing the placement of smaller particles on the base of the bed after a certain period of time.

Another limitation involves the scalability of the model; simulation times scale exponentially with particle count as significantly greater numbers of particles are scanned for potential contacts (the model takes 3 minutes to simulate 10,000 particles, 80 minutes for 50,000 particles and 7 hours for 101,189 particles). A data-structure has attempted to alleviate this problem to a certain extent, but its applicability is limited. Given more time, a more thorough data-structure could be built which would take particle height into account in addition to narrowing the 2D sector size. This would severely limit the number of potential particles to which the falling particle would have to be tested alongside and thus dramatically improve the simulation time.

The model is also pseudo-random in nature. To save processing time, a pre-randomised set of particle length data is selected for input, meaning each simulation places the particles in the same order. Improvements are identified in which a random particle would be selected from a much larger source dataset (i.e. a simulation of 100,000 particles would be selected from a greater database of many times this size), thus improving the model applicability to real systems through additional randomisation.

8.5 Conclusions

Modelling of experimental data has consisted of 2 outlets; the application of a heuristic algorithm to determine changes in size distribution due to needle breakage and the simulation of the construction of needle-like particle beds.

The crystal breakage algorithm uses particle data obtained from the Morphologi G3 optical microscope to simulate the effects of crystal breakage on the particle size distribution of a crystal mass. By assuming a 3 factor probability algorithm, particles are given a chance to break based on their overall volumetric size, aspect ratio and the filtration pressure that is acting upon them. Needles are assumed to break precisely in half at their centre-points (across the longest dimension), thus producing 2 daughter-needles of half the length of the parent crystal but with the same width.

The particle data is fed into the model and breakage performed on a number of crystals. The resultant size distributions show good agreement with the experimentally derived size distributions, showing that for the particles in the distribution that suffer peak breakage (i.e. those situated near the bottom of the cake), the assumption of crystal breakage into 2 halves

can be shown to accurately represent the real system. Fractions of broken particles ranged from 0.05 to 0.427 for low and high flowrate filtrations, respectively, meaning that at high stress, nearly half of the original crystals are expected to break.

The model displays better agreement with the low-aspect regions of the curve (i.e. for more elongated particles) by design, as these are the regions of the distribution which are of most interest. Ensuring a better fit to experimental data in the low-elongation regions reduces the fit in the (desired) high-elongation regions, which is an unfortunate limitation of the model.

Additional limitations include the lack of accountability for attritional breakage and multiple breakage events, i.e. a crystal only ever breaks once; fragments never break. Future implementations would seek to model the multiple breakage events that are thought to be evident under increasing application of stress (see Chapter 6). Therefore although the fractions of broken particles are high, it is likely that these are somewhat overestimated, as the breakage of broken fragments is a possibility.

The second application of modelling to this project is concentrated on the structure of needle-like particle beds. An emergent model is designed in which a simple set of rules is used to produce a complex result; experimentally determined particle data is used to construct a theoretical bed of needle-like particles via 'dropping' the crystals in place one-by-one. A set of algorithms determines the rules in which particles stack on top of one another to build the bed over time.

Overall the model shows good promise in its initial stages. A solid foundation is evident in which the general structure of needle-like beds can be reproduced, but the model is limited by its lack of rigour. Particles are observed to stack in more horizontal orientations initially but over time are more likely to come to rest with random orientations (particularly the larger particles in the dataset). Large particles are shown to dominate the structure of the cake, both in terms of defining the major proportions of upward building (and also voids), and also in their support of the structure – larger particles commonly harbour dozens of particle contacts, meaning they would be expected to bear the majority of any forces transmitted through the bed.

Initial simulations show good reproducibility and bulk densities are similar to those observed experimentally; although the success of this result is hindered by the tendency of the particles to stack within the centre confines of the bed. This leads to a lack of particle mass around the outer edges of the bed which distorts the figure for total bulk density. The model would certainly benefit from the incorporation of a 'wall' around the edges of the bed; a solid

structure that would allow particles to rest upon it instead of invalidating their existence. This would alleviate the problem of 'missing mass' from the outer edges.

Analysis of differential bulk density through the height of the cake also highlights the problem of small particles falling through gaps in the bed to continually come to rest on the base of the bed. This has the effect of concentrating mass in the lowest height fraction instead of evenly dispersing it through the bed. Differential bed height data also reveals the number of particle contacts is roughly even throughout the bed – at approx. 3.5 – 4 contacts per particle on average. Although this figure is likely distorted to a certain extent by the lack of smaller particles through the height of the bed, the effect is lessened as smaller particles typically have fewer contacts due to their limited physical reach.

Chapter 9

9 Conclusions and Future Experimentation

9.1 Introduction

In the pharmaceutical and fine chemical industry filtration and drying operations are typically carried out synonymously for process efficiency reasons. This means that the effects of industrial filtration and drying operations are observed as one, instead of the separate effects that they individually contribute. Although the process of filtration has been studied for many years and the underlying theory is well understood, the effect of filtration pressure on crystal breakage is a relatively understudied field. Thus there is a clear knowledge gap within this sector and a need to investigate this phenomenon further, as it has significant applications within industrial settings.

It is well known that large scale filtrations are impaired by certain particle morphologies, e.g. plate and needle shapes. Not only is this a function of the crystal morphological packing characteristics (reducing channels for liquid flow), but the effect is compounded by the breakage of fragile crystals, resulting in the production of fines and rearrangement/consolidation of particle beds; thus further reducing the ability of liquid to percolate through the bed.

This has consequences not only for filtration efficiency and process turnaround (i.e. slow filtrations are a bottleneck to the manufacturing process) but additionally for downstream operations. Formulation of final drug products is heavily dependent on the flowability of the powder (and additional derivative phenomena such as segregation); which is directly influenced by the particle size distribution. Breakage of crystals under processes can widen the size distribution and exacerbate these problems, thus providing a direct incentive to provide greater control of the particle size distribution.

This thesis represents an attempt to characterise the extent to which needle-like crystals suffer from breakage under filtration. This chapter therefore presents a series of final conclusions that have been drawn from the project.

9.2 Conclusions and Thesis Summary

In order to investigate the phenomena of breakage under filtration, a representative mass of particles in liquid was required. To retain as much industrial relevancy as possible, it was

decided that freshly crystallised particle slurries must be generated (in contrast e.g. to 'reslurrying' powders where pre-processed crystals are combined with an anti-solvent to filter them), as is the case with industrial manufacturing processes.

Crystallisations for several model crystal compounds were developed, namely glutamic acid, urea and urea-biuret impurity and the AstraZeneca compound Lesinurad. Differing morphologies of glutamic and urea/urea-biuret were grown via modification of the crystallisation conditions; e.g. long needles of glutamic acid are produced from low supersaturation slow cooling profiles, whilst the metastable alpha-glutamic acid can be grown from fast cooling crystallisations. Urea in its pure form can be grown as long needles (e.g. from methanol with fast cooling), elongated prisms (from ethanol with slow cooling), or significantly stunted 'blocky' tablets when crystallised in the presence of biuret as an impurity; this is due to the differences in crystal face growth rate experienced when modifying the crystallisation process.

Urea, although showing promising variability in its crystal habit, forms such strong solid networks that sampling handling is significantly impaired. Obtaining powder samples for particle size testing necessitates the destruction of these solid network bonds with significant force (e.g. from a spatula), meaning crystal breakage via material handling cannot be ruled out. When coupled with the fact that crystal breakage under filtration is the desired investigative variable, this was seen as untenable for further work.

The beta-glutamic acid system forms long needles and has favourable solid handling properties. Therefore this system was taken forward as the model compound for the majority of experimentation and modelling. Beta-glutamic acid was expected to suffer breakage in a total-fracture model, i.e. the crystals would split into fragments of roughly equal size. The metastable polymorph alpha-glutamic acid also presents an alternate case in which a crystal of similar molecular properties can be compared to the needle-like beta-glutamic acid. The alpha polymorph forms trapezoidal block-like particles which would not be anticipated to fracture in the same method to the beta-glutamic acid; instead undergoing attritional breakage from its edges as opposed to total fracture.

Lesinurad also presents a case of an industrial crystal system in which difficulties under filtration are known to occur. Lesinurad crystallises as small prismatic needles, therefore the small size of the particles also contributes to any difficulties in filtration experienced due to crystal breakage.

A novel method was developed in order to study the effects of pressure filtration on the particle size distribution of a bed of crystals. This involved the design and construction of the

continuous percolation rig (CPR), which provided the opportunity to study percolation for much longer periods of time than is typically encountered in laboratory-scale batch filtrations. In addition batch filtrations have been undertaken to compare the filtration performance of several compounds using methods more typical to those in industry.

Breakage of beta-glutamic acid needles has been observed to occur in both continuous (CPR) and batch settings. Particle size reduction was found to be dependent on the percolation flowrate/pressure; with an increase in driving force responsible for greater levels of crystal breakage. This has been confirmed with optical microscopy and particle size measurement instrumentation.

Size reduction in both modes of operation was found to be similar; reductions of the order of 5% - 10% in the fractions of large and elongated particles were observed. Due to the levels of size reduction being low or practically zero with lower flowrate/pressure experimentation, and a strong dependence of size reduction on driving force, it is unlikely that breakage was as a result of solids handling. A batch scale filtration conducted at negligible filtration pressure found almost no change in particle size distribution with respect to the initial crystallised batch.

Additionally crystal breakage was found to be a time-independent process; short percolations (including filtration performed at batch scale) display similar levels of size reduction to percolations performed over the course of an hour or more. Breakage is therefore found to occur within the initial stages of pressure filtration/percolation, with subsequent breakage only occurring if and when the pressure is raised.

An unexpected result observed from batch filtration is that of the significant variation in particle size with the height of the filter cake. For all 3 systems examined, the particles at the base of the filter cake are comparable in volume-weighted size to the original, vacuum filtered powder sample. Conversely, particles retrieved from the top of the filter cake are by far the smallest. Coupled with the fact that this effect is most pronounced with the large alpha-glutamic acid particles, the cause of the variation is due to pre-filtration settling of the particles within the mother liquors. Larger particles settle at faster rates, meaning these particles settle first on the filter medium. The effect of settling contributed to the poor compressibility results obtained, as the filtration rate model assumes a gradual build-up of the cake over time.

Settling was determined to be the underlying cause with a negligible pressure test that evidenced the same variability in size of the particles from the top and bottom of the filter cake. In addition CPR samples did not display significant size variations with bed height. These

observations highlight the extent to which sampling, and more specifically consistent sampling (from the same regions of the cake), has importance in the field of particle size analysis.

Particle size distribution analysis did reveal however that particles at the base of the filter cake suffer the highest levels of breakage, with particles sampled from the top of the cake suffering comparatively little breakage. Size reduction was still observed to be more dependent on filtration pressure however. These observations are mirrored in samples tested in the CPR.

The experimental findings of changes in particle size distribution are backed up by significant research into the validity of the data acquired from the Morphologi G3 particle size analysis equipment. Data obtained from automated particle counters such as these has significant depth when compared to data obtained from laser diffraction, but is less statistically relevant and suffers from long sample times.

The Morphologi G3 is limited however by the natural tendency of needle-like crystals to overlap, meaning they scanned as single particles. Additional artefacts such as fibres are also scanned as particles by the instrument. To combat this, an automated script capable of filtering out such overlapping or erroneous particles was developed in order to improve the relevancy of the data. Particles are evaluated based on a combination of their circularity and elongation. It was found that many large 'particles' are eliminated from the dataset using this method.

Research was also conducted into the generation of different representations of particle size distribution. A model was developed by assuming a 3-dimensional cuboidal shape for beta-glutamic acid based on the length and width of the scanned particles. A number distribution based on the modelled particle volume was shown to more adequately highlight subtle changes occurring within the size distributions for pre-and post-filtration crystal batches.

The particle aspect ratio was also found to be a good indicator of particle size changes occurring under pressure filtration; in particular as the fracture behaviour of needle-like crystals significantly alters the aspect ratio of the crystals as they cleave into 2 or more fragments.

Small-scale centrifugation testing has also been conducted using a photo-centrifuge (the 'LUMiSizer'). A range of particle systems were tested under centrifugal rotations of up to 2200 rpm to investigate their settling and packing behaviour. Needle-like systems such as beta-glutamic acid, urea and Lesinurad all display high initial bed heights, indicating loose packing, and high levels of consolidation under centrifugal acceleration; leading to large fractional reductions in bed height (up to 30-40%). The blocky systems of alpha-glutamic acid and urea-

biuret both display tight packing with few voids and therefore limited bed consolidation is observed.

Particle bed relaxations have provided indications of the elasticities of the crystal beds. For instance blocky particle beds exhibit elastic strain behaviour, with relaxation due to stress that squares with the input force (as predicted by theory). This is evidence that the bed is able to absorb energy, transmit it through the particle contacts and release it without significant loss of energy.

Needle particle beds display low-elasticity in response to the application of stress; evidence that a certain portion of the energy absorbed by the bed is spent in re-arrangement of the particles and/or particle contacts. This behaviour shows the beds deform plastically in response to stress.

A model of compressive pressure predicts that the stresses experienced under centrifugation are low compared to typical pressure filtrations; of the order of 0.03-0.06 bar. As forces are transmitted through beds via a network of contact points, assumption of the numbers of typical contact points allows calculation of the force imparted through each point. For beta-glutamic acid this corresponds to approximate maximum forces of several hundred μN for particles at the base of the bed, which is lower than the typical required breakage force of 1-1.5 mN. This tends to agree with the low levels of breakage of beta-glutamic acid evident from centrifugation.

Heuristic modelling of the breakage of beta-glutamic acid was performed by generation of a probability-based model that is dependent on the particle size, shape and filtration pressure. Particles are envisioned to break perpendicular to their length, along the mid-point of the needle, producing 2 crystals of equal length. The algorithm is particularly relevant as actual microscopic data is used as input to the model, with a pre-pressure filtration aspect ratio distribution modified to produce a distribution similar to that of a pressure filtered sample.

The model was fit to experimental filtration data obtained from batch and continuous percolation, with good agreement found between the predicted distribution and experimental measurements. Models showed that the number of broken particles could be up to 30-40% of the total distribution, which again highlights the need to characterise and account for this potential breakage in any downstream operations; whether they are further comminution stages or direct formulation.

Secondary modelling consisted of the generation of needle-like particle beds from experimental particle data. The model used a set of simple rules to produce a bed of particles by stacking them one on top of another. The simulation showed evidence of the structure of

the bed being largely dominated by the large particles in the dataset; larger particles tended to have a greater number of particle contact points, which directly influence the structure and force-transmission through the bed. On average particles are shown to contact approximately 3.5-4 other particles.

The model is advantaged by the fact it is generated from real particle data. Approximately 100,000 particle lengths are used as input data to the building algorithms. The model also has advantages over discrete element modelling simulations, namely the ability to process many more particles within a short space of time. It is limited mainly by the lack of mathematical rigour; particles are assumed as frictionless, massless, 1-dimensional rigid lines. However the omission of particle width is believed to have had the greatest effect on simulations thus far and hence would be the priority for future model improvements.

9.3 Future Work

Future work would largely consist of additional percolation studies in the CPR, e.g. tests on alpha-glutamic acid to compare performance with the needle-like beta-glutamic acid. In addition it is envisioned that additional needle-like systems would be tested to compare the extent of size reduction with the beta-glutamic acid case study. It would also be prudent to test alternate morphologies e.g. plate-like systems.

A range of improvements are identified for the CPR; automated transfer of the crystals into the filter tube via use of a vacuum hose, improved pressure identification by use of a pressure transducer, better control and data acquisition with improved instrument communication/software, better measurement of cake height by replacement of the steel filter chamber with a glass chamber,

Furthermore a wider-range of beta-glutamic acid properties would be tested, i.e. a continuation of the promising atomic force microscopy single-crystal breakage tests. This would enable quantification of the actual tensile limit of crystal fracture, which could be inserted into models to gain more accurate predictions of bulk particle bed breakage.

Although evidence of particle breakage has been presented, it is limited in the sense that the data was obtained from offline analysis of dry material. This presents the additional future challenge of obtaining on-line analysis of particle size distribution. As the cake is static and opaque, this would necessitate the use of x-ray or similar high-penetration technique. This could provide additional real-time data of the cake structure and size distribution as breakage events are experienced by the particles.

Additional comparative studies could also be performed to more closely correlate crystal breakage with pressure e.g. direct compression tests. This would provide the opportunity to compress crystal beds with precise pressures, and ascertain the similarity (or not) with which the particle bed suffers size reduction compared to filtration.

A similar point of note is that of wet/dry compression, i.e. do particle/bed properties differ when the bed is still submerged in the mother liquor compared to its de-liquored state. The model for solids compressive pressure (Chapter 7) implies that the difference in continuous and dispersed phase densities does affect the solids pressure, i.e. the force balance on a bed of particles in air takes into account the reduced buoyancy offered by air compared to a liquid solvent. The result is an approximate tripling of the total compressive pressure. This would seem to imply that crystal breakage would be more likely to occur in dry beds that offer less support to the crystal network.

Developments to the modelling of particle breakage would focus on the addition of more complicated breakage mechanisms; i.e. breakage of fragments and incorporation of attritional breakage into the model.

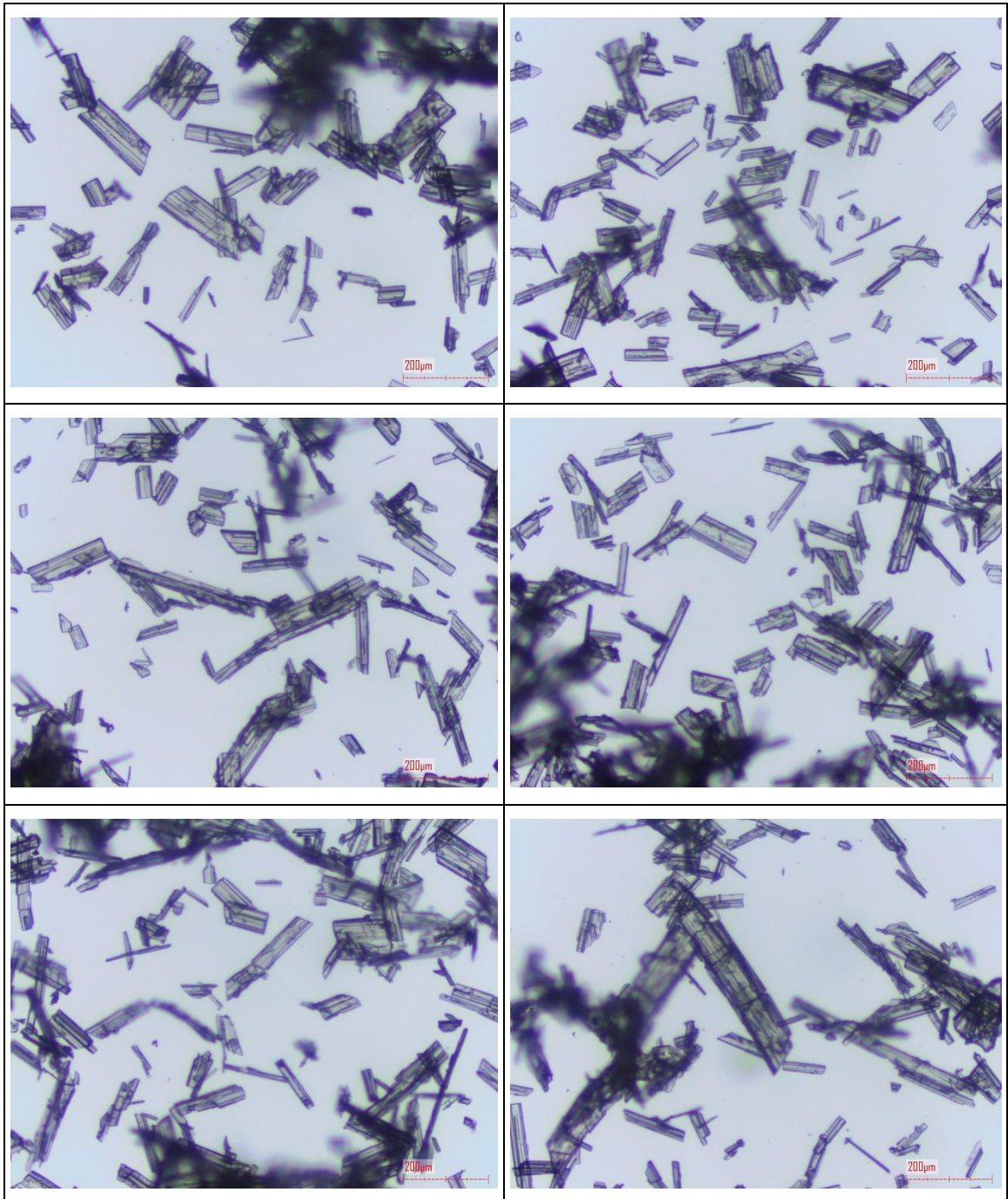
Particle bed generation modelling has significant potential for future work. Multiple improvements to the construction algorithms have been identified e.g. incorporation of particle width and addition of particle friction/movement/mass. Future tie-ins with existing work are also envisioned, i.e. with simulations of particle elasticity can the compression/relaxation behaviour observed under centrifugation be observed, or the elasticity of crystals observed under single-crystal atomic force microscopy (AFM) studies (not reported on in this thesis).

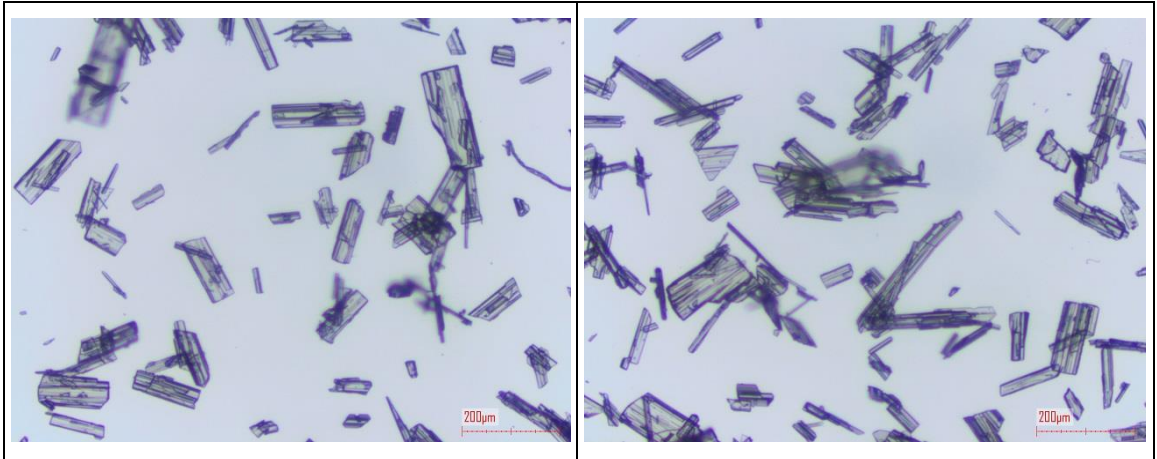
The main objective for this model moving forward however would be the incorporation of particle breakage into the bed building model. With theoretical calculations of solid compressive pressures (Chapter 7) and the ability to locate the precise points of particle contact, the application of pressure could be simulated and using the crystal tensile strengths found from AFM, particle breakage could be evaluated.

10 Appendices

10.1 Appendix A: Additional 2 Litre Filtration Microscopic Images

Table 10-1: Additional microscope images for beta-glutamic acid 'PFB' samples filtered on 2 L scale





	Simulation number for 75,000 particles			
	1	2	Mean	St.Dev
Bed height (units)	205.524	234.383	219.954	14.429
Est bed height (m)	0.00514	0.00586	0.00550	0.00036
Bed volume (m ³)	3.63E-08	4.14E-08	3.89E-08	2.55E-09
Ave bulk density (kg/m ³)	243.31	213.35	228.33	14.98
Ave Contacts per particle	2.496	2.494	2.495	0.001
	Simulation number for 101,189 particles			
	1	2	Mean	St.Dev
Bed height (units)	262.412	317.439	289.926	27.514
Est bed height (m)	0.00656	0.00794	0.00725	0.00069
Bed volume (m ³)	4.64E-08	5.61E-08	5.12E-08	4.86E-09
Ave bulk density (kg/m ³)	255.33	211.07	233.20	22.13
Ave Contacts per particle	2.631	2.614	2.622	0.008

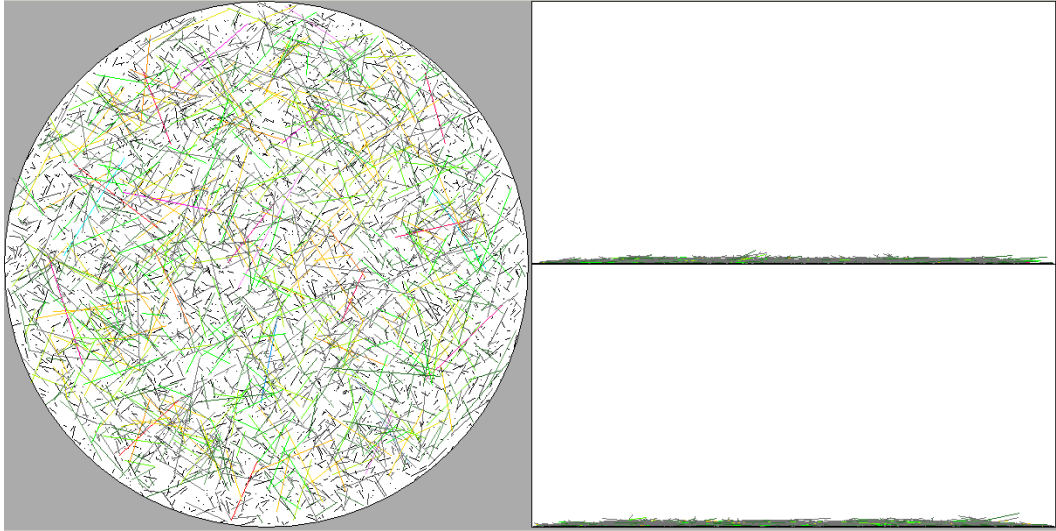


Figure 10-1: Bed structure for a simulation of 5,000 particles

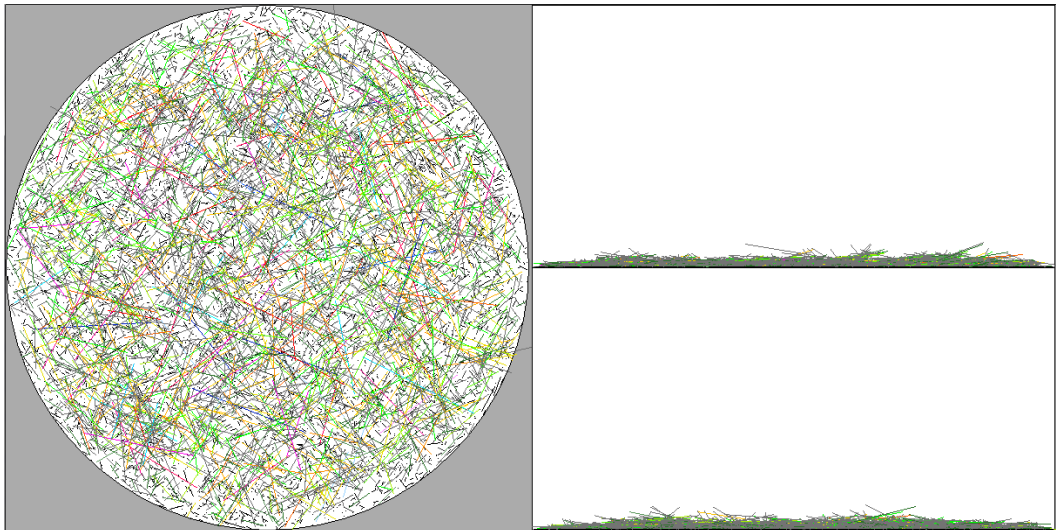


Figure 10-2: Bed structure for a simulation of 10,000 particles

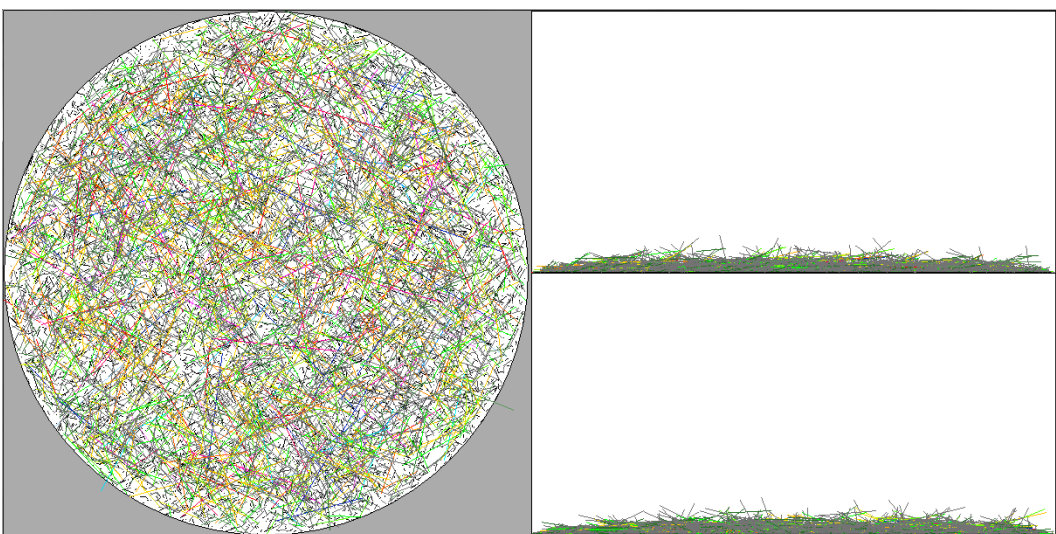


Figure 10-3: Bed structure for a simulation of 15,000 particles

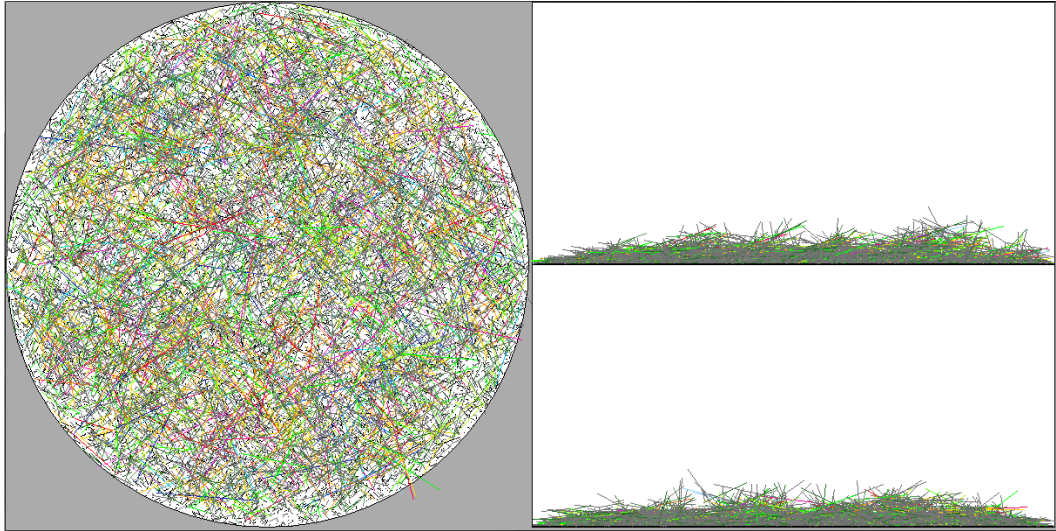


Figure 10-4: Bed structure for a simulation of 20,000 particles

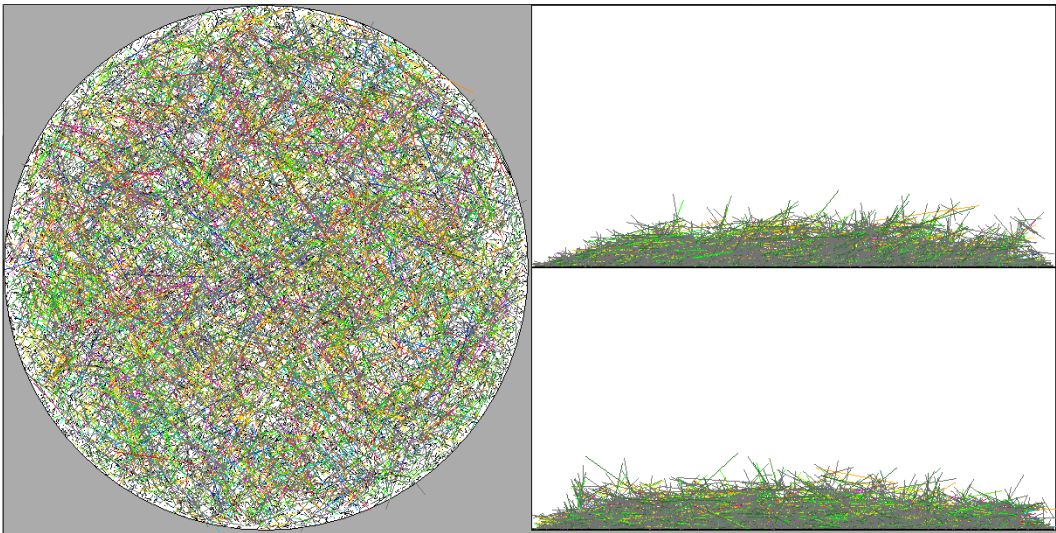


Figure 10-5: Bed structure for a simulation of 30,000 particles

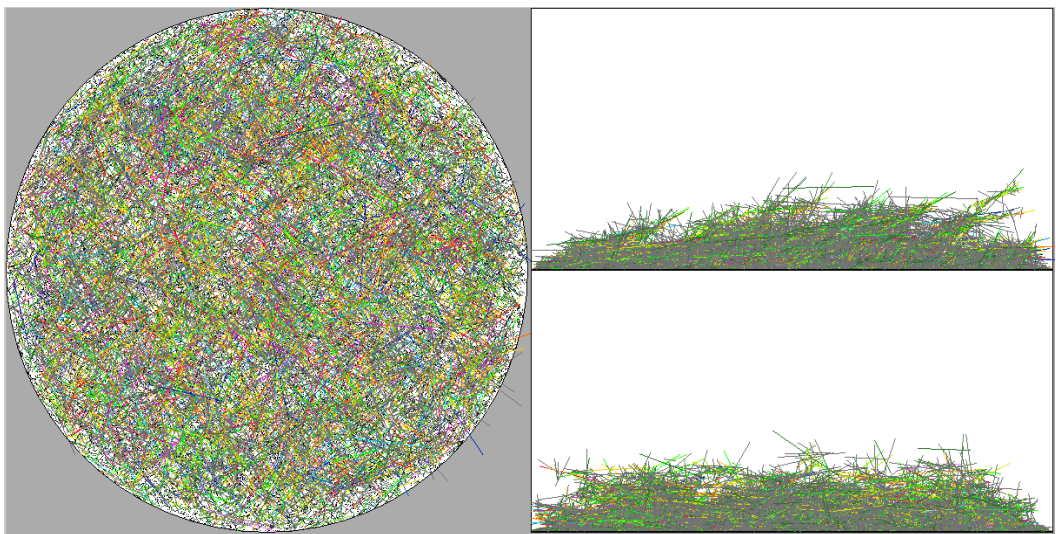


Figure 10-6: Bed structure for a simulation of 40,000 particles

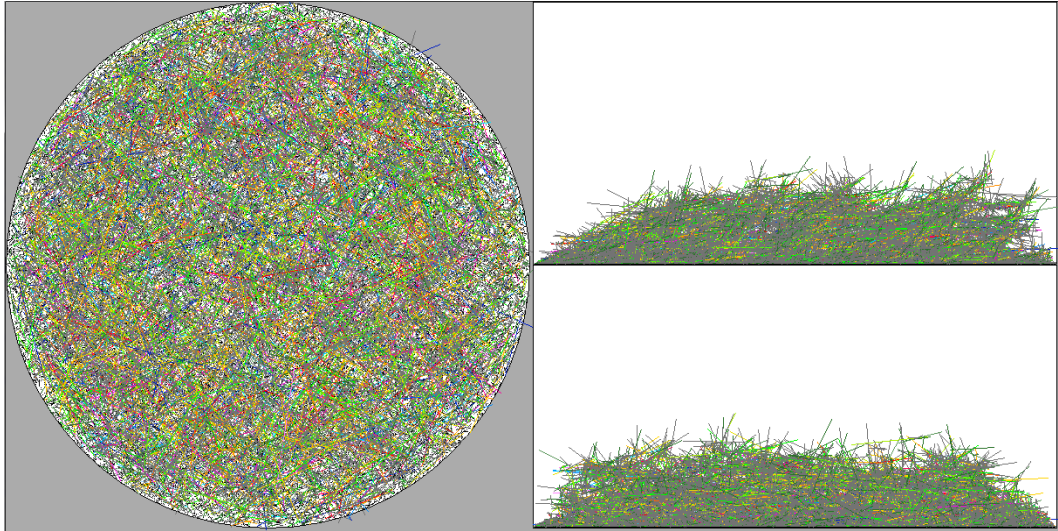


Figure 10-7: Bed structure for a simulation of 50,000 particles

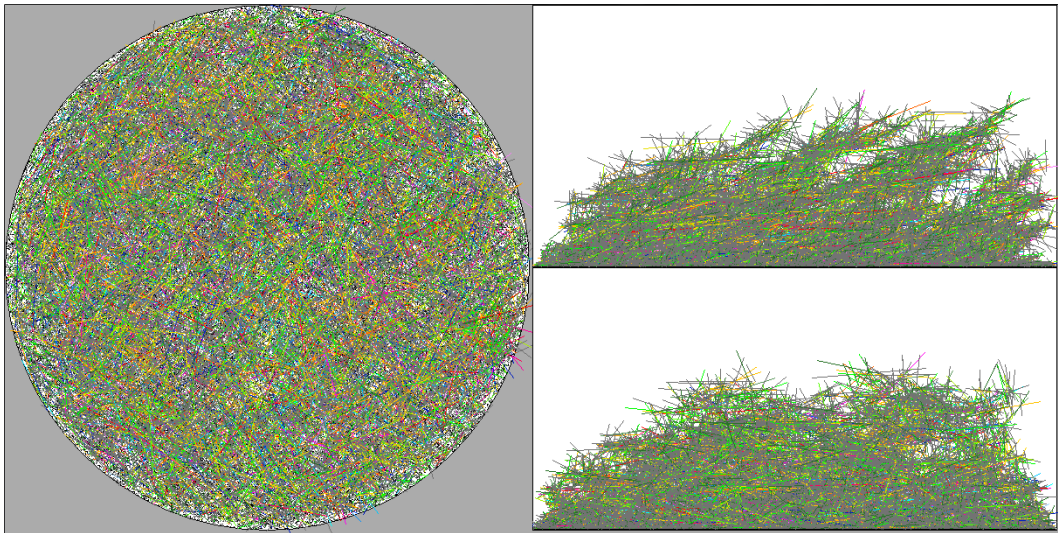


Figure 10-8: Bed structure for a simulation of 75,000 particles

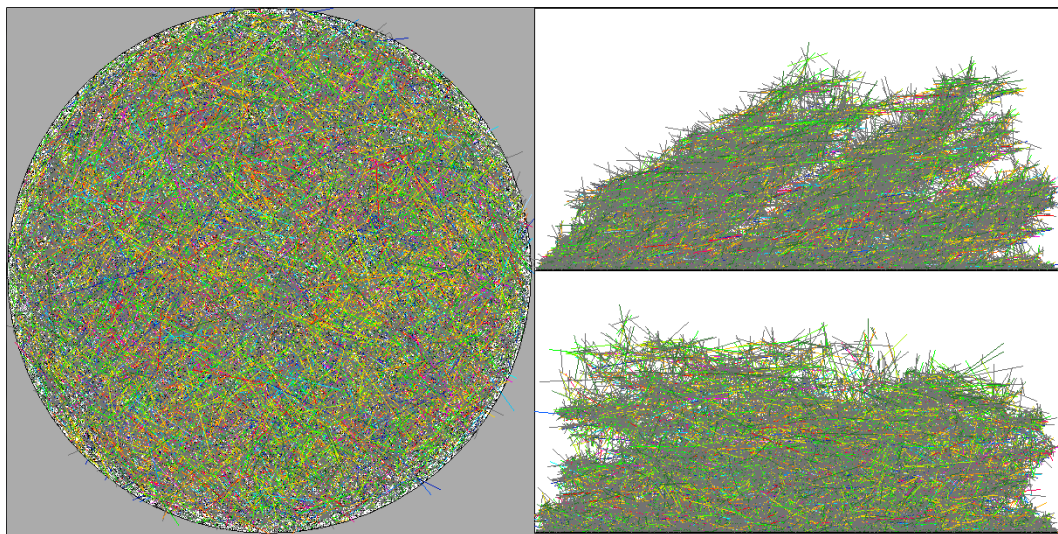


Figure 10-9: Bed structure for a simulation of 101,189 particles

11 References

1. Blacker, J. and M. Williams, *Pharmaceutical Process Development: Current Chemical and Engineering Challenges*. RSC Drug Discovery Series. Vol. 9. 2011, Cambridge: Royal Society of Chemistry.
2. Baillie, T.A., *Future of Toxicology- Metabolic Activation and Drug Design: Challenges and Opportunities in Chemical Toxicology*. Chemical Research in Toxicology, 2006. **19**(7): p. 889-893.
3. Kougoulos, E., C.E. Chadwick, and M.D. Ticehurst, *Impact of agitated drying on the powder properties of an active pharmaceutical ingredient*. Powder Technology, 2011. **210**: p. 308-314.
4. Geddes, A., *The Filtration and Drying Behaviour of Organic Crystals with Varied Morphologies following their Batch Crystallisation*, in *Institute of Particle Science and Engineering*. 2003, University of Leeds: Leeds.
5. Hamilton, P., D. Littlejohn, A. Nordon, J. Sefcik, P. Slavin, J. Andrews, and P. Dallin, *Investigation of factors affecting isolation of needle-shaped particles in a vacuum agitated filter drier through non-invasive measurements by Raman spectrometry*. Chemical Engineering Science, 2013. **101**: p. 878-885.
6. Kim, S., et al., *Control of the Particle Properties of a Drug Substance by Crystallization Engineering and the Effect on Drug Product Formulation*. Organic Process Research & Development, 2005. **9**(6): p. 894-901.
7. Lekhal, A., K.P. Girard, M.A. Brown, S. Kiang, B.J. Glasser, and J.G. Khinast, *Impact of agitated drying on crystal morphology: KCl-water system*. Powder Technology, 2003. **132**: p. 119-130.
8. Lekhal, A., K.P. Girard, M.A. Brown, S. Kiang, and J.G.K.B.K. Glasser, *The effect of agitated drying on the morphology of L-threonine (needle-like) crystals*. International Journal of Pharmaceutics, 2004. **270**: p. 263-277.
9. MacLeod, C.S. and F.L. Muller, *On the Fracture of Pharmaceutical Needle-Shaped Crystals during Pressure Filtration: Case Studies and Mechanistic Understanding*. Organic Process Research & Development, 2012. **16**(3): p. 425-434.
10. Cornehl, B., A. Overbeck, A. Schwab, J.-P.B.A. Kwade, and H. Nirschl, *Breakage of lysozyme crystals due to compressive stresses during cake filtration*. Chemical Engineering Science, 2014. **111**: p. 324-334.
11. Tait, S., E. White, and J. Litster, *Mechanical Characterisation of Protein Crystals*. Particle and Particle Systems Characterisation, 2008. **25**(3): p. 266-276.
12. Lamberto, D.J., B. Cohen, J. Marencic, C. Miranda, R. Petrova, and L. Sierra, *Laboratory methods for assessing API sensitivity to mechanical stress during agitated drying*. Chemical Engineering Science, 2011. **66**: p. 3868-3875.
13. Grof, Z., M. Kohout, and F. Štěpánek, *Multi-scale simulation of needle shaped particle breakage under uniaxial compaction*. Chemical Engineering Science, 2007. **62**: p. 1418-1429.
14. Bernhardt, C., *Particle Size Analysis - Classification and Sedimentation Methods*1994, London: Chapman & Hall.
15. Seville, J., U. Tüzün, and R. Clift, *Processing of Particulate Solids*1997, London: Chapman & Hall.

16. Peker, S. and S. Helvaci, *Solid-Liquid Two Phase Flow* 2008, Oxford, Amsterdam: Elsevier.
17. Allen, T., *Particle Size Measurement: Powder sampling and particle size measurement*. Vol. 1. 1997, Padstow: Chapman & Hall.
18. Molerus, O., *Principles of Flow in Disperse Systems*. Powder Technology Series 1993, London: Chapman & Hall.
19. Mullin, J.W., *Crystallization* 2001, Oxford: Butterworth-Heinemann.
20. Darcy, H.P., *Les Fontaines Publiques de la ville de Dijon. Exposition et application 'a suivre et des formules'a employer dans les questions de distribution d'eau.* , 1856: Dalmont, Paris.
21. Almy, C. and W.K. Lewis, *Factors Determining the Capacity of a Filter Press*. The Journal of Industrial and Engineering Chemistry, 1912: p. 528-532.
22. Kozeny, J., *Ueber kapillare Leitung des Wassers im Boden*. Sitzungsber Akad. Wiss., 1927. **136**: p. 271-306.
23. Carman, P., *Fluid flow through granular beds*. Trans. Inst. Chem. Eng., 1937. **15**: p. 150-167.
24. Carman, P., *Flow of gases through porous media* 1956, London: Butterworth.
25. S, E., *Fluid Flow Through Packed Columns*. Chem. Eng. Prog., 1952. **48**(2): p. 89-94.
26. Antelmi, D., B. Cabane, M. Meireles, and P. Aimar, *Cake Collapse in Pressure Filtration*. Langmuir, 2001. **17**: p. 7137-7144.
27. Wadel, H., *Volume, shape and roundness of rock particles*. J. Geol., 1932. **40**: p. 443-451.
28. Shekunov, B., P. Chattopadhyay, H. Tong, and A. Chow, *Particle Size Analysis in Pharmaceuticals: Principles, Methods and Applications*. Pharmaceutical Research, 2007. **24**(2): p. 203-227.
29. Maaß, S., J. Rojahn, R. Hänsch, and M. Kraume, *Automated drop detection using image analysis for online particle monitoring in multiphase systems*. Computers and Chemical Engineering, 2012. **45**: p. 27-37.
30. Holdich, R., *Fundamentals of Particle Technology* 2002, Shepshed: Midland Information Technology and Publishing.
31. Wu, J., S. Kucheryavskiy, L. Jensen, T. Rades, A. Müllertz, and J. Rantanen, *Image Analytical Approach for Needle-Shaped Crystal Counting and Length Estimation*. Crystal Growth & Design, 2015. **15**: p. 4876-4885.
32. Zhang, Z., *Particle overlapping error correction for coal size distribution estimation by image analysis*. International Journal of Mineral Processing, 2016. **155**: p. 136-139.
33. Larsen, P., J. Rawlings, and N. Ferrier, *An algorithm for analyzing noisy, in situ images of high-aspect-ratio crystals to monitor particle size distribution*. Chemical Engineering Science, 2006. **61**: p. 5236-5248.
34. British-Standards-Institute, *BS 3406-1*, 1986, BSI.
35. Fraunhofer, J., *Bestimmung des Brechungs - und Farbzerstreuungs - vermögens verschiedener Glasarten*. Gilberts Annalen der Physik, 1817. **56**: p. 193-226.
36. Heuer, M. and K. Leschonski, *Results Obtained with a New Instrument for the Measurement of Particle Size Distributions from Diffraction Patterns*. Particle Characterisation, 1985. **2**: p. 7-13.

37. Davey, R. and J. Garside, *From Molecules to Crystallizers* 2000, New York: Oxford University Press.
38. Muller, F.L., M. Fielding, and S. Black, *A Practical Approach for Using Solubility to Design Cooling Crystallisations*. Organic Process Research & Development, 2009. **13**(6): p. 1315-1321.
39. Perry, R. and D. Green, *Perry's Chemical Engineers' Handbook*. 8th ed 2008, New York: McGraw-Hill.
40. Bao, Y., J. Zhang, Q. Yin, and J. Wang, *Determination of growth and breakage kinetics of L-threonine crystals*. Journal of Crystal Growth, 2006. **289**: p. 317-323.
41. Beck, R., A. Hakkinen, D. Malthe-Sorensen, and J.-P. Andreassen, *The effect of crystallization conditions, crystal morphology and size on pressure filtration of L-glutamic acid and an aromatic amine*. Separation and Purification Technology, 2009. **66**: p. 549-558.
42. Davey, R., W. Fila, and J. Garside, *The Influence of Biuret on the Growth Kinetics of Urea Crystals from Aqueous Solutions*. Journal of Crystal Growth, 1986. **79**: p. 607-613.
43. Anderson, N., *Practical Process Research and Development* 2000, San Diego, Cf: Academic Press.
44. Hammond, R.B., X. Lai, K.J. Roberts, A. Thomas, and G. White, *Application of In-Process X-ray Powder Diffraction for the Identification of Polymorphic Forms during Batch Crystallization Reactions*. Crystal Growth & Design, 2004. **4**(5): p. 943-948.
45. Ni, X., A. Valentine, A. Liao, S. Sermage, G. Thomson, and K.J. Roberts, *On the Crystal Polymorphic Forms of L-Glutamic Acid Following Temperature Programmed Crystallization in a Batch Oscillatory Baffled Crystallizer*. Crystal Growth & Design, 2004. **4**(6): p. 1129-1135.
46. Muller, F.L., *On the rheological behaviour of batch crystallisations*. Chemical Engineering Research and Design, 2008. **87**: p. 627-632.
47. Birch, M. and I. Marziano, *Understanding and Avoidance of Agglomeration During Drying Processes: A Case Study*. Organic Process Research & Development, 2013.
48. Mullin, J.W. and J. Nyvlt, *Programmed cooling of batch crystallizers*. Chemical Engineering Science, 1971. **26**: p. 369-377.
49. Sangwal, K., *Effect of impurities on the metastable zone width of solute-solvent systems*. Journal of Crystal Growth, 2009. **311**: p. 4050-4061.
50. Zhao, Y., Y. Bao, J. Wang, and S. Rohani, *In Situ Focused Beam Reflectance Measurement (FBRM), Attenuated Total Reflectance Fourier Transform Infrared (ATR-FTIR) and Raman Characterization of the Polymorphic Transformation of Carbamazepine*. Pharmaceutics, 2012. **4**: p. 164-178.
51. Nyvlt, J., *Kinetics of Nucleation in Solution*. Journal of Crystal Growth, 1968. **3**(4): p. 377-383.
52. Sangwal, K., *Recent developments in understanding of the metastable zone width of different solute-solvent systems*. Journal of Crystal Growth, 2011. **318**: p. 103-109.
53. Sangwal, K., *On the effect of impurities on the metastable zone width of phosphoric acid*. Journal of Crystal Growth, 2010. **312**: p. 3316-3325.
54. Barrett, P. and B. Glennon, *Characterizing the metastable zone width and solubility curve using lasentec FBRM and PVM*. Trans IChemE, 2002. **80**(A).

55. Ottens, E.P., A.H. Janse, and E.J.D. Jong, *Secondary Nucleation in a Stirred Vessel Cooling Crystallizer*. Journal of Crystal Growth, 1972. **13**: p. 500-505.
56. Liang, K., G. White, D. Wilkinson, L.J. Ford, K.J. Roberts, and W.M.L. Wood, *An Examination into the Effect of Stirrer Material and Agitation Rate on the Nucleation of L-Glutamic Acid Batch Crystallized from Supersaturated Aqueous Solutions*. Crystal Growth & Design, 2004. **4**(5): p. 1039-1044.
57. Zweitering, T.N., *Suspending of solid particles in liquid by agitators*. Chemical Engineering Science, 1958. **8**: p. 244-253.
58. Groen, H. and K.J. Roberts, *An Examination of the Crystallization of Urea from Supersaturated Aqueous and Aqueous Methanol Solutions as Monitored In-Process Using ATR FTIR Spectroscopy*. Crystal Growth & Design, 2004. **4**(5): p. 929-936.
59. Muller, M., U. Meier, D. Wieckhusan, R. Beck, S. Pfeffer-Hennig, and R. Schneeberger, *Process Development Strategy to Ascertain Reproducible API Polymorph Manufacture*. Crystal Growth & Design, 2006. **6**: p. 946-954.
60. Orthmer, K., *Separation Technology*. 2nd ed. Vol. 2. 2008, New Jersey: John Wiley and Sons Inc.
61. Smiles, D.E., *A theory of constant pressure filtration*. Chemical Engineering Science, 1969. **25**: p. 985-996.
62. Cheremisinoff, N. and D. Azbel, *Liquid Filtration* 1983, Massachusetts: Ann Arbor Science Publishers.
63. Tarleton, E.S., *Predicting the Performance of Pressure Filters*. Filtration & Separation, 1998: p. 293-298.
64. Wakeman, R., *The influence of particle properties on filtration*. Separation and Purification Technology, 2007. **58**: p. 234-241.
65. Tarleton, E.S., *Using mechatronics technology to assess pressure filtration*. Powder Technology, 1999. **104**: p. 121-129.
66. Murugesan, S., D.M. Hallow, J.P. Vernille, J.W. Tom, and J.E. Tabora, *Lean Filtration: Approaches for the Estimation of Cake Properties*. Organic Process Research & Development, 2012. **16**: p. 42-48.
67. Lu, W.-M. and K.-J. Hwang, *Mechanism of cake formation in constant pressure filtrations*. Separation Technology, 1993. **3**: p. 122-132.
68. Walker, A.J. and L. Svarovsky, *Development of a Computer Model for Predicting the Filtration Characteristics of a Suspension*. Filtration & Separation, 1994: p. 57-65.
69. Tarleton, E.S. and S.A. Willmer, *The Effects of Scale and Process Parameters in Cake Filtration*. Trans IChemE, 1997. **75**: p. 497-507.
70. Ruth, B.F., *Correlating Filtration Theory with Industrial Practice*. Industrial and Engineering Chemistry, 1946. **38**: p. 564-571.
71. Wu, Y., *An Analysis of Constant-Pressure Filtration*. Chemical Engineering Science, 1994. **49**(6): p. 831-836.
72. Stamatakis, K. and C. Tien, *Cake Formation and Growth in Cake Filtration*. Chemical Engineering Science, 1991. **46**(8): p. 1917-1933.
73. Wakeman, R.J. and E.S. Tarleton, *A Framework Methodology for the Simulation and Sizing of Diaphragm Filter Presses*. Minerals Engineering, 1994. **7**(11): p. 1411-1425.

74. Lu, W.-M., Y.-P. Huang, and K.-J. Hwang, *Methods to determine the relationship between cake properties and solid compressive pressure*. Separation and Purification Technology, 1998. **13**: p. 9-23.
75. Wakeman, R.K. and E.S. Tarleton, *Modelling, Simulation and Process Design of the Filter Cycle*. Filtration & Separation, 1990: p. 412-419.
76. Tarleton, E.S., *A New Approach to Variable Pressure Cake Filtration*. Minerals Engineering, 1998. **11**(1): p. 53-69.
77. Holdich, R., *Simulation of Compressible Cake Filtration*. Filtration & Separation, 1994: p. 825-829.
78. Theliander, H. and M. Fathi-Najafi, *Simulation of the Build-up of a Filter Cake*. Filtration & Separation, 1996: p. 417-421.
79. Tarleton, E.S. and R.J. Wakeman, *Simulation, Modelling and Sizing of Pressure Filters*. Filtration & Separation, 1994: p. 393-397.
80. Holdich, R., *Solid-liquid separation equipment selection and modelling*. Minerals Engineering, 2003. **16**: p. 75-83.
81. Ruth, B.F., G.H. Montillon, and R.E. Montonna, *Studies in Filtration 1. Critical Analysis of Filtration Theory*. Industrial and Engineering Chemistry, {Carman, 1938 #73}1933. **25**(1): p. 76-82.
82. Carman, P., *Fundamental Principles of Industrial Filtration. A Critical Review of Present Knowledge*. Trans. Inst. Chem. Eng., 1938. **16**: p. 168-188.
83. Wronski, S.K., A.K. Bin, and L.K. Laskowski, *Anomalous behaviour during the initial stage of constant pressure filtration*. The Chemical Engineering Journal, 1976. **12**: p. 143-147.
84. Kozicki, W., A.R.K. Rao, and C. Tiu, *On the Parabolic Representation of Constant Pressure Filtration*. The Canadian Journal of Chemical Engineering, 1970. **48**: p. 463-465.
85. Salman, A.D., M. Ghadiri, and M.J. Hounslow, *Particle Breakage* 2007, Oxford: Elsevier.
86. Lowrison, G.C., *Crushing and Grinding: The Size Reduction of Solid Materials*. 1974, London: Butterworths.
87. Ghadiri, M. and Z. Zhang, *Impact attrition of particulate solids. Part 1: A theoretical model of chipping*. Chemical Engineering Science, 2002. **57**: p. 3659-3669.
88. Gahn, C. and A. Mersmann, *The brittleness of substances crystallized in industrial processes*. Powder Technology, 1995. **85**: p. 71-81.
89. Hare, C. and M. Ghadiri, *Attrition of paracetamol and aspirin under bulk shear deformation*. Chemical Engineering Science, 2015. **125**: p. 13-19.
90. Griffith, A.A., *Phenomena of rupture and flow in solids*. Phil. Trans. Roy. Soc., 1920. **A221**: p. 163-198.
91. Roberts, R.J., R.C. Rowe, and P. York, *The relationship between the fracture properties, tensile strength and critical stress intensity factor of organic solids and their molecular structure*. International Journal of Pharmaceutics, 1995. **125**: p. 157-162.
92. Olusanmi, D., K.J. Roberts, M. Ghadiri, and Y. Ding, *The breakage behaviour of Aspirin under quasi-static indentation and single particle impact loading: Effect of crystallographic anisotropy*. International Journal of Pharmaceutics, 2011. **411**: p. 49-63.

93. Sinnott, R.K., *Coulson & Richardson's CHEMICAL ENGINEERING*. 3rd ed. Vol. 6. 1999, Oxford: Butterworth Heinemann.
94. Rossum, G.van, *Python Tutorial Technical Report CS-R9526*, 1995, Centrum voor Wiskunde en Informatica (CWI): Amsterdam.
95. Long, B., J. Li, Y. Song, and J. Du, *Temperature Dependent Solubility of alpha-Form L-Glutamic Acid in Selected Organic Solvents: Measurements and Thermodynamic Modeling*. Industrial & Engineering Chemistry Research, 2011. **50**: p. 8354-8360.
96. Ma, C. and X. Wang, *Closed-loop control of crystal shape in cooling crystallization of L-glutamic acid*. Journal of Process Control, 2012. **22**: p. 72-81.
97. Mo, Y., L. Dang, and H. Wei, *Solubility of alpha-form and beta-form of L-glutamic acid in different aqueous solvent mixtures*. Fluid Phase Equilibria, 2011. **300**: p. 105-109.
98. Ni, X. and A. Liao, *Effects of mixing, seeding, material of baffles and final temperature on solution crystallization of L-glutamic acid in an oscillatory baffled crystallizer*. Chemical Engineering Journal, 2010. **156**: p. 226-233.
99. Belitz, H., W. Grosch, and P. Schieberle, *Food Chemistry*. 4th ed 2009, Berlin: Springer.
100. Borissova, A., S. Khan, T. Mahmud, K. Roberts, J. Andrews, P. Dallin, Z. Chen, and J. Morris, *In Situ Measurement of Solution Concentration during the Batch Cooling Crystallization of L-Glutamic Acid using ATR-FTIR Spectroscopy Coupled with Chemometrics*. Crystal Growth & Design, 2008. **9**(2): p. 692-706.
101. Manzurola, E. and A. Apelblat, *Solubilities of L-glutamic acid, 3-nitrobenzoic acid, p-toluic acid, calcium-L-lactate, calcium gluconate, magnesium-DL-aspartate, and magnesium-L-lactate in water*. J. Chem. Thermodynamics, 2002. **34**: p. 1127-1136.
102. Bisker-Leib, V. and M. Doherty, *Modelling the Crystal Shape of Polar Organic Materials: Prediction of Urea Crystals Grown from Polar and Nonpolar Solvents*. Crystal Growth & Design, 2001. **1**(6): p. 455-461.
103. Zeng, L., M. Zha, M. Ardoino, P. Franzosi, L. Zanotti, G. Zuccalli, and C. Paorici, *Solution crystal growth of urea and derivatives for nonlinear optical applications*. Journal of Crystal Growth, 1996. **166**: p. 528-532.
104. Hughes, E. and H. Yakel, *The Crystal Structure of Biuret Hydrate*. Acta Cryst., 1961. **14**: p. 345-352.
105. Kirsch, R., *Kinetics and mechanism of urea aggregation*, in *School of Chemical and Process Engineering 2014*, University of Leeds.
106. Lee, F. and L. Lahti, *Solubility of Urea in Water-Alcohol Mixtures*. Journal of Chemical Engineering Data, 1972. **17**(3): p. 304-306.
107. AstraZeneca. *Zurampic (lesinurad) approved in the European Union for patients with gout*. 2016 [1/09/2016]; Available from: <https://www.astrazeneca.com/media-centre/press-releases/2016/zurampic-lesinurad-approved-in-the-european-union-for-patients-with-gout-19022016.html>.
108. Quart, B., J. Girardet, E. Gunic, and L. Yeh, *NOVEL COMPOUNDS AND COMPOSITIONS AND METHODS OF USE*, WIPO, Editor 2008: USA.
109. Gamble, J., et al., *Application of imaging based tools for the characterisation of hollow spray dried amorphous dispersion particles*. International Journal of Pharmaceutics, 2014. **465**: p. 210-217.
110. Olusanmi, D., D. Jayawickrama, D. Bu, G. McGeorge, H. Sailes, J. Jelleher, J. Gamble, U. Shah, and M. Tobyn, *A control strategy for bioavailability enhancement by size*

- reduction: Effect of micronization conditions on the bulk, surface and blending characteristics of an active pharmaceutical ingredient.* Powder Technology, 2014. **258**: p. 222-233.
111. Kinnunen, H., G. Hebbink, H. Peters, D. Huck, L. Makein, and R. Price, *Extrinsic lactose fines improve dry powder inhaler formulation performance of a cohesive batch of budesonide via agglomerate formation and consequential co-deposition.* International Journal of Pharmaceutics, 2015. **478**: p. 53-59.
 112. Qu, L., Q. Zhou, J. Denman, P. Stewart, K. Hapgood, and D. Morton, *Influence of coating material on the flowability and dissolution of dry-coated fine ibuprofen powders.* European Journal of Pharmaceutical Sciences, 2015. **78**: p. 264-272.
 113. Qu, L., P. Stewart, K. Hapgood, S. Lakio, D. Morton, and Q. Zhou, *Single-step Coprocessing of Cohesive Powder via Mechanical Dry Coating for Direct Tablet Compression.* Journal of Pharmaceutical Sciences, 2016.
 114. Petrak, D., S. Dietrich, G. Eckardt, and M. Köhler, *Two-dimensional particle shape analysis from chord measurements to increase accuracy of particle shape determination.* Powder Technology, 2015. **284**: p. 25-31.
 115. Ulusoy, U. and I. Kursun, *Comparison of different 2D image analysis measurement techniques for the shape of talc particles produced by different media milling.* Minerals Engineering, 2011. **24**: p. 91-97.
 116. Yanrong, Z., K. Xiangming, G. Liang, and B. Yun, *Characterization of the mesostructural organization of cement particles in fresh cement paste.* Construction and Building Materials, 2016. **124**: p. 1038-1050.
 117. Pretoro, G., L. Zema, A. Gazzaniga, and P. Kleinebudde, *Impact of needle-like crystals on wet and solid-lipid extrusion processes.* Powder Technology, 2015. **270**: p. 476-483.
 118. Liu, W., C. Ma, and X. Wang, *Novel Impinging Jet and Continuous Crystallizer Design for Rapid Reactive Crystallization of Pharmaceuticals.* Procedia Engineering, 2015. **102**: p. 499-507.
 119. Zhang, R., C. Ma, J. Liu, and X. Wang, *On-line measurement of the real size and shape of crystals in stirred tank crystalliser using non-invasive stereo vision imaging.* Chemical Engineering Science, 2015. **137**: p. 9-21.
 120. Krupa, A., R. Jachowicz, M. Kurek, W. Figiel, and M. Kwiecien, *Preparation of solid self-emulsifying drug delivery systems using magnesium aluminometasilicates and fluid-bed coating process.* Powder Technology, 2014. **266**: p. 329-339.
 121. Sochan, A., P. Zielinski, and A. Bieganowski, *Selection of shape parameters that differentiate sand grains, based on the automatic analysis of two-dimensional images.* Sedimentary Geology, 2015. **327**: p. 14-20.
 122. Campaña, I., A. Calvo, A. González, J. Bermúdez, and E. Carbonell, *Assessing automated image analysis of sand grain shape to identify sedimentary facies, Gran Dolina archaeological site (Burgos, Spain).* Sedimentary Geology, 2016.
 123. Duval, M., I. Campaña, V. Guilarte, L. Miguens, J. Iglesias, and S. Sierra, *Assessing the uncertainty on particle size and shape: Implications for ESR and OSL dating of quartz and feldspar grains.* Radiation Measurements, 2015. **81**: p. 116-122.
 124. Das, S., S. Behara, D. Morton, I. Larson, and P. Stewart, *Importance of particle size and shape on the tensile strength distribution and de-agglomeration of cohesive powders.* Powder Technology, 2013. **249**: p. 297-303.

125. Ripperger, S., W. Gösele, C. Alt, and T. Loewe, *Filtration, 1. Fundamentals*. Ullmann's Encyclopedia of Industrial Chemistry, 2013: p. 1-38.
126. Mahdi, F. and R. Holdich, *Laboratory cake filtration testing using constant rate*. Chemical Engineering Research and Design, 2013. **91**: p. 1145-1154.
127. LUM-GmbH, *STEP-Technology*, 2006: Germany. p. 1.
128. Sutherland, K., *Filters and Filtration Handbook*. 5th ed2008, Oxford: Butterworth-Heinemann.
129. Green, M., M. Eberl, and K. Landman, *Compressive Yield Stress of Flocculated Suspensions: Determination via Experiment*. Materials, Interfaces, and Electrochemical Phenomena, 1996. **42**(8): p. 2308-2318.
130. Kumar, S., T. Pirog, and D. Ramkrishna, *A new method for estimating hindered creaming/settling velocity of particles in Polydisperse Systems*. Chemical Engineering Science, 2000. **55**: p. 1893-1904.
131. Buscall, R. and L. White, *The Consolidation of Concentrated Suspensions Part 1. - The Theory of Sedimentation*. J. Chem. Soc., Faraday Trans. 1, 1987. **83**(3): p. 873-891.
132. Landman, K., L. White, and M. Eberl, *Pressure Filtration of Flocculated Suspensions*. AIChE Journal, 1995. **41**(7): p. 1687-1700.
133. Lerche, D. and T. Sobisch, *Evaluation of particle interactions by in situ visualization of separation behaviour*. Colloids and Surfaces A: Physicochem. and Eng. Aspects, 2014. **440**: p. 122-130.
134. Palhares, L., C.d. Santos, and T. Hunter, *Study of citric acid dispersant in the settling behavior of slate powder suspensions*. International Journal of Mineral Processing, 2016. **150**: p. 39-46.
135. Loginov, M., E. Vorobiev, N. Lebovka, and O. Larue, *Compression-permeability characteristics of mineral sediments evaluated with analytical photocentrifuge*. Chemical Engineering Science, 2011. **66**: p. 1296-1305.
136. Loginov, M., N. Lebovka, and E. Vorobiev, *Multistage centrifugation method for determination of filtration and consolidation properties of mineral and biological suspensions using the analytical photocentrifuge*. Chemical Engineering Science, 2014. **107**: p. 277-289.
137. Knoll, J., W. Dammert, and H. Nirschl, *Integration of a microscope into a centrifuge for adhesion force measurement of particles*. Powder Technology, 2017. **305**: p. 147-155.
138. Beer, *Bestimmung der Absorption des rothen Lichts in farbigen Flüssigkeiten" (Determination of the absorption of red light in colored liquids)*. Annalen der Physik und Chemie, 1852. **86**: p. 78-88.
139. Curvers, D., H. Saveyn, P. Scales, and P. Meeren, *A centrifugation method for the assessment of low pressure compressibility of particulate suspensions*. Chemical Engineering Journal, 2009. **148**: p. 405-413.
140. Usher, S., L. Studer, R. Wall, and P. Scales, *Characterisation of dewaterability from equilibrium and transient centrifugation test data*. Chemical Engineering Science, 2013. **93**: p. 277-291.
141. Kirsch, R., R. Williams, U. Bröckel, R. Hammond, and X. Jia, *Direct Observation of the Dynamics of Bridge Formation between Urea Prills*. Industrial & Engineering Chemistry Research, 2011. **50**: p. 11728-11733.

142. Grof, Z., C. Schoellhammer, P. Rajniak, and F. Štěpánek, *Computational and experimental investigation of needle-shaped crystal breakage*. International Journal of Pharmaceutics, 2011. **407**: p. 12-20.
143. Grof, Z. and F. Štěpánek, *Distribution of breakage events in random packings of rodlike particles*. Physical Review E, 2013. **88**(1): p. 1-5.
144. Grof, Z. and F. Štěpánek, *Quantifying the effect of fillers on the breakage behaviour of needle-shaped particles*. Advanced Powder Technology, 2016. **27**: p. 1093-1100.
145. Golchert, D., R. Moreno, M. Ghadiri, and J. Litster, *Effect of granule morphology on breakage behaviour during compression*. Powder Technology, 2004. **143**: p. 84-96.
146. Sato, K., H. Nagai, K. Hasegawa, K. Tomori, H. Kramer, and P. Jansens, *Two-dimensional population balance model with breakage of high aspect ratio crystals for batch crystallization*. Chemical Engineering Science, 2008. **63**: p. 3271-3278.
147. Namazu, T., Y. Isono, and T. Tanaka, *Evaluation of Size Effect on Mechanical Properties of Single Crystal Silicon by Nanoscale Bending Test Using AFM*. Journal of Microelectromechanical Systems, 2000. **9**(4): p. 450-459.
148. Sohi, S., S. Conell, D. Harbottle, and F. Muller, *A Method for the Determination of Mechanical Properties of Needle Shaped Crystals Using Atomic Force Microscopy*, 2016, University of Leeds: Leeds.
149. Weibull, W., *A Statistical Distribution Function of Wide Applicability*. Journal of Applied Mechanics, 1951. **18**(3): p. 293-297.
150. Haynes, W.M., *CRC Handbook of Chemistry and Physics*. 95th ed2015, Boca Raton, FL: CRC Press LLC.
151. Downey, A., J. Elkner, and C. Meyers, *How to Think Like a Computer Scientist*. 1st ed2002, Wellesley, MA; USA: Green Tea Press.